

國立臺灣大學工學院材料科學與工程學系

博士論文

Department of Materials Science and Engineering

College of Engineering

National Taiwan University

Doctoral Dissertation

AISI 440C合金鋼透鏡狀麻田散鐵

次微米結構分析

The Analysis of Lenticular Martensite Submicron

Structure in AISI 440C Alloying Steel

張雅齡

Ya-Ling Chang

指導教授：楊哲人 博士

Advisor: Jer-Ren Yang, Ph.D.

中華民國104年07月

July, 2015



# 國立臺灣大學博士學位論文 口試委員會審定書

論文中文題目： AISI 440C 合金鋼透鏡狀麻田散鐵  
次微米結構分析

論文英文題目： The Analysis of Lenticular Martensite  
Submicron Structure in AISI 440C  
Alloying Steel

本論文係張雅齡君 (D99527007) 在國立臺灣大學材料  
科學與工程學系、所完成之博士學位論文，於民國 104 年 07  
月 30 日承下列考試委員審查通過及口試及格，特此證明

口試委員： 楊哲人 楊哲人  
(指導教授)

林新智 林新智

熊樂群 熊樂群

王星豪 王星豪

王樂民 王樂民

黃慶淵 黃慶淵

陳志遠 陳志遠

系主任、所長 林招松 林招松 (簽名)

## 誌謝




騎著腳踏車徜徉在校園中正要去買台大牛奶，環顧校園處處可見穿著學士服的畢業生們在拍照留戀著，今年的我也有幸與他們一同參加畢業典禮，想起當初帶著兒時的夢想來到台大念博士班，回顧在台大生活的點點滴滴，嘗盡酸甜苦辣，終日不是泡在圖書館念 paper 就是在實驗室磨試片，充實而忙碌著。

在碩班期間經常耳聞楊哲人老師的事蹟，因此懷抱著敬佩的心情來到相變態實驗室求學，果然老師真真切切的在學術上、研究經驗上和資源給予我充沛的指導與幫助，開啟我對微觀材料科學中的新視野，從奈米的角度走入鋼鐵材料；在生活中，老師更是給予我很多鼓勵與支持，在我最低潮的時候，協助我排解與盡力提供協助；在國際交流上，使我有機會與新加坡國立大學呂力老師結識，一同專研與發表文章，因此對楊哲人老師有著滿滿的感謝。除此之外，我要感激論文口試主持人王星豪教授，王老師也給予我很多鼓勵與加油，使我心中倍感溫馨與感動，同時感謝王樂明教授、熊樂群教授、林新智教授、黃慶淵博士和陳志遠博士撥空前來參加論文口試，並對論文提出建議與指導，使論文更加完善。

在這幾年，首先感謝，實驗室的學長姐們——陳學人先生、廷玉學長、威志學長、鴻威學長、欣怡學姊、孝慈學姊、正勳學長、柏銘、苡彥、孟揚教導我儀器的使用與做研究的細節，當我研究遇到困難時，感謝宇庭提出有效的見解，感謝實驗室的學弟妹們——申賀、俊源、宜良、惠琴、家瑋、以澄、德徵、景明、承佑、紹璞、昱文、亦傑、至閔、博彥、采甫、致睿、承翰、啟任、王涵、世雯、世寧在實驗室的陪伴，為生活中增添不少有趣的色彩，感謝馬龍學長、廖先生、家煒在儀器上的指導，感謝遠在新加坡的呂力老師、李柳和呂佳，在 paper 上的協助。

最後，我要感謝我的父母，含辛茹苦的將我們三姐弟拉拔長大，總是擔心我們穿不好吃不飽，時時耳提面命生活中的細節，終於家族中第一位博士畢業了，



謝謝阿伯、爸爸、媽媽、介霖、維鈞無私無悔的支持我，讓我無後顧之憂的完成學位。在對的地方、對的時間，我遇到我生命中對的人——伯宇，沒有他就沒有這本論文，他在各方面都將我照顧了無微不至，即使當老天爺跟他開了一個大玩笑，他都沒有半點憂傷，只有我大哭不止，還要反過來安慰我、關心我，在此時此刻真的已經到達一個言語完全無法表示其情與意之境界，而隨及面對的是爸爸的突然倒下，2014/2 到 2015/2 真的是我生命中最黑暗的日子，到現在我都不知道我怎麼走過來，好險！可謂是傻人有傻福，關關難過關關過，這一切都過去了，它們將隨著時間的流逝成為我生命的養份與軌跡，最後我向曾經幫助過我的人，至上一十二萬分的謝意與敬意——謝謝有你(妳)！



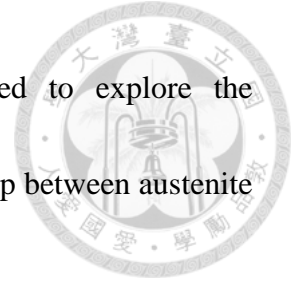
## Abstract



This work mainly focuses on the investigation of the microstructure and transformation of lenticular martensite in AISI 440C stainless steel. The research can be divided into two parts. The goal of the first is to analyze the transformation and morphology of lenticular martensite; the goal of the second is to observe the evolution of carbide formation in lenticular martensite during tempering treatment.

In the first part, by controlling the homogenization temperature, an appropriate lenticular martensite structure was obtained, facilitating the following observation. The influences of the alloying element content on  $M_s$  temperature and the transformed martensite morphology were analyzed with electrical microscopy. Due to the high alloying element content of AISI 440C stainless steel, even after homogenization treatment, the  $M_7C_3$  carbides are still distributed in the austenite matrix and therefore become the nucleation sites of lenticular martensite. During the martensite transformation process, the initial nucleation product is plate martensite, which then grows into a lenticular martensite structure. Lenticular martensite contains three regions: a midrib (which can be seen as the former plate martensite structure), a twinned region, and an untwinned region. These three regions differ not only in their morphologies but also in their misorientation distribution. Transmission electron microscopy (TEM) and

electron backscatter diffraction (EBSD) techniques were applied to explore the misorientation in these regions and the crystal orientation relationship between austenite and martensite.



In our observations, a single lenticular martensite grain shows an elliptical morphology. Furthermore, a specimen polished with the focus ion beam (FIB) method provides 3-D images information and confirms that lenticular martensite is shaped like a thick shell. The crystallography of lenticular martensite formed in coarse austenite grains was investigated using electron backscattered diffraction (EBSD). Although the spread in diffracted intensity within pole figures was significant, due to the orientation gradient within lenticular martensite, the trend of pole figures indicated that the lenticular martensite approximately adopted a Kurdjumov-Sachs (K-S) orientation relationship with respect to the austenite matrix. The orientation relationships of variant pairings (zigzag, spear, and kink types) have been analyzed.

The aim of the second part of this research is to discuss the effects of tempering treatment on lenticular martensite. After tempering at 400°C, there exist two different kinds of cementite: the "needle" type, which does not transform into  $M_7C_3$  even after a long tempering treatment, and the "rice" type, which first nucleates at twins in the midrib region and dislocations in the untwinned region, continues to grow during

tempering treatment, and finally becomes a parallelogram-shaped  $M_7C_3$  carbide. The discrepancies between the two types of cementites in shape and crystallographic relationship can be attributed to the nucleation and growing mechanisms. With electrical microscopy analysis, the displacive mechanism and diffusion mechanism are applied to elucidate the formation of cementites in lenticular martensite.

**Keywords:** *lenticular martensite, variant pair, tempering, cementite, nucleation mechanisms*

## 中文摘要



本研究是以 AISI 440C 中生成的透鏡狀麻田散鐵為研究對象，首先試著控制均質化溫度，使碳化物融入基體中，探討基體中合金元素的含量對 Ms 溫度與麻田散鐵形貌的影響。透鏡狀麻田散鐵分別在沃斯田鐵晶界與未完全固溶的  $M_7C_3$  邊界優先成核，透鏡狀麻田散鐵的生長過程是先生成板片狀麻田散鐵再轉變成透鏡狀麻田散鐵，因此造成透鏡狀麻田散鐵含有三個區域；含有兩種缺陷-雙晶與差排，利用穿透式電子顯微鏡 (TEM) 與背向散射電子繞射分析 (EBSD) 微觀觀察其三個區域與 misorientation 的變化，並觀察透鏡狀麻田散鐵的 2-D 形貌，發現雙晶具有彎曲現象，與藉著聚焦式離子束顯微鏡 (FIB) 觀察透鏡狀麻田散鐵的 3-D 形貌為橢圓體，巨觀觀察透鏡狀麻田散鐵間相互連結的樣貌有 spear, kink 及 zigzag array 三種，均與沃斯田鐵基體呈現 Kurdjumov-Sachs (K-S) 方位關係。

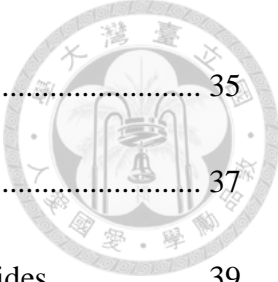
以 400°C 回火熱處理的透鏡狀麻田散鐵微結構變化，在同一透鏡狀麻田散鐵晶粒內有兩種雪明碳鐵生成，一種是 needle 型，與肥粒鐵呈現 Isaichev OR，只具有一個方向性，不會隨時間轉變成  $M_7C_3$ ；另一種為 rice 型，與肥粒鐵呈現 Bagaryatskii OR，先在中脊區(雙晶)與無雙晶區(差排)生成，隨著時間拉長 cementite 越來越多、越來越大，為降低表面能而聚集成圓形，再聚集經由 in-situ 機制轉變為平行四邊形的  $M_7C_3$ ，前述兩種雪明碳鐵的成核機制分別為剪切機制與擴散機制。

**關鍵字：**透鏡狀麻田散鐵、聯結、回火熱處理、雪明碳鐵、成核機制

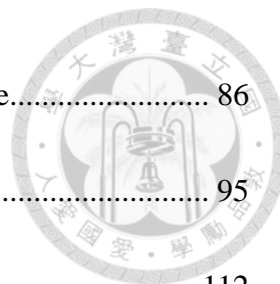
# Contents



誌謝.....	I
Abstract.....	III
中文摘要.....	VI
Contents.....	VII
Figure content.....	XI
Table content.....	XXVII
Chapter 1 Introduction.....	1
Chapter 2 Literature Review.....	5
2.1 Introduction of martensite .....	5
2.1.1 Martensitic phase transformation .....	5
2.1.2 The orientation relationships of martensite transformation.....	7
2.1.3 The phenomenological theory of martensite crystallography .....	9
2.2 The microstructure of martensites .....	17
2.2.1 Lath martensites.....	18
2.2.2 Plate martensites .....	19
2.2.3 Lenticular martensites.....	21
2.3 The tempering of martensite.....	35



2.3.1 Introduction of tempered martensite .....	35
2.3.2 Tempering of Chromium-containing alloy steels .....	37
2.4 Carbides in martensitic steel and transformation of carbides.....	39
2.4.1 Categories of carbides .....	40
2.4.2 Transformation and mechanism.....	45
Chapter 3 Lenticular martensite in AISI 440C stainless steel .....	51
3.1 Introduction .....	51
3.2 Experimental procedure.....	52
3.3 Results and Discussion .....	55
3.3.1 The influence of different austenitization temperature.....	55
3.3.2 The transformation of lenticular martensite .....	67
3.3.3 The morphologies of lenticular martensite .....	75
3.4 Conclusions .....	80
Chapter 4 Crystallographic analysis of lenticular martensite by electron backscattered diffraction .....	81
4.1 Introduction .....	81
4.2 Experimental procedure.....	85
4.3 Results and Discussion .....	86



4.3.1 Crystallographic analysis of lenticular martensite.....	86
4.3.2 Coupling of lenticular martensite .....	95
4.4 Conclusions .....	112
Chapter 5 Tempered lenticular martensite in AISI 440C stainless steel by transmission electron microscopy .....	114
5.1 Introduction .....	114
5.2 Experimental procedure.....	116
5.3 Results .....	118
5.3.1 Needle-like cementite carbides.....	119
5.3.2 Rice-like cementite carbides.....	130
5.3.3 $M_7C_3$ carbides .....	137
5.4 Discussion.....	144
5.4.1 Carbide precipitation .....	144
5.4.2 Diffusion mechanism for alloy carbide precipitation .....	146
5.5 Conclusion.....	149
Chapter 6 The misorientation change in lenticular martensite by Electron Backscattered Diffraction and Convergent Beam Kikuchi Line Diffraction Pattern.....	151

6.1 Introduction .....	151
6.2 Experimental Procedure .....	157
6.3 Results and Discussion .....	158
6.3.1 Convergent beam Kikuchi line diffraction patterns (CBKLDP) .	158
6.3.2 Electron Backscatter Diffraction (EBSD) .....	160
6.4 Conclusions .....	167
Chapter 7 General conclusion.....	168
References... ..	172

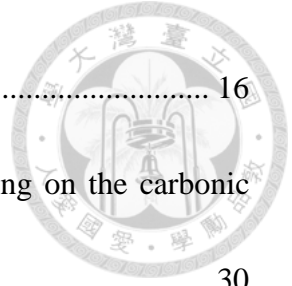




## Figure content



Figure 2-1	Diagram of martensite crystal, showing shear and surface tilting[2].....	14
Figure 2-2	Schematic representation of the Bain lattice correspondence between principal axes of BCT martensite and FCC austenite unit cells[24]... ..	14
Figure 2-3	Three kinds of Invariant plane Strains. The heavy lines indicate the shape before deformation $\delta$ , $s$ and $m$ represent the magnitudes of the dilatational strain shear strain and general displacement respectively[26].....	15
Figure 2-4	(a) and (b) show the effect of the Bain strain on austenite, which when undeformed is represented as a sphere of diameter $wx=yz$ in three-dimensions. The strain transforms it to an ellipsoid of revolution. (c) shows the <b>ILS</b> obtained by combining the Bain strain with a rigid body rotation through an angle $\theta$ . $a_1$ , $a_2$ and $a_3$ refer to $[100]_\gamma$ , $[010]_\gamma$ and $[001]_\gamma$ axes respectively[25]. .....	15
Figure 2-5	The phenomenological theory of martensite crystallography[25]. ....	16
Figure 2-6	Formation of martensite plate, illustrating two types of lattice	



	deformation: slip and twinning[28].....	16
Figure 2-7	Martensites exhibit various morphologies depending on the carbonic content[30]. .....	30
Figure 2-8	Optical micrograph shows packets and blocks within individual prior austenite grains. The prior austenite grain boundaries enclosing the grain in the middle of the micrograph are indicated by dotted lines[34]. .....	30
Figure 2-9	Transmission electron micrograph showing internally twinned martensite plate in a matrix of retained austenite in an Fe-Ni-C alloy. The fine twins in the martensite are transformation twins[27]. .....	31
Figure 2-10	Schematic representation of martensite lens during growth. Origin of axes coincides with position of embryo[54]. .....	31
Figure 2-11	Summary of the stress-induced growth behavior of thin plate martensite by tensile deformation at various temperature in Fe-31Ni-10Co-3Ti steel [48].....	32
Figure 2-12	Optical metallographs taken from the homogenized specimens subzero cooled at -196°C for (a) 8s, (b) 10s, (c) 12s, and (d) 30 min[55].....	32
Figure 2-13	Fraction of twinned region as a function of formation temperature of	



martensite: O, Fe-31Ni-0.23C;  $\Delta$ , Fe-29Ni-0.26C;  $\square$ ,  
Fe-31Ni-0.29C[57]. ..... 33

Figure 2-14 Schematic illustration showing the development of the substructure in  
lenticular martensite: (a)  $\rightarrow$  (b)  $\rightarrow$  (c-1)  $\rightarrow$  (c-2) in Fe-33Ni alloy  
( $M_s=171K$ ), (a)  $\rightarrow$  (b)  $\rightarrow$  (c-1')  $\rightarrow$  (c-2') in Fe-31Ni alloy  
( $M_s=223K$ )[62]. ..... 33

Figure 2-15 (a) The open and solid symbols, i.e., circles, square and triangles,  
show the measured points of the orientations in the martensite and  
austenite, respectively. (b) and (c) are the corresponding stereographic  
projections around  $[101]_A$  and  $[111]_A$  axes, respectively, showing the  
change in local orientation relationship. The  $(011)_M$  and  $[111]_M$  of  
K-S and N-W OR are shown as solid circles. The solid stars show the  
calculated  $(011)_M$  and  $[111]_M$  using the PTMC. Each shaped open  
symbol shows the measured  $(011)_M$  and  $[111]_M$  direction between the  
austenite and martensite with the same symbols in (a)[21]. ..... 34

Figure 2-16 Microstructure showing the *in situ* transformation of cementite to  
 $M_7C_3$  in 16.5%Cr-3.65%C steel tempered for 1 hr at 600°C after  
rapid quenching. (a) bright field image, (b) selected area diffraction



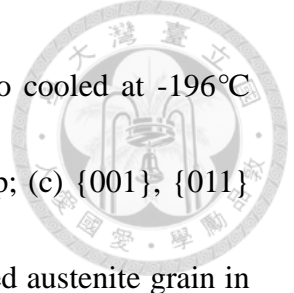
	pattern and its schematic key diagram, (c) dark field images taken respectively from the 120 reflection spot of $M_3C$ , and (d) the 2641 reflection spot of $M_7C_3$ [129].	48
Figure 2-17	Schematic drawing of the processes of $M_3C \rightarrow M_7C_3$ and $M_7C_3 \rightarrow M_{23}C_6$ reactions. (a) $M_3C \rightarrow M_7C_3$ reaction, (b) $M_7C_3 \rightarrow M_{23}C_6$ reaction[130].	48
Figure 2-18	Microstructure showing the <i>in situ</i> transformation of $M_7C_3$ to $M_{23}C_6$ in 18.6 %Cr-3.40%W-3.63%C steel tempered for 10h at 700°C. (a) Bright field image, (b) selected area diffraction pattern and its schematic key diagram, (c) and (d) dark field images taken respectively from the 220 reflection spot of $M_{23}C_6$ and the 4261 reflection spot of $M_7C_3$ [130].	49
Figure 2-19	Schematic illustration representing the process of $M_{23}C_6 \rightarrow M_6C$ reaction[130].	49
Figure 2-20	Microstructure showing the <i>in situ</i> transformation of $M_{23}C_6$ to $M_6C$ in 18.4%Cr-8.31W-3.6%C steel tempered for 120h at 700°C. (a) Bright field image, (b) selected area diffraction pattern and its key diagram, (c) and (d) dark field images taken respectively from the 202	

	reflection spot of $M_{23}C_6$ and the 333 reflection spot of $M_6C[130]$ . ....	50
Figure 2-21	Microstructure showing the <i>in situ</i> transformation of cementite to $M_7C_3$ in 16.5%Cr-3.65%C steel tempered for 1 hr at 600°C after rapid quenching, (a) bright field image, (b) selected area diffraction pattern and its schematic key diagram, (c) dark field images taken respectively from the 113 reflection spot of cementite and (d) the 4400 reflection spot of $M_7C_3[129]$ . ....	50
Figure 3-1	Schematic representation showing the production procedure of the original material. ....	54
Figure 3-2	Schematic representation showing the subzero treatment of the material. ....	54
Figure 3-3	Optical microscopy image of (a) As-received AISI 440C steel (b) lath martensite microstructure austenitized at 1000°C, (c) lenticular martensite microstructure austenitized at 1150°C and (d) lenticular martensite microstructure austenitized at 1200°C. ....	61
Figure 3-4	(a) TEM bright field image, (b) dark field image and (c) the corresponding diffraction pattern of $M_7C_3$ carbides. ....	62
Figure 3-5	TEM image shown the (a) twin and (b) antiphase boundaries within	



	the $M_7C_3$ carbides.....	62
Figure 3-6	TEM bright field, dark field image and the corresponding diffraction pattern image of (a) lath martensite microstructure austenitized at 1000°C (b) lenticular martensite microstructure austenitized at 1200°C .....	64
Figure 3-7	BES image of (a), (c) lath martensite microstructure austenitized at 1000°C and (b), (d) lenticular martensite microstructure austenitized at 1200°C in AISI 440C. ....	65
Figure 3-8	(a) and (b) Thermo-Calc data indicating the chemical composition of austenite phase in the 1000°C and 1200°C equilibrium state. ....	66
Figure 3-9	TEM bright field and dark field images and the corresponding diffraction pattern image of thin-plate martensite microstructure.....	71
Figure 3-10	TEM bright field and dark field images and the corresponding diffraction pattern image of lenticular martensite microstructure.....	72
Figure 3-11	TEM bright field and dark field images and the corresponding diffraction pattern image of lenticular martensite microstructure.....	73
Figure 3-12	Some of the area of the untwinned region observed by different two beam condition: (a) $g=101$ and (b) $g=011$ . ....	74

Figure 3-14	SEM image showing the substructure morphologies of lenticular martensite. ....	77
Figure 3-15	TEM observation of lenticular martensite (a) bright field image, (b) dark field image, (c) illustration of the bending of twins near the midrib, (d) corresponding diffraction pattern image. ....	78
Figure 3-16	3-D observation of lenticular martensite in SEM by FIB technique..	79
Figure 3-17	Illustration of the 3-D structure of lenticular martensite.....	79
Figure 4-1	(a) OM taken from the homogenized specimen; (b) OM taken from the homogenized sample subzero cooled at -196 °C for 30 s, showing three characteristic morphologies of non-parallel martensite variants: (i) zigzag, (ii) spear and (iii) kink arrays. (The lump-shaped particles: $M_7C_3$ .).....	100
Figure 4-2	(a) and (b) Thermo-Calc data indicate that the chemical composition of austenite phase in the 1200°C equilibrium state consists of 0.60C-14.1Cr (wt.%), and 1000°C, 0.24C-10.8Cr (wt.%); (c) lath martensite obtained from the sample austenitized at 1000°C for 3 days and cooled to ambient temperature. ....	103
Figure 4-3	(a) Image quality map of lenticular martensite variants within	



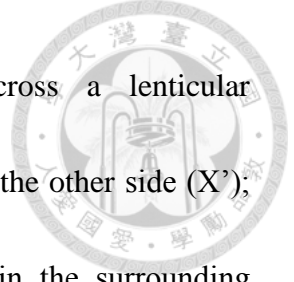
austenite grains of a homogenized sample subzero cooled at  $-196^{\circ}\text{C}$  for 15 min.; (b) the corresponding orientation map; (c)  $\{001\}$ ,  $\{011\}$  and  $\{111\}$  pole figures obtained from the delineated austenite grain in (b); (d) the simulated pole figures for K-S OR; (e) the simulated pole figures for N-W OR. (The red spots are related to the diffraction from the austenite matrix; the black spots, to that from the different martensite plates.)..... 104

Figure 4-4 In the 001 pole figure of 24 variants of K-S OR, a Bain zone consists of one ring and two corresponding bars, each containing eight poles. For example, eight variants, V1, V4, V8, V11, V13, V16, V21 and V24, are in the same Bain Zone. (The red spots are related to the diffraction from the  $\{0\ 0\ 1\}$  poles of the austenite matrix.)..... 105

Figure 4-5 (a) Orientation map of lenticular martensite variants within austenite grains, showing zigzag and spear couplings; (b) the corresponding misorientation map of the austenite grains; (c) orientation map of a lenticular martensite plate with kink couplings. (The lump-shaped particles:  $\text{M}_7\text{C}_3$ .) ..... 106

Figure 4-6 (a) Orientation map of lenticular martensite zigzag variants within an





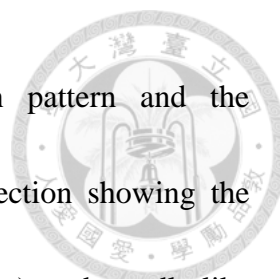
austenite grain; (b) misorientation profile across a lenticular martensite plate transversely from one side (X) to the other side (X'); (c) misorientation profile along the line Y–Y' in the surrounding austenite. (The lump-shaped particles:  $M_7C_3$ ). ..... 107

Figure 4-7 (a) Orientation map of a lenticular martensite plate; (b) corresponding misorientation map of the surrounding austenite; (c) misorientation profile along the longitudinal axis (midrib), the line L – L'; (d) misorientation profile across the lenticular plate transversely from one side (M) to the other side (M'); (e) misorientation profile along the line N – N' in the surrounding austenite; (f) misorientation profile along the line O – O' in the surrounding austenite. .... 108

Figure 4-8 (a) Poles of  $(3\ 15\ 10)_\gamma$ ,  $(3\ 10\ 15)_\gamma$ ,  $(3\ 15\ 10)_\gamma$  and  $(3\ 10\ 15)_\gamma$  are located symmetrically around the pole of  $(0\ 1\ 1)_\gamma$ . (b) If the pole of the V1 variant is fixed on the pole of  $(3\ 15\ 10)_\gamma$ , then the V6, V16 and V17 poles can be set on the poles of  $(3\ 10\ 15)_\gamma$ ,  $(3\ 15\ 10)_\gamma$  and  $(3\ 10\ 15)_\gamma$ . .... 109

Figure 4-9 SEM images showing the (a) kink, (b) zigzag array, (c) spear, and (d) crossed region morphologies of coupling of lenticular martensite. ...110

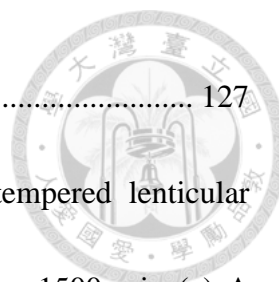
Figure 4-10	Orientation map of (a) spear ( <b>A-C</b> ) and kink ( <b>A-B</b> ) (b) zigzag ( <b>H-G</b> ) (c) kink ( <b>E-D</b> and <b>E-F</b> ) (d) misorientation map of austenite corresponding to (c). ....111
Figure 4-11	Orientation map of a sample (a) cooled to Ms (cryogenic treatment) for 8 seconds; then (b) cooled down to Ms (cryogenic treatment) for 30 seconds. ....112
Figure 4-12	Formation process of different couplings of lenticular martensite. ..112
Figure 5-1	Schematic profiles of the site fractions of the substitutional elements ( $y_I$ ) and C ( $y_C$ ) across the transforming interface associated with (a) OE and (b) PE phase transformation involving ferrite ( $\alpha$ ) and cementite ( $\theta$ ). The X-axis represents distance and the Y-axis represents concentration. The cementite is the growing phase[154].....116
Figure 5-2	Schematic representation showing the tempered heat treatment of material.....117
Figure 5-3	TEM images showing the microstructure of a tempered lenticular martensite from a specimen tempered at 400°C for 30 sec (a) A bright-field image of a tempered lenticular martensite. (b) - (c) The corresponding dark-field images for twin and needle-like cementite,



respectively. (d) The selected area diffraction pattern and the corresponding analysis. (e) A stereographic projection showing the orientation relationship between the matrix(ferrite) and needle-like cementite. .... 122

Figure 5-4 TEM images showing the microstructure of a tempered lenticular martensite from a specimen tempered at 400°C for 30 sec (a) A bright-field image of a tempered lenticular martensite. (b) The corresponding dark-field images for twin cementite. (c) The selected area diffraction pattern and the corresponding analysis. (d) A bright-field image of needle-like carbide; (e) and (f) are magnified images of (d)..... 125

Figure 5-5 TEM images showing the microstructure of a tempered lenticular martensite from a specimen tempered at 400°C for 3 min (a) A bright-field image of a tempered lenticular martensite. (b) HRTEM image of the plate-like cementite (c) SEM image of the plate-like cementite. (d) The selected area diffraction pattern and the corresponding analysis. (e) A stereographic projection showing the orientation relationship between matrix(ferrite) and plate-like



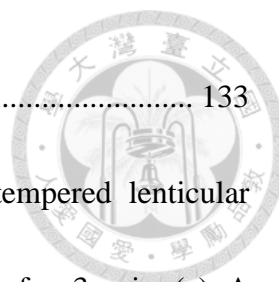
cementite. .... 127

Figure 5-6

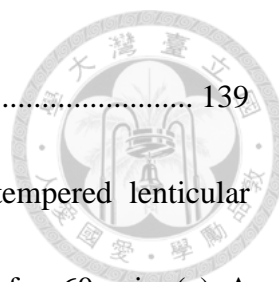
TEM images showing the microstructure of a tempered lenticular martensite from a specimen tempered at 400°C for 1500 min (a) A bright-field image of a tempered lenticular martensite. (b) - (c) The corresponding dark-field images for plate-like cementite and  $M_7C_3$  carbide, respectively. (d) Partial enlarged drawing of the  $M_7C_3$  carbide. (e) The selected area diffraction pattern and the corresponding analysis. (f) A stereographic projection showing the orientation relationship between matrix(ferrite) and plate-like cementite. (g) The selected area diffraction pattern and the corresponding analysis. (h) A stereographic projection showing the orientation relationship between matrix(ferrite) and  $M_7C_3$  carbide..... 130

Figure 5-7

TEM images showing the microstructure of a tempered lenticular martensite from a specimen tempered at 400°C for 1 min (a) A bright-field image of a tempered lenticular martensite. (b) The corresponding dark-field images for rice-like cementite. (c) The selected area diffraction pattern and the corresponding analysis. (d) A stereographic projection showing the orientation relationship between



	matrix(ferrite) and rice-like cementite. ....	133
Figure 5-8	TEM images showing the microstructure of a tempered lenticular martensite from a specimen tempered at 400°C for 3 min (a) A bright-field image of a tempered lenticular martensite. (b) Partial enlarged drawing of the rice-like cementite. (c) HRTEM image of the rice-like cementite. (d) The selected area diffraction pattern and the corresponding analysis. (e) A stereographic projection showing the orientation relationship between matrix(ferrite) and rice-like cementite. ....	134
Figure 5-9	TEM images (bright-field) showing the microstructure of a tempered lenticular martensite from a specimen tempered at 400°C for 3 min. ....	135
Figure 5-10	SEM images showing the microstructure of a tempered lenticular martensite from a specimen tempered at 400°C for (a) 10 min, (b) Partial enlarged drawing of (a), (c) 30 min .....	136
Figure 5-11	TEM images showing the microstructure of a tempered lenticular martensite from a specimen tempered at 400°C for 60 min (a) A bright-field image of a tempered lenticular martensite. (b) SEM	

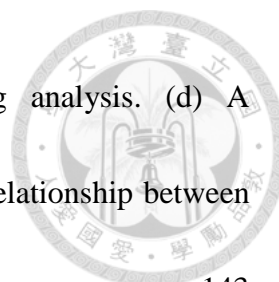


images..... 139

- Figure 5-12 TEM images showing the microstructure of a tempered lenticular martensite from a specimen tempered at 400°C for 60 min (a) A bright-field image of a tempered lenticular martensite. (b) Partial enlarged drawing of the  $M_7C_3$  carbide. (c) HRTEM image of the  $M_7C_3$  carbide. (d) - (e) The corresponding dark-field images for cementite and  $M_7C_3$  carbide, respectively. (f) The selected area diffraction pattern and the corresponding analysis. .... 140

- Figure 5-13 TEM images showing the microstructure of a tempered lenticular martensite from a specimen tempered at 400°C for 240 min (a) A bright-field image of a tempered lenticular martensite. (b) SEM image. (c) The selected area diffraction pattern and the corresponding analysis. (d) A stereographic projection showing the orientation relationship between matrix(ferrite) and  $M_7C_3$  carbide. .... 141

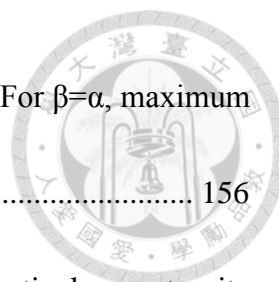
- Figure 5-14 TEM images showing the microstructure of a tempered lenticular martensite from a specimen tempered at 400°C for 1040 min (a) A bright-field image of a tempered lenticular martensite. (b) The corresponding dark-field images for  $M_7C_3$  carbide. (c) The selected



area diffraction pattern and the corresponding analysis. (d) A stereographic projection showing the orientation relationship between matrix(ferrite) and  $M_7C_3$  carbide..... 143

Figure 5-15 Possible diffusion directions of carbon (white arrows) and chromium (black arrows) atoms (schematic) as a result of the driving forces which exist when (a), (b) various carbides precipitate at the reaction front and (c) carbides coexist together as the reaction passes[168].  
.....148

Figure 6-1 Scheme of backscatter Kikuchi pattern formation: The primary beam enters the sample at the angle  $\alpha$ . It travels a distance  $r/\cos \alpha$  inside of the material until it has reached a maximum depth  $d$  below the surface;  $r$  indicates the approximate spatial resolution of the technique. On its way, more and more primary electrons are incoherently scattered with an intensity distribution indicated by the ellipsis. The incoherently scattered electrons are subsequently coherently scattered by the lattice planes  $p$  into pairs of Kikuchi cones (1) and (2) with an opening angle  $2(90^\circ - 2\theta)$  around the cone axis. The cones leave the surface at approximately the angle  $\beta$ . The path length on which electrons



undergo coherent scattering is therefore  $t = d/\sin\beta$ . For  $\beta=\alpha$ , maximum electron intensity is obtained[171]. ..... 156

Figure 6-2      (a) TEM image showing the substructures of a lenticular martensite plate; convergent beam Kikuchi line diffraction patterns (CBKLDLP) taken from (b-c) midrib region, (d-f) extended twinned region, and (g-i) untwinned region; (i) misorientation profile indicating that a given lenticular martensite plate changes gradually from the midrib region, reaching about 3° at the martensite/austenite interface. .... 164

Figure 6-3      Interaction volume of the electron beam with the lenticular martensite ..... 165

Figure 6-4      (a) and (b) show the PQ and IPF map of lenticular martensite in AISI 440C steel; (c) shows the misorientation profile across the martensite from one side to the other side (as the arrow indicates). ..... 166



## Table content



Table 2-1 Features of plate, lenticular, butterfly, and lath martensite[15] .....	14
Table 2-2 Tempering stages and their interpretations[84] .....	37
Table 3-1 The fraction of each phase for different austenitization temperatures .....	66
Table 3-2 Chemical composition of matrix for different austenitization temperature ...	67
Table 4-1 24variants of Kurdjumov-Sachs (K-S)orientation relationship.....	101
Table 4-2 12 variants of Nishiyama-Wasserman orientation relationship.....	102
Table 4-3 Equivalant axis/angle pair (for smallest angle) .....	109
Table 6-1 Comparison of crystal orientation analysis techniques .....	167

# Chapter 1 Introduction



Martensite transformation is a typical example of shear transformation. In iron-based alloys, the martensite structure (body-centered tetragonal, BCT) appears after cooling from high temperature. The parent phase is austenite (face-centered cubic, FCC). Some researchers have deeply explored this mechanism, and they accordingly suggested a “two shear theory” [25]. In other words, the martensite transformation can be seen as a two-step process: the first shear occurs and causes shape deformation, and the second shear then turns the former crystal structure (FCC) into the martensite structure (BCT). It is noticeable that the martensite transformation in steels combines uniform shape deformation and lattice invariant deformation, and consequently the interface is not distorted during this transformation. Such characteristic lattice invariant deformation, regarded as deformation by dislocation slipping or twinning, provides an explanation for the formation of different martensite structures. When dislocation slipping occurs, lath martensite appears. The thin-plate martensite is thus a product of twinning. However, only lenticular martensite has both features in its microstructure and therefore has a very special morphology. That is why we use lenticular martensite as our experimental material. The aim of this present study is to discuss the transformation of

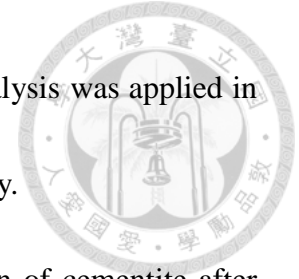
lenticular martensite and the crystallographic features in such a complicated microstructure.



Lenticular martensite was first named about 40 years ago and has attracted much attention. Nevertheless, few studies have examined the crystallographic structure in lenticular martensite and the cementite formation mechanism after tempering treatment. The present study investigates the martensite transformation in AISI 440C steel, which has a high alloying content, and can be applied to the production of a desirable martensite structure by appropriate heat treatment.

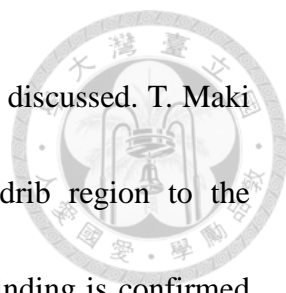
One of the objectives of this research is to clarify the morphology of lenticular martensite, which is noted in Chapter 3 of this study. By adjusting the austenitization temperature, the alloying composition in austenite matrix can be controlled and then an appropriate size of lenticular martensite can be obtained. Transmission electron microscopy (TEM) shows details of the structure of lenticular martensite, which contains three regions distinguished by the distribution of defects such as twinning and dislocations. With further reconstruction of 2-D and 3-D images, we reveal the morphology of lenticular martensite, and this result matches the simulation by M. A. Meyers [54]. In addition, little completed work has been published on the relationships between the individual lenticular martensites. The lenticular martensite grains, which nucleate and grow along a typical direction, have a significant morphology. A

combination of macrostructure observation and crystallographic analysis was applied in our research to explore the cause of the formation of this morphology.



Another objective of our research is to consider the formation of cementite after tempering treatment. Tempered martensite has been the subject of many studies because it plays such an important role in the production of high strength steels. However, little attention has been paid to the changes in the lenticular martensite structure after tempering treatments. In Chapter 4 of this study, we report our observations and analysis of the precipitation behavior in the three regions of lenticular martensite after different heat treatments. Cementite, the main product of this tempering treatment, usually precipitates at defects in lenticular martensite, such as the  $\{112\}$  twin plane (the midrib region) and dislocations (the untwinned region). It is interesting that these cementites have two types of morphology: fine needle-like and rice-like. The nucleation mechanisms and orientation relationships of these two precipitates are deeply influenced by the parent circumstances, the three regions of lenticular martensite. The subsequent growth of these two kinds of cementites also produces different results: The needle-like cementite is stable, and the rice-like cementite transforms into alloying carbides, such as  $M_7C_3$  carbides. Future studies will focus on the relation between the diffusional and displacive precipitation mechanisms and the growth behavior in lenticular martensite.

In the last section of this work, the application of the electron backscatter



diffraction (EBSD) technique in the study of lenticular martensite is discussed. T. Maki et al. noted that the misorientation angles change from the midrib region to the untwinned region in a single lenticular martensite grain, and their finding is confirmed by EBSD analysis. However, the effective spatial resolution of EBSD is limited by its signal collection method. Therefore, we conduct further investigation by electron microscopy, using Convergent Beam Kikuchi Line Diffraction Pattern (CBKLD) in TEM, on the misorientation changes in lenticular martensite. By applying these two powerful crystallographic analysis tools, we hope to provide comprehensive understanding of the inner structure of lenticular martensite.

## Chapter 2 Literature Review



### 2.1 Introduction of martensite

Martensitic transformation is a displacive transformation without random diffusion of atoms in crystalline materials, and the product phase is generally called "martensite". A shear mechanism controls this transformation, wherein a large number of atoms move cooperatively and almost at the same time, as opposed to the atom-by-atom movement that occurs in diffusional transformations. A diagram of a martensite crystal in an austenite matrix is shown in Figure 2-1[1, 2].

#### 2.1.1 Martensitic phase transformation

The austenite-martensite phase transformation starts at a certain start-temperature,  $M_s$  (thermally induced martensitic transformation), when a specimen is rapidly quenched or cooled to subzero temperatures from the austenitic region of certain ferrous alloys and steel[3]. The variation in  $M_s$  temperature with carbon content is explained by considering the strain which carbon atoms induce in the lattice when in solid solution with iron[4]. However, carbon is not the only element that affects the martensite transformation temperature. Most alloying elements, such as Mn, Cr, and Ni, lower the

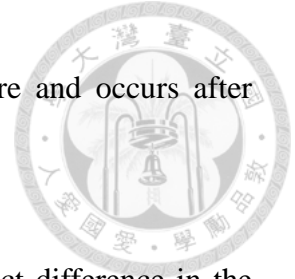
Ms temperature[2]. Various investigations into the phenomenon have produced equations that can be used to predict the effect of composition on Ms temperature, such as the following, determined by Andrews[5]:

$$M_s(^{\circ}C) = 512 - 453C - 16.9Ni + 15Cr - 9.5Mo + 217(C)^2 - 71.5(C)(Mn) - 67.6(C)(Cr)$$

The plastic deformation of the austenite phase can also induce martensitic transformation at a start-temperature, Md (deformation induced martensitic transformation), which is different from the thermally induced transformation[6, 7]. The transformation from austenite to martensite can be accomplished solely by deformation, without a quenching process. Two different types of this deformation-induced martensite, stress-assisted and strain-induced, have been observed. Stress-assisted martensite is produced when an applied stress provides the reduction in driving force for the reaction to occur. The resulting microstructure is typically twin martensite. Strain-induced martensite occurs when applied strain produces a plastic deformation that causes the transformation. This type of deformation-induced martensite usually results in a lath microstructure in ferrous systems[1, 8].

From the viewpoint of kinetics, martensitic transformations can be broadly classified into two main groups: time-independent “athermal transformation” and time-dependent “isothermal transformation”. Athermal transformation has a well defined Ms temperature and occurs instantaneously at the Ms temperature, while

isothermal transformation does not have a definite  $M_s$  temperature and occurs after some finite incubation time during isothermal holding[9].

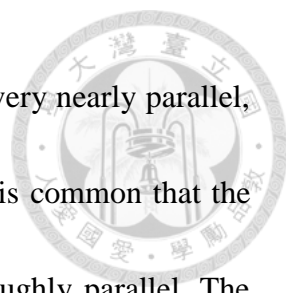


In addition to this difference in kinetics, there can be a distinct difference in the martensite morphology resulting from these two types of transformation. The occurrence of athermal or isothermal kinetics in a given ferrous alloy has been found to be mainly associated with the alloy composition[10, 11]. However, as Nishiyama has pointed out, for differing homogenization conditions of the pre-existing austenite, martensitic transformations may exhibit both athermal and isothermal kinetics for the same alloy composition[11]. The prior austenite homogenization temperature plays a significant role on the martensitic transformation kinetics. As the homogenization temperature increases, the kinetics of the transformation show a tendency to transit from purely athermal to both athermal and isothermal kinetics for the same alloy composition[12].

### **2.1.2 The orientation relationships of martensite transformation**

Since there is no diffusion during martensite transformation, atoms must be transferred across the interface in a coordinated manner, and it follows that the austenite and martensite lattices should be closely related. In experimental observation, there is an **orientation relationship (OR)** between the parent and product crystals in the






martensite transformations. The OR usually consists of parallel, or very nearly parallel, corresponding closest packed planes from the two lattices, since it is common that the corresponding closest packed directions in these planes are also roughly parallel. The interface, which is between the parent and product crystals, has a regular and undistorted plane that is usually called a “**habit plane**”. The habit planes in martensite transformation are not always the same, for they change with the carbon content of the alloys.

Martensite in steels generally has a BCC or BCT structure, which evolves from austenite with an FCC structure. Therefore, the martensite phase maintains a particular crystallographic orientation relationship with the austenite phase. There exist different orientation relationships (ORs), such as the Kurdjumov-Sachs (K-S) OR, the Nishiyama-Wassermann (N-W) OR, and the Greninger-Troiano (G-T) OR, between martensite and austenite. These ORs have been reported in various steel alloys, depending on the chemical compositions[13, 14].

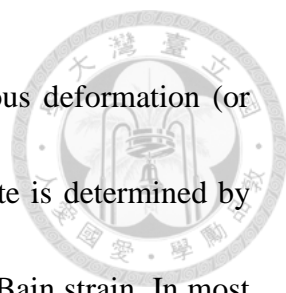
Table 2-1 shows features of the different martensite types in Fe-based alloys[15]. Among all martensite types, lath martensite forms at the highest temperature, and twin martensite, at the lowest. For the latter, which forms at a temperature as low as that of liquid nitrogen, accommodation occurs by twinning and the created morphology is plate-like. The thin plate martensite ( $\alpha$ ) has a G-T OR ( $\{111\}_{\gamma} // 1^{\circ}$  from  $\{011\}_{\alpha}$ ,



$\langle \bar{1}\bar{1}2 \rangle_{\gamma} // 2.5^{\circ}$  from  $\langle 0\bar{1}1 \rangle_a$ ) with austenite ( $\gamma$ ) and a  $\{3\ 10\ 15\}_{\gamma}$  habit plane. At slightly higher temperature, twinning and single-slip dislocation form lenticular martensite. Lenticular martensite exhibits  $\{2\ 5\ 9\}_{\gamma}$  or  $\{3\ 10\ 15\}_{\gamma}$  habit planes. At intermediate temperature, accommodation occurs by twinning and dislocation slip in a limited slip system, and the morphology becomes butterfly martensite. The habit plane of butterfly martensite is usually  $\{2\ 2\ 5\}_{\gamma}$  [16-20]. The ORs of lenticular martensite and butterfly martensite have been reported as G-T, N-W ( $\{111\}_{\gamma} // \{011\}_a, \langle \bar{1}\bar{1}2 \rangle_{\gamma} // \langle 0\bar{1}1 \rangle_a$ ) or K-S ( $\{111\}_{\gamma} // \{011\}_a, \langle \bar{1}01 \rangle_{\gamma} // \langle \bar{1}\bar{1}1 \rangle_a$ ) ORs [16-22]. At high temperature, lath martensite is formed by accommodation due to multiple dislocation slips. Lath martensite exhibits K-S OR with the  $\gamma$ , and its habit plane is  $\{5\ 5\ 7\}_{\gamma}$  or  $\{1\ 1\ 1\}_{\gamma}$  [15, 23].

### 2.1.3 The phenomenological theory of martensite crystallography

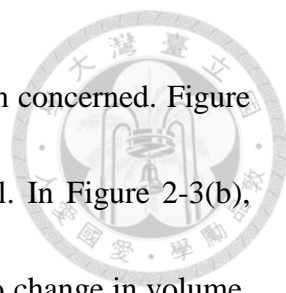
At the structural level, martensitic transformation is characterized by the maintenance of a lattice correspondence, which associates uniquely a unit cell of the parent lattice with a unit cell of the product. The Bain correspondence between FCC austenite and BCC or BCT martensite (Figure 2-2) identifies a BCT cell of axial ratio  $\sqrt{2}$  within the FCC structure, with a cube axis becoming the tetragonal c axis and two cubic  $\langle 110 \rangle$  directions normal to this defining the remaining  $\langle 100 \rangle$  axes of the tetragonal cell. This correspondence implies that the change in structure may be



accomplished by atomic displacements equivalent to a homogeneous deformation (or Bain strain) of the parent lattice, and the symmetry of the martensite is determined by the point symmetry of the parent austenite and the symmetry of the Bain strain. In most instances, the symmetry of the martensite structure is thus lower than that of the parent phase and that of the low-temperature equilibrium phase, which it most closely resembles.

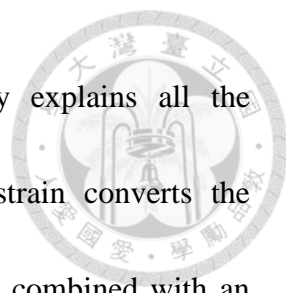
This shape change has the geometric characteristics of an **invariant plane strain (IPS)**, in which the interface plane (habit plane) remains invariant (i.e., undistorted and unrotated). Accordingly, this also minimizes the strain energy associated with the homogeneous deformation of a macroscopic region of the parent crystal. Evidence for this change in shape is readily observed at a free surface, where the intersection of a martensite plate with the surface leads to a uniform tilting of the surface and pronounced surface relief[24].

In addition, because there is no change in the relative positions of atoms in the slip plane and the plane on which the twinning shear occurs is again unaffected by the deformation, the invariant-plane strains contain both slip and twinning. The nature of invariant-plane strain is illustrated in Figure 2-3, which shows three types of these strains, defined with respect to a right-handed orthonormal basis  $Z$ , such that  $z_3$  is parallel to the unit normal  $p$  of the invariant-plane, and  $z_1$  and  $z_2$  lie within the



invariant-plane,  $z_1$  being parallel to the shear component of the strain concerned. Figure 2-3(a) illustrates an invariant-plane strain that is purely dilatational. In Figure 2-3(b), the invariant-plane strain corresponds to a simple shear, involving no change in volume, as in the homogeneous deformation of crystals by slipping. The most general invariant-plane strain (Figure 2-3(c)) involves both a volume change and shear. In Figure 2-3(c),  $m_d$  represents the displacement vector;  $m_d = sz_1 + \delta z_3$ , where  $s$  and  $\delta$  are the shear and dilatational components, respectively.

In order to further understand the changes in the crystal lattice during transformation, the concept of Bain strain is needed (Figure 2-4). The austenite is represented in Figure 2-4 (a) and (b) as a sphere which, as a result of the Bain strain,  $\mathbf{B}$ , is deformed into an ellipsoid of revolution representing the martensite. There are no lines that are left undistorted or unrotated by  $\mathbf{B}$ . There are no lines in the FCC of (001) plane that are undistorted. The lines  $\underline{wx}$  and  $\underline{yz}$ , though undistorted, are rotated to the new positions  $\underline{w'x'}$  and  $\underline{y'z'}$ . Such rotated lines are not invariant. However, the combined effect of the Bain strain,  $\mathbf{B}$ , and the rigid body rotation,  $\mathbf{R}$ , is indeed an invariant-line strain ( $\mathbf{ILS}$ ) because it brings  $\underline{yz}$  and  $\underline{y'z'}$  into coincidence (Fig. 4(c)). This is the reason why the observed irrational orientation relationship differs from that implied by the Bain strain. The rotation required to convert  $\mathbf{B}$  into an  $\mathbf{ILS}$  precisely corrects the Bain orientation into that which is observed experimentally.



The phenomenological theory of martensite crystallography explains all the observed features of the martensite crystallography. The Bain strain converts the structure of the parent phase into that of the product phase. When combined with an appropriate rigid body rotation, the net homogeneous lattice deformation, **RB**, is an **ILS** (Figure 2-5). The observed shape deformation is an **IPS**, **P<sub>1</sub>** (step (a) to (b) in Figure 2-5), but this gives the wrong crystal structure. If a second homogeneous shear, **P<sub>2</sub>**, is combined with **P<sub>1</sub>** (step (b) to (c)), then the correct structure is obtained, but it is the wrong shape, since

$$\mathbf{P}_1\mathbf{P}_2=\mathbf{RB}$$

These discrepancies are all resolved if the shape-changing effect of **P<sub>2</sub>** is cancelled macroscopically by an inhomogeneous lattice-invariant deformation, which may be slip or twinning, as illustrated in Figure 2-5[25-27].

The above theory explains all the observed features of martensite crystallography. The orientation relationship is predicted by deducing the rotation needed to change the Bain strain into an **ILS**. The habit plane does not have rational indices because the amount of lattice-invariant deformation needed to recover the correct macroscopic shape is not usually rational. The theory predicts a substructure in plates of martensite (either twins or slip steps), as is observed experimentally. The transformation goes to all the trouble of ensuring that the shape deformation is macroscopically an invariant-plane

strain because this reduces the strain energy as compared to the case where the shape deformation might be an ILS.

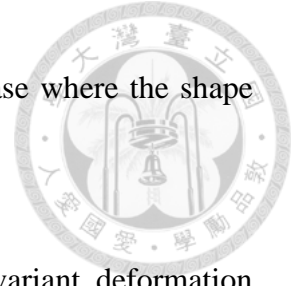


Figure 2-6 shows schematically the two types of lattice invariant deformation occurring within a martensite plate. It should be noted that the block of martensite formed has produced a surface tilt and that the observed habit is preserved by the accommodation provided by either slip (Figure 2-6(a)) or twinning (Figure 2-6(b)). The result is a macroscopically planar interface that would clearly have irregularities on a very fine scale[28].

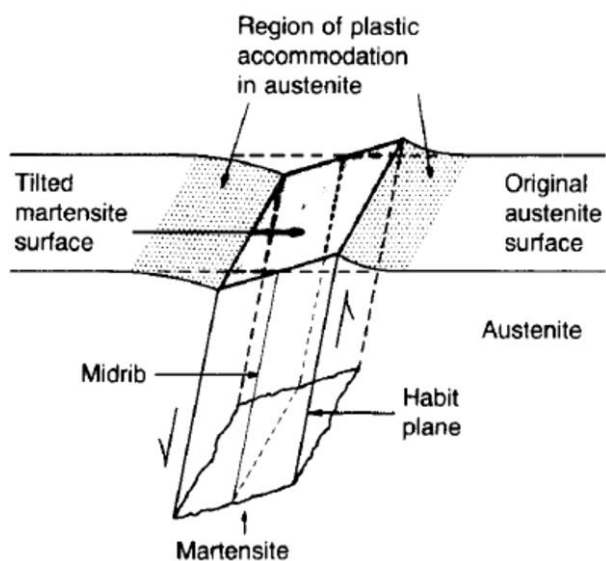


Figure 2-1 Diagram of martensite crystal, showing shear and surface tilting[2].

Table 2-1 Features of plate, lenticular, butterfly, and lath martensite[15]

Martensite type	Plate	Lenticular	Butterfly	Lath
Shape				
Ni concentration in Fe-Ni alloy	High			Low
Formation temperature	Low			High
Substructure	Twins	Twins + dislocations	Twins + dislocations	Dislocations
Crystal orientation relationship	G-T	G-T, N-W or K-S	K-S or N-W	K-S
Habit plane	$\{3\ 10\ 15\}_\gamma$	$\{3\ 10\ 15\}_\gamma$ or $\{2\ 5\ 9\}_\gamma$	$\{2\ 2\ 5\}_\gamma$	$\{5\ 5\ 7\}_\gamma$ or $\{1\ 1\ 1\}_\gamma$

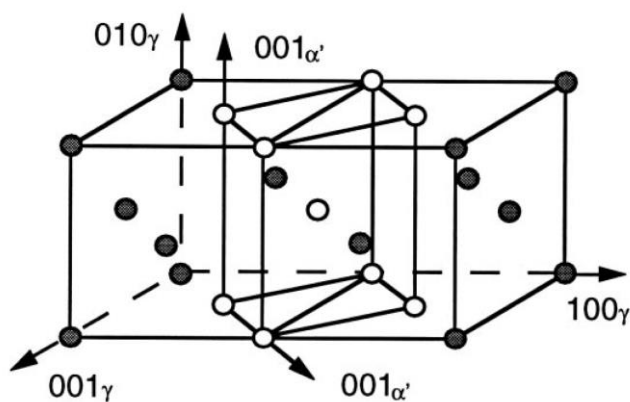


Figure 2-2 Schematic representation of the Bain lattice correspondence between principal axes of BCT martensite and FCC austenite unit cells[24].

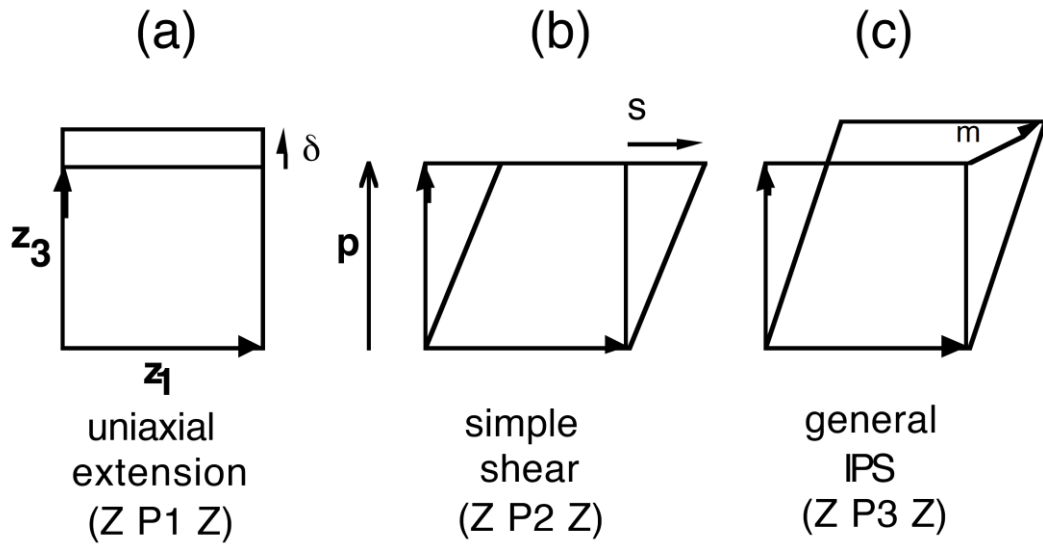


Figure 2-3 Three kinds of Invariant plane Strains. The heavy lines indicate the shape before deformation  $\delta$ ,  $s$  and  $m$  represent the magnitudes of the dilatational strain shear strain and general displacement respectively[26].

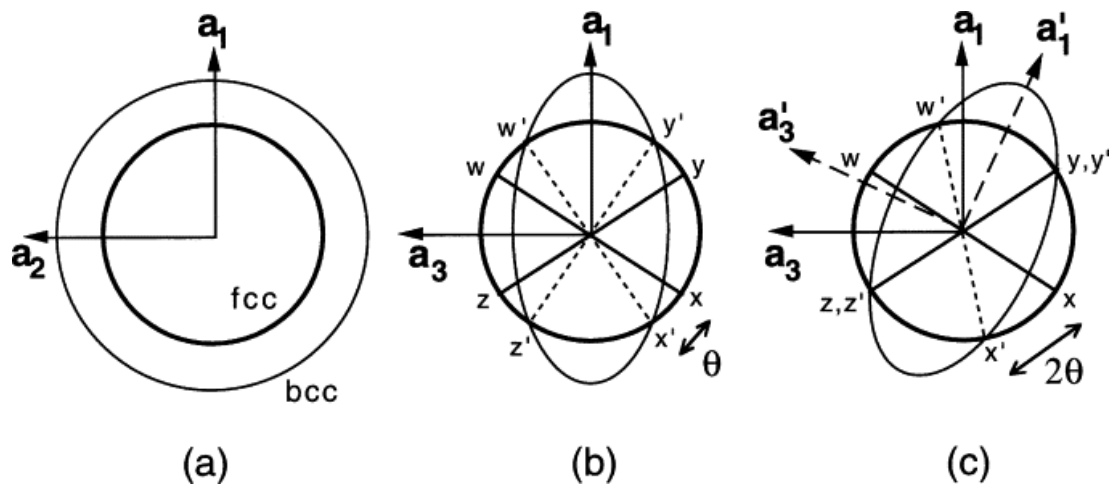


Figure 2-4 (a) and (b) show the effect of the Bain strain on austenite, which when undeformed is represented as a sphere of diameter  $w$  ( $x=y=z$ ) in three-dimensions. The strain transforms it to an ellipsoid of revolution. (c) shows the **ILS** obtained by combining the Bain strain with a rigid body rotation through an angle  $\theta$ .  $a_1$ ,  $a_2$  and  $a_3$  refer to  $[100]_\gamma$ ,  $[010]_\gamma$  and  $[001]_\gamma$  axes respectively[25].



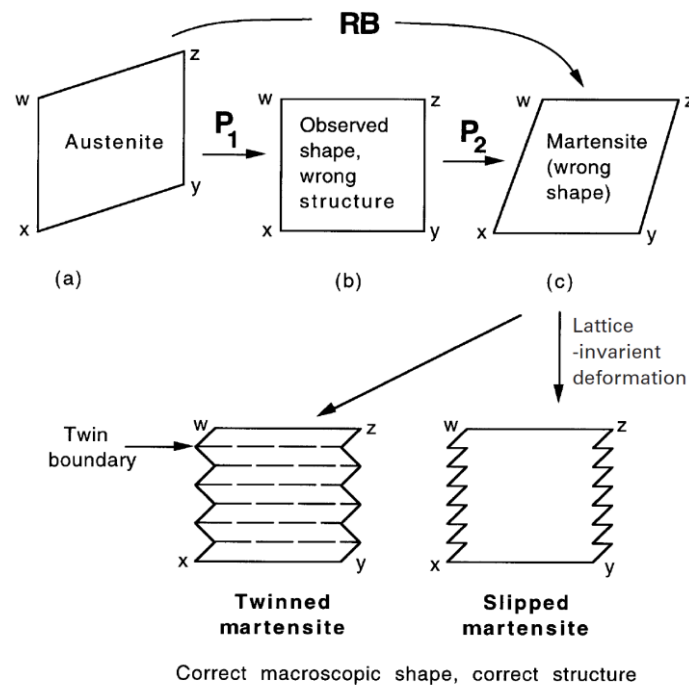


Figure 2-5 The phenomenological theory of martensite crystallography[25].

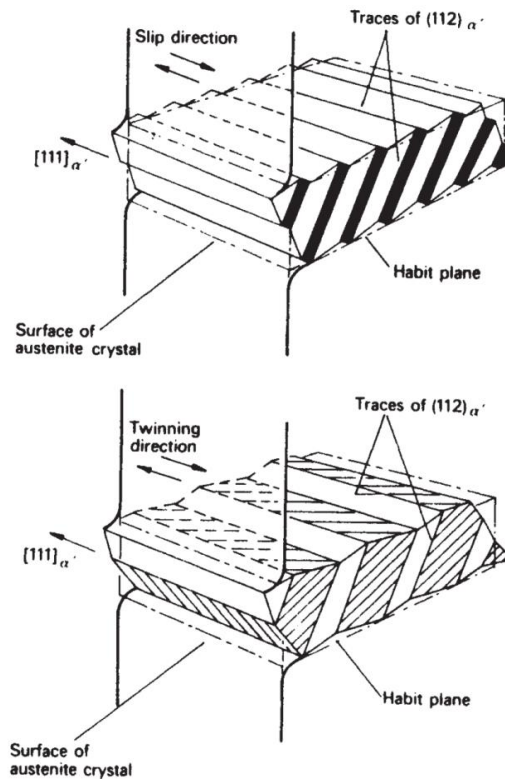
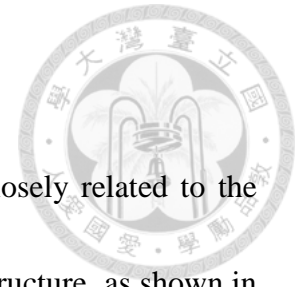


Figure 2-6 Formation of martensite plate, illustrating two types of lattice deformation: slip and twinning[28].

## 2.2 The microstructure of martensites



The martensite transformation starting temperature ( $M_S$ ) is closely related to the carbon content, which also results in different types of martensite structure, as shown in Figure 2-7. Three different martensite morphologies have been recognized in steel: **lath martensite**, **plate martensite**, and **lenticular martensite**. In plain carbon and low alloy steel (<0.6wt% carbon), the morphology is **lath-like**. Lath martensite has the highest  $M_S$  temperature and a high density of dislocations. When the carbon content is higher than 1.2wt%, the martensite structure becomes **plate-like**. This thin-plate martensite structure consists of a set of regularly-spaced transformation twins extending completely from one interface to the other. The  $M_S$  temperature for this high carbon content is usually lower than room temperature, so the lattice imperfections in plate martensite change from dislocations to twins. For steel with a medium carbon content (0.6-1.2wt% carbon), the characteristic martensite morphology is **lenticular martensite**, and the  $M_S$  temperature is at an intermediate temperature between those of lath martensite and thin plate martensite[2, 16, 28-30]. The  $M_S$  temperature, rather than the austenite stacking fault energy, determines whether or not internal transformation twinning takes place[17, 30].

### 2.2.1 Lath martensites

In lath martensite, the morphology is lath-like; the laths are very long and about 0.5  $\mu\text{m}$  wide. These are grouped together in packets with low angle boundaries between each lath, although some laths are separated by high angle boundaries.

The crystal structure of lath martensite includes 24 unique martensite variants, which may in turn be divided into four groups. Each group consists of six martensite variants with a common parallel relationship of close-packed planes. These four groups have thus been named “**packets**”[31, 32], and martensite variants within one packet have nearly the same habit plane. The packet may be further subdivided into three “**blocks**”, wherein each block consists of two martensite variants with a low misorientation. The substructure of the laths consists of dislocations, which are a result of the accommodation deformation due to the large shape strain[33]. Lath morphology may be regarded as a hierarchical structure, "parent grain" - "packet" - "block" - "sub-block" - "individual lath", where the individual lath can be considered as the basic building block of the microstructure, as shown in Figure 2-8.

Blocks consist of laths with a single variant, and six blocks with different orientations exist in a packet. The formation of six variants with an equal volume fraction in a packet can be well understood in terms of shape strain minimization. However, the preferential formation of pairs of low-misorientation variants spatially in a

packet may not be directly related to the shape strain minimization. Its cause may lie in specific mechanisms of the nucleation and growth of laths of different variants during martensitic transformation[34].



The basic microstructural unit controlling the strength and toughness of lath martensite is known to be the packet or the block. A block consists of a set of parallel laths with essentially the same orientation that are separated from one another by high angle boundaries. It should be noticed that the block, rather than the packet, is the basic structural unit of lath martensite structure that acts as a barrier to deformation and fracture. Consequently, it may be reasonable to consider that the basic structural unit controlling the strength and toughness of low carbon martensite is the packets rather than the blocks. The mechanical property of lath martensite structure is improved by the refinement of packets and blocks[17].

### **2.2.2 Plate martensites**

The morphology of high carbon content ( $> 1.2\text{wt}\%$ ) martensite is plate-like. These plates form individually and are heavily twinned. There is no midrib in plate martensite, and it has straight and smooth planar interfaces, as shown in Figure 2-9. In addition, the surrounding austenite grains rarely show slip lines. The plate martensite nucleates dominantly at austenite boundaries, twin boundaries, or triple points, and usually forms

as a very narrow plate at the  $M_s$  temperature. To explain the occurrence of twinned martensite in steels containing C or Ni, researchers have proposed two factors: the  $M_s$  temperature and the stacking fault energy.



### **$M_s$ temperature**

Since both C and Ni lower the  $M_s$  temperature and promote twinning, it has been suggested that a low  $M_s$  temperature favors twinned martensites. This is in agreement with results on both FCC and BCC metals, wherein plastic deformation takes place by twinning at low temperatures, suggesting that at these temperatures, the critical resolved shear stress for twinning is lower than that for slip. On this basis, low  $M_s$  temperatures would be expected to favor transformation twinning in martensite. Thus all alloying elements that lower the  $M_s$  temperature should favor twinning.

### **Stacking fault energy**

The influence of the stacking fault energy on transformation substructures has been discussed by Kelly and Nutting. They postulated that twinning in body-centered martensite is favored due to the high stacking fault energy in austenite[35]. This effect of stacking fault energy is opposite to what is found for mechanical twinning in FCC metals, where a lower stacking fault energy tends to be associated with a higher tendency for deformation by twinning[22, 36]. These considerations strongly suggest that as far as transformation twinning in martensite structures is concerned, the effect of

solute on  $M_s$  temperature is more important than their effect on stacking fault energy[37].



The following features in the process of transformation into thin plate martensite have been observed: (a) During subsequent cooling, the thin plate martensite itself thickens, as new thin plate martensite forms in the other parts of the austenite. (b) No burst phenomenon is observed. (c) Accommodation slip caused by martensitic transformation is rare in the austenite adjacent to the thin plate martensite. These phenomena are entirely different from those of common lenticular martensite. From these observations, it appears that the austenite adjacent to martensite is barely deformed if the martensite is thin plate martensite. Whether the matrix is deformed elastically or plastically due to the formation of martensite is a very important factor in the movement of the martensite boundary. In order that the martensite plate may thicken by successive cooling, it is required that the interface remain glissile. Generally, it is considered that, to achieve the condition for the interface to remain glissile, martensite plate growth must cease before plastic deformation of the matrix[27, 38-41].

### **2.2.3 Lenticular martensites**

Lenticular martensite is the main focus of this research, and the following section will introduce lenticular martensite in detail.



## A. Morphology

Lenticular martensite is usually observed in steel with medium carbon content (0.6-1.2wt% carbon). Under 3-D observation, this kind of martensite has curved interfaces, and the surrounding austenite shows many slip lines. A straight line at the center of lenticular martensite is called a midrib. It has been revealed that  $\{112\}_\alpha$  transformation twins and planar defects exist on  $\{101\}_\alpha$  in the lenticular martensite and that the density of twins is highest near the midrib region[42-45]. The midrib plane is usually taken as the habit plane, which is reported to be close to  $\{2\ 5\ 9\}_\gamma$  or  $\{3\ 10\ 15\}_\gamma$ . This midrib region can be considered the origin of martensite growth, which has a substructure of fine and regular aligned transformation twins and then grows into a lenticular shape by twinning and dislocation slip[46-48]. The twins are replaced by a regular dislocation network as the austenite-martensite interface is approached. The  $\{101\}_\alpha$  planar defects are accommodation distortion imposed by the growing martensite. As described above, the substructure of lenticular martensite contains three regions: (1) the **midrib**, which is completely twinned as the thin plate martensite, (2) the **twinned region**, in which some twins extend from the midrib, and (3) the **untwinned region**, which contains no twins but many dislocations[42, 49-53].

The low temperature dependence of the growth velocity of lenticular martensite, as well as the fact that growth cannot be reinitiated once it is stopped, is consistent with the

wave mechanism of propagation. A mathematical description of the 3-D lenticular martensite morphology was discussed by M. A. Meyers[54]. The model allows the determination of the shape of a growing lenticular martensite, which is close to elliptical.

Figure 2-10 shows a martensite lens during propagation: The plane  $xy$  is the longitudinal propagation plane (shear direction  $ox$ ), and  $oy$  is the direction of transverse propagation.

The equation for the growing martensite lens will be derived.

Three-dimensional propagation, at time  $t_i$ :

$$\frac{(x^2 + z^2)^{3/2}}{x^2 v_{ed} + z^2 v_{ed}} - \frac{1}{k} \ln\left(1 - \frac{k|y|}{v_{ed}}\right) = t_i$$

A general point  $P_3 (x, y, z)$  is chosen on the austenite-martensite interface (Figure 2-10), and the propagation is considered to be composed of a longitudinal term (from the origin to  $x, 0, z$ ) and a transverse term (from  $x, 0, z$  to  $x, y, z$ ).

## **B. Transformation and growth process**

According to T. Maki et al.[47, 48], the morphology of the midrib in lenticular martensite is almost the same as that of thin plate martensite. Figure 2-11 shows the stress-induced growth behavior of thin plate martensite, caused by tensile deformation at various temperatures. When deformed at temperatures below 110K, the thermally-transformed thin plate maintains a thin plate shape as the martensite grows,

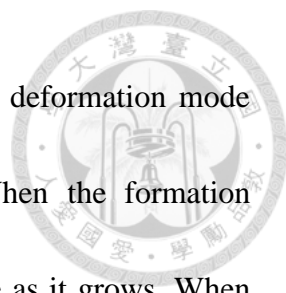


and above 160K, it grows into a lenticular shape. In the temperature range between 110 and 160K, both martensite plates with a thin plate shape and those with a lenticular shape are observed. Therefore, the stress-induced growth behavior of thin plate martensite changes with deformation temperature[48].

Patterson and Wayman[49] observed similar intersections of martensite plates in an Fe-32Ni alloy and noticed that a plate intersecting another always penetrates to a point near the boundary of the twinned region. From this, they concluded that partially twinned plates thicken in two stages (perhaps separated by a time lapse) and that the thickening plate during the first stage (that involving twinning) is greater than that during the second stage (that involving slip).


Figure 2-12 shows the thermally-induced growth behavior of thin plate martensite to lenticular martensite from homogenized specimens subzero cooled to  $-196^{\circ}\text{C}$  at various times. The thin plate martensite (Figure 2-12 (a) and (b)) forms at the earliest stage of the transformation, and the lenticular martensite (Figure 2-12 (c) and (d)) occurs after prolonged holding. It is notable that both lenticular and thin plate martensites coexist (Figure 2-12 (c) and (d))[55].

The above examples clearly indicate that the midrib in lenticular martensite is thin plate martensite itself. During the growth of lenticular martensite, the former keeps the lattice-invariant deformation mode of twinning, whereas the latter combines both



twinning and slip modes. It is considered that the lattice invariant deformation mode changes from twinning to slip due to the high temperature. When the formation temperature is quite low, martensite can maintain a thin plate shape as it grows. When the formation temperature is relatively high, the change in deformation mode from twinning to slip results in the growth of martensite into a lenticular shape. This change in the lattice invariant deformation mode is due to the local temperature increase caused by latent heat, as proposed by Patterson and Wayman[56].

The extent of the twinned region in Fe-Ni-C alloys has been observed to increase with decreasing martensite formation temperature, even in alloys of the same chemical composition. Figure 2-13 shows the mean fraction of the twinned region as a function of formation temperature. It can be seen that the data from three different alloys all lie on a straight line and that the fraction of the twinned region increases linearly with the decrease in the martensite formation temperature[57, 58]. R. P. Reed reported that the amount of the twinned areas, as opposed to the dislocation area, depends on composition; the amount of twinning in the martensite plates increases as the Ni content increases. He also suggested that the martensite plates become more irregular or fragmented as the Ni content decreases. Pre-straining at room temperature can influence the martensite morphology. The crystals are extremely fragmented, almost feathery in appearance, but continue to form into a long, consistently thick products[59, 60].

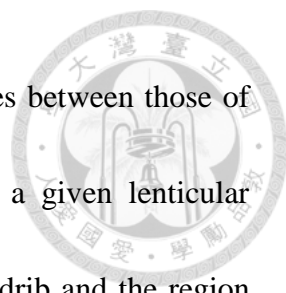


T. Maki proposed a morphology of the untwinned region. In 2006, the addition of Co to Fe-Ni binary alloy was shown to decrease  $\Delta V/V$  at the same  $M_s$  temperature. When the  $M_s$  temperature is low and  $\Delta V/V$  is almost zero, or even negative, the morphology of lenticular martensite in general exhibits a smoother M/A interface[61]. In 2009, substructures of lenticular martensites with different martensite origins were studied. The formation of the untwinned region is presented in Figure 2-14[62]. The untwinned region consists of two distinctive regions with different substructures. In contrast to those in the Fe-33Ni alloy, curved and tangled dislocations have been observed in the entire untwinned region of the Fe-31Ni alloy. These walls were considered to have originated from coalescence with parts of the irregular untwinned region.

Most of the dislocations in untwinned regions are curved and tangled, though the directions of some dislocation lines, determined by trace analysis using multiple zones, are close to the  $\langle 111 \rangle_M$  direction. On the basis of this observation, Shibata concluded that martensite inherits the accommodation dislocations in austenite even in the twinned region, as the fairly high  $M_s$  temperature of the alloy induces plastic deformation of the surrounding austenite as soon as the midrib is formed[62, 63].

### **C. Crystallographic analysis**

The OR is also a very interesting topic in lenticular martensite research. T. Maki et



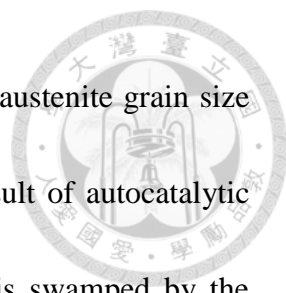
al. investigated the OR in lenticular martensite, which has properties between those of lath martensite and thin plate martensite. The orientation within a given lenticular martensite plate changes gradually and by about  $3^\circ$  between the midrib and the region near the M/A interface. The midrib and the twinned regions both contain high densities of transformation twins holding nearly a G–T OR with the austenite, similarly to the case of thin plate martensite. The untwinned region contains a high density of dislocations and displays nearly a K–S OR with the austenite across the M/A interface, similarly to the case of lath martensite. The OR change is caused by heterogeneous distribution of defects in martensite and also the surrounding austenite[21]. The measured points and the ORs, which are located between the midrib and the M/A interface in the lenticular martensite, are shown in Figure 2-15.

The facts indicate that most of the shape strain associated with the formation of lenticular martensite is plastically accommodated in the austenite near the interface and that the introduction of geometrically necessary dislocations results in a local orientation change. Most of the shape strain associated with the formation of thin plate martensite is accommodated by the elastic deformation of the austenite matrix on both sides of the martensite plate. The austenite matrix is plastically deformed to accommodate the shape strain of lenticular and lath martensite. Plastic deformation tends to accumulate on the side of the austenite in contact with the martensite lath,

whereas deformed zones form on both sides of lenticular martensite[15, 23, 64-66].

The K-S OR between lenticular martensite and austenite matrix exists in Fe-C alloy steels. There are 24 unique crystallographic variants in the transformation of martensite from a single austenite grain, while the annealing twins are disregarded. In most cases, there exist some variant selection rules in lenticular martensitic transformation. The 24 variants are groups of four located symmetrically about the six  $\{110\}$  poles. These groups are called “**pole groups**” or “**plate groups**”, since the four variants are observed to form together in clusters. On the basis of the characteristics of the coupled plate martensites, the following might be favorable for the formation of the coupled plates: (1) two variants with opposite shape deformation; (2) elastic accommodation in the surrounding austenite; and (3) **self-accommodation** and **autocatalysis** between two martensite plates[67].

The number of martensite plates increases with time. Previous studies have noted that the intersection between martensite plates and parent austenite boundaries is a preferred nucleation site for new martensite plates, so these martensite plates show a **burst** arrangement[11]. Autocatalysis is believed to be the cause of the bursts of transformation in lenticular martensite steels. In most cases, the thickening of the initial plate seems to be limited, and the other martensite plates autocatalytically nucleate along the sides[68]. The size of the burst depends on the driving force (burst



temperature), but the size of the plates formed is controlled by the austenite grain size and by the arrangement of the plates. Bursts of this kind are a result of autocatalytic nucleation, in which the role of the initial distribution of nuclei is swamped by the creation of numerous new nuclei, whose origins can probably be attributed to the plastic deformation effects that accompany the growth of martensite. These new nuclei grow such that they form into plates, which accommodate the strains resulting from the formation of the first plate, and a repetition of this basic process triggers the sudden zig-zag propagation of groups of mutually accommodating plates[69-74].

The coupled plate martensite variants form **spear**, **wedge**, **kink**, and **zig-zag** couplings, leading to the characteristic morphologies[75-77]. Autocatalysis will generate well-defined kink type crystallographic boundaries between neighboring martensite units. Spear type and wedge type pairs are self-accommodating. A zig-zag type can also be regarded as self-accommodating.

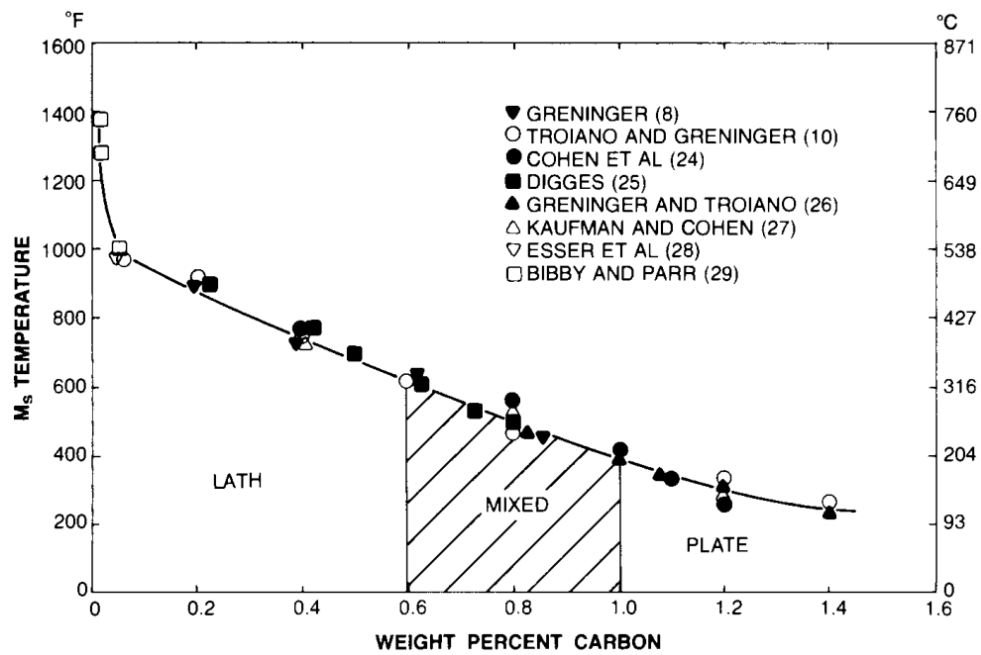


Figure 2-7 Martensites exhibit various morphologies depending on the carbonic content[30].

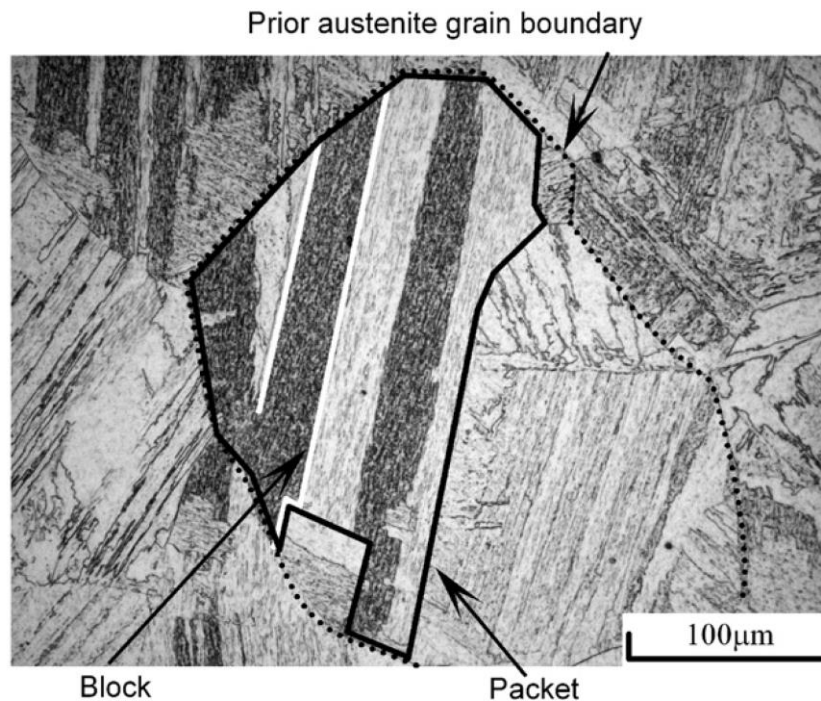


Figure 2-8 Optical micrograph shows packets and blocks within individual prior austenite grains. The prior austenite grain boundaries enclosing the grain in the middle of the micrograph are indicated by dotted lines[34].

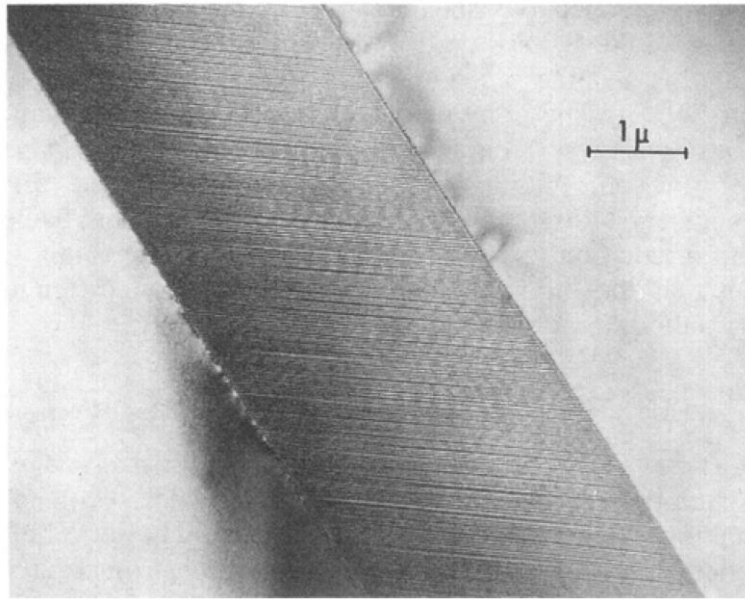


Figure 2-9 Transmission electron micrograph showing internally twinned martensite plate in a matrix of retained austenite in an Fe-Ni-C alloy. The fine twins in the martensite are transformation twins[27].

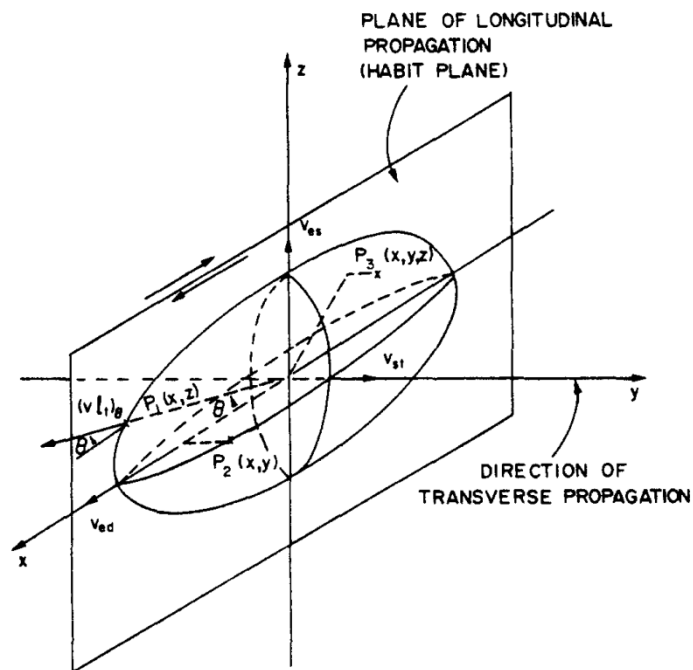


Figure 2-10 Schematic representation of martensite lens during growth. Origin of axes coincides with position of embryo[54].



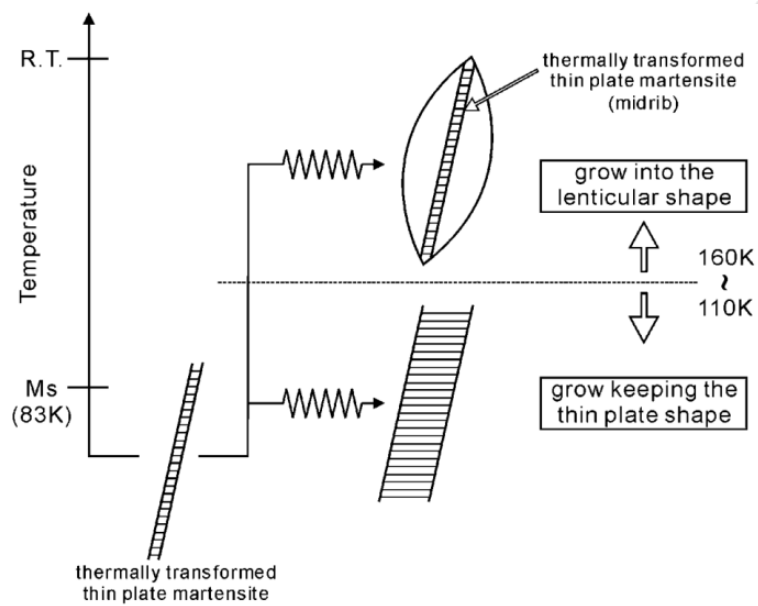


Figure 2-11 Summary of the stress-induced growth behavior of thin plate martensite by tensile deformation at various temperature in Fe-31Ni-10Co-3Ti steel [48].

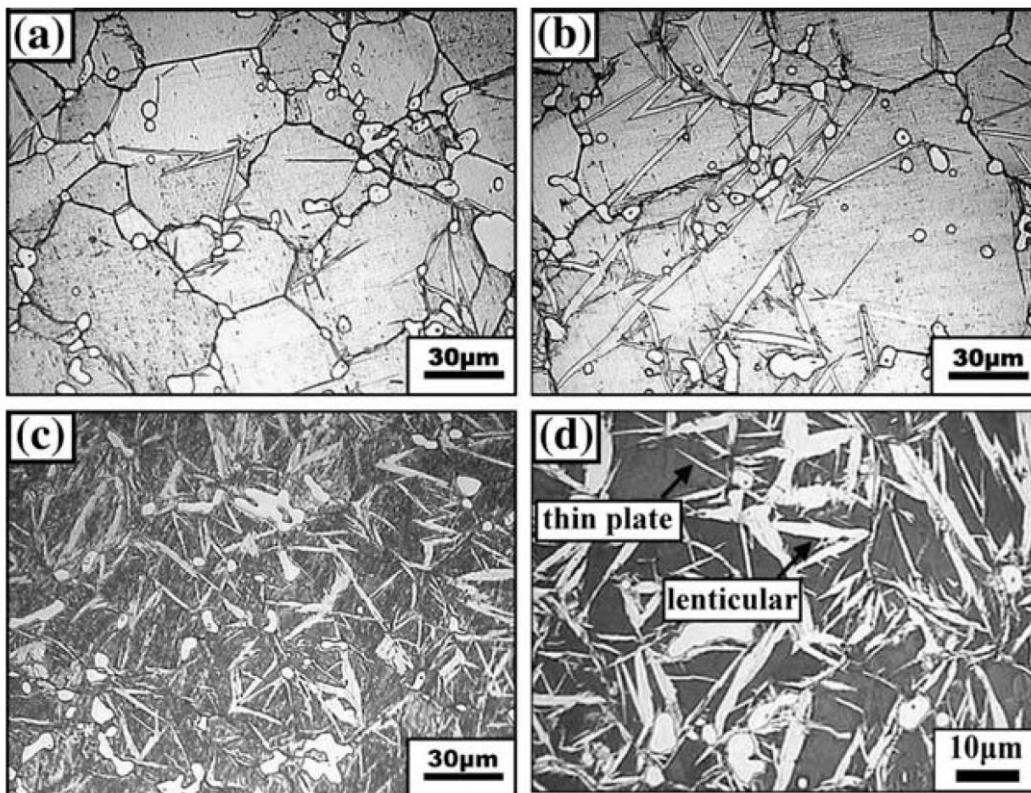


Figure 2-12 Optical metallographs taken from the homogenized specimens subzero cooled at  $-196^{\circ}\text{C}$  for (a) 8s, (b) 10s, (c) 12s, and (d) 30 min[55].

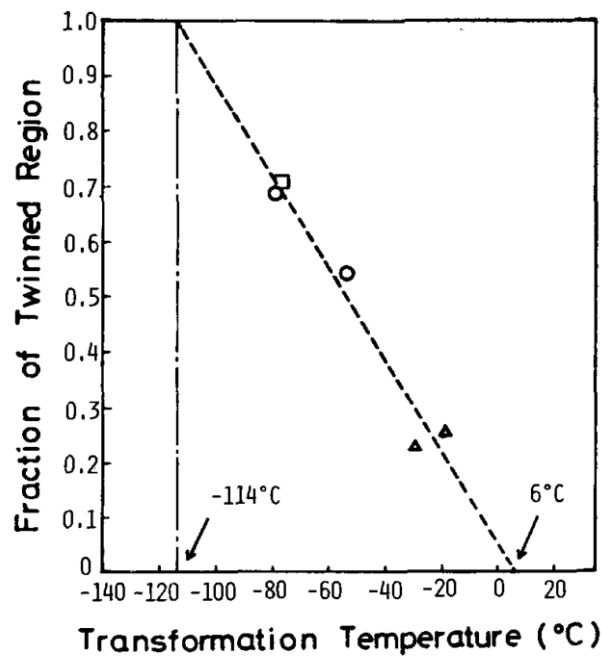


Figure 2-13 Fraction of twinned region as a function of formation temperature of martensite: O, Fe-31Ni-0.23C;  $\Delta$ , Fe-29Ni-0.26C;  $\square$ , Fe-31Ni-0.29C[57].

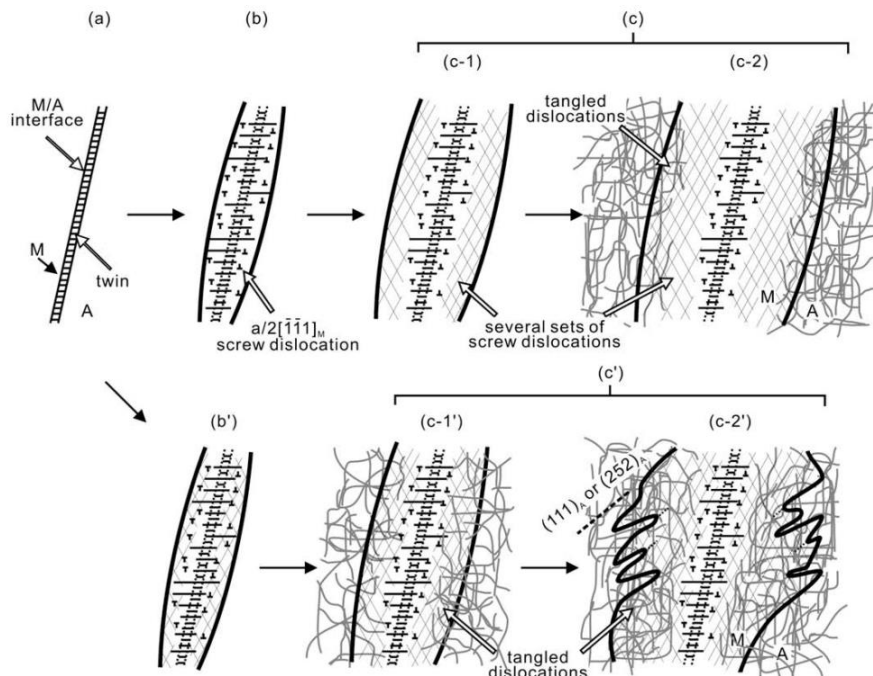


Figure 2-14 Schematic illustration showing the development of the substructure in lenticular martensite: (a)→(b)→(c-1)→(c-2) in Fe-33Ni alloy ( $M_s=171K$ ), (a)→(b)→(c'-1)→(c'-2) in Fe-31Ni alloy ( $M_s=223K$ )[62].

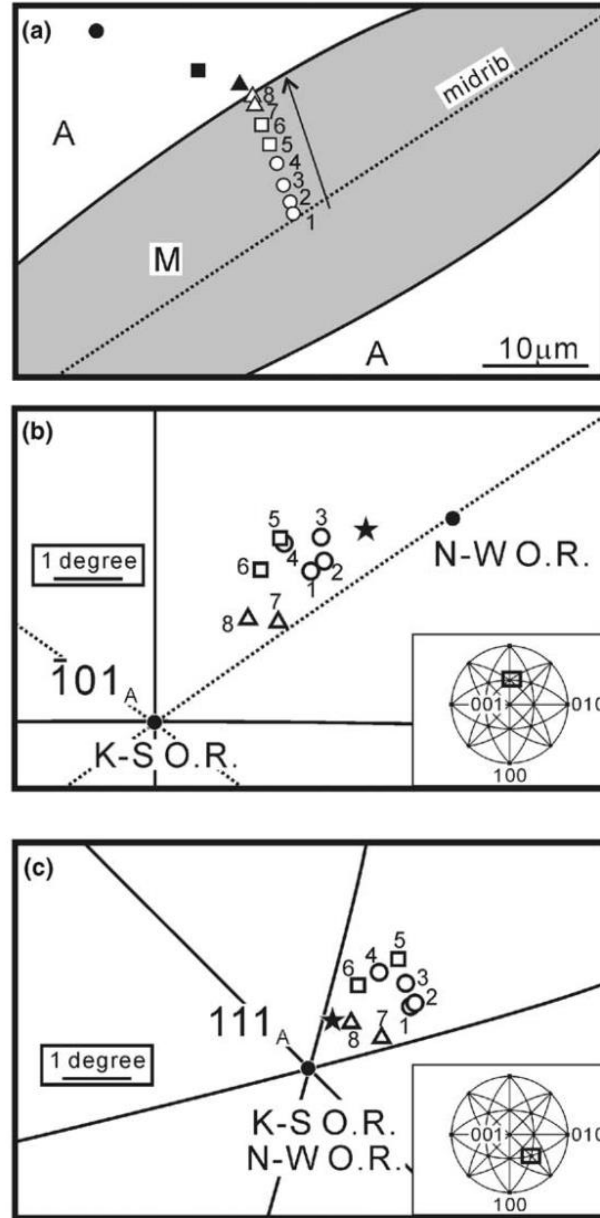


Figure 2-15 (a) The open and solid symbols, i.e., circles, square and triangles, show the measured points of the orientations in the martensite and austenite, respectively. (b) and (c) are the corresponding stereographic projections around  $[\bar{1}01]_A$  and  $[111]_A$  axes, respectively, showing the change in local orientation relationship. The  $(011)_M$  and  $[\bar{1}\bar{1}1]_M$  of K-S and N-W OR are shown as solid circles. The solid stars show the calculated  $(011)_M$  and  $[\bar{1}\bar{1}1]_M$  using the PTMC. Each shaped open symbol shows the measured  $(011)_M$  and  $[\bar{1}\bar{1}1]_M$  direction between the austenite and martensite with the same symbols in (a)[21].

## 2.3 The tempering of martensite

For commercial use, alloyed steels are first austenitized and quenched to encourage transformation into martensite, and finally tempered at various temperatures to provide a beneficial combination of strength, toughness, and fracture resistance. The martensite structure is relieved by precipitation of a variety of carbide types during tempering.

### 2.3.1 Introduction of tempered martensite

The tempering of martensite has been the subject of many studies because it plays an important role in the production of high strength steels. The tempering of martensitic alloy steels increases ductility and decreases strength as the tempering temperature rises through the range of 80-700°C. It involves the segregation of carbon to lattice defects and the precipitation of carbides, the decomposition of retained austenite, and the recovery and recrystallization of the martensitic structure[78-83].

All the structural changes during tempering are introduced in Table 2-2[84]. In the first stage of the tempering of plain carbon steels (80-200°C), the diffusion of carbon in ferrite is activated, and  $\epsilon$ -carbide forms[85]. Subsequently, the  $\epsilon$ -carbide is replaced by  $\chi$ -carbide or cementite, usually occurring in the range of 200-400°C. The decomposition of retained austenite to ferrite and carbide also starts, and the martensite loses its tetragonality, becoming ferrite. In the third stage, cementite forms and gradually

coarsens, growing rapidly in the ferrite matrix, between 400-700°C, which is the prime cause of the changes in the mechanical properties[85-91].



The alloying additions influence the tempering process in two ways: by altering the growth characteristics of the cementites, and by replacing cementites with more stable alloy carbides. For example, Si stabilizes  $\epsilon$ -carbides, retards the growth of cementites, and can enhance the resistivity of softening up to 500°C[86]. The addition of carbide-forming elements such as Mo, V, and Nb, even in small amounts, gives a pronounced softening resistance[87]. Cr and Mn are markedly enriched in the cementites, consistent with the carbide forming tendencies of these elements, and Ni, a non-carbide forming element, is depleted in the cementites and concentrated in the matrix adjacent to the cementites[92].

The rates of nucleation and growth of different alloy carbides will depend on differences in the diffusivity of the elements in ferrite. Consequently, the alloy carbide dispersion is finer and much more resistant to coarsening than cementite. With this result of comparable heat treatment, the mechanical properties of these alloy steels are far superior to those of plain carbon steels. The sluggish diffusion controlled redistribution of the alloying elements reduces the rate of cementite coarsening and associated reductions in hardness, in comparison to an Fe-C alloy, in which cementite coarsening is dependent only on rapid interstitial diffusion of carbon[92]. It is

concluded that the dispersion of alloy carbide is influenced by two further factors: the nature of the prior cementite dispersion, and the mode of transformation from cementite to alloy carbide[86].

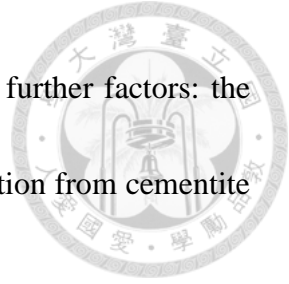


Table 2-2 Tempering stages and their interpretations[84]

Temperature	R. T. $\longleftrightarrow$ 150°C	130°C $\longleftrightarrow$ 250°C	230°C $\longleftrightarrow$ 330°C	330°C $\longleftrightarrow$ 400°C
Electrical resistivity	Decrease	Decrease	Decrease	—
Dilatometry	Contraction	—	Expansion	Contraction
Electron microscopy	(1) Martensite (2) Retained austenite	(1) Tempered martensite ( $\epsilon$ -carbide) (2) Retained austenite	(1) Tempered martensite ( $\epsilon$ -carbide in the matrix $\chi$ -carbide on the twin interfaces) (2) Lower bainite	Tempered martensite (cementite and $\chi$ -carbide on the twin interfaces)
Interpretation	Segregation of carbon atoms to the lattice defects or the carbon cluster formation	Precipitation of $\epsilon$ -carbide	Precipitation of $\chi$ -carbide on the twin interfaces and the decomposition of retained austenite	Transition of $\chi$ -carbide into cementite

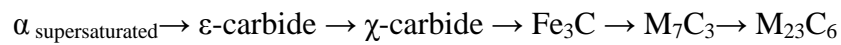
### 2.3.2 Tempering of Chromium-containing alloy steels

For stainless steel, chromium is the necessary and most important alloying element, and it is also a chromium carbide former. Chromium increases the hardenability and the corrosion and oxidation resistance of steels, improves high-temperature strength and high-pressure hydrogenation properties, and enhances abrasion resistance in high-carbon grades. In the low Cr/C ratio range, only alloyed cementite forms. If the Cr/C ratio is increased, chromium carbides  $(\text{Cr,Fe})_7\text{C}_3$  or  $(\text{Cr,Fe})_{23}\text{C}_6$ , or both, appear. Complex chromium-iron carbides go into solution slowly in austenite; therefore, a longer time at high temperature is necessary to allow solution to take place before

quenching is accomplished. However, the addition of Cr in steels enhances the segregation of impurities, such as P, Sn, Sb, and As, to grain boundaries, which induces temper embrittlement[93].

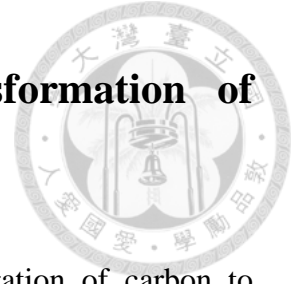


Honeycombe and his coworkers have surveyed the carbide reactions that occur in chromium steels, the following sequence being typical for high chromium content[85]:



The transformation of  $\text{Fe}_3\text{C}$  to  $(\text{Cr,Fe})_7\text{C}_3$  occurs by the nucleation at the ferrite/ $\text{Fe}_3\text{C}$  interface and dislocation within the ferrite. Since chromium easily diffuses in ferrite, the alloy carbide precipitates rapidly coarsen and become ineffective in altering the properties. Prolonged tempering of a chromium-containing alloy steel at 500°C and above leads to the formation of massive particles of  $\text{Cr}_{23}\text{C}_6$  at both austenite and ferrite lath boundaries. A chromium-containing alloy steel continuously softens during tempering in the range 500-700°C. With subsequent quenching to form martensite,  $(\text{Cr,Fe})_7\text{C}_3$  is detected with tempering as low as 500°C[85].

## 2.4 Carbides in martensitic steel and transformation of carbides



Tempering of martensite in carbon steels causes the segregation of carbon to dislocations and various boundaries, and the rearrangement and clustering of carbon into a modulated structure[94]. Because of the stress fields around individual dislocations and cell walls in lath martensite, certain interstitial lattice sites near these defects provide lower-energy sites for carbon than the normal interstitial lattice positions. When martensite is tempered at low temperatures, the first step in the tempering process is a redistribution of carbon to these lower energy sites, indicating the segregation of most of the carbon to dislocations[93, 94]. The plate martensite has an internally twinned substructure, and carbon segregation to dislocations is not the only segregation. Mossbauer indicated that precipitation clustering of carbon also occurs. Izotov and Utevskii have reported the clustering of carbon atoms along  $\{100\}$  planes and their distribution on one of the three sets of interstitial sub-lattices, which leads to tetragonality. Subsequent tempered heating at 100°C or higher leads to the growth of the clusters and the eventual formation of  $\epsilon$ -carbide[79, 96-100]. As the tempering temperature increases, the alloying carbides start to precipitate.





### 2.4.1 Categories of carbides

In the following, ‘M’ stands for metallic elements and ‘X’ represents the interstitial elements C or N. In  $M_7C_3$  and  $M_{23}C_6$ , M represents a mixture of transition metals such as Cr, Fe, Mn, Nb, and Mo. It can also be simply written as  $(Cr_{1-x}Fe_x)_7C_3$  and  $(Cr_{1-x}Fe_x)_{23}C_6$ [101, 102].

#### $\epsilon$ -carbide ( $Fe_xC$ )

Jack first established the structure of the phase as HCP and named it  $\epsilon$ -carbide[103]. As mentioned before, most of the carbon in low alloy steels is distributed at dislocation sites. Most of these sites have a lower energy than those available in  $\epsilon$ -carbide, so there is little driving force for precipitation[79]. For higher carbon contents, not all the carbon can be associated with dislocations, and carbide precipitation occurs rapidly, even at a temperature as low as 150°C[79, 104, 105]. The  $\epsilon$ -carbide itself is a highly unstable phase. Jack proposed the following orientation relationship between martensite and the  $\epsilon$ -carbide:

$$(011)_\alpha // (0001)_{\epsilon\text{-carbide}}$$

$$(101)_\alpha // (10\bar{1}1)_{\epsilon\text{-carbide}}$$

$$[11\bar{1}]_\alpha // (1\bar{2}10)_{\epsilon\text{-carbide}}$$

Wells[78] found evidence to suggest that  $\epsilon$ -carbide precipitates on sub-boundaries in the martensite. It generally grows as long narrow plates or laths, usually in more than

one direction or on more than one plane in the martensite plate.

### **$\chi$ -carbide or Hägg carbide ( $\text{Fe}_5\text{C}_2$ )**

The carbon atoms in  $\chi$ -carbide are surrounded by trigonal prisms of metal atoms, and the prisms are similarly arranged in sheets. In  $\chi$ -carbide, the sheets of prisms are joined differently from those in cementite, and the structure is described in terms of a monoclinic unit cell. The orientation relationship between  $\chi$ -carbide and ferrite is expected to be [103, 106]:

$$(100)_{\chi\text{-carbide}} // (\bar{1}21)_{\alpha}$$

$$[010]_{\chi\text{-carbide}} // [101]_{\alpha}$$

$$[001]_{\chi\text{-carbide}} // [\bar{1}11]_{\alpha}$$

The  $\chi$ -carbide is metastable carbide intermediate between  $\varepsilon$ -carbide and cementite. Nagakura et al. have reported that the transition from  $\chi$ -carbide to cementite occurs by microsyntactic growth, or carbide intergrowth, requiring only iron atom displacements and carbon diffusion [90, 98].

### **$\text{M}_3\text{C}$ ( $\text{Fe}_3\text{C}$ )**

The carbon atom environment in  $\text{Fe}_3\text{C}$  is a triangular prism of iron. The structure has been described in terms of a distorted hexagonal close packing of iron atoms [107] or in terms of the arrangement of triangular prisms. Several researchers have considered the mechanisms by which  $\alpha$ -iron can transform into cementite, and, as stated earlier, the



mechanisms are frequently elaborate, involving the cooperative movements of many atoms. The concept of a "transition cell", introduced by Andrews[108] and adopted by other authors, essentially involves describing the unit cells of both ferrite and cementite in terms of a least-common multiple unit cell, which is an intermediate in the transformation[103]. Cementite has a more complex structure: the orthorhombic unit cell with space group  $P_{anm}$ .

Over the past decades, a number of experimental determinations of ORs between ferrite and cementite have been consistently reported in the literature[109-117]. They are:

**The Isaichev OR[109]:**

$$(\bar{1}03)_{Fe_3C} // (110)_{\alpha}$$

$$[010]_{Fe_3C} // (1\bar{1}\bar{1})_{\alpha}$$

$$[311]_{Fe_3C} \text{ } 0.91^{\circ} \text{ from } [1\bar{1}1]_{\alpha}$$

**The Bagaryatskii OR[110]:**

$$(001)_{Fe_3C} // (211)_{\alpha}$$

$$[100]_{Fe_3C} // [0\bar{1}1]_{\alpha}$$

$$[010]_{Fe_3C} // [1\bar{1}\bar{1}]_{\alpha}$$

**The Pitsch-Petch OR[111]:**

$$(001)_{Fe_3C} // (5\bar{2}\bar{1})_{\alpha}$$

$$[100]_{\text{Fe}_3\text{C}} 2.6^\circ \text{ from } [13\bar{1}]_\alpha$$

$$[010]_{\text{Fe}_3\text{C}} 2.6^\circ \text{ from } [113]_\alpha$$



Although the Bagaryatskii OR is very close to the Isaichev OR, the difference between the Bagaryatskii OR and the Isaichev OR is a rotation of only  $3.59^\circ$  about  $[010]_{\text{Fe}_3\text{C}} // [111]_\alpha$ . Many previous publications[78, 79, 118] have indicated that the OR between cementite and the ferrite matrix depends on the nucleation site of cementite in the ferrite matrix. Ohmori et al.[118] studied a steel similar to that used in the present work and concluded that the Isaichev OR was observed when cementite precipitated at the martensite twin boundaries, and that the Bagaryatskii OR was observed when the cementite formed within the twin free regions. For this high carbon steel used in the present work, previous study suggested that the cementite would be expected to form at the twin boundaries[78]. Thus the Isaichev OR is expected, and the present results are therefore consistent with the work of Ohmori et al.[118]. However, some cementite particles should have precipitated in the twin free regions[111] and, if the previous work is correct, the Bagaryatskii OR should have been observed. It has been shown that precipitation of cementite at twin boundaries in alloy steel occurs due to the particular arrangement of ferrite-iron atoms, which resembles that in cementite. The cementite-like structure of the ferrite-iron forms along the twin interfaces as a consequence of the twinning shear. The twinning shear brings the ferrite-iron atoms into

positions which are close to that in the cementite[78, 119]. On the other hand, if the high density of dislocations were not affected by the tempering, then carbide precipitation along the dislocation and between some lath martensites would also occur[120].

### **M<sub>7</sub>C<sub>3</sub>**

The M<sub>7</sub>C<sub>3</sub> carbides have hexagonal unit cells, space group P31c, in which the carbon atoms are contained in trigonal prisms. Hence the derived orientation relationship:

$$(0001)_{M_7C_3 \text{ carbide}} // (101)_\alpha$$

$$[\bar{1}100]_{M_7C_3 \text{ carbide}} // [\bar{1}11]_\alpha$$

$$[11\bar{2}0]_{M_7C_3 \text{ carbide}} // [\bar{1}21]_\alpha$$

This is one of the orientations found by Dyson and Andrews for M<sub>7</sub>C<sub>3</sub> carbides precipitated in steel[103, 121].

The M<sub>7</sub>C<sub>3</sub> carbides are well known for their characteristic crystalline faults. The diffraction patterns obtained from these carbides are therefore characterized by forbidden reflection, systematic absences, satellite spots, and streaks that frequently occur across diffraction maxima. The structure of the M<sub>7</sub>C<sub>3</sub> carbide can also be interpreted as the orthorhombic crystal structure, as reported in detail by J. P. Morniroli et al.[122-124].

## $M_{23}C_6$

The structure of this carbide belongs to the space group  $F_{m\bar{3}m}$  and has a cubic-f unit cell[125]. The carbon-atom environment in  $M_{23}C_6$  is unique in that it is neither an octahedron nor a trigonal prism, but a square anti-prism[103]. The orientation relationship can be written as:

$$(\bar{1}\bar{1}\bar{1})_{M_{23}C_6 \text{ carbide}} // (1\bar{1}0)_\alpha$$

$$[0\bar{1}\bar{1}]_{M_{23}C_6 \text{ carbide}} // [11\bar{1}]_\alpha$$

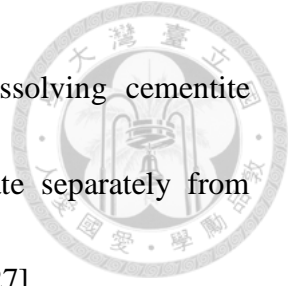
$$[\bar{2}\bar{1}0]_{M_{23}C_6 \text{ carbide}} // [112]_\alpha$$

The orientation between this  $M_{23}C_6$  and the ferrite can be expressed by the K-S relationship. Honeycombe et al. established the interphase precipitation on stepped austenite/ferrite interfaces in Fe-Cr-C alloy[126]. Interphase precipitation is associated with the coherent growth of the austenite/ferrite interface, which predominates at lower temperatures.

### 2.4.2 Transformation and mechanism

Alloy carbides can form in a variety of ways. Sites for carbide precipitation include dislocations, grain boundaries, twin boundaries, and sub-boundaries, which are energetically favorable sites providing high diffusivity paths for the rapid diffusion of solute. Stable alloy carbides can nucleate *in situ* on pre-existing cementite particles,

with carbon being provided for their subsequent growth by dissolving cementite particles. It has also been shown that alloy carbides can nucleate separately from dissolving carbides within the ferrite matrix, often on dislocations[127].



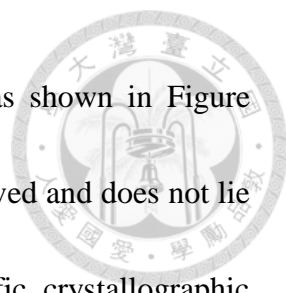
Two basic modes of transformation have been observed: *in situ* and separate nucleation.

### **In-situ transformation**

*In situ* transformation is defined as individual cementite particles appearing to transform directly to groups of alloy carbide particles. It has been shown that the alloy carbide nucleates at numerous points on the cementite-ferrite interface[128] and grows until the cementite disappears, leaving groups of smaller alloy carbide particles[85].

Figure 2-16 shows the transformation of cementite to  $M_7C_3$  carbide taking place by *in situ* transformation. The boundary between cementite and the  $M_7C_3$  carbides is straight, and the trace lies along the (010) plane of cementite, suggesting that a crystallographic coherency exists between the lattices of the two carbides. The interface of cementite/ferrite is a preferred site for  $M_7C_3$  nucleation, and the subsequent growth of  $M_7C_3$  in cementite is more rapid than that in the ferrite matrix by an *in situ* mechanism[129]. The schematic diagram of the reaction process is shown in Figure 2-17 (a).

Figure 2-18 clearly shows that an  $M_7C_3$  carbide transforms to an  $M_{23}C_6$  carbide by an *in situ* mechanism.  $M_{23}C_6$  nucleates at first over the entire interface between the



ferrite, and the  $M_7C_3$  and then grows toward the  $M_7C_3$  crystal, as shown in Figure 2-19(b). The boundary between the  $M_{23}C_6$  and  $M_7C_3$  carbides is curved and does not lie on any crystallographic plane, suggesting that there is no specific crystallographic relationship between the lattices of these two carbides. In Figure 2-20, it is observed that the transformation of  $M_{23}C_6$  to  $M_6C$  also occurs by an *in situ* mechanism. A number of  $M_6C$  carbide particles appear at the  $M_{23}C_6$ /ferrite interface and inside the  $M_{23}C_6$  carbide, as shown in Figure 2-19. The particle size and the area of the  $M_6C$  carbide increases as tempering time increases[130-131].

### **Separate nucleation**

Separate nucleation, on the other hand, is defined as the original cementite dissolving in the ferrite matrix and the alloy carbide separately nucleating at new sites, primarily on dislocations inherited from the martensite transformation[132]. This type of dispersion is usually much finer than that produced by nucleation on pre-existing cementite and thus has a larger effect on the mechanical properties[85].

In Figure 2-21(d), the small bright contrast marked by arrow A shows that  $M_7C_3$  has nucleated on the interface between cementite and ferrite. The bright contrast shown by the mark B shows that  $M_7C_3$  has precipitated within the ferrite matrix by a separate nucleation mechanism[129].



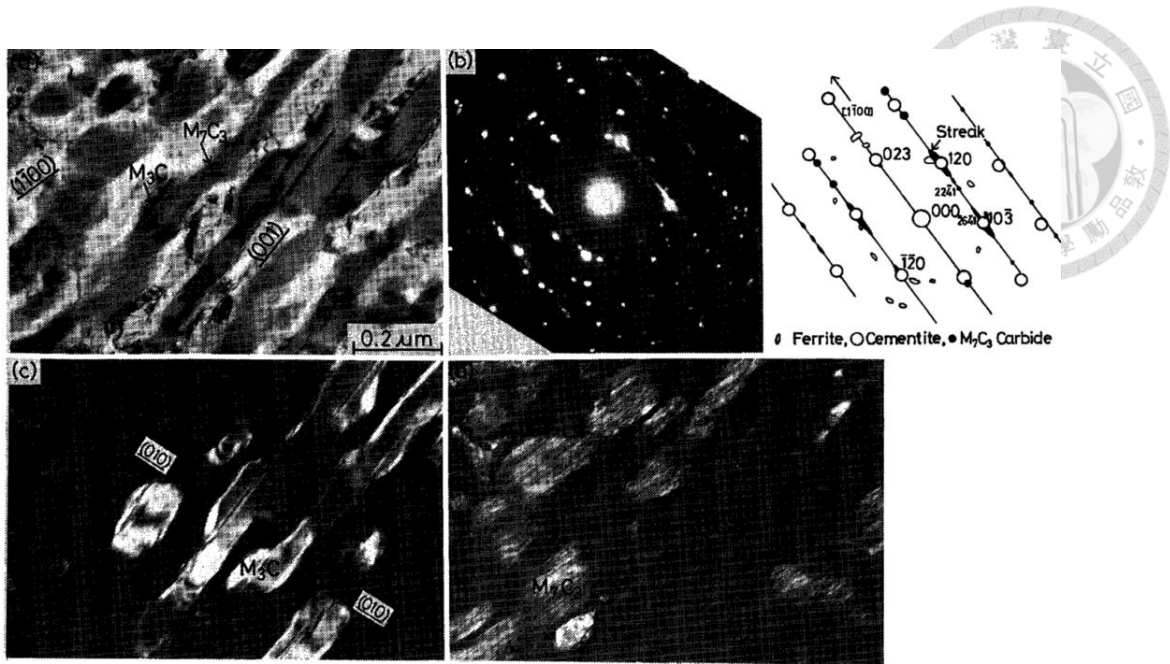


Figure 2-16 Microstructure showing the *in situ* transformation of cementite to  $M_7C_3$  in 16.5%Cr-3.65%C steel tempered for 1 hr at 600°C after rapid quenching. (a) bright field image, (b) selected area diffraction pattern and its schematic key diagram, (c) dark field images taken respectively from the  $\bar{1}20$  reflection spot of  $M_3C$ , and (d) the  $\bar{2}6\bar{4}1$  reflection spot of  $M_7C_3$ [129].

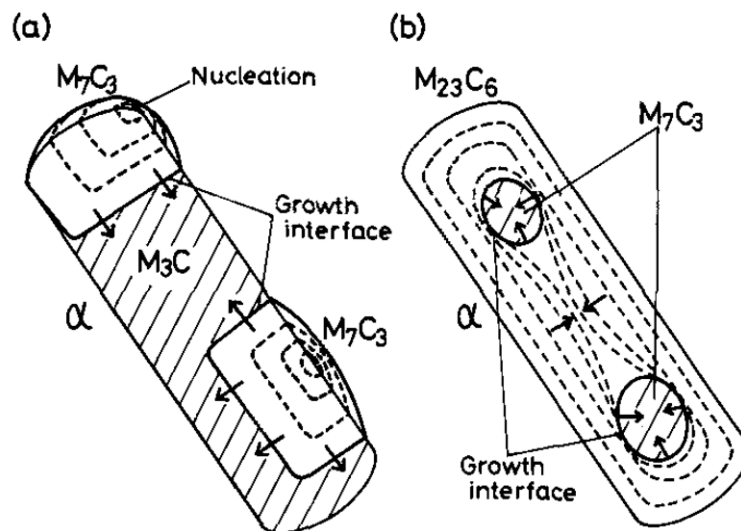


Figure 2-17 Schematic drawing of the processes of  $M_3C \rightarrow M_7C_3$  and  $M_7C_3 \rightarrow M_{23}C_6$  reactions. (a)  $M_3C \rightarrow M_7C_3$  reaction, (b)  $M_7C_3 \rightarrow M_{23}C_6$  reaction[130].

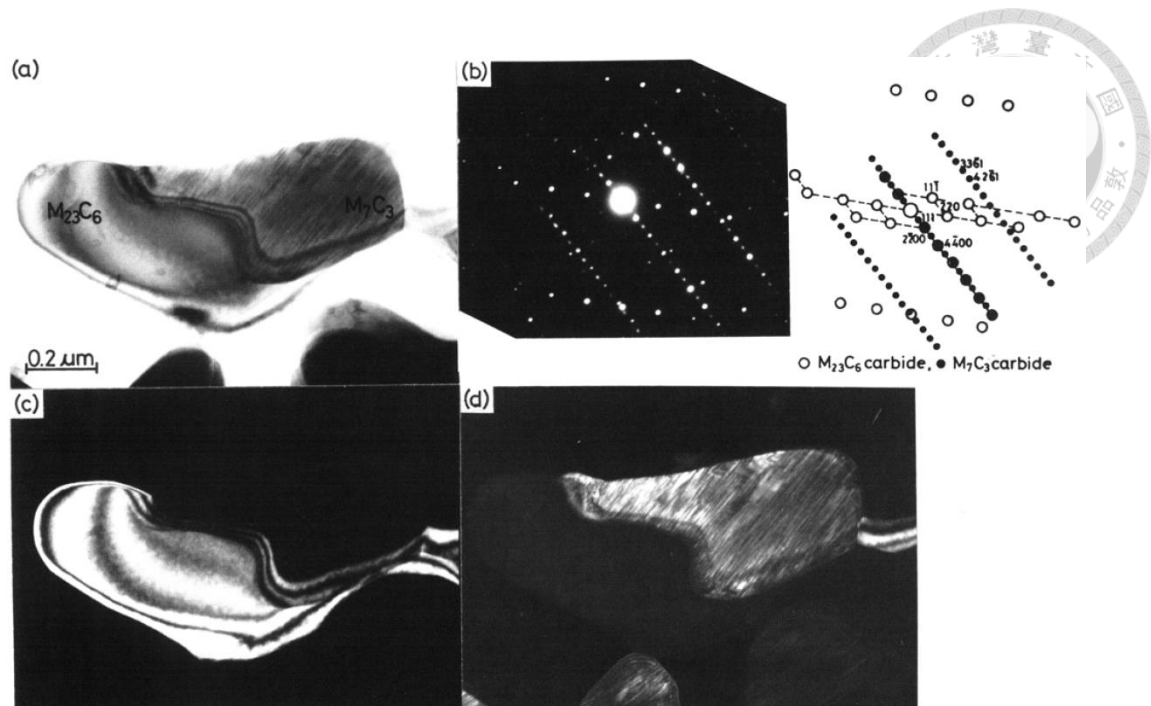


Figure 2-18 Microstructure showing the *in situ* transformation of  $M_7C_3$  to  $M_{23}C_6$  in 18.6 %Cr-3.40%W-3.63%C steel tempered for 10h at 700°C. (a) Bright field image, (b) selected area diffraction pattern and its schematic key diagram, (c) and (d) dark field images taken respectively from the 220 reflection spot of  $M_{23}C_6$  and the  $\overline{4}26\overline{1}$  reflection spot of  $M_7C_3$ [130].

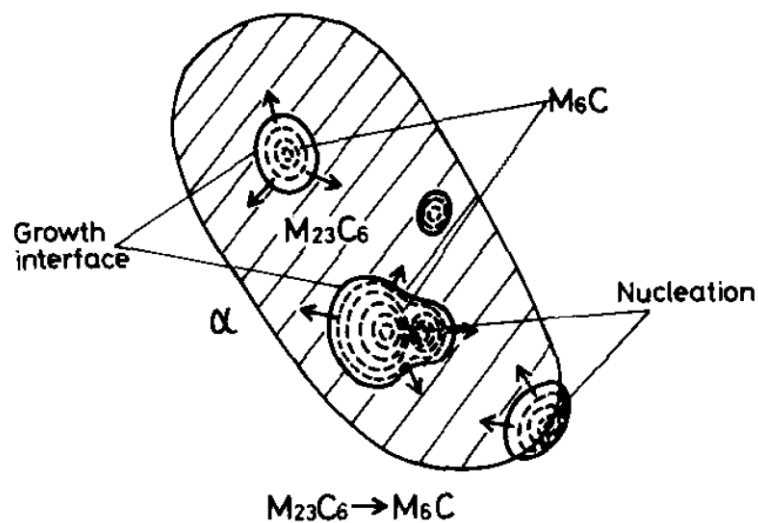


Figure 2-19 Schematic illustration representing the process of  $M_{23}C_6 \rightarrow M_6C$  reaction[130].

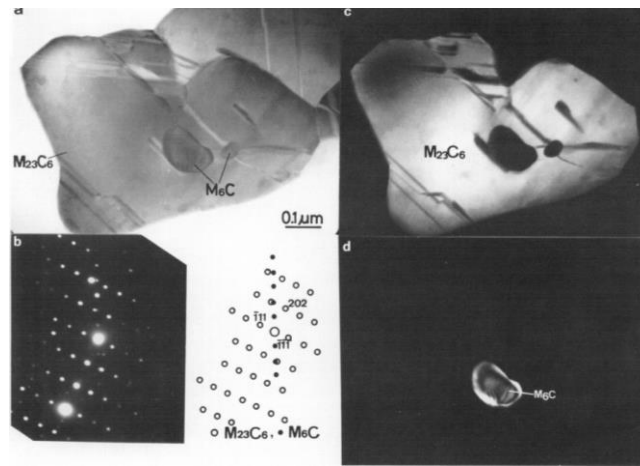


Figure 2-20 Microstructure showing the *in situ* transformation of  $M_{23}C_6$  to  $M_6C$  in 18.4%Cr-8.31W-3.6%C steel tempered for 120h at 700°C. (a) Bright field image, (b) selected area diffraction pattern and its key diagram, (c) and (d) dark field images taken respectively from the 202 reflection spot of  $M_{23}C_6$  and the 333 reflection spot of  $M_6C$ [130].

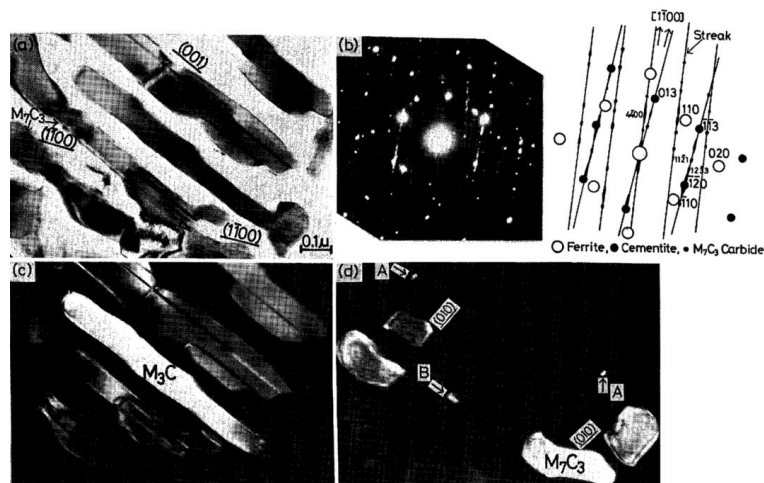


Figure 2-21 Microstructure showing the *in situ* transformation of cementite to  $M_7C_3$  in 16.5%Cr-3.65%C steel tempered for 1 hr at 600°C after rapid quenching, (a) bright field image, (b) selected area diffraction pattern and its schematic key diagram, (c) dark field images taken respectively from the  $\bar{1}13$  reflection spot of cementite and (d) the  $4\bar{4}00$  reflection spot of  $M_7C_3$ [129].

## Chapter 3 Lenticular martensite in AISI 440C

### stainless steel



### 3.1 Introduction

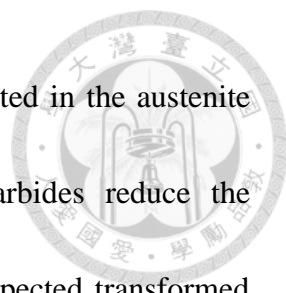
In the past, the lenticular martensite structure has been investigated by many researchers, such as Wayman C. M. and Maki T. [21, 48, 50, 55, 56, 62, 63, 145].

Lenticular martensite has a special structure, one which combines characteristics of both lath martensite and thin plate martensite, including the midrib region, where twins occur, and the untwinned regions, which, though twin-free, have a high density of dislocations.

Lenticular martensite has three regions: midrib, twinned region and untwinned region.

The lenticular martensite has specific characteristics: the twin plane of the midrib is (112) and the twinning direction is  $[\bar{1}\bar{1}1]$ , and the partial growth of twins in the midrib introduces a set of screw dislocations with Burgers vectors of  $a/2[\bar{1}\bar{1}1]$  and forms the untwinned region.

Many researchers have defined the transformed martensite structure by its carbon concentration. The investigated material in this research has high-carbon and high-chromium contents, which should be a thin-plate martensite structure, judging by its 1 wt% carbon. However, the lenticular martensite structure can still be seen after



deep cryogenic treatment because many  $M_7C_3$  carbides are distributed in the austenite matrix in this high-carbon and high-chromium steel. These carbides reduce the concentration of carbon in the austenite matrix and cause the unexpected transformed structure. Therefore, the austenitization temperature is the key factor to control the transformed martensite structure, as it decides the amount of solid solute alloying elements in the matrix [146, 147].

In the present study, austenitization treatments at different temperatures were conducted to further investigate the influence of the incomplete solid solution, which resulted in the change from lath martensite to lenticular martensite. The comparison and calculation of this effect were also studied in this work. In addition, the lenticular martensite structure in this high-carbon and high-chromium stainless steel was analyzed by TEM, FIB, EBSD and SEM techniques.

## 3.2 Experimental procedure

The experimental material used in this work was AISI 440C stainless steel. The as-received material was a commercially wrought AISI 440C stainless steel bar (with a diameter of 29 mm) produced by Gloria Material Technology Corporation through four-folded forging of a cast slab at 1130°C and annealing at 870°C for 8hrs, followed by furnace cooling to ambient temperature (as shown in Figure 3-1). The chemical

composition of the steel is Fe-1.0C-17.4Cr-0.45Mo-0.40Mn-0.38Si-0.40Ni (wt%). The specimens were machined into 3 mm diameter cylindrical rods, which were austenitized at 1000°C, 1150°C and 1200°C for 3 days and cooled to room temperature for 15 min. After that, the specimens were quenched in liquid nitrogen (-196°C) for 15 min to obtain a martensite structure (as shown in Figure 3-2).

A Vickers hardness machine was used to measure the hardnesses of the lenticular martensite, surrounding austenite and  $M_7C_3$  carbide. The corresponding microstructures were examined by OM, SEM, and TEM. Those specimens were cut from the heat-treated rods. The specimens for OM and SEM were mechanically polished and then etched in a mixture of 40 ml HCl, 25 ml ethanol, 30 ml distilled water, and 5 g  $CuCl_2$ . TEM samples were sliced from the rod specimens, thinned to 0.08 mm by abrasion with SiC papers, and twin-jet electro-polished using a mixture of 5% perchloric acid, 25% glycerol, and 70% ethanol at 5~10°C with 45~55V polishing potential. EBSD measurement was carried out with an FEI NOVA 450 operated at 25 kV with EDAX detector. The mapping by EBSD was conducted at a step size of 300 nm. The orientation measurement and analysis were done with TSL-OIM software. The thin foils were then examined using an FEI Tecnai G2 20 TEM operated at 200KV. For the chemical composition measurements, a JEOL JXA-8200 Electron Probe X-Ray Microanalyzer (EPMA) was used to analyze the changes in the chromium content in the

austenite phase after different heat treatments.

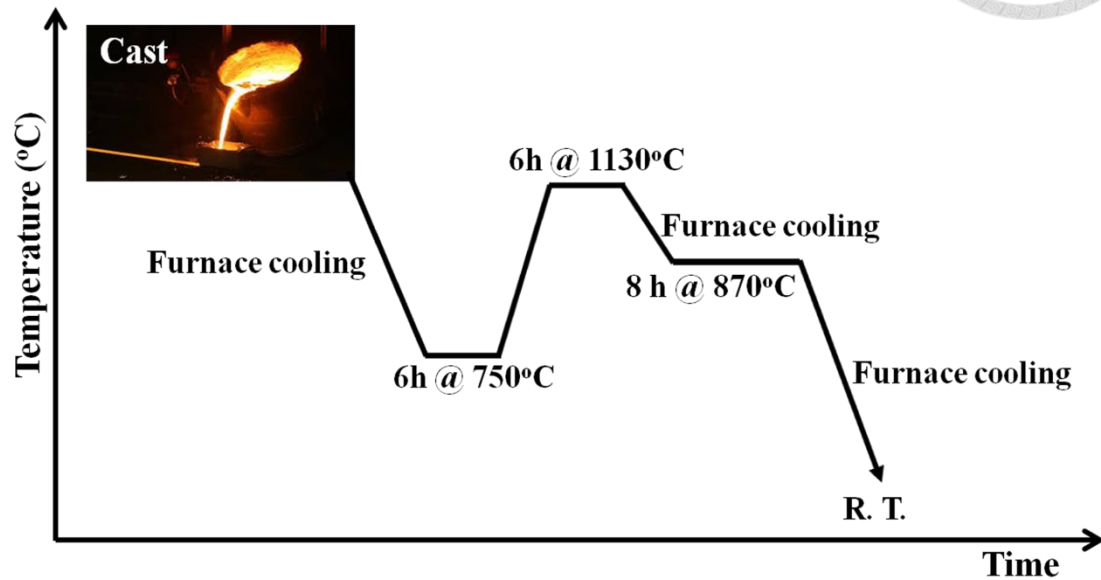


Figure 3-1 Schematic representation showing the production procedure of the original material.

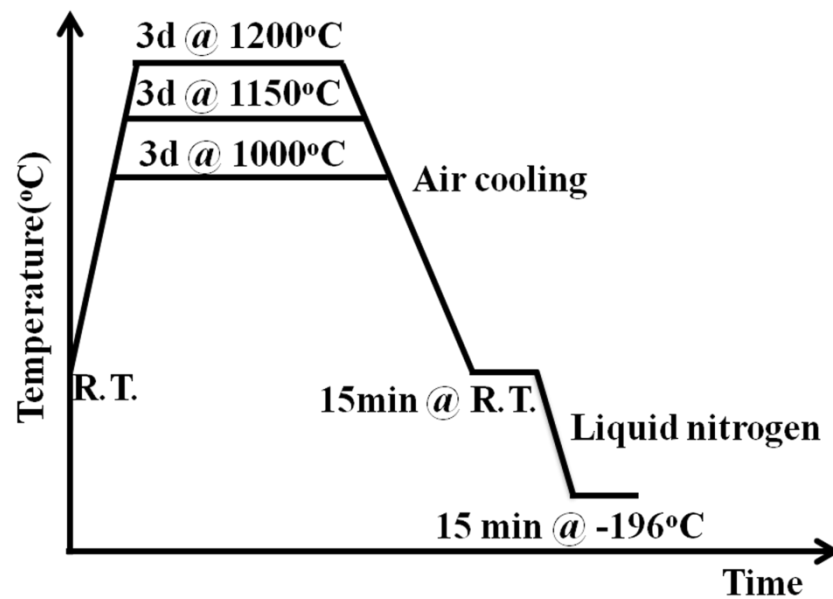


Figure 3-2 Schematic representation showing the subzero treatment of the material.

### 3.3 Results and Discussion

#### 3.3.1 The influence of different austenitization temperature



The AISI 440C steel has high carbon and chromium contents, so carbides form easily during the manufacturing process. The carbides are uniformly dispersed in the matrix by hammering at high temperature (Figure 3-3(a)). Due to the high alloy content, the solution degree of carbides decides the carbon concentration in the matrix, which also affects the final resulting martensite structure. These carbides are  $M_7C_3$  carbides (as shown in Figure 3-4). The eutectic carbide within a high chromium content white iron is of the type  $M_7C_3$ . The amounts of solute carbon and chromium in AISI 440C stainless steel are influenced by the applied austenitization temperature. In order to verify the relation between the morphology of martensite and its formation temperature, the  $M_s$  temperature was adjusted by varying the austenitization temperature, and microstructural observation was carried out using specimens cooled to a temperature just below the  $M_s$  temperature.

$M_7C_3$  carbides were identified by electron diffraction pattern analysis (Figure 3-4). Three cells with trigonal, orthorhombic, and hexagonal symmetry have been proposed to describe the structure of  $M_7C_3$  carbides. The  $M_7C_3$  carbides appeared to contain a large number of stacking faults when examined by TEM (Figure 3-5). The defects present in  $M_7C_3$  carbides are twins or anti-phase boundaries between the orientation



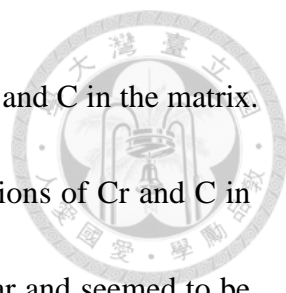
variants of the orthorhombic cell (in Figure 3-5).

OM images of the resulting microstructure are shown in Figure 3-3. After homogenization at 1000°C (Figure 3-3(b)), the white islands, or  $M_7C_3$  carbides that did not dissolve into the austenite during austenitization, were distributed in the matrix, which was lath martensite phase (Figure 3-6(a)). The prior-austenite grain size was about 23 $\mu$ m. After austenitization at 1200°C Figure 3-3(d)), there were three phases after transformation: fewer  $M_7C_3$  carbides, lenticular martensite, and residual austenite (Figure 3-6(b)). This result shows that the amount of retained austenite increases with the austenitization temperature, which is associated with the solution of  $M_7C_3$  carbides into the matrix. The prior-austenite grain size was about 60 $\mu$ m.

The fraction and chemical composition of martensite and retained austenite for different austenitization temperatures were calculated from Backscattered Electron (BSE) images and EBSD results, which are provided in Table 3-1. The BSE technique provides detailed information on the crystal orientation image (Figure 3-7), which can help to distinguish the phases in the sample, such as carbides and retained austenite. After austenitization at 1000°C, the BSE images (Figure 3-7(a)) indicated the fraction of various phases as 84.6% martensite, 15.4%  $M_7C_3$  carbides, and 0% retained austenite. The EBSD image results for austenitization at 1000°C were nearly the same: 84.7% martensite, 15.3%  $M_7C_3$  carbides, and 0% retained austenite (Figure 3-7(c)). Due to the

lower austenitization temperature (1000°C), only the carbides and lath martensite were observed in this sample, and no retained austenite was observed. It is obvious that the  $M_s$  of this sample was higher than that of the 1200°C sample, and thus the austenite almost completely transformed into lath martensite after deep cryogenic treatment. The carbon and alloy elements in prior austenite grains consequently stayed in the lath martensite as it formed.

After austenitization at 1200°C, the BSE images (Figure 3-7(b)) showed the fraction of various phases as 36.7% martensite, 6.4%  $M_7C_3$  carbides, and 56.9% retained austenite. The EBSD image result for the same austenitization temperature was also nearly the same: 33% martensite, 6.4%  $M_7C_3$  carbides, and 60.6% retained austenite (Figure 3-7(d)). Due to the high austenitization temperature (1200°C), carbides, lenticular martensite and retained austenite were distributed in the sample. In addition, since more alloying elements dissolve into the austenite matrix at higher austenitization temperature, these retained austenite grains are very stable. The amount of lenticular martensite remains the same even after further cryogenic treatment at 4K. At this austenitization temperature, the transformed lenticular martensite has large spaces to grow in the prior austenite grain and can avoid deformation after impacting with each other. This facilitates observation of the complete three regions in lenticular martensite and measurement of the changes in misorientation between lenticular martensite grains.

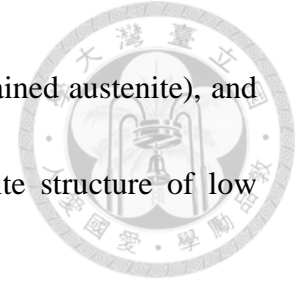


The high austenitization temperature resulted in large amounts of Cr and C in the matrix. In contrast, a low austenitization temperature caused low concentrations of Cr and C in the matrix. The statistical results from different methods were similar and seemed to be reliable for the calculated concentration as compared with the EPMA and Thermo-Calc (Figure 3-8) results. In conclusion, the carbon and chromium contents in the matrix were higher after austenitization at 1200°C than after austenitization at 1000°C, as shown in Table 3-2.

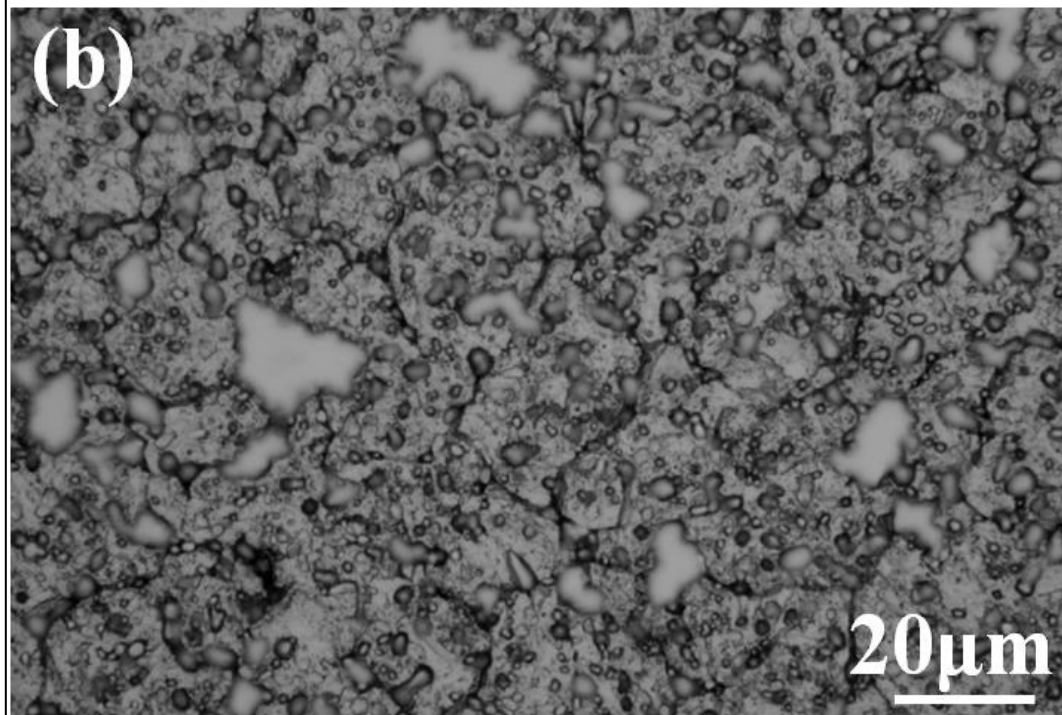
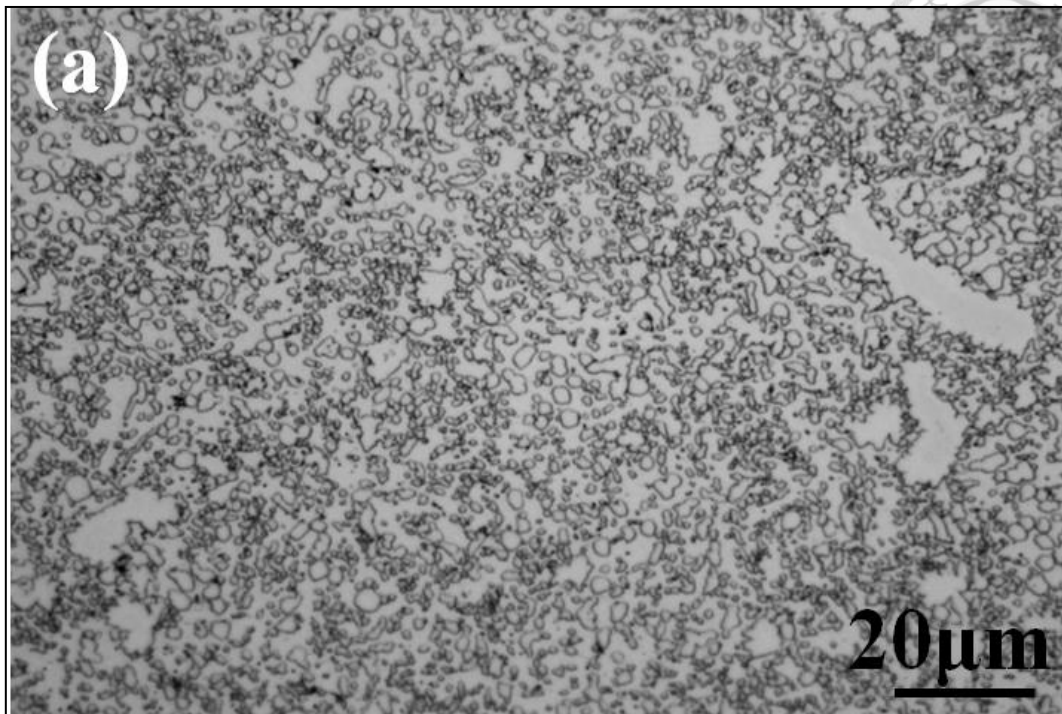
The high austenitization temperature also increased the austenite grain size and reduced the amount of undissolved carbides, which indicates that the loss of the pinning effect by carbides helps the growth of austenite grains. The high amount of dissolved carbides results in the high contents of C and Cr in the matrix and lowers the Ms temperature. Consequently, the forming lenticular martensite, with high internal stress, suffered cracking, as observed in the polished (not etched) sample shown in Figure 3-7(b). The resulting structure was composed of little lenticular martensite and large amounts of retained austenite. The retained austenite becomes more stable at room temperature with increasing austenitization temperature.

With the low austenitization temperature, it was obvious that the amount of undissolved carbides was much greater than that after high temperature austenitization. This led to less dissolved C and Cr and a high Ms temperature. The final structure

consisted of  $M_7C_3$  carbides and lath martensite (with almost no retained austenite), and the morphology was nearly identical to that of the lath martensite structure of low carbon steel.



It should be noted that, after austenitization at 1150°C, the products of cryogenic treatment also include three phases:  $M_7C_3$  carbides, many lenticular martensites, and fewer retained austenites. Although at this medium austenitization temperature the preferred martensite structure is also lenticular martensite, a complicated distribution of lenticular martensite in a prior austenite grain is fairly hard to analyze, as shown in (Figure 3-3(c)). Since the  $M_s$  is higher after 1150°C austenitization than after 1200°C austenitization, there exists more transformed lenticular martensite. During transformation, these martensite grains easily impinge on the growth process of each other. Thus, this austenitization temperature is not so suitable for observation.



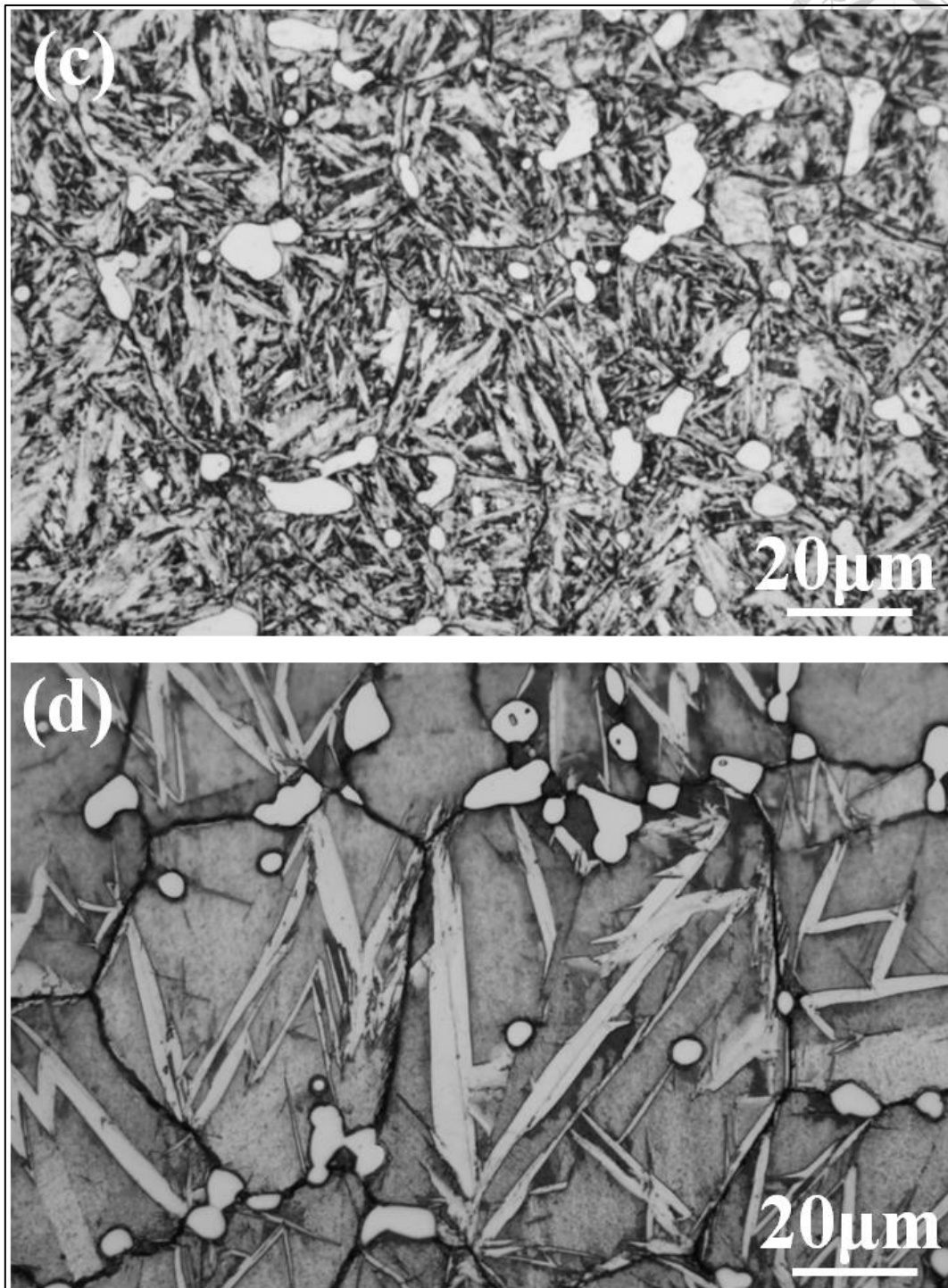


Figure 3-3 Optical microscopy image of (a) As-received AISI 440C steel (b) lath martensite microstructure austenitized at 1000°C, (c) lenticular martensite microstructure austenitized at 1150°C and (d) lenticular martensite microstructure austenitized at 1200°C.

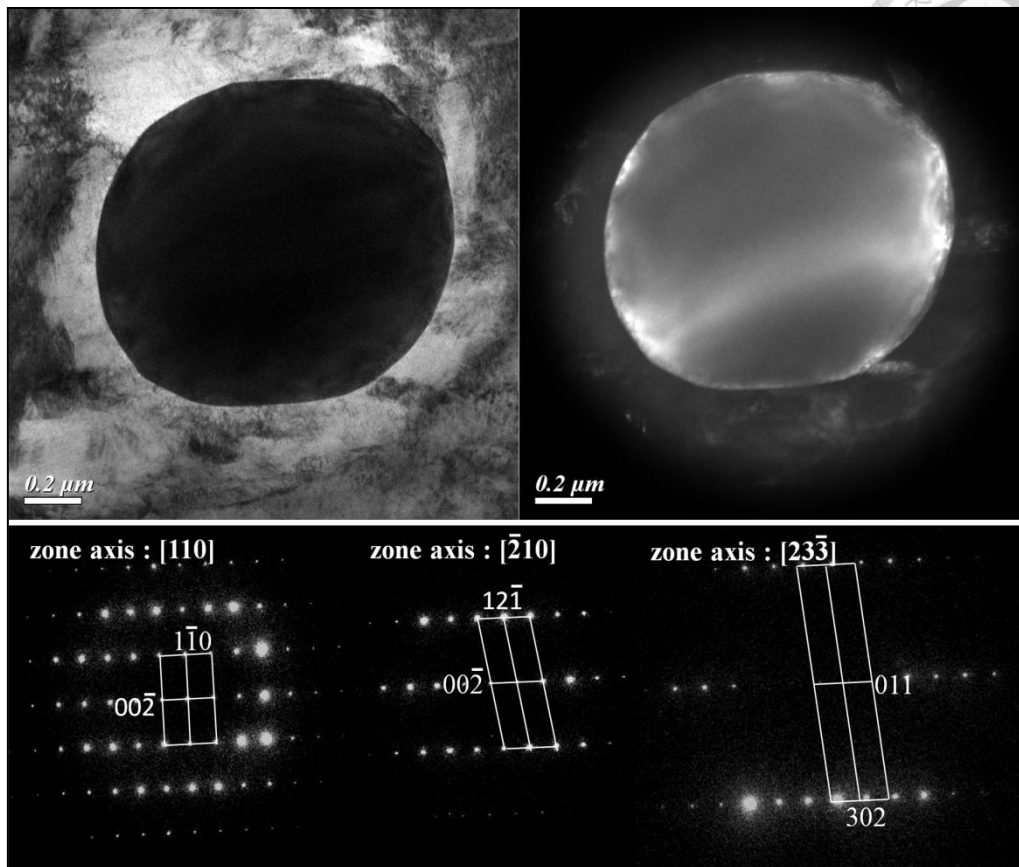


Figure 3-4 (a) TEM bright field image, (b) dark field image and (c) the corresponding diffraction pattern of  $\text{M}_7\text{C}_3$  carbides.

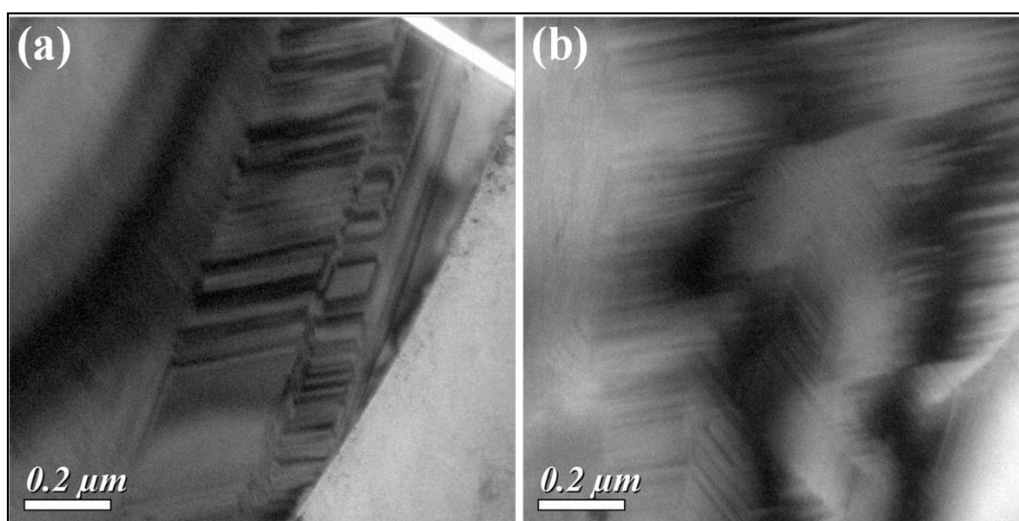
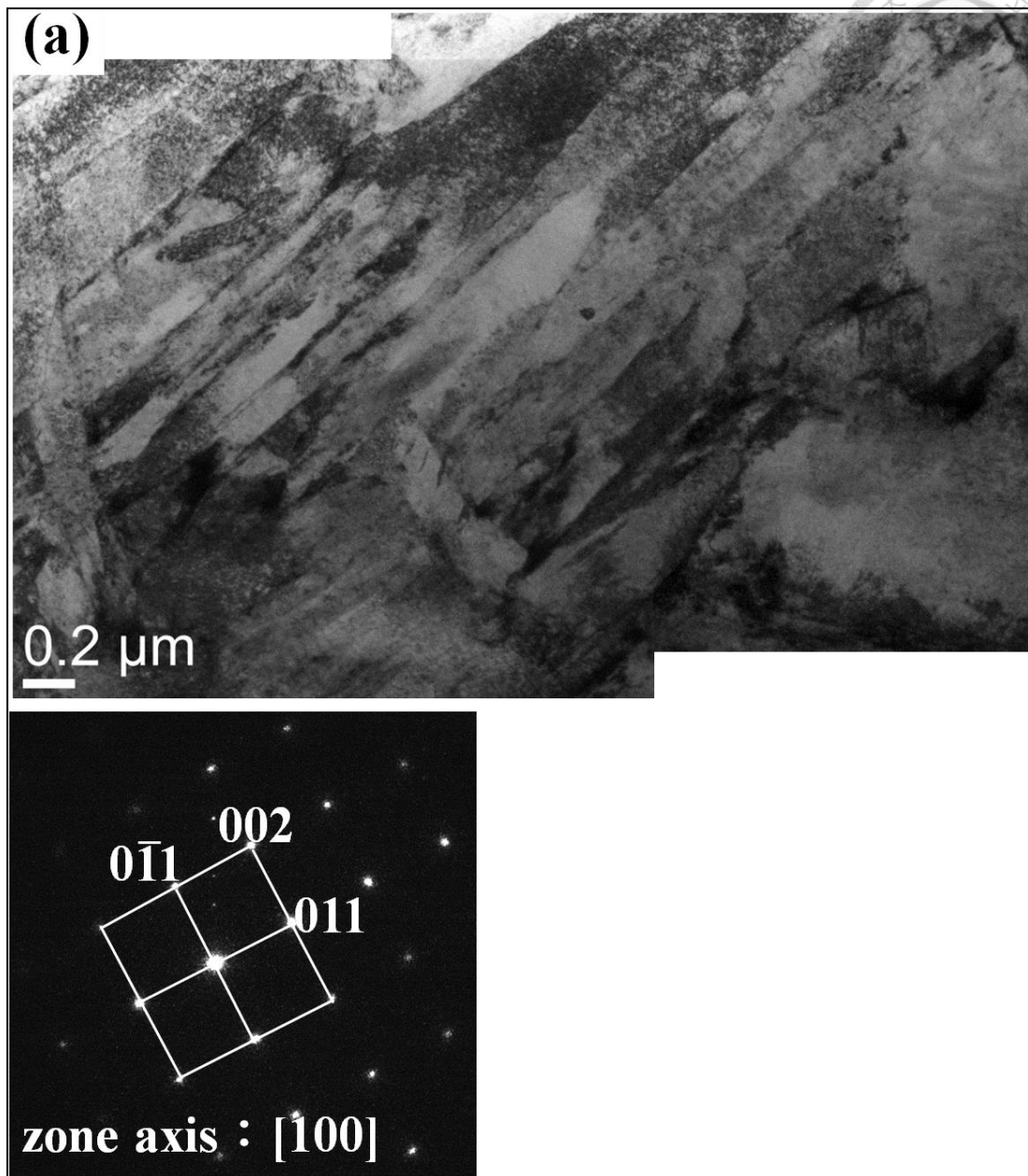


Figure 3-5 TEM image shown the (a) twin and (b) antiphase boundaries within the  $\text{M}_7\text{C}_3$  carbides





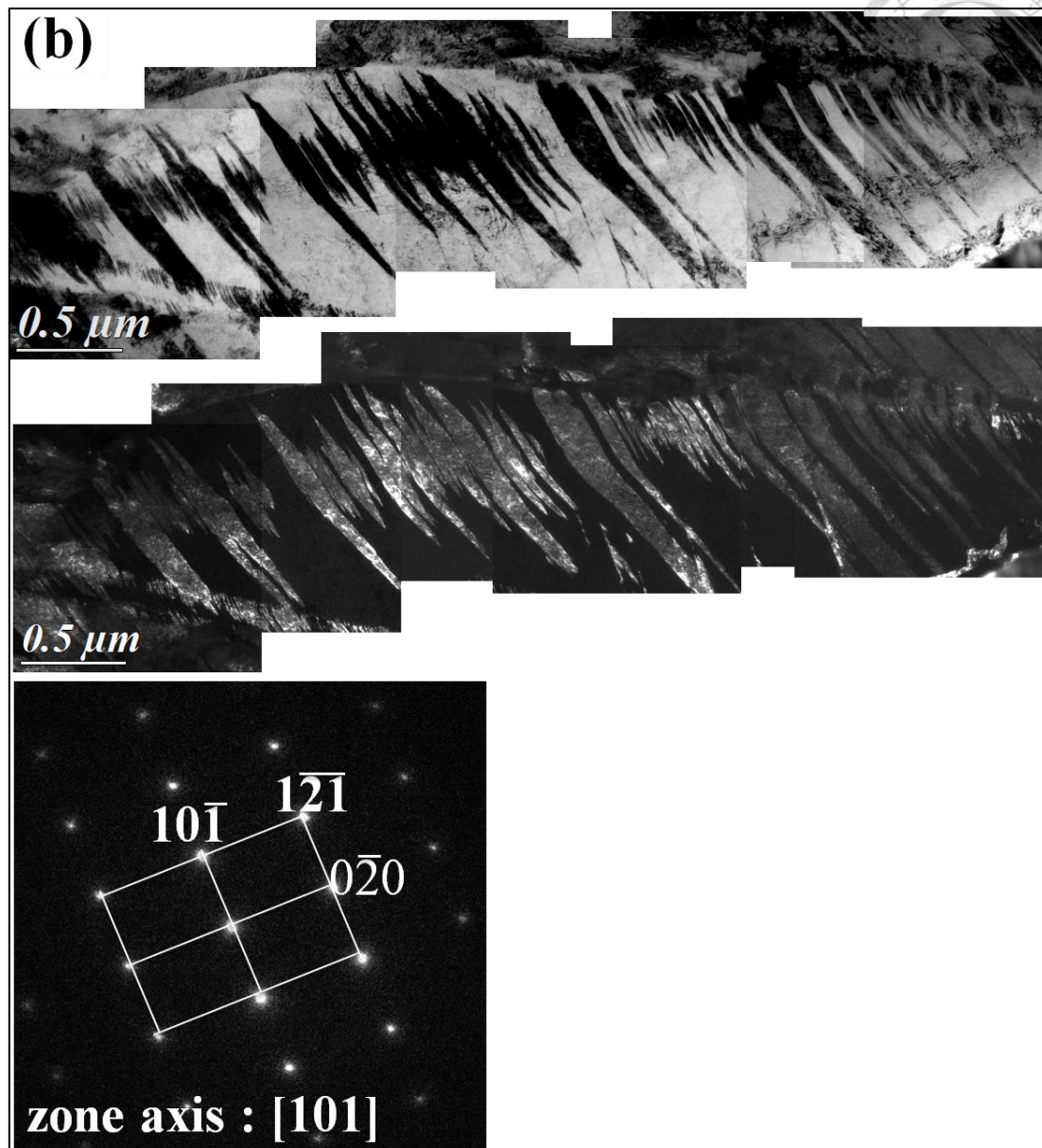


Figure 3-6 TEM bright field, dark field image and the corresponding diffraction pattern image of (a) lath martensite microstructure austenitized at 1000°C (b) lenticular martensite microstructure austenitized at 1200°C

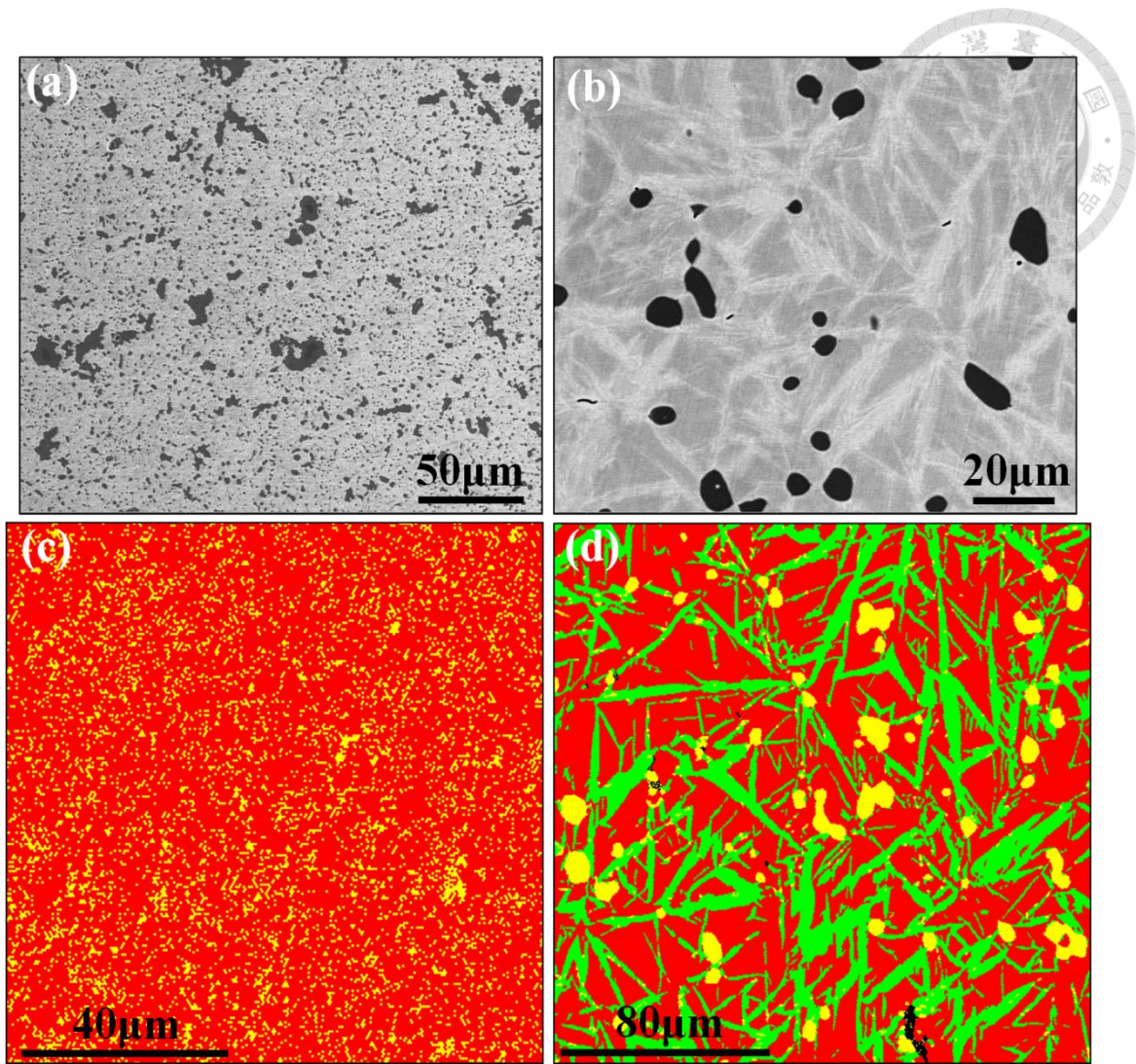


Figure 3-7 BES image of (a), (c) lath martensite microstructure austenitized at 1000°C and (b), (d) lenticular martensite microstructure austenitized at 1200°C in AISI 440C.

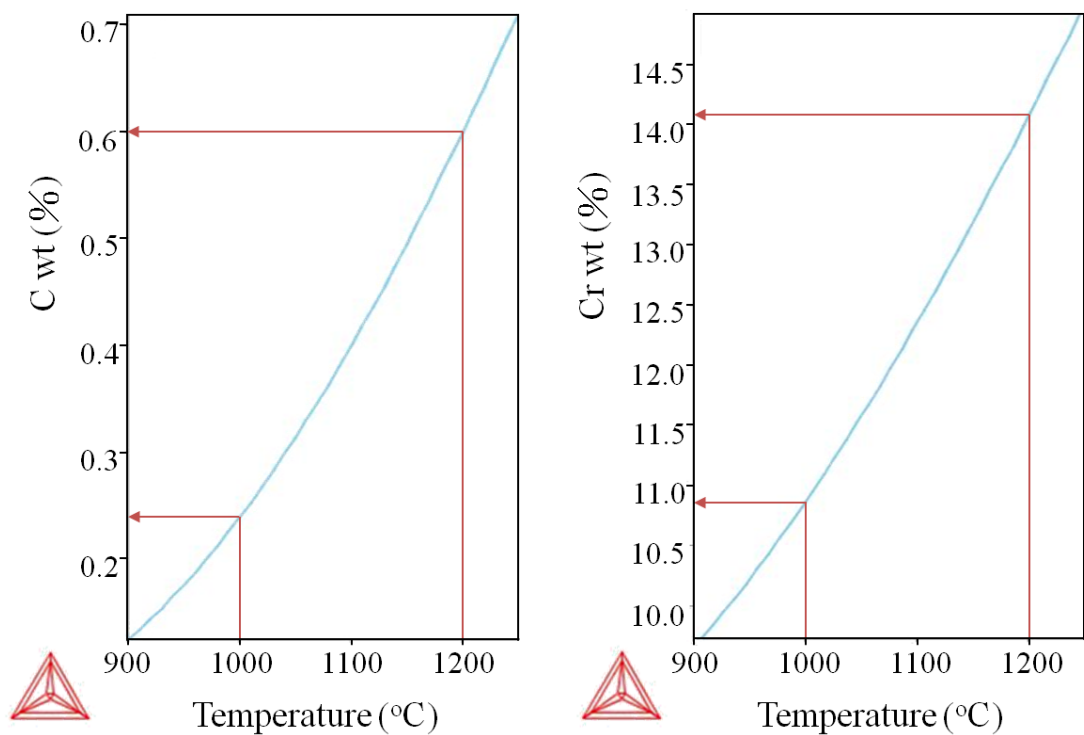


Figure 3-8 (a) and (b) Thermo-Calc data indicating the chemical composition of austenite phase in the 1000°C and 1200°C equilibrium state.

Table 3-1 The fraction of each phase for different austenitization temperatures

Temperature (°C)	1000			1200		
Phase (%)	Martensite	Austenite	M <sub>7</sub> C <sub>3</sub> carbides	Martensite	Austenite	M <sub>7</sub> C <sub>3</sub> carbides
BSE image	84.6	0	15.4	36.7	56.9	6.4
EBSD image	84.7	0	15.3	33.0	60.6	6.4
PAGS* (μm)		23			60	

\*Prior-austenite grain size

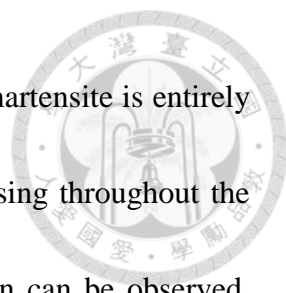
Table 3-2 Chemical composition of matrix for different austenitization temperature

Temperature (°C)	1000		1200	
Mass (wt%) in matrix	Cr	C	Cr	C
EPMA	11.47	0.21	14.78	0.30
Thermo-Cal	10.9	0.16	13.59	0.47

### 3.3.2 The transformation of lenticular martensite

Figure 3-3 (d) indicates that both lenticular martensite and thin plate martensite coexist in the sample austenitized at 1200°C. The thin plate martensite has a morphology quite distinguishable from that of lenticular martensite. The former exhibits a narrower structure. The initial nucleation of thin plate martensite and lenticular martensite is mostly confined to the austenite boundary, the  $M_7C_3$  carbide/austenite boundary, and the annealing twin/austenite boundary, owing to favorable energy. It is taken as a heterogeneous nucleation. The number of lenticular martensites increases with time, and the successive formation of lenticular martensites with specific directions builds up. This phenomenon appears like a burst phenomenon. In a sample austenitized at 1200°C and subzero-treated, the hardness value of lenticular martensite was 542Hv; that of the austenite matrix, 290Hv; and that of the  $M_7C_3$  carbide, 1035Hv.

The growth of lenticular martensite starts at the midrib region, which can be seen



to be thin plate martensite, as shown in Figure 3-9. This thin plate martensite is entirely a set of uniformly-spaced internal transformation  $\{112\}$  twins crossing throughout the plate. Along the parallel twinning planes, the disconnected junction can be observed. This result suggests that when the formation of the midrib and twinned region is the lattice-invariant deformation twin mode, there is a particular period of stasis growth in the earliest stage of the lenticular martensitic transformation.

Figure 3-6 (b) and Figure 3-10 show the substructure of lenticular martensite, where the high density twins appear at the central region of the lenticular martensite. The region can be viewed as the midrib region. The lenticular martensite transformation initiates at the midrib region, and the growth of lenticular martensite accompanies the extension of twins (the extended twinned region). The degree of the extension of the transformation twins in the lenticular martensite is not entirely the same in each grain, as indicated by Figure 3-6 (b), Figure 3-10 and Figure 3-11.

As shown in Figure 3-6 (b), slip lines exist between the extended twinned region and the M/A boundary. The region is an untwinned region. It should be noted that the untwinned region is associated with another lattice-invariant deformation slip mode, which must involve twinning so that perfect dislocations can subsequently slip along the twinning plane. The untwinned region is composed of the movement of perfect dislocations. The untwinned region has some planar faults and dislocations, which can

be seen in Figure 3-6(b), Figure 3-10, Figure 3-11 and Figure 3-12.

Figure 3-11 presents TEM micrographs showing lenticular martensite. As shown in Figure 3-12, the area of the twinned and untwinned region was observed with different two beam conditions: (a)  $g=10\bar{1}$  and (b)  $g=01\bar{1}$ . By contrast analysis, the Burgers vector of these dislocations was determined to be  $a/2[1\bar{1}1]$  in the twinned and untwinned regions of lenticular martensite. In 1966, Wayman have proposed that the change in lattice-invariant deformation of lenticular martensite from twinning to slip is caused by the local temperature increase produced by latent heat in the formation of the untwinned region [56]. However, does this latent heat still work at a temperature as low as  $-196^{\circ}\text{C}$ ? In the present study, liquid nitrogen, which is about  $-196^{\circ}\text{C}$ , was used as the cryogenic treatment source. We suggest another explanation based on the transformation strain. While the sample was put into liquid nitrogen, the lenticular martensite transformation (starting to form twins) was initiated in the prior austenite grain, and therefore the austenite matrix was deformed and produced dislocations. The extension of twins also gradually decreased this deformation strain energy. Sleswyk proposed that the energy of twin boundary decreases via the following dislocation reaction [62]:

$$a/6[\bar{1}\bar{1}1]_M = a/3[11\bar{1}]_M + a/2[\bar{1}\bar{1}1]_M$$

where  $a/6[\bar{1}\bar{1}1]_M$  is the twinning dislocation on successive twin plans  $(112)_M$ ,  $a/3[11\bar{1}]_M$  is complementary dislocation, and  $a/2[\bar{1}\bar{1}1]_M$  is the emissary dislocation.

There are dislocations that result from slip systems. Therefore, it is suggested that the twinned region consists of twins extending from the midrib, and that the twinned and untwinned region consists of a high density of dislocations.





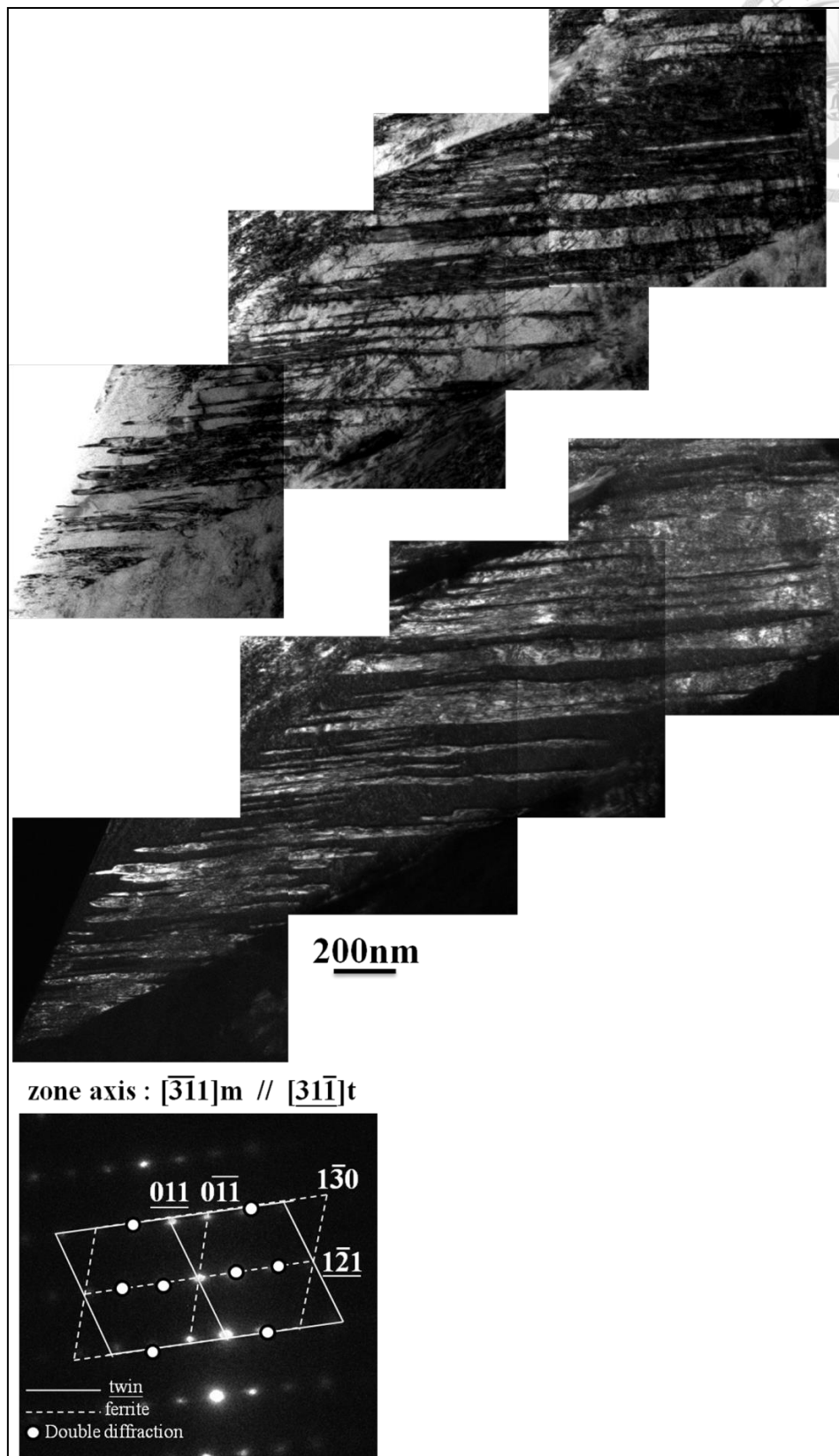


Figure 3-9 TEM bright field and dark field images and the corresponding diffraction pattern image of thin-plate martensite microstructure.



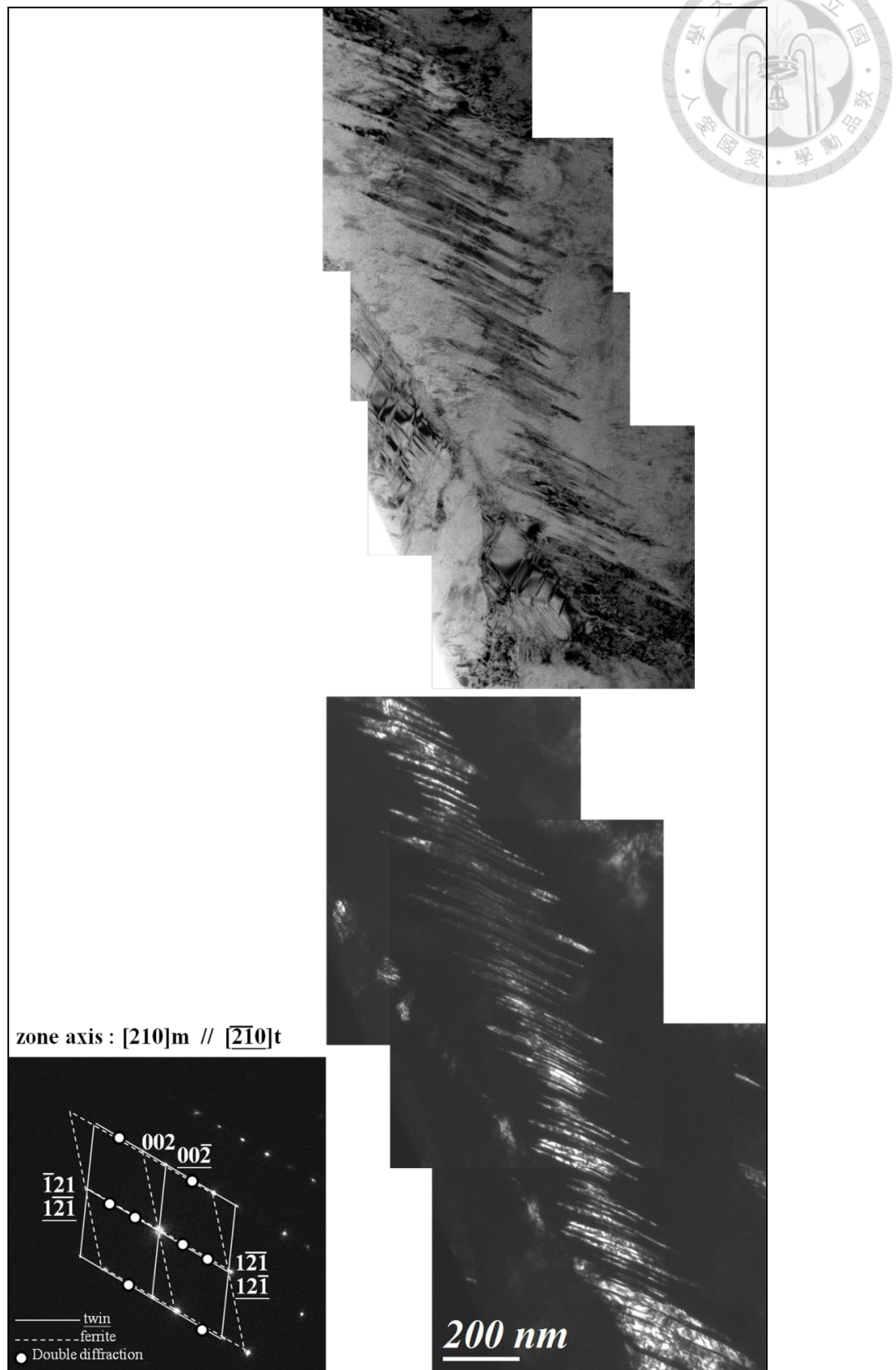


Figure 3-10 TEM bright field and dark field images and the corresponding diffraction pattern image of lenticular martensite microstructure.

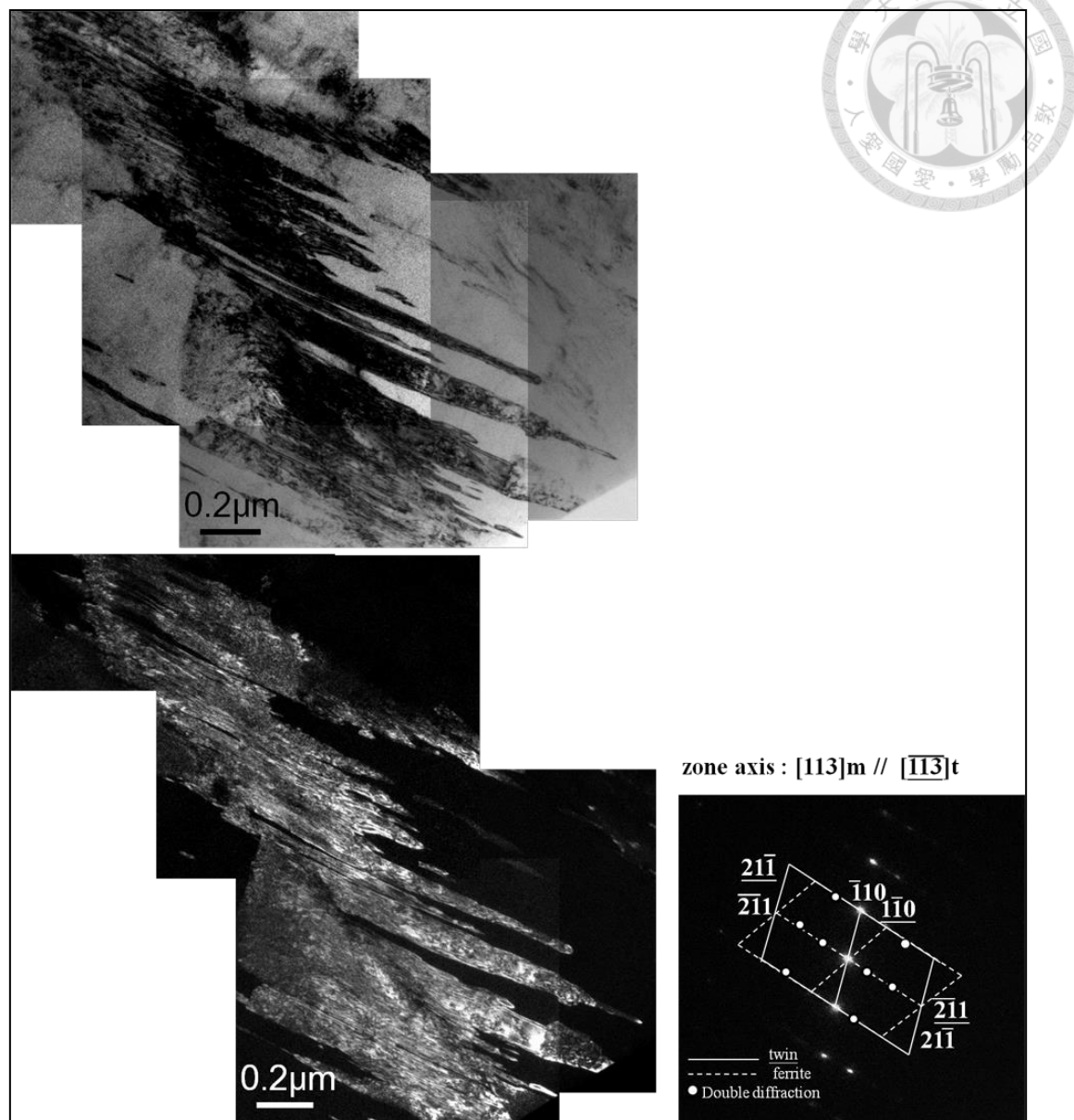


Figure 3-11 TEM bright field and dark field images and the corresponding diffraction pattern image of lenticular martensite microstructure.

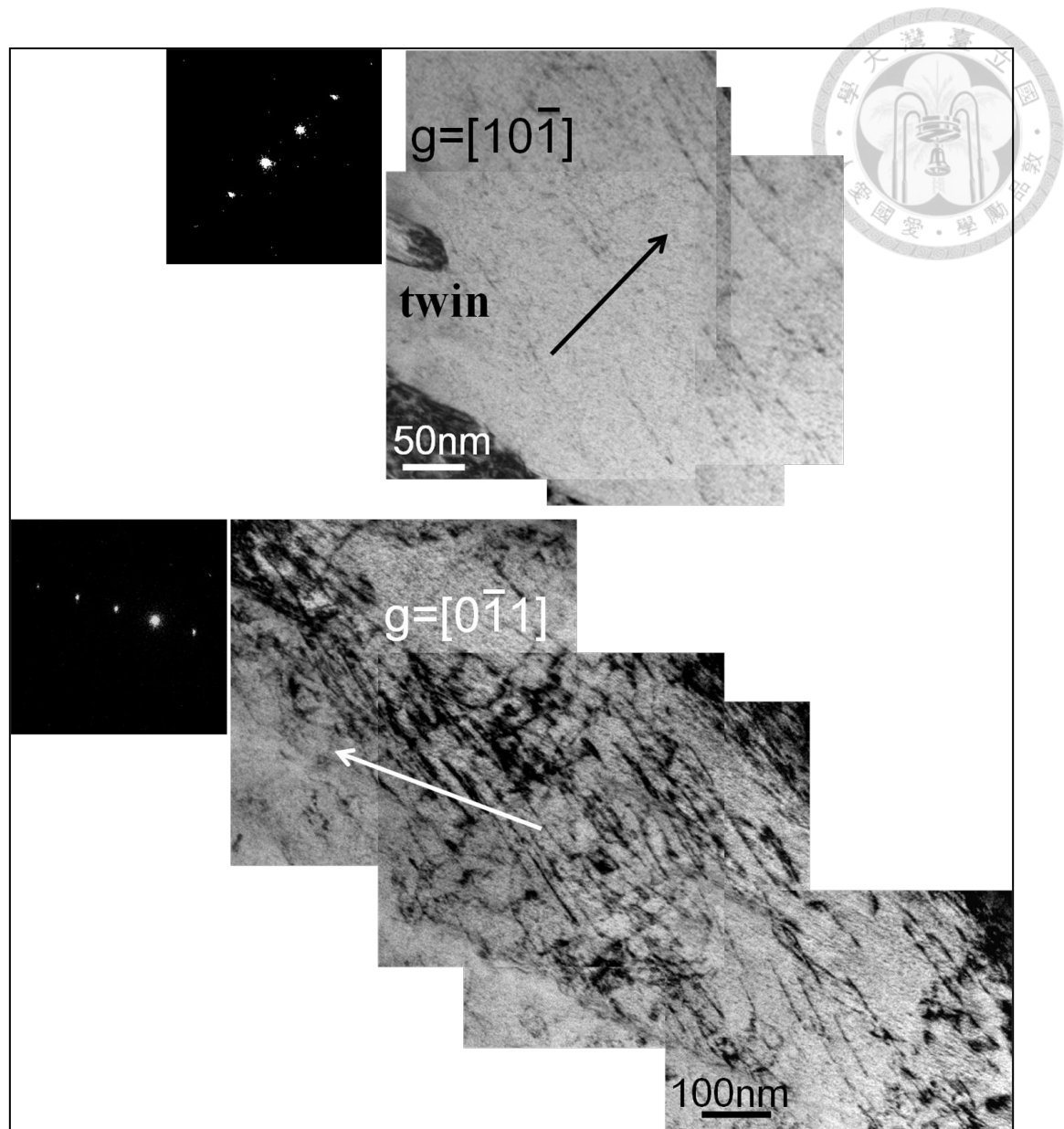


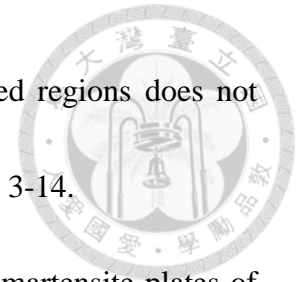
Figure 3-12 Some of the area of the untwinned region observed by different two beam condition: (a) $g=10\bar{1}$  and (b) $g=0\bar{1}1$ .

### 3.3.3 The morphologies of lenticular martensite

Typical substructure morphologies of lenticular martensite include three regions: the midrib, the twinned region, and the untwinned region. These are indicated in the SEM images shown in Figure 3-13. In the twinned region of lenticular martensite, the extension of twins is very dense, and the degree of the extension of twins varies. Some twins grow almost completely through the plate, but some stop growing midway. The interference of each twin boundary during extension causes this discrepancy.

From comparison with a TEM image of lenticular martensite, it can be observed that the twins are bent near the midrib region, which shows a disconnected characteristic between the midrib and extended twins, as shown in Figure 3-6(b), Figure 3-10, and Figure 3-14. It is interesting that not all the twins are bent. The shorter twins, which have no expansion through the middle of the plate, are not bent. On the other hand, the longer twins, which completely expand through the plate, are bent and show a disconnected junction characteristic. Since the formation of the disconnected junctions may result from the two-stage growth of lenticular martensite, one is longitudinal and the other is transverse. The longitudinal formation initiates the transformation process, and the midrib forms. The second stage is transverse formation, which propagates perpendicularly to the midrib[55]. The bending of the disconnected junction occurs due to the change in growing stages in the lenticular martensite transformation. However,

the orientation of the midrib and the surrounding extended twinned regions does not change anything, as shown in Figure 3-6(b), Figure 3-10, and Figure 3-14.



In Figure 3-3(c), the OM observation indicates that lenticular martensite plates of different sizes have fairly constant width/diameter ratios, which supports the contention that no portions of the front can freely propagate once growth has stopped in an adjacent region. If the above description were the case, smaller lenticular martensite plates would have proportionally greater thickness than large ones.

For further understanding of the morphology of lenticular martensite, the focused ion beam (FIB) technique was applied to obtain three-dimensional (3-D) images in SEM observations, as indicated in Figure 3-15. According to these observations, lenticular martensite can be seen as a flat elliptical disk (Figure 3-16). These experimental results match the mathematical simulation established by Prof. Meyers[54]. The lenticular martensite does not thicken (in Figure 3-16). This indicates that if the lenticular martensite plate growth is arrested, it cannot restart, and implies that the growth will be interrupted if either the longitudinal or transverse propagation is inhibited.

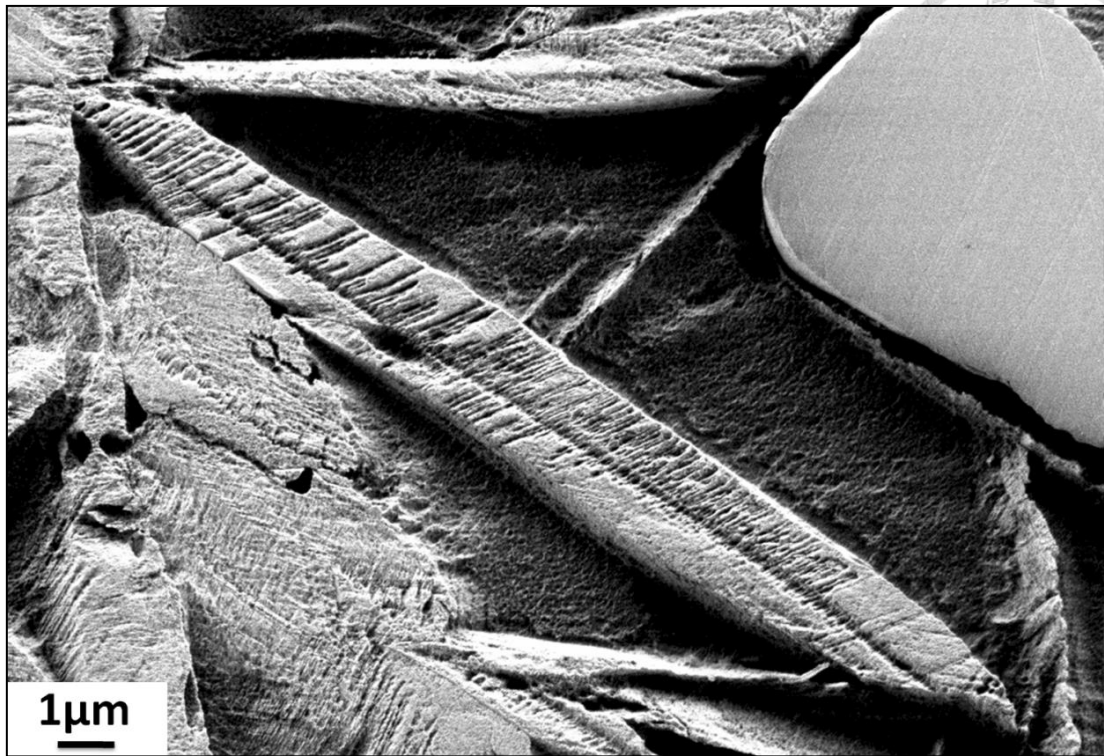


Figure 3-13 SEM image showing the substructure morphologies of lenticular martensite.

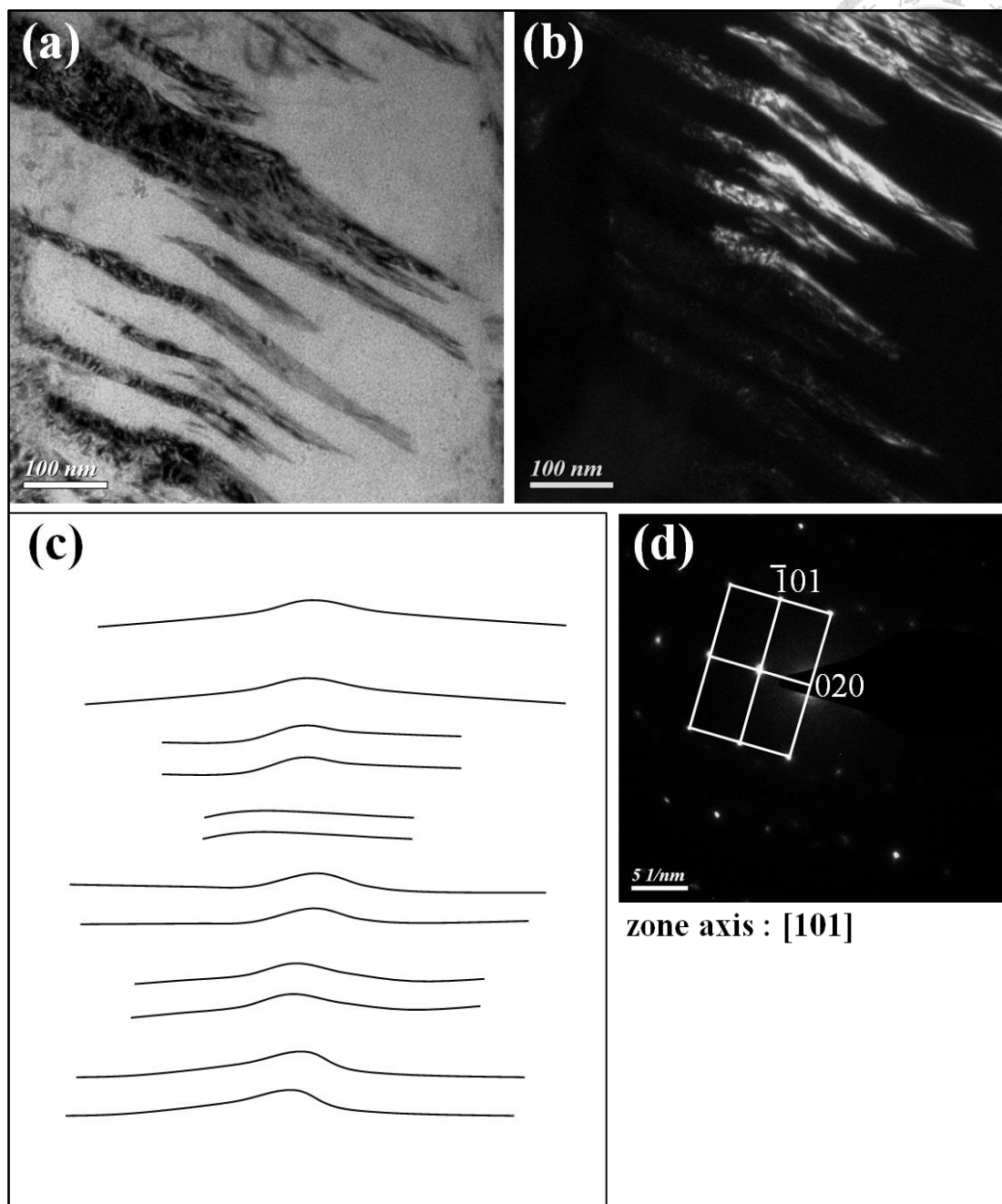


Figure 3-14 TEM observation of lenticular martensite (a) bright field image, (b) dark field image, (c) illustration of the bending of twins near the midrib, (d) corresponding diffraction pattern image.

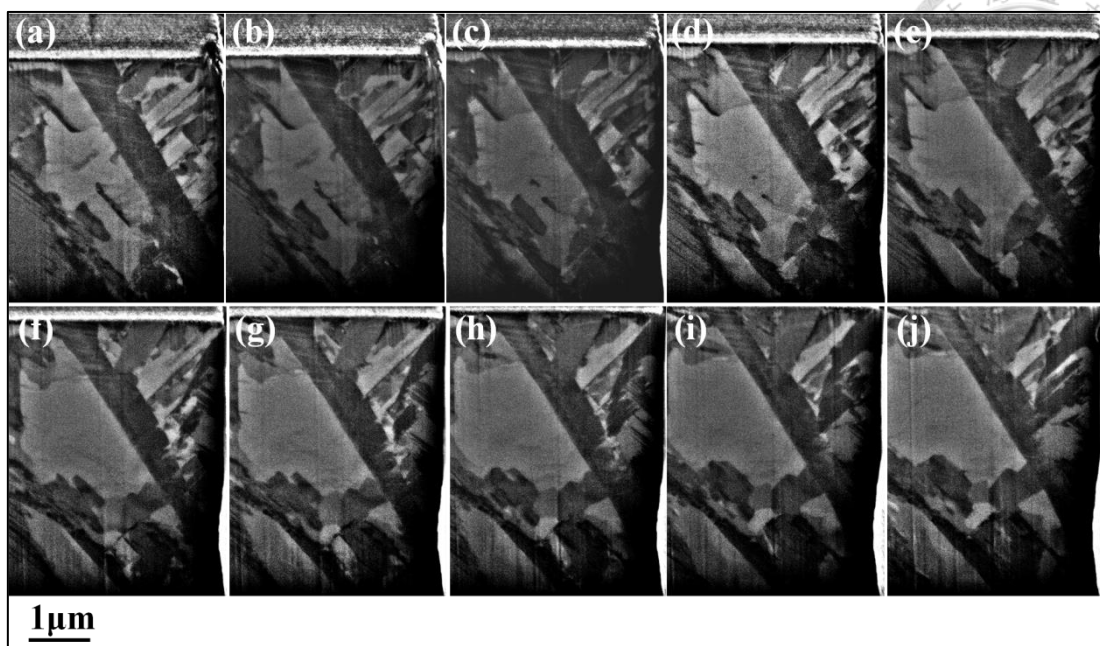


Figure 3-15 3-D observation of lenticular martensite in SEM by FIB technique

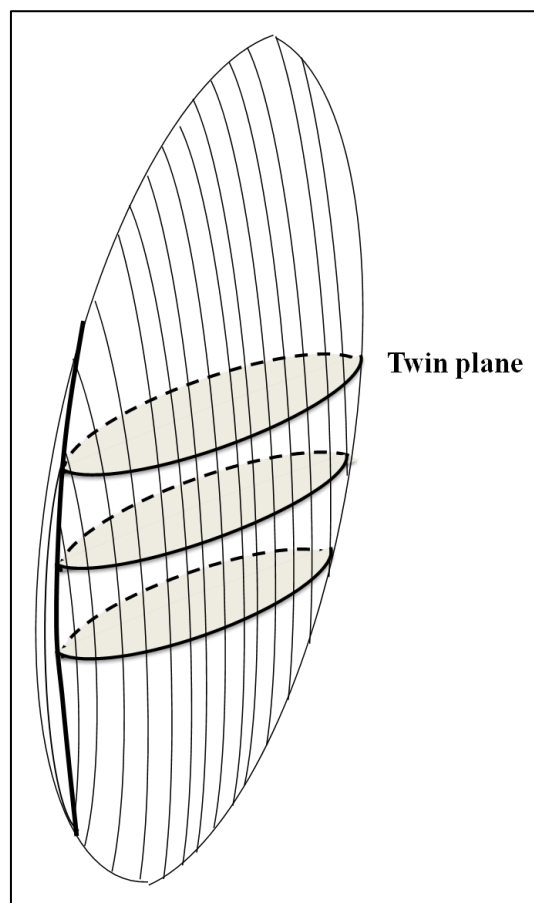


Figure 3-16 Illustration of the 3-D structure of lenticular martensite

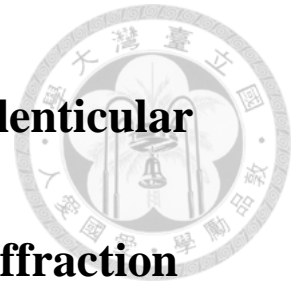


### 3.4 Conclusions

1. The choice of austenitization temperature deeply influences the resulting structure after deep cryogenic treatment.
2. The substructure of lenticular martensite consists of three distinct regions: the midrib, the twinned region, and the untwinned region. In the untwinned region, dislocations with the Burgers vector were determined to be  $a/2[1\bar{1}1]$ .
3. It can be seen that the twins are bent between the midrib and the twinned region, as shown in the 2-D structure of lenticular martensite. In 3-D observation, the lenticular martensite was revealed to be a flat elliptical disk.




## **Chapter 4 Crystallographic analysis of lenticular martensite by electron backscattered diffraction**



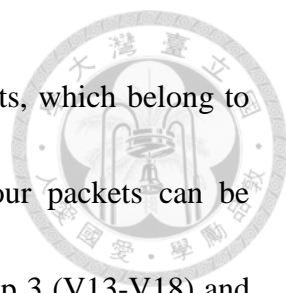
### **4.1 Introduction**

The morphology of ferrous martensite, which is contingent on the chemical composition and martensite start temperature ( $M_s$ ), is generally of three types: lath, lenticular, and thin-plate. Lath martensite forms in the highest temperature range in low-carbon steel (up to about 0.5C wt%) and some Fe-Ni alloys. The high dislocation density usually observed within lath martensite results from the accommodation strains induced by transformation. Thin-plate martensite, which forms in the lowest temperature range in high alloyed steels, consists of a set of uniformly spaced transformation twins crossing throughout the plate. Lenticular martensite forms at the intermediate temperature between lath martensite and thin-plate martensite. Under an optical microscope, typical lenticular martensite resembles a symmetrical lens divided in half by a straight-line midrib. In fact, the substructures of lenticular martensite are more complicated than those of thin plate martensite. Transmission electron microscopy has revealed that lenticular martensite contains three regions: the midrib, the extended twinned region, and the untwinned region. The midrib is composed of highly dense,



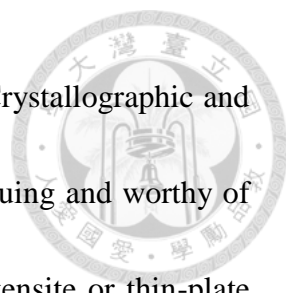
regularly spaced transformation twins. The extended twins give a lens-like feature; they emanate laterally from the midrib region and form a symmetrical pattern of parallel vertex pillars. In the untwinned region, several sets of screw dislocations with a high density of tangled dislocations can be observed. The transformations of both thin-plate martensite and lenticular martensite are initiated at the midrib region. However, during growth, the former retains the lattice-invariant deformation mode of twinning, while the latter has a combination of twinning and slip modes.

Extensive work has been done on the crystallographic and morphologic analyses of lath martensite. Maki et al. have given an excellent review, and they proposed that the morphology of lath martensite transformed from a prior austenite grain can be regarded as a hierarchic structure: parent grain – packet – block – sub-block – individual lath. An individual lath, the basic unit for building lath martensite, is a few microns long and about 0.5  $\mu\text{m}$  thick. Lath martensite generally adopts a K-S OR with respect to the austenite matrix, and 24 independent crystallographic variants of lath can be developed within a single crystal of austenite, as shown in Table 1. Four groups can be assigned to the four independent  $\{111\}_{\gamma}$  planes in a given austenite crystal. In each of the four groups, six independent variants have a common parallel relationship of close-packed planes. Because martensite variants within one packet have nearly the same habit plane, it is therefore appropriate to conclude that only one of these four groups constitutes a




packet structure; in other words, a packet may consist of six variants, which belong to the same group. Using the nomenclature used by Morito, the four packets can be expressed as follows: Group 1 (V1-V6), Group 2 (V7 – V12), Group 3 (V13-V18) and Group 4 (V19-V24). A packet may be subdivided into three parallel blocks, each consisting of two sub-blocks (two different variants). For example, the three blocks of the “Group 1” packet are V1-V4, V2-V5 and V3-V6, where each block is made up of two sub-blocks with a misorientation of about  $10^\circ$ [16]. The sub-block contains several individual laths with a very small misorientation ( $1-2^\circ$ ). Through electron backscattered diffraction coupled with transmission electron microscopy, comprehensive orientation image microscopy (OIM) of lath martensite has been achieved.

Unlike the laths of lath martensite, the plates of lenticular martensite and thin-plate martensite form in isolation rather than in packets within a prior austenite grain. Hereafter, both lenticular martensite and thin-plate martensite are called plate martensite. The size of an individual plate is limited by the prior austenite grain size and by the preceding martensite plate, which inhibit the growth of a fresh plate. When the first plate of martensite forms, it can induce a new embryo of a secondary plate for further transformation. During transformation, the austenite is not as uniformly eliminated as occurs with lath martensite, so the morphology of plate martensite is rather more complex than that of lath martensite. The resulting non-parallel variant pairing of plates



could be associated with a good match for strain accommodation. Crystallographic and morphologic analyses of variant pairs for plate martensite are intriguing and worthy of investigation. A number of studies have focused on lenticular martensite or thin-plate martensite in alloys: Fe-31.0Ni-0.02C, Fe-28.0Ni-0.41C, Fe-30.70Ni-0.28C, Fe-Pt, Fe-20.0Ni-0.73C, Fe-1.40C-12.0Cr, Fe-1.0C-7.2Cr and Fe-1.80C (wt.%). However, it should be noted that the plates can appear to be adjacent to one another for two reasons: autocatalytic nucleation (the formation of one plate may trigger the growth of another) and hard impingement (plates which have formed at completely separate sites may come into contact as a consequence of impingement). It is fundamentally difficult to distinguish between autocatalytic nucleation and hard impingement in specimens composed of high quantities of plates because hard impingement is a sufficiently likely result of martensite platelets from different nucleation sites growing in contact with each other. In this work, care was taken to examine the case of variant pairings with a few martensite plates formed in the specimens, which had been subzero treated at -196°C (in liquid nitrogen) for short holding times. The purpose of the present study was to perform crystallographic analysis of lenticular martensite in Fe-1.0C-17Cr (wt.%) steel by field-emission-gun scanning electron microscopy coupled with electron backscattered diffraction.

## 4.2 Experimental procedure



The as-received material was a commercially wrought AISI 440C stainless steel bar (with a diameter of 50 mm), produced by Gloria Materials Technology, Taiwan, through four-folded forging of a cast slab at 1130°C and annealing at 870°C, followed by furnace cooling to ambient temperature. The chemical composition of the steel was Fe-1.0C-17.4Cr-0.45Mo-0.40Mn-0.38Si (wt.%). The pieces of steel rod (with a diameter of 3 mm) were machined from the half radius position of the original bar. After homogenization at 1200°C for 3 days in quartz capsules containing pure argon, the steel rods were cooled to ambient temperature. The homogenized specimens were then subzero cooled by immersion into 1,000 ml liquid nitrogen (-196°C) in a vessel for different holding times (ranging from 5 s to 15 min) in order to examine the variant pairings of plate martensite without the interference of hard impingement.

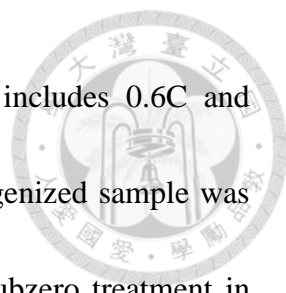
The corresponding microstructures were examined using optical microscopy (OM) and field-emission-gun scanning electron microscopy combined with electron backscatter diffraction (FEG-SEM/EBSD). Both specimens were sliced from the rod specimens. The specimens for OM were mechanically polished and then etched in a mixture of 40 ml HCl, 25 ml ethanol, 30 ml distilled water, and 5 g CuCl<sub>2</sub>. FEG-SEM-EBSD specimens were prepared by cutting discs from the rod specimens, thinning the discs mechanically to 60 μm, and then twin jet electropolishing them using

a mixture of 5% perchloric acid, 20% glycerol, and 75% ethanol at  $-2^{\circ}\text{C}$  and a potential of 35 V, the same as for TEM thin foils, but without the perforation. FEG-SEM/EBSD was carried out in an FEI NOVA 450 operated at 25 kV. Orientation mapping of the EBSD data was performed on an observation area ( $120\text{ }\mu\text{m} \times 120\text{ }\mu\text{m}$ ) of each sample with a step size of 300 nm. TSL-OIM software was used for orientation measurement and analysis.

## 4.3 Results and Discussion

### 4.3.1 Crystallographic analysis of lenticular martensite

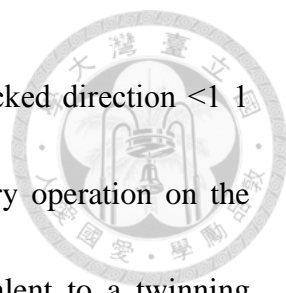
An optical metallograph (OM) of the homogenized specimen (after homogenization at  $1200^{\circ}\text{C}$  for 3 days) is presented in Figure 4-1(a); it reveals that the microstructure consisted of austenite with a small amount of undissolved  $\text{M}_7\text{C}_3$  carbide.  $\text{M}_7\text{C}_3$  carbide particles with a lump-shaped morphology were located on the austenite grain boundaries and within the austenite grains. These particles seemed to have a retarding effect on the austenite grain growth. The higher austenitization temperature caused greater amounts of  $\text{M}_7\text{C}_3$  carbide to dissolve into the austenite matrix. The austenitization temperature decisively controlled the exact chemical composition of the austenite matrix, which determined the morphology of the resulting martensite structure. Thermo-Calc data (Figure 4-2) for the steel studied indicates that the chemical



composition of austenite phase in the 1200°C equilibrium state includes 0.6C and 14.1Cr (wt.%). The martensite start temperature ( $M_s$ ) of the homogenized sample was measured by TA differential scanning calorimetry to be - 48°C. Subzero treatment in liquid nitrogen (-196°C) for 30s brought about three characteristic morphologies of non-parallel martensite variants, as shown in the OM of Figure 4-1(b): (i) zigzag, (ii) spear and (iii) kink (also called fork) couplings, following the terminology used by Okamoto et al [75]. The crystallographic analysis of these non-parallel martensite variant pairings investigated by SEM-EBSD will be presented later.


For the present work, the possible orientation relationship between the austenite matrix and lenticular martensite variants was preliminarily considered to be Kurdjumov-Sachs (K-S) OR or Nishiyama-Wasserman (N-W) OR. For K-S OR, as listed in Table 4-1, the  $\{111\}_\gamma$  plane is taken to be parallel to the  $(011)_{\alpha'}$  plane, and the  $\langle 10\bar{1} \rangle_\gamma$  direction is taken to be parallel to the  $[\bar{1}\bar{1}1]_{\alpha'}$  direction. For describing the orientation relationship between any two variants of plate martensite, there are 24 equivalent ways (axis/angle pairs), and only the lowest angle of rotation (with the corresponding axis) is listed under the column heading “Equivalent axis/angle pair”. It should be noted that 24 independent crystallographic variants of K-S OR can be obtained within a single crystal of austenite. These 24 K-S ORs have the special property that variants of martensite can be twin-related in pairs (i.e., variants V1-V2,





V3-4V, V5-V6, etc...). It can be illustrated as follows. A close packed direction  $\langle 1\ 1\ 0 \rangle_\gamma$  is parallel to a close packed direction  $\langle 1\ 1\ 1 \rangle_{\alpha'}$ . A symmetry operation on the austenite lattice, of a rotation of  $180^\circ$  about  $\langle 1\ 1\ 0 \rangle_\gamma$ , is equivalent to a twinning rotation of  $180^\circ$  about  $\langle 1\ 1\ 1 \rangle_{\alpha'}$ . In this way, a twin of martensite is generated while retaining the K-S OR. For N-W OR, as listed in Table 4-2, the  $\{111\}_\gamma$  plane is taken to be parallel to the  $(011)_{\alpha'}$  plane, and the  $\langle 10\bar{1} \rangle_\gamma$  direction is taken to be parallel to the  $[100]_{\alpha'}$  direction. The lowest angle of rotation (with the corresponding axis) between any two variants of plate martensite is listed under the column heading “Equivalent axis angle pair” in Table 4-2. Therefore, 12 independent crystallographic variants of N-W OR can be obtained within a single crystal of austenite. From the axis/angle pair data of K-S and N-W ORs, simulated  $\{001\}$ ,  $\{011\}$  and  $\{111\}$  pole figures for K-S and N-W ORs can be constructed.

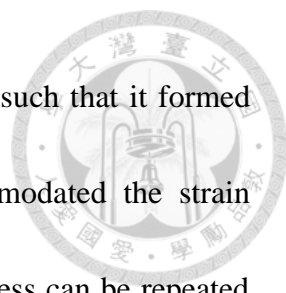
In this work, the homogenized samples were treated with a series of isothermal treatments at  $-196^\circ\text{C}$  (liquid nitrogen), and the martensite was observed to form isothermally. OM observation indicated that thin plate martensite formed in the early stage, and lenticular martensite, after prolonged holding. It is appropriate to conclude that the reaction proceeded as the result of the nucleation of additional thin-plates and the growth of existing thin-plates into lenticular martensites. The total number of martensite and its volume fraction increased as holding time increased, and the



transformation ceased after 15 min of holding. Figure 4-3(a) and (b) show the image quality (IQ) map and the orientation map of lenticular martensite variants within austenite grains, respectively, obtained by FEG-SEM/EBSD measurement of a homogenized sample subzero cooled at  $-196^{\circ}\text{C}$  for 15 min. More than 50 martensite plates (with a thickness of larger than  $1\text{ }\mu\text{m}$ ) formed within a coarse austenite grain, whose grain-boundary is delineated by the red line Figure 4-3(b). The austenite matrix with considerable variants of martensite plates can be provided for direct crystallographic analysis of the orientation relationships of the individual martensite plates with respect to the austenite matrix. The  $\{001\}$ ,  $\{011\}$  and  $\{111\}$  pole figures obtained from the delineated austenite grain in Figure 4-3(b) are presented in Figure 4-3(c). The red spots are related to the diffraction from the austenite matrix; the black spots, to that from the different martensite plates. The simulated pole figures for K-S and N-W ORs are shown in Figure 4-3(d) and (e) respectively, where the poles of austenite have been fixed with the same orientations as those in Figure 4-3(c). It is clear that the experimental data (Figure 4-3(c)) well match up with the simulated data of K-S OR (Figure 4-3(d)), although the former exhibits a certain degree of orientation spreading. The simulated 001 pole figure for K-S OR is composed of seventy-two poles (Figure 4-3(d)), which are distributed among three rings and six bars, each containing eight poles. Austenite 001 poles are located at the geometric centres of the rings. One

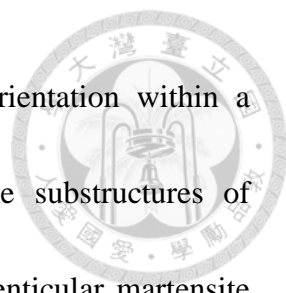
ring and two corresponding bars constitute a Bain zone (as shown in Figure 4-4), so the 001 pole figure can be illustrated by three Bain zones. The detection of a Bain zone becomes easier as the number of observed variants increases. In the {001} pole figure of Figure 4-3(c), it can be found that several poles of some variants did not appear. Despite this imperfection, the overall spots still reflect approximately the K-S OR.

Through EBSD measurement, an orientation map of lenticular martensite variants within austenite grains (Figure 4-5(a)) and the corresponding misorientation map of the austenite grains (Figure 4-5(b)) were obtained. The morphologies of variant pairs can be identified as the zigzag type (as shown by the A-B variant pair in  $\gamma_1$ ) and the spear type (as shown by the C-D variant pair in  $\gamma_2$ ). As seen in Figure 4-5(b), the change in crystallographic orientation of austenite surrounding the lenticular martensite variants can be discerned, and the misorientation in austenite in the vicinity of  $M_7C_3$  carbide particles and austenite grain-boundaries can also be identified. Misorientation angles from a reference point are represented by gradation according to a color bar covering the maximum angle deviation of  $3^\circ$ . The dark regions correspond to lenticular martensite variants and lump-shaped  $M_7C_3$  carbide particles. The misorientation in austenite at the local region was associated with the accommodation strain. The shape deformation accompanying the martensite transformation caused the severe elastic and plastic disturbance of the austenite in the immediate vicinity of a plate of martensite,

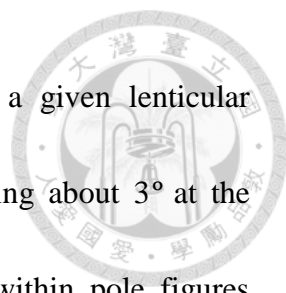


inducing so-called autocatalytic nucleation. The new nucleus grew such that it formed into a plate at a different orientation, which presumably accommodated the strain resulting from the formation of the preceding plate. This basic process can be repeated many times as the transformation propagates; it is well-known as bursts of transformation. In addition to the austenite grain-boundaries,  $M_7C_3$  carbide particles were apparently potent nucleation sites. It is notable that the zone of misorientation in austenite surrounding the lenticular martensite was rather shallow. Plastic deformation in the austenite matrix clearly plays an important role in accommodating the shape strain of martensite. In this work, the austenite matrix (with a chemical composition of 0.6C and 14.1Cr, wt.%) would have a high yield strength at  $-196^\circ\text{C}$ , so the plastic accommodation in austenite in the vicinity of austenite/lenticular martensite was just extended to a small scale. However, the accommodation strain around the tip of the lenticular martensite was greatly intensified, and it may preferably have brought about the autocatalytic nucleation, leading to the zigzag and spear couplings (Figure 4-5(a) and (b)). On the other hand, kink (also called fork) couplings can be observed within some austenite grains (as shown by the E-F variant pair in Figure 4-5(c) and (d)), but with less frequency. In this case, the nucleation occurred at the broad face of the preceding lenticular martensite, and formed the Widmanstätten-type plates.

In order to analyze the orientation relationship (OR) for the variant pairs of




lenticular martensite plate, it is necessary to clarify the local orientation within a lenticular martensite plate, which is closely associated with the substructures of lenticular martensite. Figure 4-6(a) shows an orientation map of lenticular martensite zigzag variants within an austenite grain, and Figure 4-6 (b) presents the misorientation profile across a lenticular plate transversely from one side (X) to the other side (X'), showing the accumulated point to origin orientation differences. In this work, under the EBSD measurement using a step size of 300 nm, it was difficult to reveal the ultra-fine platelets of nanotwins (having a thickness of about 50-100 nm); the EBSD data points presented here were presumed to have been acquired from the matrix adjacent to the ultra-fine platelets of nanotwins. It is clear that the local orientations around the central area (midrib) were almost the same. However, the orientation changed gradually in the vicinity of the martensite/austenite interface. The misorientation within a lenticular martensite plate from the midrib region is about  $3^\circ$  at the martensite/austenite interface. The misorientation profile across another lenticular martensite plate presents a similar result, as illustrated in Figure 4-7. Convergent beam Kikuchi line diffraction patterns (CBKLD) have been employed to measure the misorientation with the matrix of a lenticular martensite plate trapped between ultra-fine platelets of nanotwins, as shown in Figure 6-2. The data were taken from the midrib region, an extended twinned region, and an untwinned region (the dense dislocation area) near the martensite/austenite



interface. The result again indicates that the orientation within a given lenticular martensite plate changes gradually from the midrib region, reaching about  $3^\circ$  at the martensite/austenite interface. The spread in diffracted intensity within pole figures shown in Figure 4-3(c) can therefore be elucidated. Figure 4-6(c) shows a misorientation profile along the line Y – Y' in the surrounding austenite, which is changed by about  $1.5^\circ$ , but it also indicates that the misorientation zone is shallow and apparently confined to the vicinity of the austenite/martensite interface. This result is consistent with the misorientation map in austenite shown in Figure 4-5(b). It is clear that the plastic accommodation in austenite near the austenite/martensite interface is narrow and the corresponding misorientation is small. One may be forced to presume that when the new plate forms from the preceding plate, the neighboring austenite matrix roughly maintains the original orientation. On the above assumption, the orientation relationship between the adjacent variant plates of lenticular martensite in a pair has been estimated from the corresponding orientations of midrib regions. It is important to acquire an appropriate orientation relationship (OR) when conducting variant pairing analysis. After EBSD measurement, two sets of Euler angles representing two variant plates in pairs were determined from the average values (5-10 data points obtained from the midrib region for each plate), and then derived to the rotation matrix. The related calculations have been reported elsewhere. Crystallographic

analysis of variant pairings for zigzag, spear and kink couplings was performed, and the OR is expressed in Table 4-3 by axis/angle pair (using the smallest angle). Some representative examples are illustrated as follows. A zigzag type (A-B variant pair as shown in Figure 4-5(a)) possesses an axis/angle pair of  $[-0.662 \ -0.379 \ 0.647] / 53.0^\circ$ ; a spear type (C-D variant pair as shown in Figure 4-5(a)),  $[0.670 \ -0.651 \ -0.357] / 53.4^\circ$ ; a kink type,  $[0.668 \ 0.314 \ -0.675] / 16.4^\circ$ . After a comparison between the ORs for zigzag and spear couplings in Table 4-3, it may be concluded that these two types of couplings are approximately equivalent in crystallography.

For ferrous alloys, several researchers have investigated the crystallography of variant pairs of lenticular martensite with the habit plane  $\{3 \ 15 \ 10\}_\gamma$ . They suggested that the nucleation event for the variant pairing may originate in the same “plate group”, which is composed of four variants. This can be illustrated as follows. As shown in Figure 4-8(a), the poles of  $(3 \ 15 \ 10)_\gamma$ ,  $(3 \ 10 \ 15)_\gamma$ ,  $(\bar{3} \ 15 \ 10)_\gamma$  and  $(\bar{3} \ 10 \ 15)_\gamma$  are located symmetrically around the pole of  $(0 \ 1 \ 1)_\gamma$ . For 24 various K-S martensite variants, if the pole of V1 variant is fixed on the pole of  $(3 \ 15 \ 10)_\gamma$ , then V6, V16 and V17 poles can be set on the poles of  $(3 \ 10 \ 15)_\gamma$ ,  $(\bar{3} \ 15 \ 10)_\gamma$  and  $(\bar{3} \ 10 \ 15)_\gamma$ , respectively, as shown in Figure 4-8(b). V1, V6, V16 and V17 constitute the  $(0 \ 1 \ 1)_\gamma$  plate group (designated as Plate Group 1 in Table 4-1), so there are six  $\{0 \ 1 \ 1\}_\gamma$  plate groups in a given austenite grain, each plate group being associated with four various K-S martensite variants.




Previous studies suggested that the couplings of plate martensite are presumably limited to the variants in the same plate group. In the present work, variant pairings of lenticular martensite plates have been checked with Plate Group 1 using V1 as the reference variant. Pairing of V1 with variants V16 and V17 is frequently observed when considering an angle deviation of 2-4°. There appears to be a trend of plate group formation with dominance of V1/V17 pairing for zigzag (or spear) arrays, and with V1/V16 for kink arrays. In this way, the resulting non-parallel variant pairing probably brings about a good match for strain accommodation. In this work, the substructures of lenticular martensite are complicated, as nanotwins emanate laterally from the midrib region to the extended twinned region, adjacent to the untwinned region with highly dense dislocations near the martensite/austenite interface. As a result, finding an appropriate orientation relationship (OR) to conduct the variant pairing analysis is rather difficult. More detailed investigation will be needed to understand the mechanisms of the variant pairings.

#### **4.3.2 Coupling of lenticular martensite**

The morphologies of the coupling of lenticular martensite can be sorted into several conditions, including spear, kink, zigzag array, and crossed region, as shown in Figure 4-9.

Common characteristic morphologies for lenticular martensite transformation,





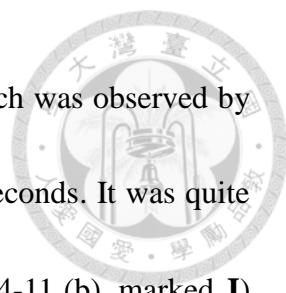
spear, zigzag, and kink, were observed in this high-carbon high chromium steel. Figure 4-10(a) is an example of spear and kink morphologies. In this single austenite grain, martensite **A** and **C** form a typical spear morphology, having a crystallographic relationship V1-V17 in K-S OR, and the equivalent axis/angle pair is  $[2\bar{2}\bar{1}]/53.4^\circ$ . Meanwhile, martensite **A** and **B** look like a kink morphology and have a V1-V16 relationship of K-S OR, whose equivalent axis/angle pair is  $[133]/16.1^\circ$ . The above result indicates that those morphologies may happen simultaneously and depend on the strain energy and local environment.

EBSD can also provide the information of residual stress distribution by misorientation analysis. Figure 4-10 (b) and (c) are the inverse pole figure (IPF) map and the misorientation distribution map of an example of kink morphology. In the lenticular martensite **E** in Figure 4-10 (b) can be observed a significant midrib region in the middle, and the grain is surrounded by several lenticular martensite grains (marked **D** and **F**) with kink morphology. Both **D** and **F** have the same relationship with grain **E**, V1-V17 in K-S OR. The former has the equivalent axis/angle pair of  $[12\bar{2}]/17.3^\circ$  and the latter is  $[122]/15.9^\circ$ . Regarding the residual stress distribution, one can expect that if the higher residual stress exists at the boundary, the measured misorientation of this boundary will also rise. By comparison with the regular grain boundary between lenticular martensite and austenite, the misorientation distribution map (Figure 4-10 (c))

indicates that a much higher misorientation angle exists around the kink morphology. This appears to be a likely explanation for the formation of lenticular martensite by an autocatalysis mechanism. While the lenticular martensite transforms from the austenite phase, it may induce deformation in the adjacent austenite matrix, and this strain will then accumulate at the boundary, which is a high priority nucleation site. Afterwards, the formation of lenticular martensite therefore has no specific growth direction but must have a relationship with the former lenticular martensite grain.

Figure 4-10(c) shows a clear and typical zigzag morphology of lenticular martensite. In this case, marks **G** and **H** represent two specific variants of lenticular martensite grains, respectively. These two variants have a crystallographic relationship of V1-V17 in K-S OR, and the equivalent axis/angle pair is  $[\bar{1}\bar{1}22]/53.0^\circ$ . The formation process of this zigzag morphology is introduced as follows. These two non-parallel lenticular martensites (mark **H**) may form initially in the austenite matrix, and afterwards, transformed lenticular martensites (mark **G**) appear between the former ones and link to each other. Such a zigzag morphology then can be taken as a combination of two spear-type morphologies.

Figure 4-11 is a series of morphology changes in the transformation of lenticular martensite within an austenite grain. In the beginning, the sample was cooled down to  $M_s$  (cryogenic treatment) for 8 seconds, and some single-direction lenticular martensite



(in Figure 4-11 (a), marked **I**) appeared in the austenite matrix, which was observed by EBSD. Then the sample was put into liquid nitrogen again for 30 seconds. It was quite interesting to discover that new lenticular martensite grains (Figure 4-11 (b), marked **J**) appeared next to the former lenticular martensite grain (marked **I**) and formed as the spear morphology in the same austenite grain. According to EBSD analysis, these two lenticular martensite grains have a crystallographic relationship of V1-V6 in K-S OR, and the equivalent axis/angle pair is  $[\bar{1}0\bar{1}]/53.1^\circ$ . Therefore, the formation of the spear morphology can be taken as a self-accommodation mechanism. The lenticular martensite first nucleates at a prior site such as a high-energy defect and grows along one direction. After the first nucleation, the defect may still have sufficient energy to induce a second nucleation of lenticular martensite, which grows in another direction. The spear morphology can then be observed.

However, Figure 4-11 (b) also shows a possible formation process of the zigzag morphology, whose mechanism differs from that in a previous study[75]. In the circled area in Figure 4-11(b), it is observed that the typical zigzag morphology formed after the second cryogenic treatment. This phenomenon can be seen as a product of the spear mechanism. When two non-parallel lenticular martensite grains (the same variant) are at an appropriate distance, the subsequent formation of lenticular martensite by the spear mechanism may connect these two non-parallel martensite grains and turn them into the

so-called “zigzag” morphology. In addition, the grain size of lenticular martensite **I** does not increase obviously after second cryogenic treatment, which means that the growth of lenticular martensite stops as the temperature higher than  $M_s$  and remains almost the same size, even at a temperature below  $M_s$ .

The observation results of lenticular martensite morphology provide further understanding of the formation of different coupling conditions. It can be assumed that the initial martensite plates may transform in one variant in a single austenite grain, which is the preferred variant, and then the following transformed martensite plates will nucleate and grow in another variant, and finally connect with each other in several types of coupling, such as spear, kink or zigzag arrays. This assumption, which can be seen as a kind of variant selection, is illustrated in Figure 4-12.

Compared with other coupling martensite morphologies, the formation of the crossed region is somewhat special. A typical crossed region morphology is depicted in Figure 4-9 (d). The crossing mechanism can be understood as follows. When a martensite plate grows into another existing plate, the latter will be deformed by the shape strain of the former. If this deformation produces more than a certain amount of stress on the other side of the latter plate, then the same variant of the former plate is nucleated on the other side and keeps growing, giving rise to a crossed morphology.

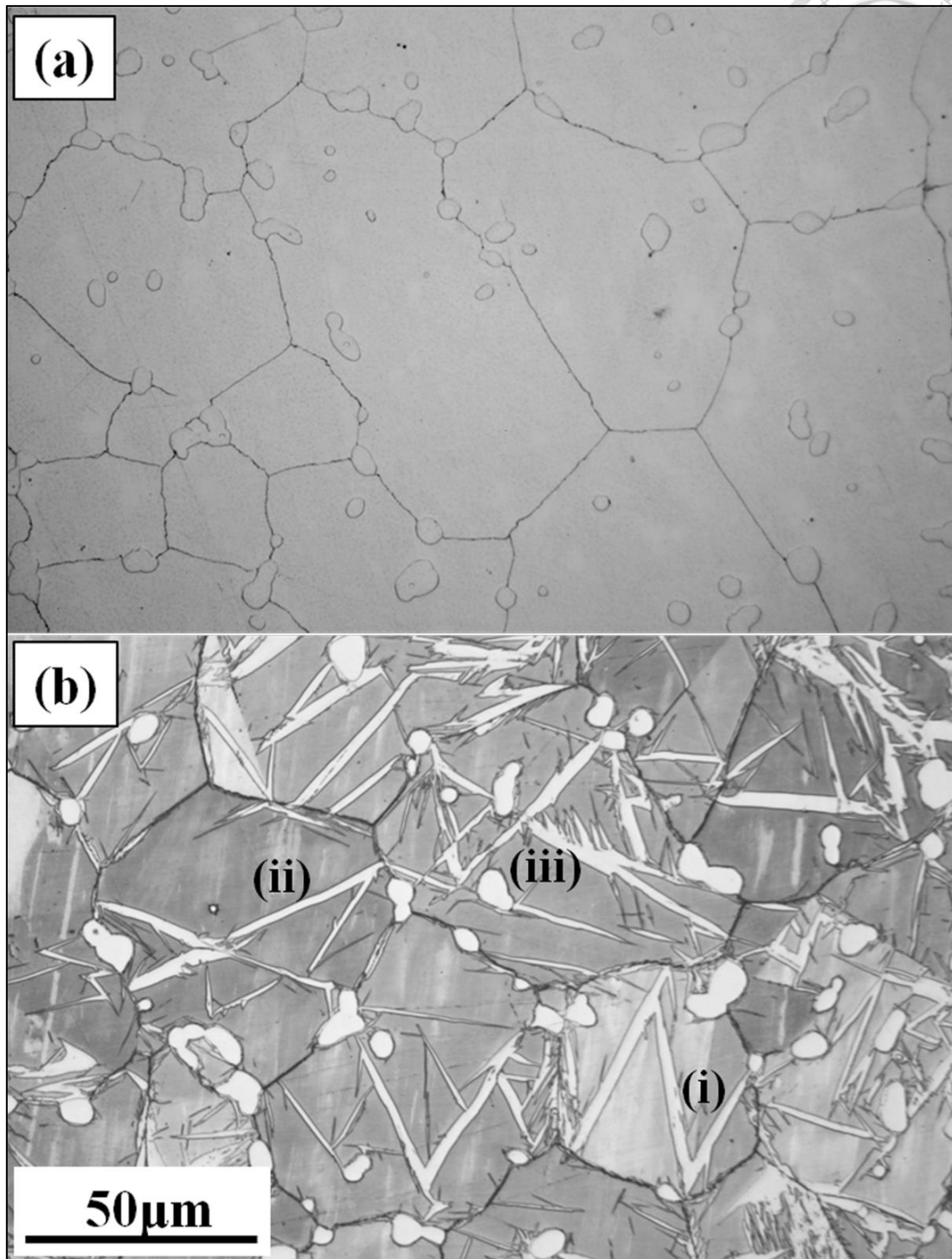


Figure 4-1 (a) OM taken from the homogenized specimen; (b) OM taken from the homogenized sample subzero cooled at  $-196\text{ }^{\circ}\text{C}$  for 30 s, showing three characteristic morphologies of non-parallel martensite variants: (i) zigzag, (ii) spear and (iii) kink arrays. (The lump-shaped particles:  $\text{M}_7\text{C}_3$ .)

Table 4-1 24 variants of Kurdjumov-Sachs (K-S) orientation relationship

$\gamma$ orientation	Axis angle pair ( $\alpha$ )			Equivalent axis angle pair ( $\alpha$ )			PG	
Kurdjumov-Sachs $\alpha$ - $\gamma$ orientation relationship (23 other variants of ferrite)**								
V1	(1 1 1)[ $\bar{1}$ 0 1]	[ 1.000	0.000	0.000] / 0°	---			A1
V2	( $\bar{1}$ $\bar{1}$ $\bar{1}$ )[ $\bar{1}$ 0 1]	[ 0.577	0.577	0.577] / 180°	[ 0.576	0.577	0.578] / 60.00°	A5
V3	(1 1 1)[0 1 $\bar{1}$ ]	[ 0.000	-0.707	-0.707] / 120°	[ -0.001	-0.707	-0.707] / 60.00°	D5
V4	( $\bar{1}$ $\bar{1}$ $\bar{1}$ )[0 1 $\bar{1}$ ]	[ 0.966	0.065	0.065] / 180°	[ 0.000	0.707	-0.707] / 10.53°	A2
V5	(1 1 1)[1 $\bar{1}$ 0]	[ 0.000	0.707	0.707] / 120°	[ -0.001	0.707	0.707] / 60.00°	D2
V6	( $\bar{1}$ $\bar{1}$ $\bar{1}$ )[1 $\bar{1}$ 0]	[ 0.418	0.642	0.642] / 180°	[ -0.001	-0.707	0.707] / 49.47°	D1
V7	(1 $\bar{1}$ 1)[1 0 $\bar{1}$ ]	[ 0.471	0.342	0.813] / 180°	[ 0.577	0.578	-0.577] / 49.47°	A6
V8	( $\bar{1}$ 1 $\bar{1}$ )[1 0 $\bar{1}$ ]	[ 0.667	0.742	0.075] / 180°	[ -0.575	0.576	0.582] / 10.53°	A3
V9	(1 $\bar{1}$ 1)[ $\bar{1}$ $\bar{1}$ 0]	[ 0.742	0.650	0.167] / 90°	[ 0.614	-0.182	0.767] / 50.51°	D3
V10	( $\bar{1}$ 1 $\bar{1}$ )[ $\bar{1}$ $\bar{1}$ 0]	[ -0.087	-0.900	0.428] / 120°	[ 0.739	0.463	-0.489] / 50.51°	C2
V11	(1 $\bar{1}$ 1)[0 1 1]	[ 0.075	0.167	-0.983] / 90°	[ -0.933	-0.355	-0.065] / 14.88°	B2
V12	( $\bar{1}$ 1 $\bar{1}$ )[0 1 1]	[ -0.856	-0.043	0.515] / 120°	[ 0.356	-0.603	-0.713] / 57.21°	D6
V13	( $\bar{1}$ 1 1)[0 $\bar{1}$ 1]	[ -0.075	-0.167	0.983] / 90°	[ -0.355	0.933	0.065] / 14.88°	B4
V14	(1 $\bar{1}$ $\bar{1}$ )[0 $\bar{1}$ 1]	[ 0.087	0.900	-0.428] / 120°	[ 0.490	-0.463	0.739] / 50.51°	C6
V15	( $\bar{1}$ 1 1)[ $\bar{1}$ 0 $\bar{1}$ ]	[ 0.667	-0.742	-0.075] / 90°	[ -0.739	-0.246	-0.628] / 57.21°	B6
V16	(1 $\bar{1}$ $\bar{1}$ )[ $\bar{1}$ 0 $\bar{1}$ ]	[ 0.742	0.650	0.167] / 180°	[ -0.659	0.660	0.361] / 20.61°	B1
V17	( $\bar{1}$ 1 1)[1 1 0]	[ 0.524	0.407	0.748] / 180°	[ 0.659	0.363	-0.659] / 51.73°	C1
V18	(1 $\bar{1}$ $\bar{1}$ )[1 1 0]	[ -0.770	0.149	-0.621] / 120°	[ 0.719	0.303	-0.626] / 47.11°	C3
V19	(1 1 $\bar{1}$ )[ $\bar{1}$ 1 0]	[ -0.742	-0.650	-0.167] / 90°	[ 0.186	-0.767	-0.615] / 50.51°	C4
V20	( $\bar{1}$ $\bar{1}$ 1)[ $\bar{1}$ 1 0]	[ 0.856	0.043	-0.515] / 120°	[ -0.356	-0.713	0.604] / 57.21°	D4
V21	(1 1 $\bar{1}$ )[0 $\bar{1}$ $\bar{1}$ ]	[ 0.053	0.984	0.171] / 180°	[ -0.955	0.000	0.296] / 20.61°	A4
V22	( $\bar{1}$ $\bar{1}$ 1)[0 $\bar{1}$ $\bar{1}$ ]	[ 0.770	-0.149	0.621] / 120°	[ 0.302	-0.626	-0.719] / 47.11°	C5
V23	(1 1 $\bar{1}$ )[1 0 1]	[ -0.667	0.742	0.075] / 90°	[ 0.246	0.628	0.739] / 57.21°	B5
V24	( $\bar{1}$ $\bar{1}$ 1)[1 0 1]	[ 0.075	0.167	0.983] / 180°	[ 0.912	-0.410	0.000] / 21.06°	B3

\* Axis angle pairs (with respect to martensite plates) relating variant number V1 to other variants that may form within same austenite crystal.

\*\* Plate Group 1: (A1, B1, C1 and D1); Plate Group 2: (A2, B2, C2 and D2); Plate Group 3: (A3, B3, C3 and D3); Plate Group 4: (A4, B4, C4 and D4); Plate Group 5: (A5, B5, C5 and D5); Plate Group 6: (A6, B6, C6 and D6).

Table 4-2 12 variants of Nishiyama-Wasserman orientation relationship

	$\gamma$ orientation	Axis angle pair ( $\alpha$ )			Equivalent axis angle pair		
1	$(1\ 1\ 1)[\bar{1}\ 0\ 1]$	[ 1.000	0.000	0.000] / $0^\circ$	---	---	---
2	$(1\ 1\ 1)[0\ 1\ \bar{1}]$	[ 0.000	-0.707	-0.707] / $120^\circ$	[-0.001	-0.707	-0.707] / $60.00^\circ$
3	$(1\ 1\ 1)[1\ \bar{1}\ 0]$	[ 0.000	0.707	0.707] / $120^\circ$	[-0.001	0.707	0.707] / $60.00^\circ$
4	$(1\ 1\ \bar{1})[\bar{1}\ 1\ 0]$	[-0.707	-0.697	-0.120] / $90^\circ$	[ 0.222	-0.697	-0.682] / $53.69^\circ$
5	$(1\ 1\ \bar{1})[1\ 0\ 1]$	[ 0.000	-0.169	0.986] / $90^\circ$	[-0.706	0.706	0.060] / $13.76^\circ$
6	$(1\ 1\ \bar{1})[0\ \bar{1}\ \bar{1}]$	[ 0.500	0.373	0.782] / $180^\circ$	[ 0.624	0.471	-0.624] / $50.05^\circ$
7	$(1\ \bar{1}\ 1)[\bar{1}\ \bar{1}\ 0]$	[-0.707	0.697	0.120] / $90^\circ$	[ 0.222	0.697	0.682] / $53.69^\circ$
8	$(1\ \bar{1}\ 1)[1\ 0\ \bar{1}]$	[ 0.000	0.986	0.169] / $180^\circ$	[-1.000	0.000	0.000] / $19.47^\circ$
9	$(1\ \bar{1}\ 1)[0\ 1\ 1]$	[-0.707	-0.697	-0.120] / $90^\circ$	[ 0.222	-0.697	-0.682] / $53.69^\circ$
10	$(\bar{1}\ 1\ 1)[\bar{1}\ 0\ \bar{1}]$	[ 0.000	0.169	-0.986] / $90^\circ$	[-0.706	-0.706	-0.060] / $13.76^\circ$
11	$(\bar{1}\ 1\ 1)[1\ 1\ 0]$	[ 0.500	0.373	0.782] / $180^\circ$	[-0.624	0.471	0.624] / $50.05^\circ$
12	$(\bar{1}\ 1\ 1)[0\ \bar{1}\ 1]$	[ 0.707	0.697	0.120] / $90^\circ$	[ 0.682	-0.222	0.697] / $53.69^\circ$

\*\*\* Axis angle pairs (with respect to  $\alpha$ ) relating variant number 1 to other variants that may form within same austenite crystal.

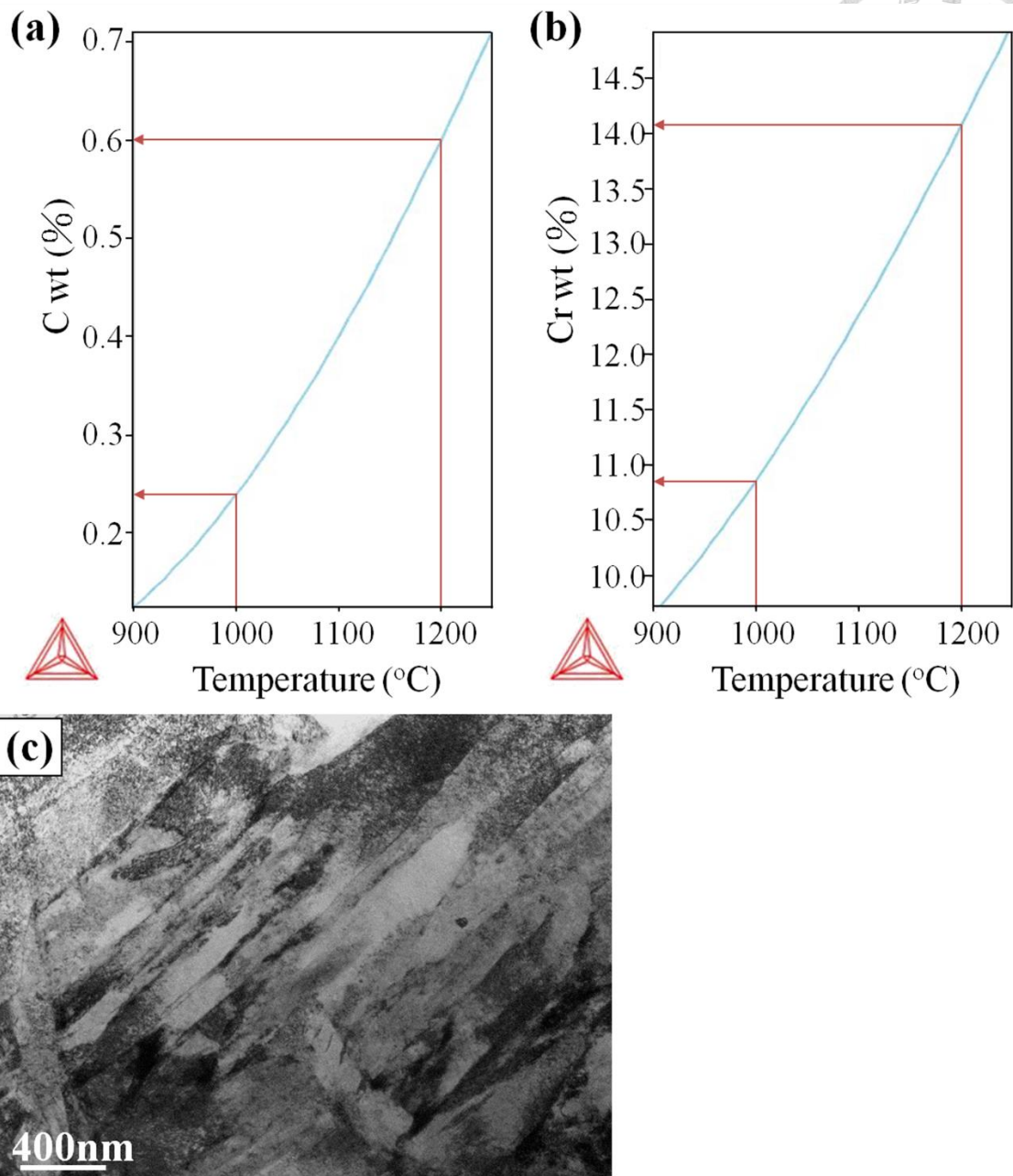


Figure 4-2 (a) and (b) Thermo-Calc data indicate that the chemical composition of austenite phase in the 1200°C equilibrium state consists of 0.60C-14.1Cr (wt.%), and 1000°C, 0.24C-10.8Cr (wt.%); (c) lath martensite obtained from the sample austenitized at 1000°C for 3 days and cooled to ambient temperature.



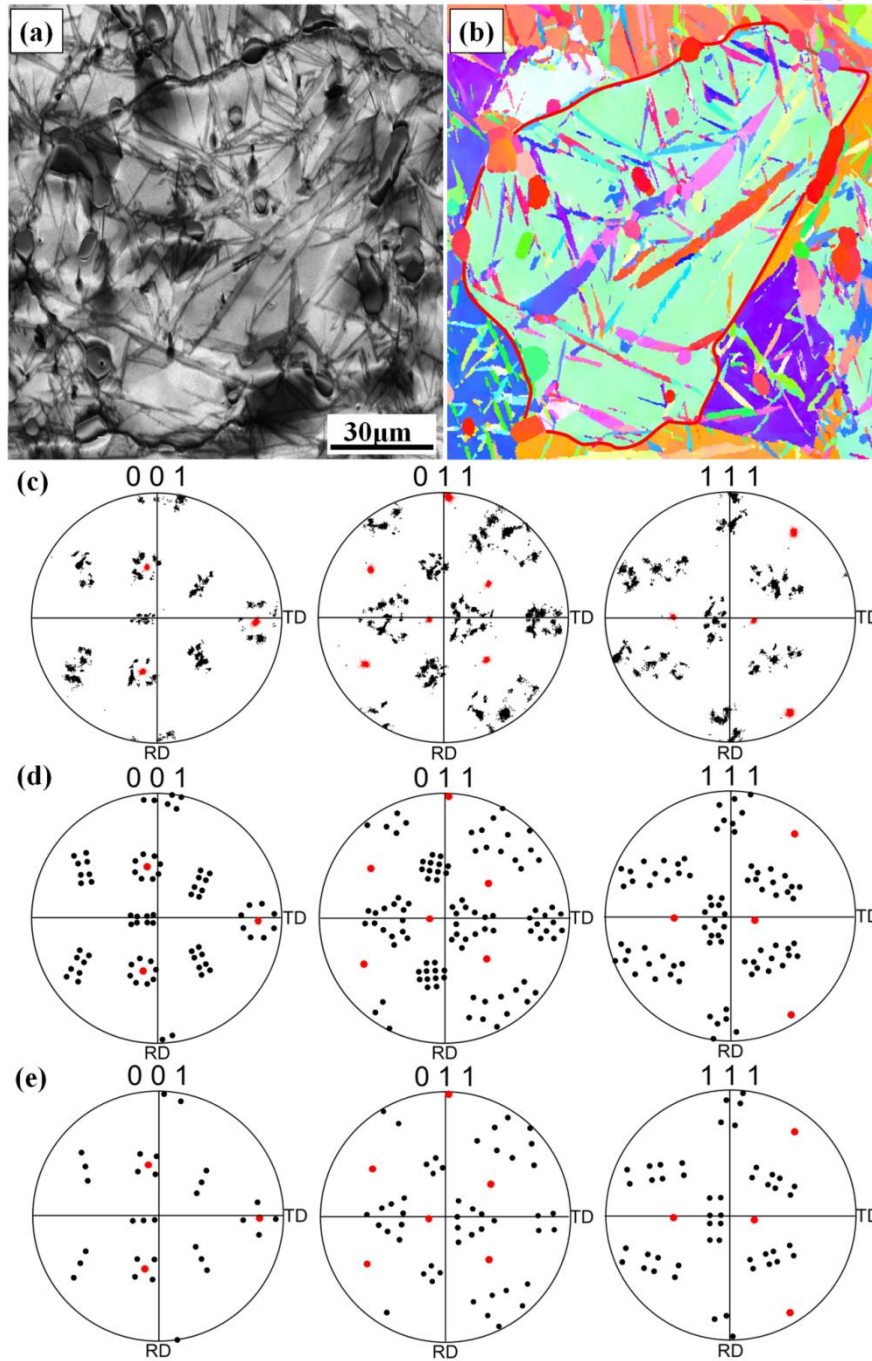


Figure 4-3 (a) Image quality map of lenticular martensite variants within austenite grains of a homogenized sample subzero cooled at  $-196^{\circ}\text{C}$  for 15 min.; (b) the corresponding orientation map; (c)  $\{001\}$ ,  $\{011\}$  and  $\{111\}$  pole figures obtained from the delineated austenite grain in (b); (d) the simulated pole figures for K-S OR; (e) the simulated pole figures for N-W OR. (The red spots are related to the diffraction from the austenite matrix; the black spots, to that from the different martensite plates.)

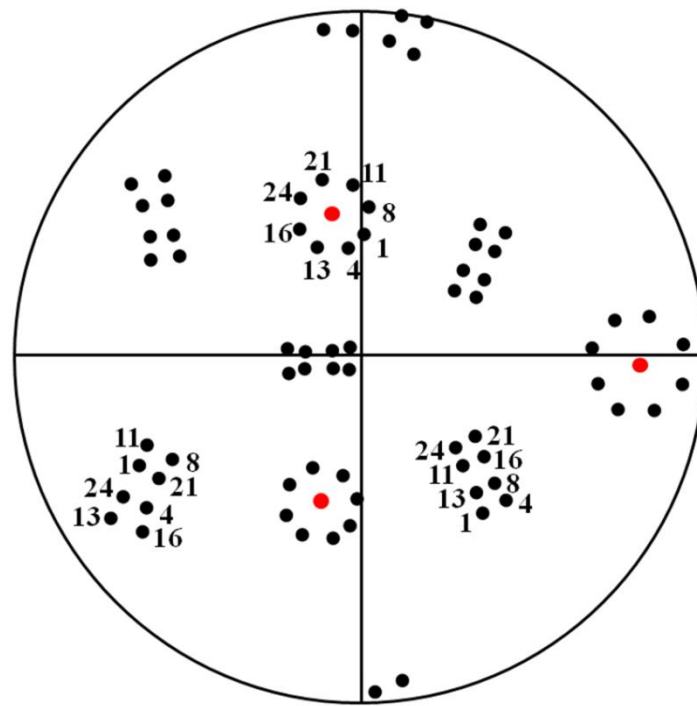


Figure 4-4 In the 001 pole figure of 24 variants of K-S OR, a Bain zone consists of one ring and two corresponding bars, each containing eight poles. For example, eight variants, V1, V4, V8, V11, V13, V16, V21 and V24, are in the same Bain Zone. (The red spots are related to the diffraction from the  $\{0\ 0\ 1\}$  poles of the austenite matrix.)

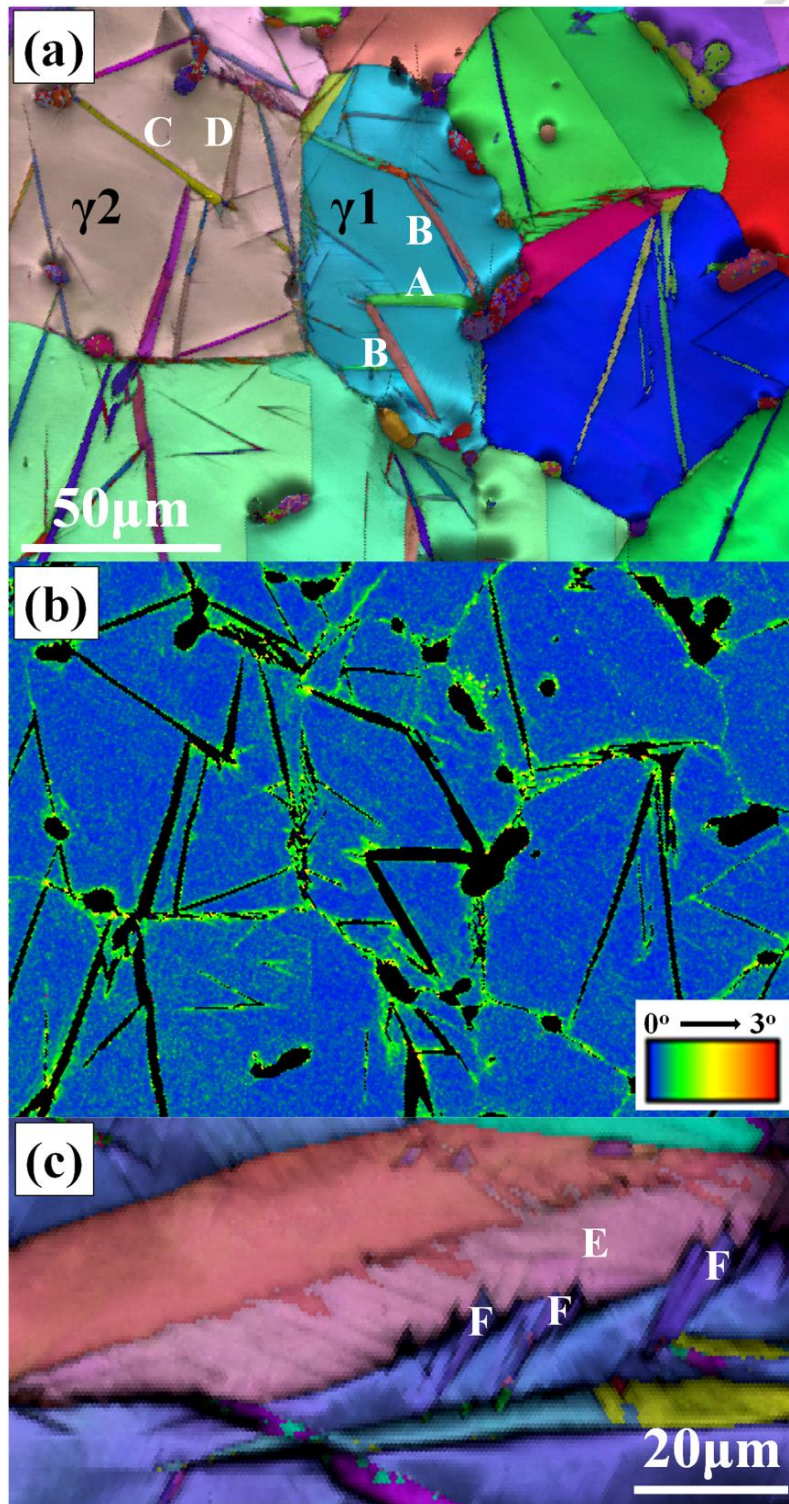


Figure 4-5 (a) Orientation map of lenticular martensite variants within austenite grains, showing zigzag and spear couplings; (b) the corresponding misorientation map of the austenite grains; (c) orientation map of a lenticular martensite plate with kink couplings. (The lump-shaped particles:  $\text{M}_7\text{C}_3$ .)

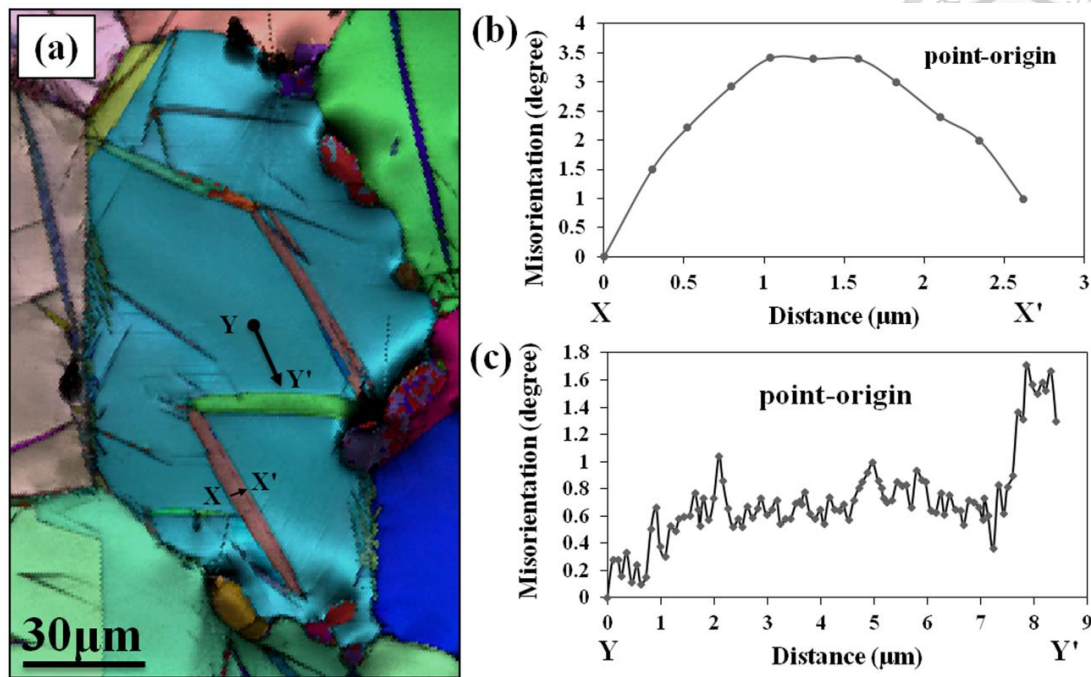


Figure 4-6 (a) Orientation map of lenticular martensite zigzag variants within an austenite grain; (b) misorientation profile across a lenticular martensite plate transversely from one side (X) to the other side (X'); (c) misorientation profile along the line Y–Y' in the surrounding austenite. (The lump-shaped particles:  $M_7C_3$ .)



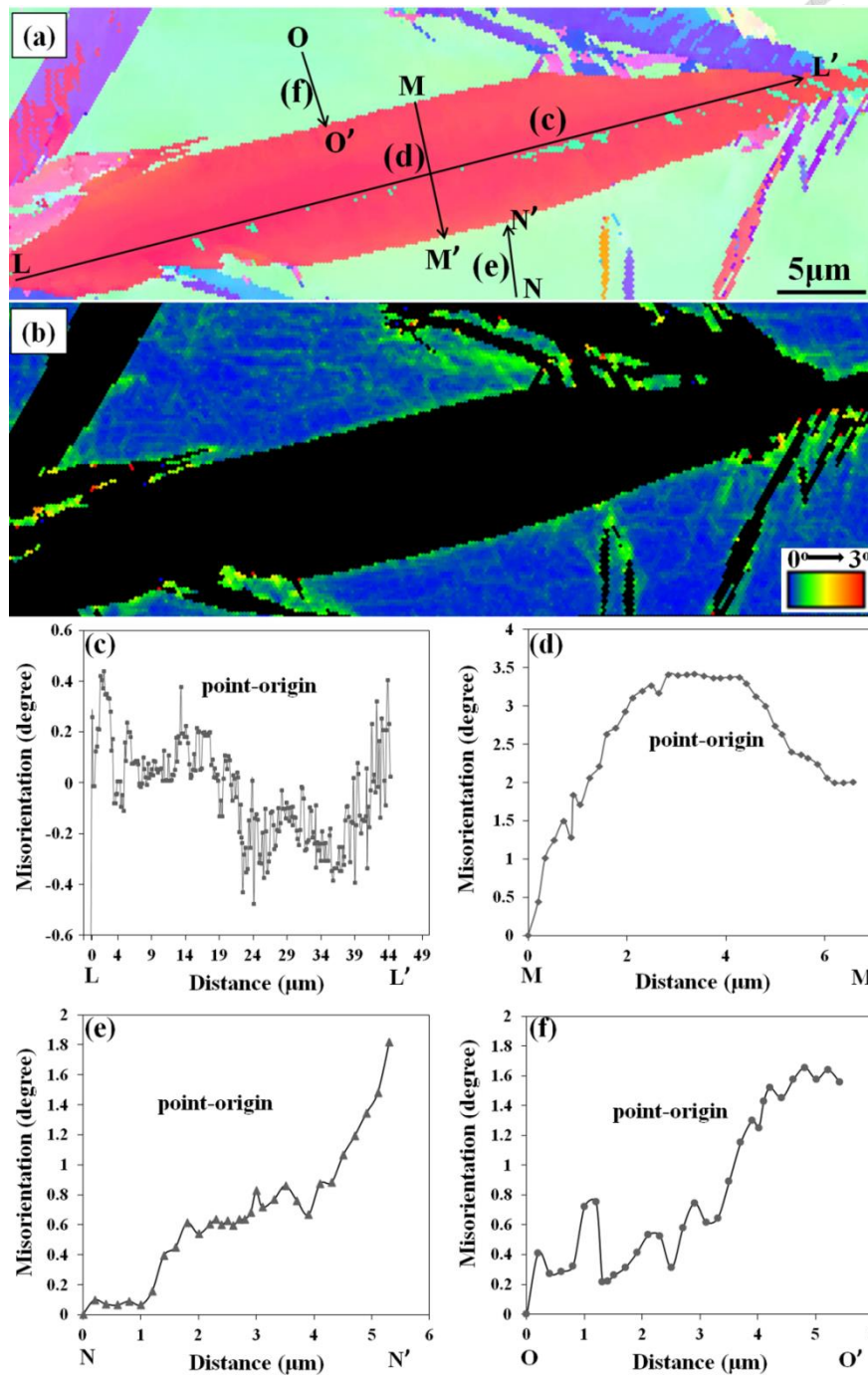


Figure 4-7 (a) Orientation map of a lenticular martensite plate; (b) corresponding misorientation map of the surrounding austenite; (c) misorientation profile along the longitudinal axis (midrib), the line L – L'; (d) misorientation profile across the lenticular plate transversely from one side (M) to the other side (M'); (e) misorientation profile along the line N – N' in the surrounding austenite; (f) misorientation profile along the line O – O' in the surrounding austenite.

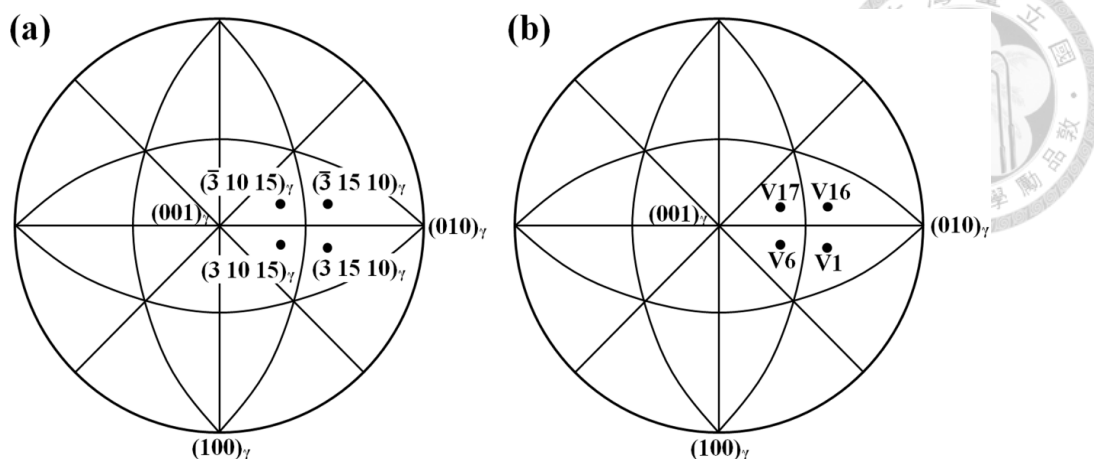


Figure 4-8 (a) Poles of  $(3\ 15\ 10)_\gamma$ ,  $(3\ 10\ 15)_\gamma$ ,  $(\bar{3}\ 15\ 10)_\gamma$  and  $(\bar{3}\ 10\ 15)_\gamma$  are located symmetrically around the pole of  $(0\ 1\ 1)_\gamma$ . (b) If the pole of the V1 variant is fixed on the pole of  $(3\ 15\ 10)_\gamma$ , then the V6, V16 and V17 poles can be set on the poles of  $(3\ 10\ 15)_\gamma$ ,  $(\bar{3}\ 15\ 10)_\gamma$  and  $(\bar{3}\ 10\ 15)_\gamma$ .

Table 4-3 Equivalent axis/angle pair (for smallest angle)

Pair No.	Morphology	Equivalent axis/angle pair (for smallest angle)			Possible variant pair
1	Zigzag type	[-0.662	-0.379	0.647] /53.01°	V1-V17
2	Zigzag type	[ 0.699	-0.022	0.715] /51.30°	V1- V6
3	Zigzag type	[-0.698	-0.348	0.675] /53.60°	V1-V17
4	Zigzag type	[-0.650	0.325	-0.630] /53.80°	V1-V17
5	Zigzag type	[-0.695	-0.676	-0.344] /53.60°	V1-V17
6	Zigzag type	[-0.662	-0.378	0.647] /51.30°	V1-V17
7	Spear type	[ 0.670	-0.651	-0.357] /53.43°	V1-V17
8	Spear type	[ 0.273	-0.696	0.664] /53.80°	V1-V17
9	Spear type	[ 0.371	0.664	-0.649] /50.70°	V1-V17
10	Spear type	[-0.706	-0.708	0.011] /53.80°	V1- V6
11	Spear type	[-0.616	-0.494	-0.614] /53.60°	V1-V17
12	Spear type	[ 0.666	-0.375	-0.645] /51.99°	V1-V17
13	Kink type	[ 0.212	0.614	0.760] /16.14°	V1-V16
14	Kink type	[ 0.628	0.298	-0.719] /16.49°	V1-V16
15	Kink type	[-0.652	-0.700	0.302] /16.29°	V1-V16
16	Kink type	[ 0.668	0.314	-0.675] /16.42°	V1-V16

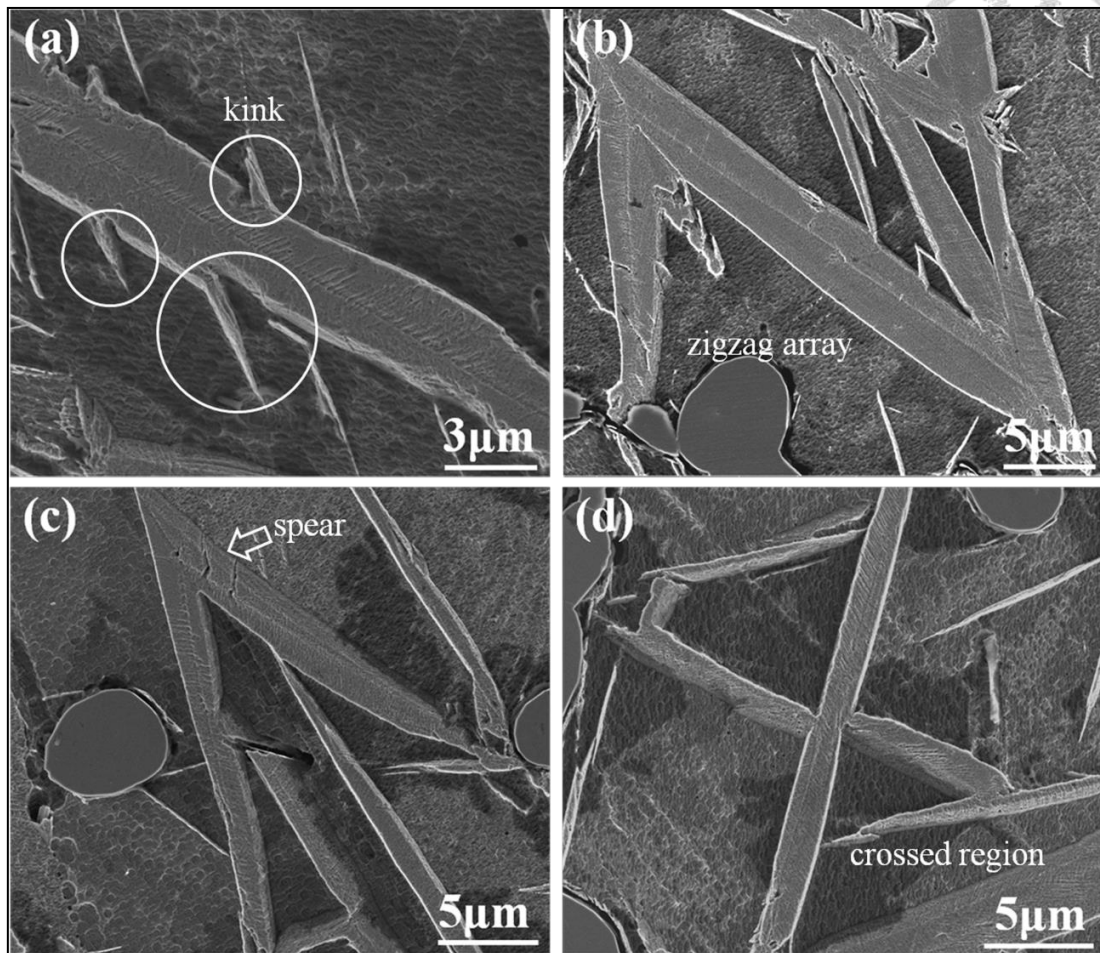


Figure 4-9 SEM images showing the (a) kink, (b) zigzag array, (c) spear, and (d) crossed region morphologies of coupling of lenticular martensite.

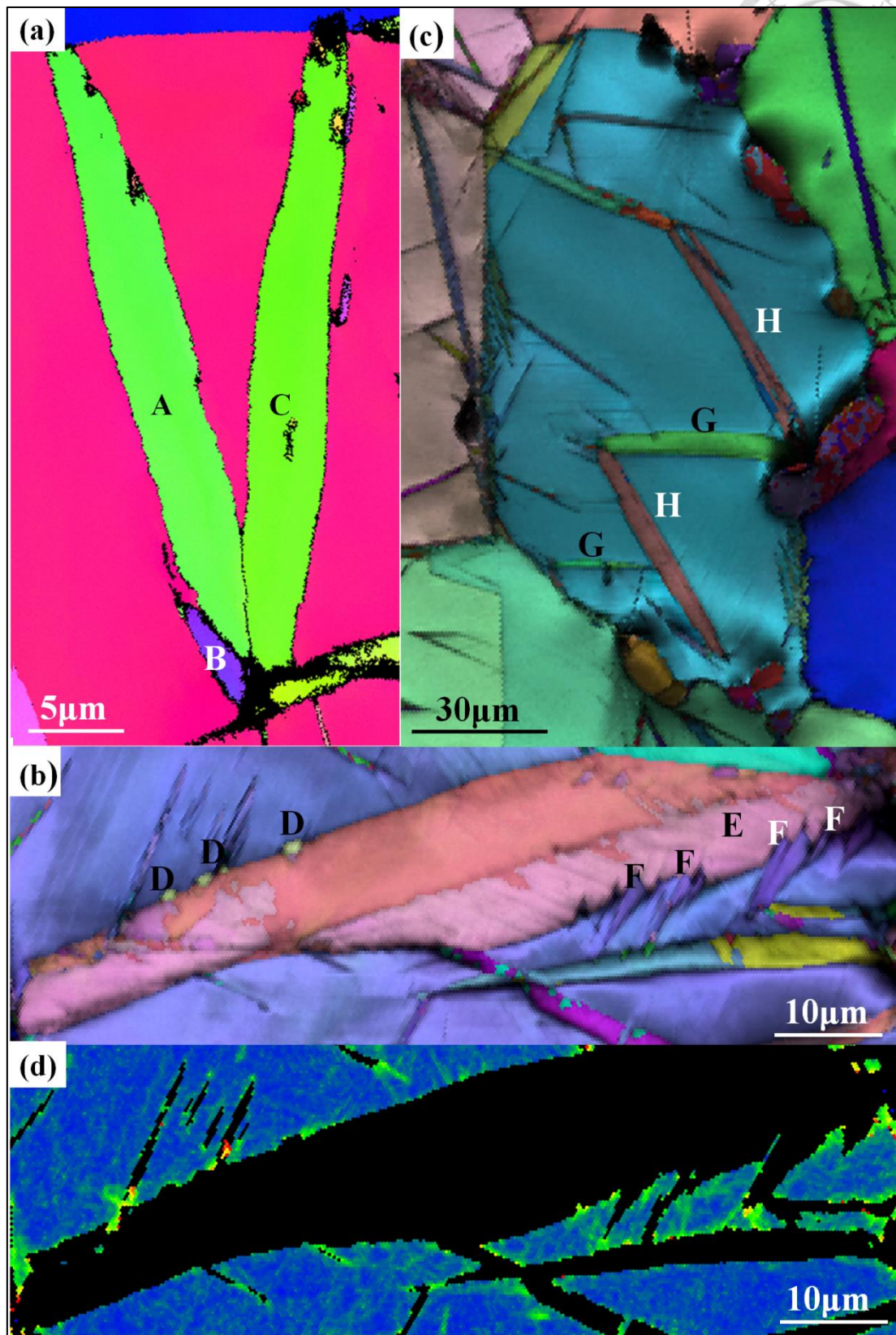


Figure 4-10 Orientation map of (a) spear (A-C) and kink (A-B) (b) zigzag (H-G) (c) kink (E-D and E-F) (d) misorientation map of austenite corresponding to (c).



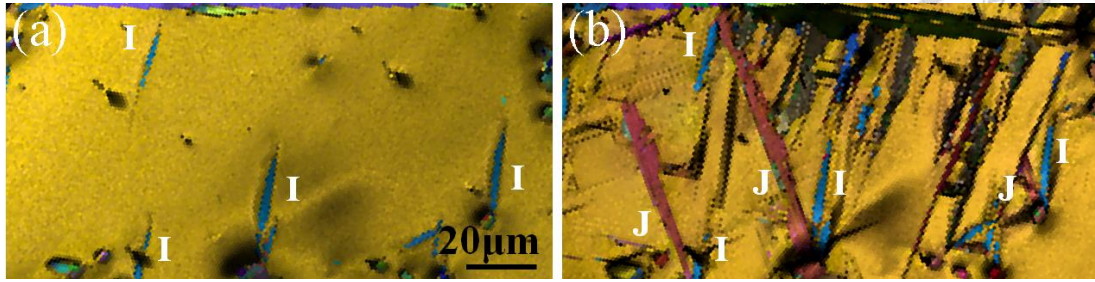


Figure 4-11 Orientation map of a sample (a) cooled to Ms (cryogenic treatment) for 8 seconds; then (b) cooled down to Ms (cryogenic treatment) for 30 seconds.

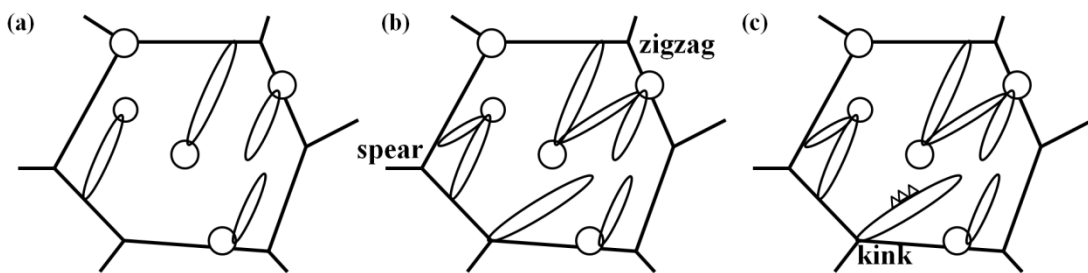
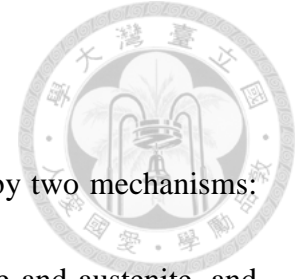


Figure 4-12 Formation process of different couplings of lenticular martensite.

## 4.4 Conclusions

In summary, for a given coarse austenite grain with considerable variants of lenticular martensite, the pole figures indicate that the lenticular martensite in this steel approximately adopts a Kurdjumov-Sachs orientation relationship with respect to the austenite matrix. It has been clarified that the spread in diffracted intensity within pole figures is related to the misorientation gradient within the lenticular martensite plate. On the other hand, a given coarse austenite grain with a few variants of lenticular martensite was employed to analyze the orientation relationships of the variant pairs of lenticular martensite plate. The results suggest that the coupling may be associated with

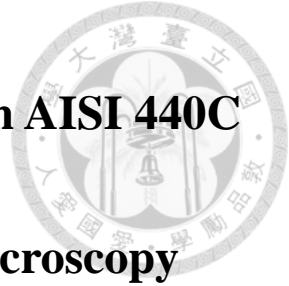
variant selection.



The formation of new lenticular martensite can be described by two mechanisms: autocatalysis for nucleation at the boundary of lenticular martensite and austenite, and self-accommodation for a series of nucleations from a single site. Based on these mechanisms, three different morphologies of lenticular martensite appear: spear, kink and zigzag array. In our research, it is noted that the zigzag array morphology may be composed of the spear type, which can be seen as a product of variant selection, as mentioned in the above section. A special form of coupling, crossed region coupling, occurs when two lenticular martensite plates grow into each other.

## **Chapter 5 Tempered lenticular martensite in AISI 440C**

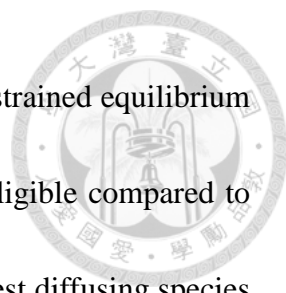
### **stainless steel by transmission electron microscopy**



### **5.1 Introduction**

The tempering behavior of martensite has received considerable attention and has been the subject of many research and review articles. It involves the segregation of carbon at dislocations and defects, the clustering of carbon into a modulate structure, the precipitation of carbides, the decomposition of retained austenite, and the formation of alloying carbide in steels.

The precipitation of cementite in steel is of great technological importance, so the mechanism of precipitation has received much attention in recent years, particularly with respect to the substitutional elements present in commercial alloys[154-156]. According to the local equilibrium assumption, two transformation modes have been proposed for transformations in steels involving the diffusion of both substitutional and interstitial elements. (1) Partitioning local equilibrium (PLE) is defined by a low interface velocity while local equilibrium is maintained at the interface. The transformation occurs at low supersaturation, and its kinetics is governed by the slow-diffusing species (substitutional elements). The condition is also referred to as



orthoequilibrium (OE). (2) Paraequilibrium (PE) is a kinetically constrained equilibrium that occurs when the diffusivity of the substitutional species is negligible compared to that of interstitial species. The kinetics of PE is governed by the fastest diffusing species, which in steels is C. It is shown that once nucleated, the full growth of paraequilibrium cementite, determined by C diffusion alone, takes place on a time scale of seconds. These two mechanisms are illustrated in Figure 5-1[154-156].

In this study, the decomposition mechanism and the microstructure of tempered lenticular martensite and cementite precipitates have been studied in high carbon steel. However, regarding the detailed study of tempered lenticular martensite, few articles have been published. The morphology of carbide precipitates at different positions (the midrib, the extended twinned region, and the untwinned region) in lenticular martensite and the crystallography of their formation in a Fe-17.4Cr-1.0C wt.% alloy have been examined by means of TEM after tempering at 400°C for various holding times. It is found that the cementite-ferrite orientation relationships follow both the Bagaryatski and the Isaichiv orientation relationships simultaneously. The results show various precipitation sequences with constant tempering temperature. The transformation of cementite to  $M_7C_3$  carbide is achieved by prolonged tempering treatment.

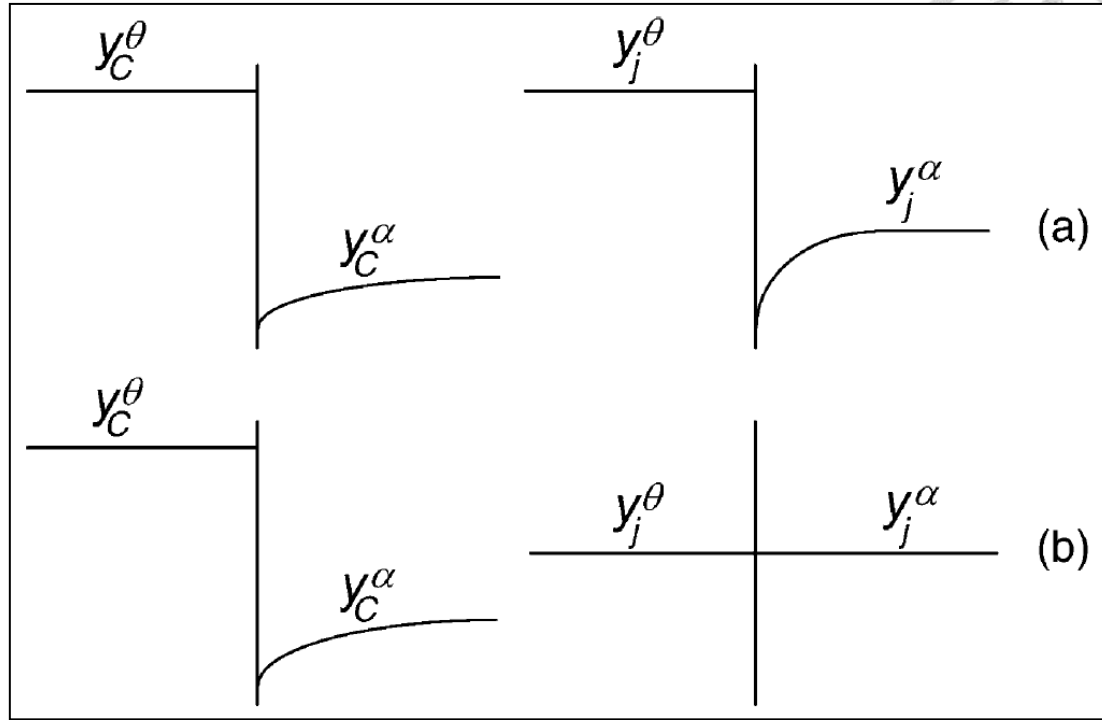


Figure 5-1 Schematic profiles of the site fractions of the substitutional elements ( $y_j$ ) and C ( $y_C$ ) across the transforming interface associated with (a) OE and (b) PE phase transformation involving ferrite ( $\alpha$ ) and cementite ( $\theta$ ). The X-axis represents distance and the Y-axis represents concentration. The cementite is the growing phase[154].

## 5.2 Experimental procedure

The as-received material was a commercially wrought AISI 440C stainless steel bar (with a diameter of 122 mm). The chemical composition of this steel was Fe–1.0C–17.4Cr–0.45Mo–0.40Mn–0.38Si–0.40Ni (wt%). The pieces of steel rod were machined from the half radius position of the original bar and homogenized at 1200°C for 3 days in quartz capsules containing pure argon. After that, the specimens were quenched in liquid nitrogen (-196°C) for 15 min to obtain thin-plate and lenticular

martensite. These as-quenched specimens were tempered at 400°C for 10 and 30 sec, and for 1, 3, 10, 30, 60, 120, 240, 1040, and 1500 min (as shown in Figure 5-2).

The corresponding microstructures were examined by OM, SEM, and TEM. Both types of specimens were cut from the heat-treated rods. The specimens for OM and SEM were mechanically polished and then etched in a mixture of 40 ml HCl, 25 ml ethanol, 30 ml distilled water, and 5 g CuCl<sub>2</sub>. TEM samples were sliced from the rod specimens, thinned to 0.08 mm by abrasion with SiC papers, and twin-jet electropolished using a mixture of 5% perchloric acid, 25% glycerol, and 70% ethanol at 5~10°C with 45~55V polishing potential. The thin foils were then examined using a FEI Tecnai F20 TEM operated at 200KV.

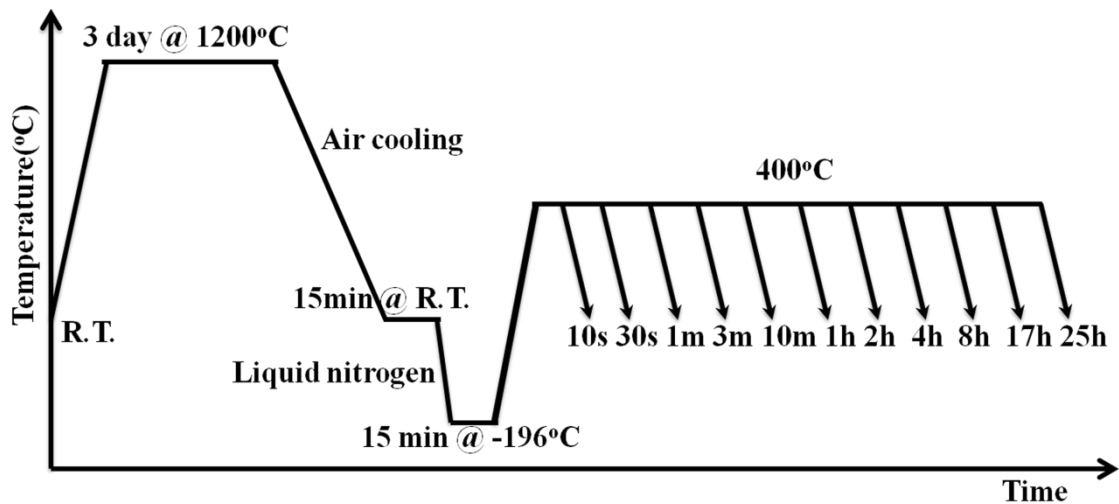


Figure 5-2 Schematic representation showing the tempered heat treatment of material.

### 5.3 Results

Before the tempering treatment, the formation process of lenticular martensite occurs as follows: First, the thin plate martensite nucleates at the prior austenite grain boundaries and  $M_7C_3$  carbides owing to favorable energy, and then the thin plate martensite transforms into lenticular martensite. The substructure of lenticular martensite consists of three distinct regions: the midrib, the twinned region, and the untwinned region.

During the tempering process, the first step of carbide precipitation is the formation of carbon clusters in lenticular martensite. Because of the stress fields around individual defects (dislocations and twins) and cell walls in martensite, certain interstitial lattice sites near these defects provide lower-energy sites for carbon than the normal interstitial lattice positions. Therefore, when martensite is tempered at low temperatures (e.g., 400°C), the redistribution of carbon to these lower energy sites occurs first[159].

In order to clarify what happens in high Cr and high C lenticular martensite during tempering treatment, a series of TEM examinations were performed. Two cementite morphologies and ORs within the decomposed region were distinguished.



### 5.3.1 Needle-like cementite carbides

After tempering at 400°C for 10~30 sec, the cementite precipitated preferentially at the M/A interface. A high density of curved and tangled dislocations was observed in the surrounding austenite near the M/A interface. The dislocations in the surrounding austenite might have been inherited from martensite near the M/A interface. The high strain energy caused by this high density of dislocations induces a high driving force for the nucleation of cementite at the M/A interface, and it is then relaxed with the growth of cementite during the tempering process.

At the same time, the carbides, which are cementites, also precipitate in the lenticular martensite, as shown in Figure 5-3. The cementites are about 15~20 nm wide and needle-like. These cementites and the ferrite matrix follow the Isaichiv orientation relationship:

$$(100)_\theta // (111)_f$$

$$(031)_\theta // (01\bar{1})_f$$

$$(113)_\theta // (\bar{1}11)_f$$

It is a well-known fact that carbides usually precipitate at defects due to the high diffusion rate or high strain energy at these sites. Figure 5-4 (a) serves as an example of the precipitation of needle-like cementite by the paraequilibrium growth mode. It shows that these needle-like cementites nucleate at the twin boundary and then extend. This



morphology is somewhat like the cementite in pearlite. Only a single variant of needle-like carbides could be found in some tempered lenticular martensite.

In a single lenticular martensite grain, there exist twins, dislocations, and other distortion defects. It is suggested that carbides may prefer to nucleate at twin boundaries with high carbon concentration gradients, as shown in Figure 5-4 ((d)-(f)). The nucleation of a cementite lamella can decrease the carbon concentration in the lenticular martensite.

As indicated in Figure 5-5, the observed cementites had different morphologies in different regions of lenticular martensite. The TEM image shows that the needle-like cementite and dislocations were both distributed in the lenticular martensite, and the dislocations located in the untwinned region can be clearly observed not to have any precipitates on them.

After tempering at 400°C for 1500 min, the cementites at the midrib start to transform into  $M_7C_3$  carbides, as shown in Figure 5-6. The particle was identified as an  $M_7C_3$  carbide, and the OR between the ferrite and  $M_7C_3$  carbide was deduced to be

OR-I:

$$(001)_{M_7C_3 \text{ carbide}} // (\bar{1}10)_\alpha$$

$$(\bar{1}10)_{M_7C_3 \text{ carbide}} // (111)_\alpha$$

$$(\bar{1}\bar{1}0)_{M_7C_3 \text{ carbide}} // (11\bar{2})_\alpha$$



The OR-I is close to the Dyson and Andrews OR:

$$(001)_{M_7C_3 \text{ carbide}} // (011)_\alpha$$

$$(\bar{1}10)_{M_7C_3 \text{ carbide}} // (\bar{1}00)_\alpha$$

$$[110]_{M_7C_3 \text{ carbide}} // (01\bar{1})_\alpha$$

In Figure 5-6(d), a clear stacking fault structure can be observed in the surface of the  $M_7C_3$  carbide. However, the needle-like cementite still maintains the same morphology after such a long period of tempering. It is hard to explain with orthoequilibrium. Thus, we propose certain possibilities for the formation of needle-like cementite. If it follows the paraequilibrium condition, there is no redistribution of substitutional elements between the precipitated phase and the matrix. The ratio of the Fe/X (X=substitutional elements) concentration remains constant at both sides of the interface. Paraequilibrium growth is possible if C reaches its equilibrium concentration in both the matrix and the precipitated phase. The growth of the precipitated phases is controlled only by C diffusion[156].

In contrast, diffusion transformation can easily explain the nucleation of needle-like cementite, which eliminates the high carbon concentration gradients in the lenticular martensite grain. These cementites are thus pretty stable and independent of the diffusion of Cr. The final state is cementite, which does not transform into  $M_7C_3$ .

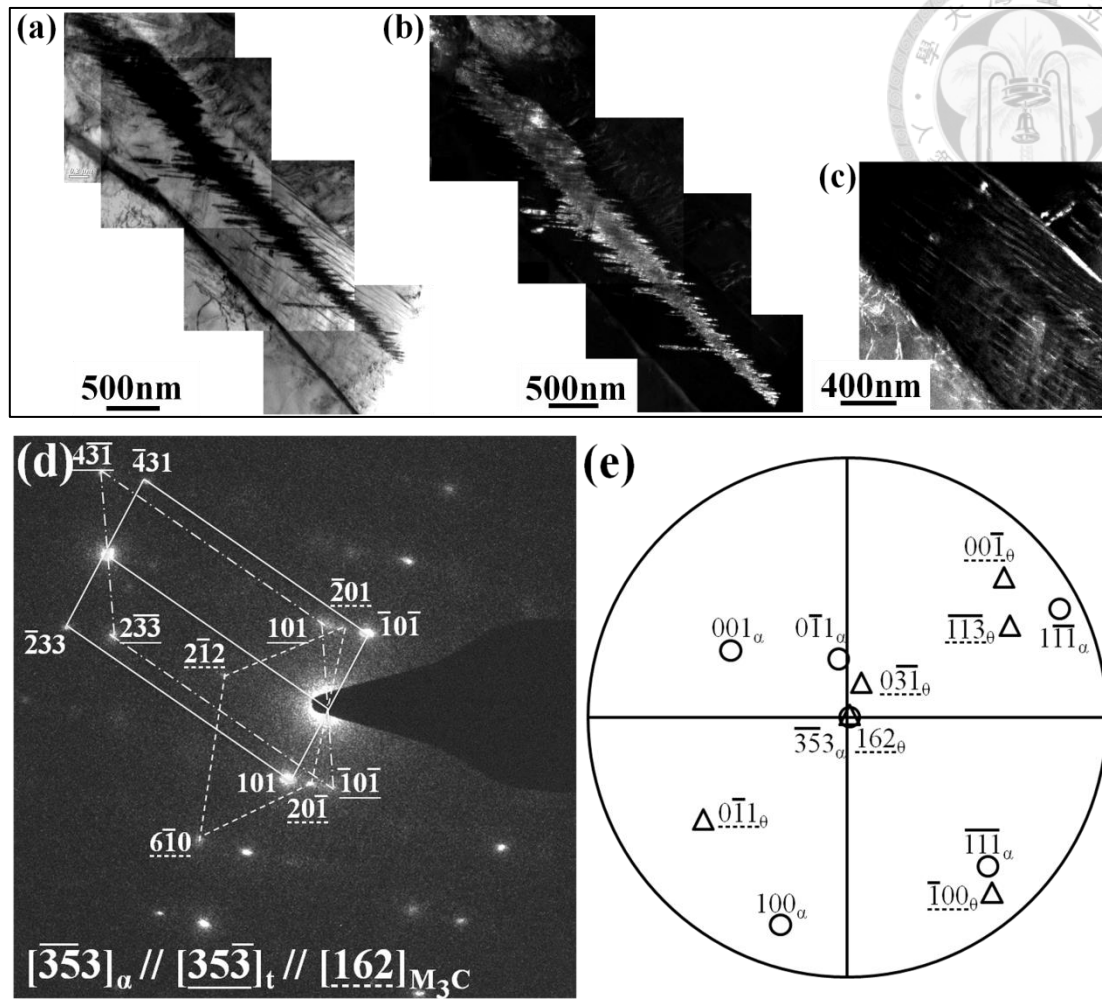
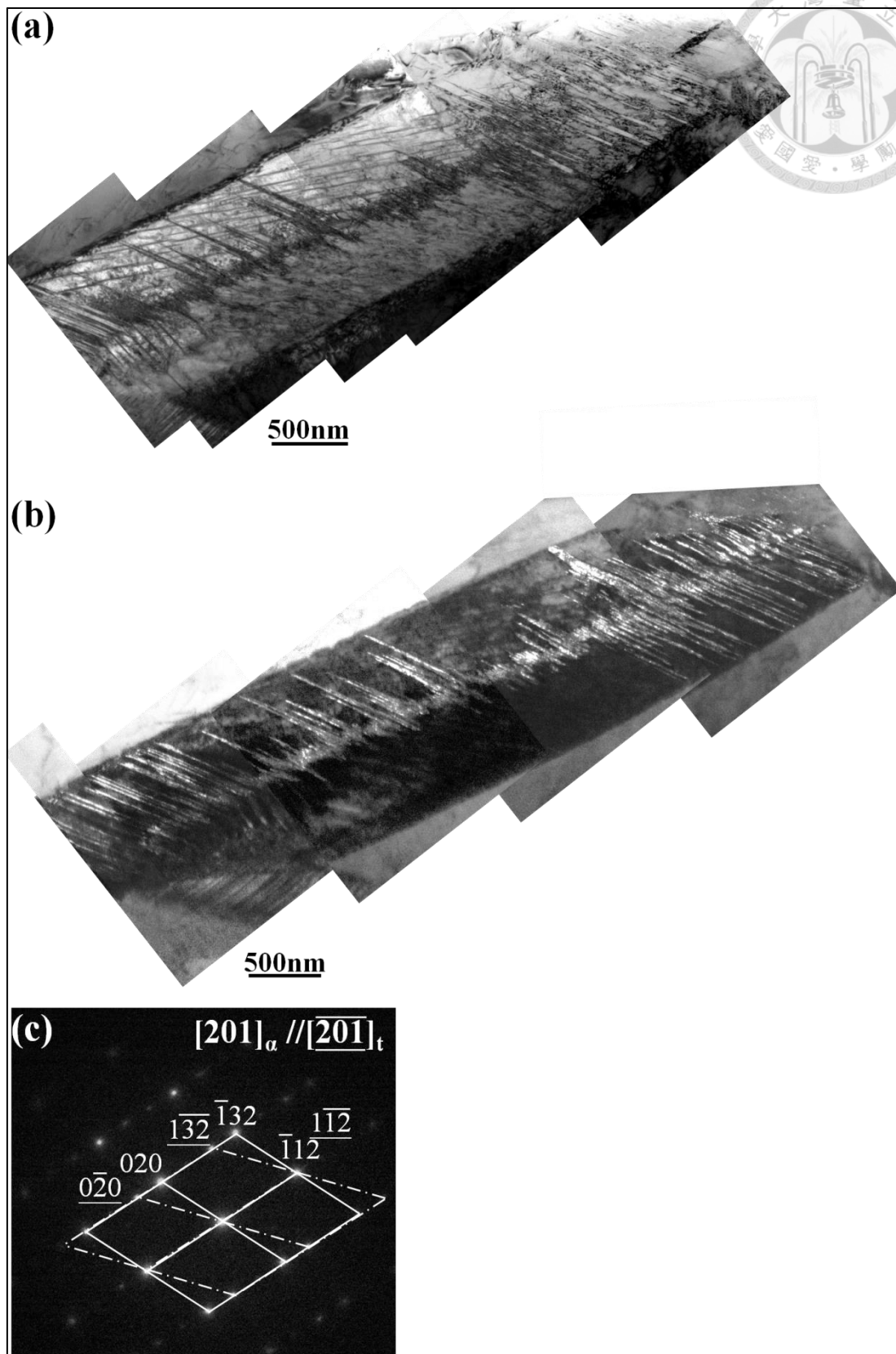
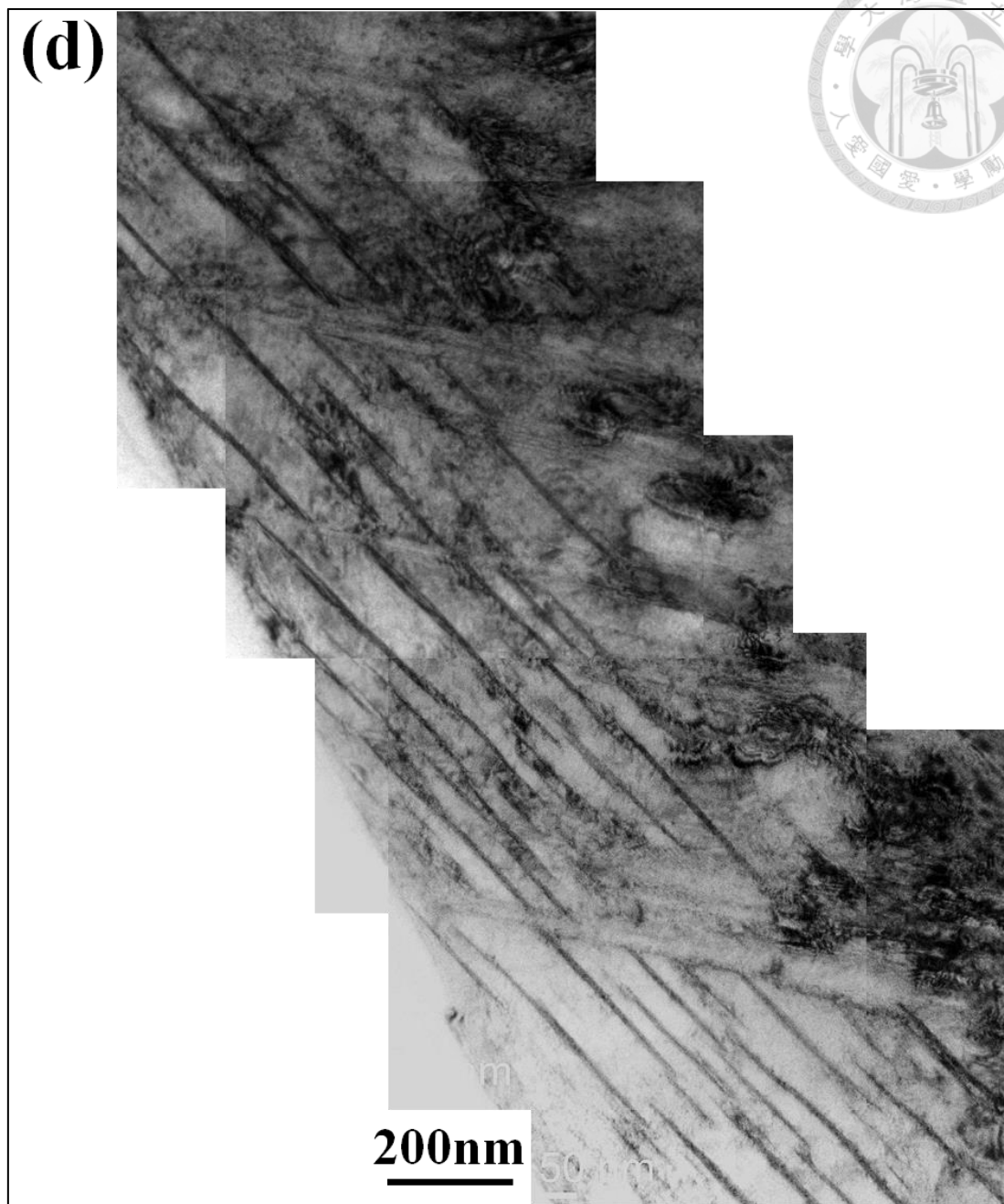


Figure 5-3 TEM images showing the microstructure of a tempered lenticular martensite from a specimen tempered at 400°C for 30 sec (a) A bright-field image of a tempered lenticular martensite. (b) - (c) The corresponding dark-field images for twin and needle-like cementite, respectively. (d) The selected area diffraction pattern and the corresponding analysis. (e) A stereographic projection showing the orientation relationship between the matrix(ferrite) and needle-like cementite.





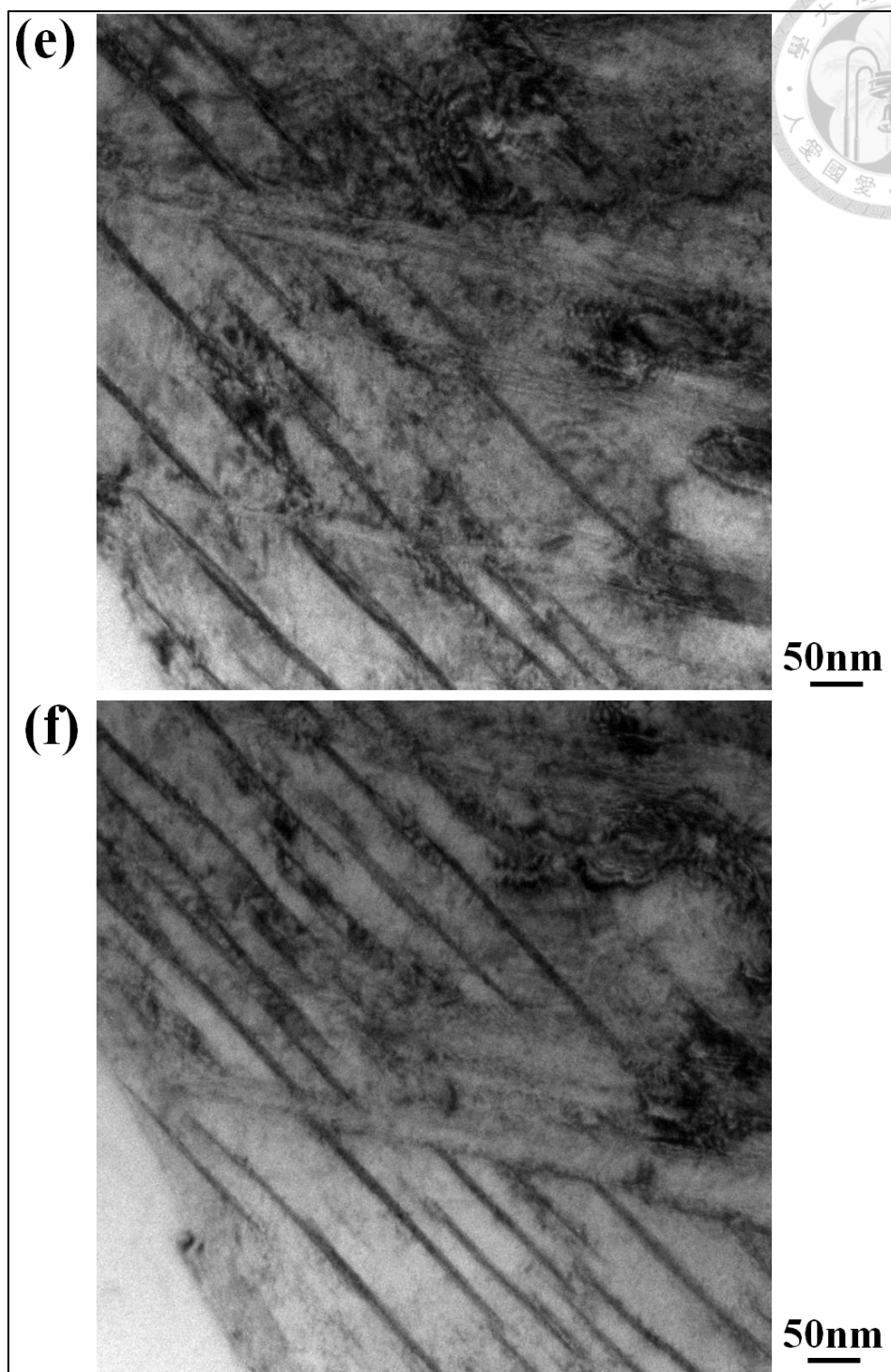
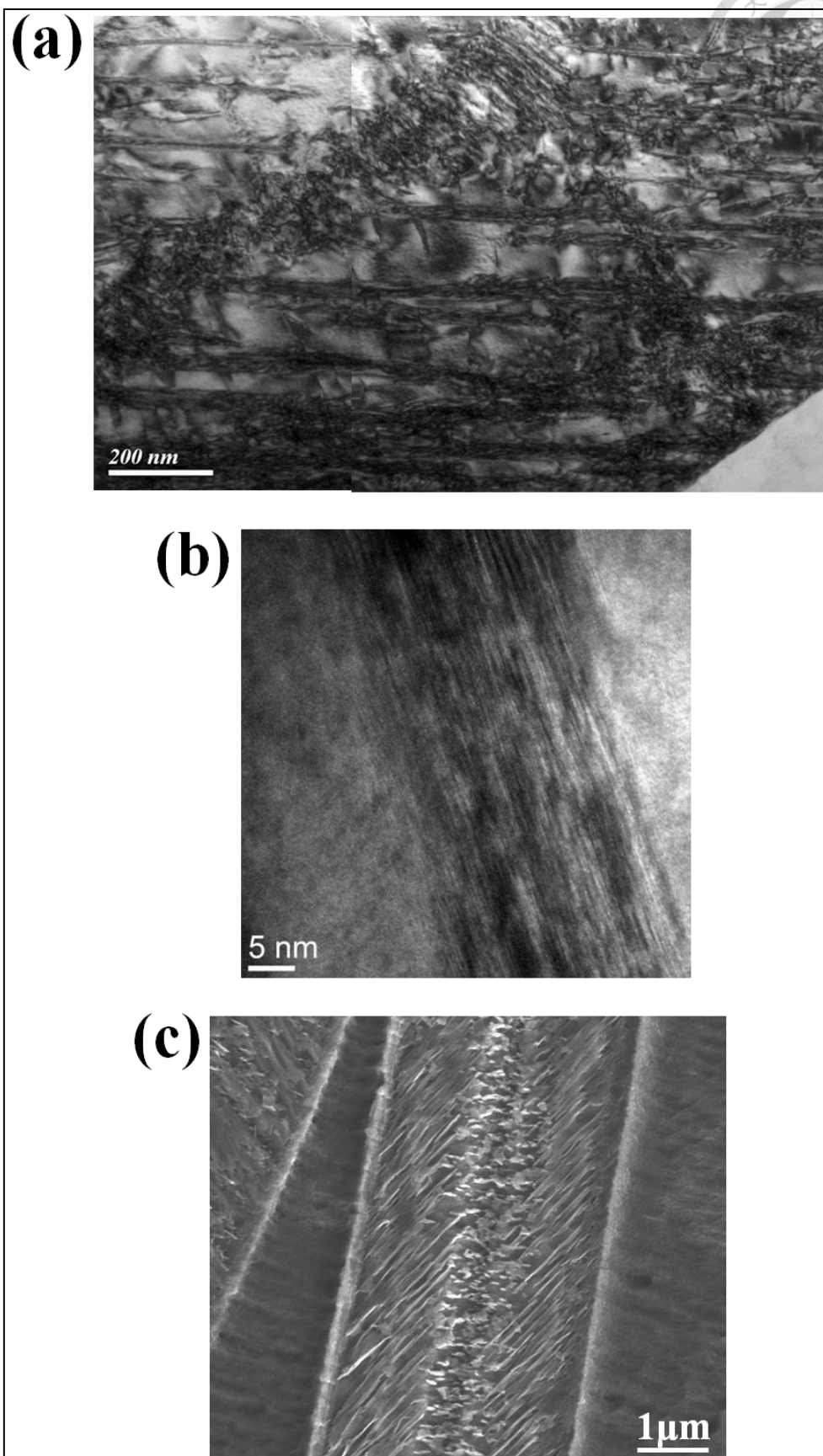


Figure 5-4 TEM images showing the microstructure of a tempered lenticular martensite from a specimen tempered at 400°C for 30 sec (a) A bright-field image of a tempered lenticular martensite. (b) The corresponding dark-field images for twin cementite. (c) The selected area diffraction pattern and the corresponding analysis. (d) A bright-field image of needle-like carbide; (e) and (f) are magnified images of (d).



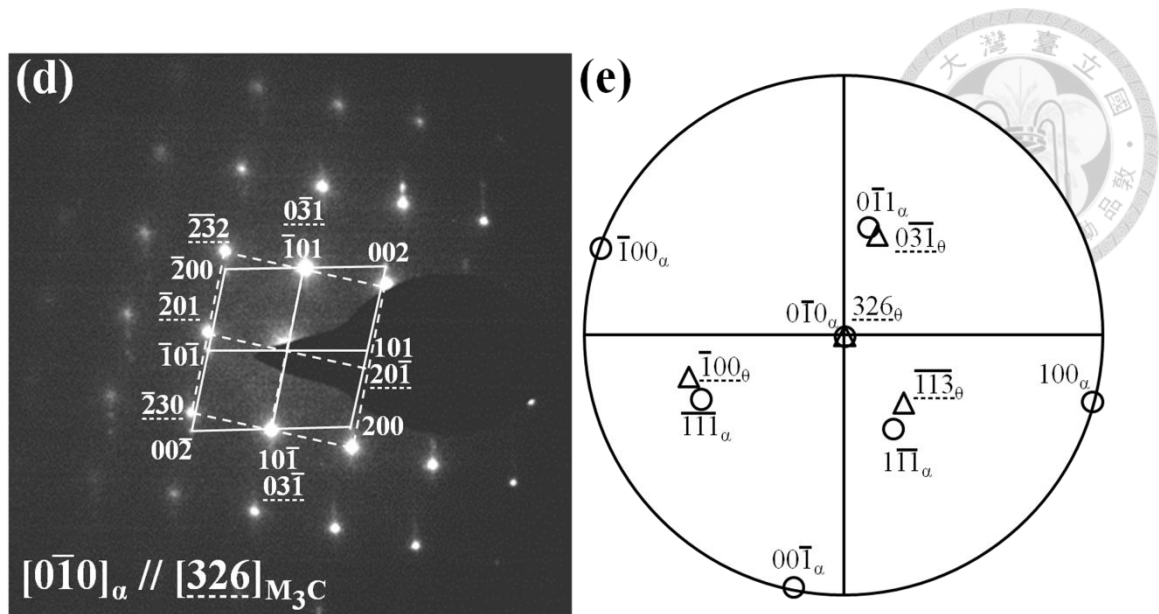
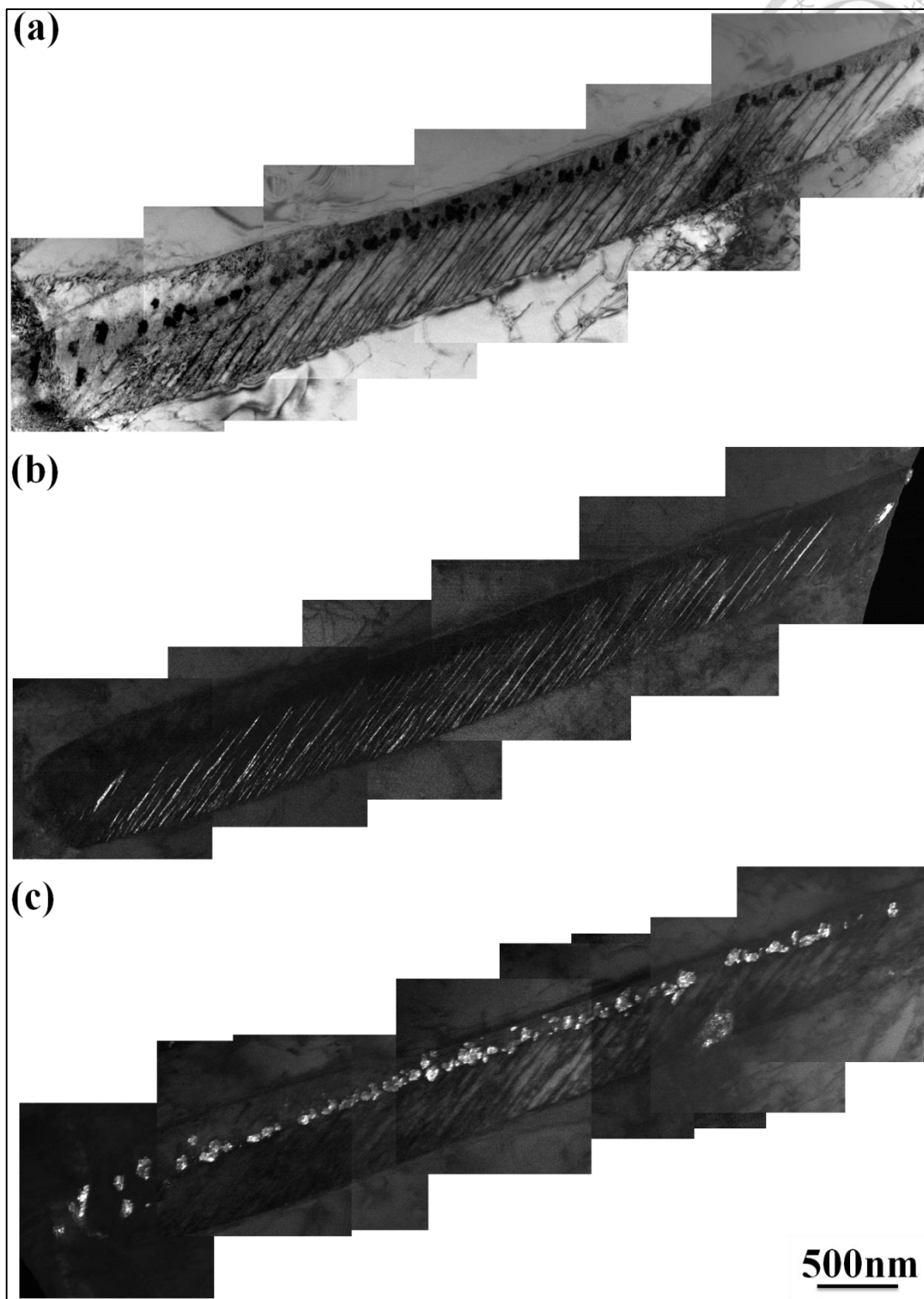
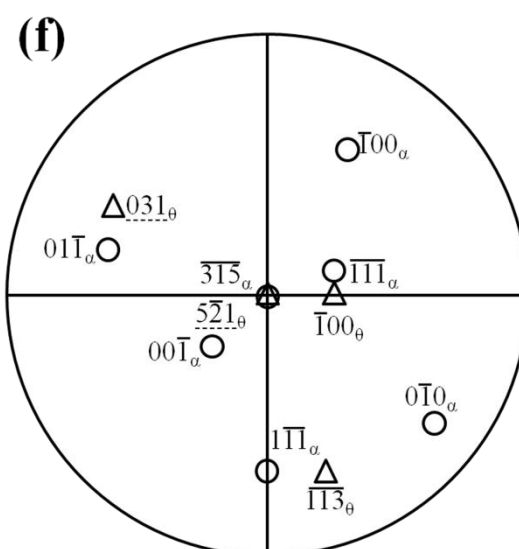
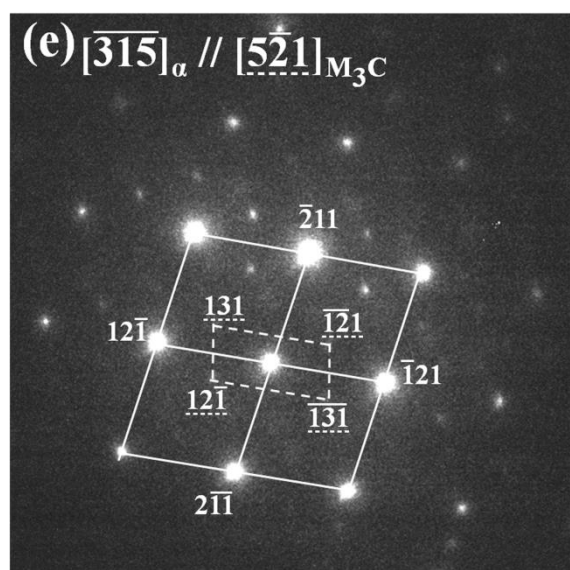
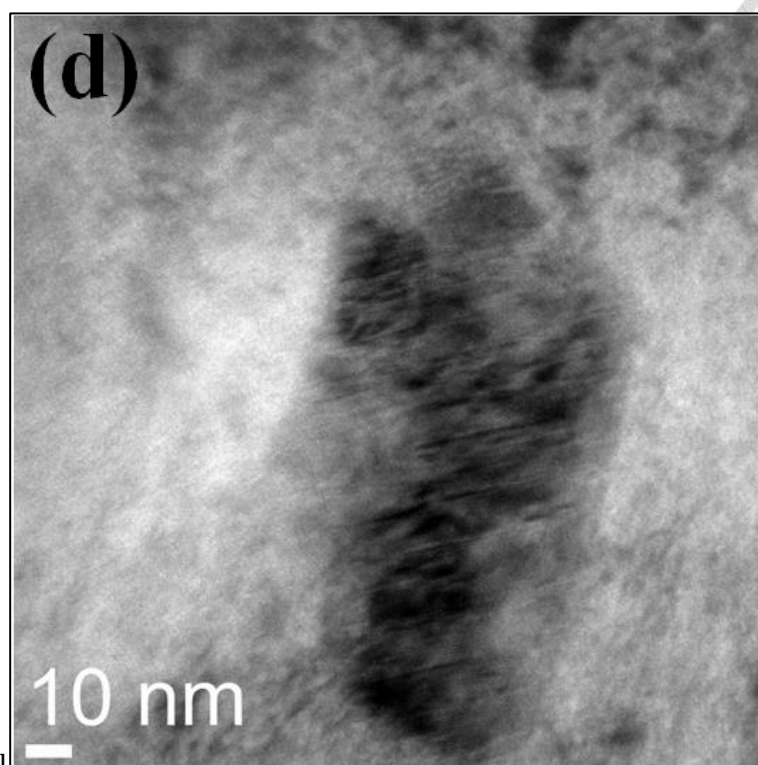
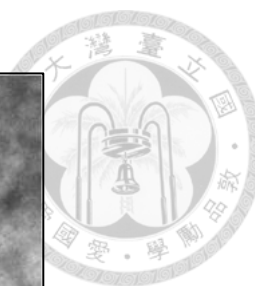


Figure 5-5 TEM images showing the microstructure of a tempered lenticular martensite from a specimen tempered at 400°C for 3 min (a) A bright-field image of a tempered lenticular martensite. (b) HRTEM image of the plate-like cementite (c) SEM image of the plate-like cementite. (d) The selected area diffraction pattern and the corresponding analysis. (e) A stereographic projection showing the orientation relationship between matrix(ferrite) and plate-like cementite.







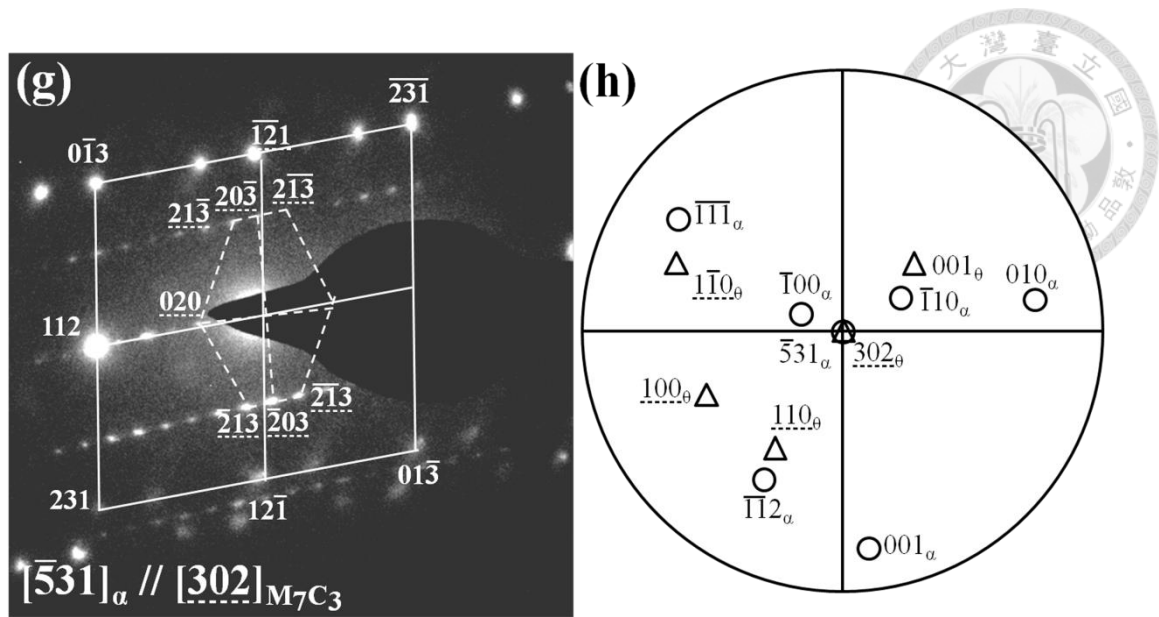


Figure 5-6 TEM images showing the microstructure of a tempered lenticular martensite from a specimen tempered at 400°C for 1500 min (a) A bright-field image of a tempered lenticular martensite. (b) - (c) The corresponding dark-field images for plate-like cementite and  $M_7C_3$  carbide, respectively. (d) Partial enlarged drawing of the  $M_7C_3$  carbide. (e) The selected area diffraction pattern and the corresponding analysis. (f) A stereographic projection showing the orientation relationship between matrix(ferrite) and plate-like cementite. (g) The selected area diffraction pattern and the corresponding analysis. (h) A stereographic projection showing the orientation relationship between matrix(ferrite) and  $M_7C_3$  carbide.

### 5.3.2 Rice-like cementite carbides

After tempering at 400°C for 10~30 sec, nano-sized cementite carbides start to precipitate at the midrib region in lenticular martensite, where the stress concentration is very high because of its twinning structure. After tempering at 400°C for 1 min, the orientation relationship between precipitated cementite carbides and martensite matrix

follows the Bagaryatsky OR:

$$(001)_\theta // (0\bar{1}1)_f$$

$$(100)_\theta // (1\bar{1}\bar{1})_f$$

$$(010)_\theta // (211)_f$$



After a longer tempering time, these rice-like cementite carbides grow and are distributed within the midrib of lenticular martensite. There are two different cementite carbide variants observed in these tempered samples. One is related to the matrix twinning plane  $\{112\}$  in the midrib, and the other one grows along the matrix plane  $\{110\}$ . It is frequently discovered that the growth of cementite stops at the interface between twin and matrix. The cementites precipitate and then gradually coalesce and develop into parallel line-shapes in the midrib region. In contrast with the nucleation of cementite during low-temperature tempering, the rice-like cementite grows by the partitioning local equilibrium growth mode. These rice-like cementites are indicated in Figure 5-7, where the needle-like cementites also precipitate in the lenticular martensite.

After tempering at 400°C for 3 min, the cementites start precipitating at the untwinned region. Instead of twinning, these dislocations are the preferred nucleation sites, which leads to two growth directions of cementites. The morphology of these cementites is also rice-like in shape, and they follow the Bagaryatsky OR with the matrix, as shown in Figure 5-8.

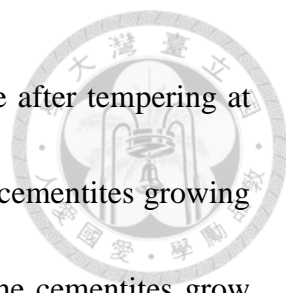


Figure 5-9 is the morphology of tempered lenticular martensite after tempering at 400°C for 3 min. The lenticular martensite marked A clearly shows cementites growing in two directions at the midrib. On the upper side of the midrib, the cementites grow perpendicular to the twins; on the lower side of the midrib, the cementites grow parallel to the twins. On the other hand, the cementites also precipitate in the untwinned and twinned regions after this tempering time. The lenticular martensite marked B shows a different morphology of cementite distributions, which grow in line-shapes perpendicular to the twins. According to the diffraction pattern analysis, such a morphology forms due to the differences in variants.

From TEM observation, it is found that the cementite does not extend from the midrib region to the twinned region, preferring instead to nucleate in the untwinned region. This is due to several dislocations in the untwinned region, which induce large strain energy and high driving force for cementite growth. However, this driving force is not large enough for the nucleation of  $M_7C_3$  carbides. Therefore, after tempering at 400°C for 10~30 min, the amount of cementites in the twinned region increases, and these carbides also become larger and start to assemble, but no transformation into  $M_7C_3$  carbides occurs, as shown in Figure 5-10.

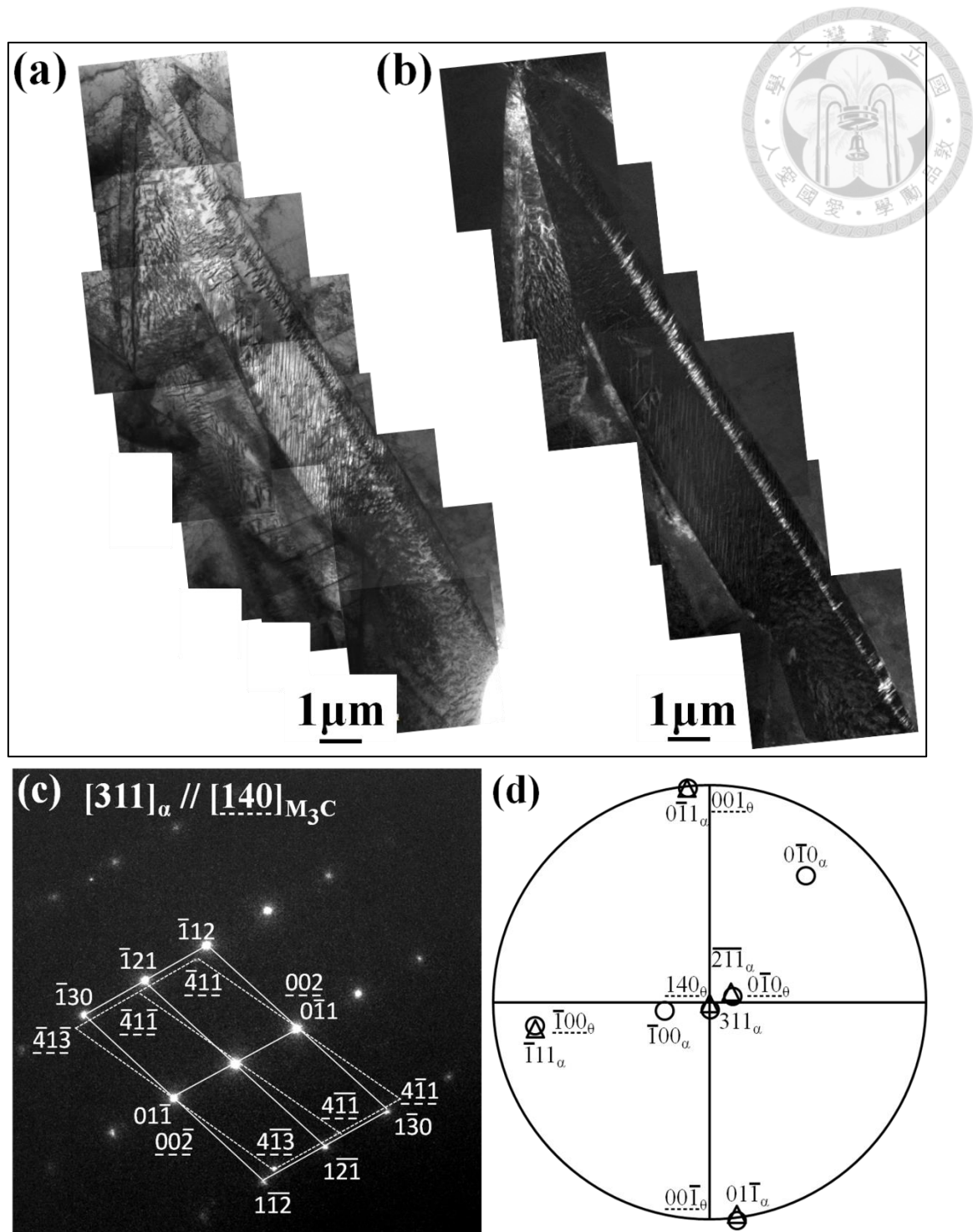


Figure 5-7 TEM images showing the microstructure of a tempered lenticular martensite from a specimen tempered at 400°C for 1 min (a) A bright-field image of a tempered lenticular martensite. (b) The corresponding dark-field images for rice-like cementite. (c) The selected area diffraction pattern and the corresponding analysis. (d) A stereographic projection showing the orientation relationship between matrix(ferrite)

and rice-like cementite.

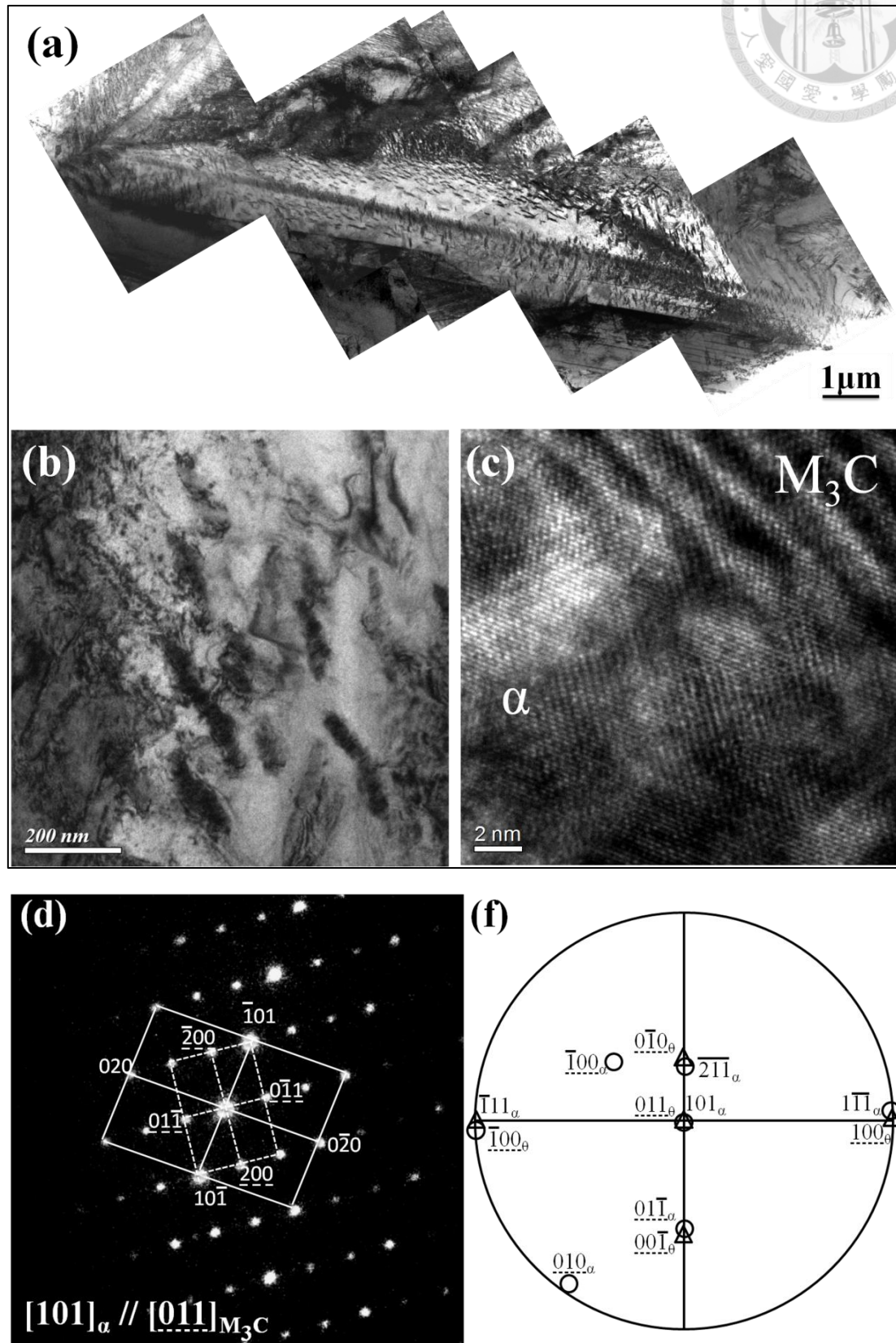


Figure 5-8 TEM images showing the microstructure of a tempered lenticular



martensite from a specimen tempered at 400°C for 3 min (a) A bright-field image of a tempered lenticular martensite. (b) Partial enlarged drawing of the rice-like cementite. (c) HRTEM image of the rice-like cementite. (d) The selected area diffraction pattern and the corresponding analysis. (e) A stereographic projection showing the orientation relationship between matrix(ferrite) and rice-like cementite.

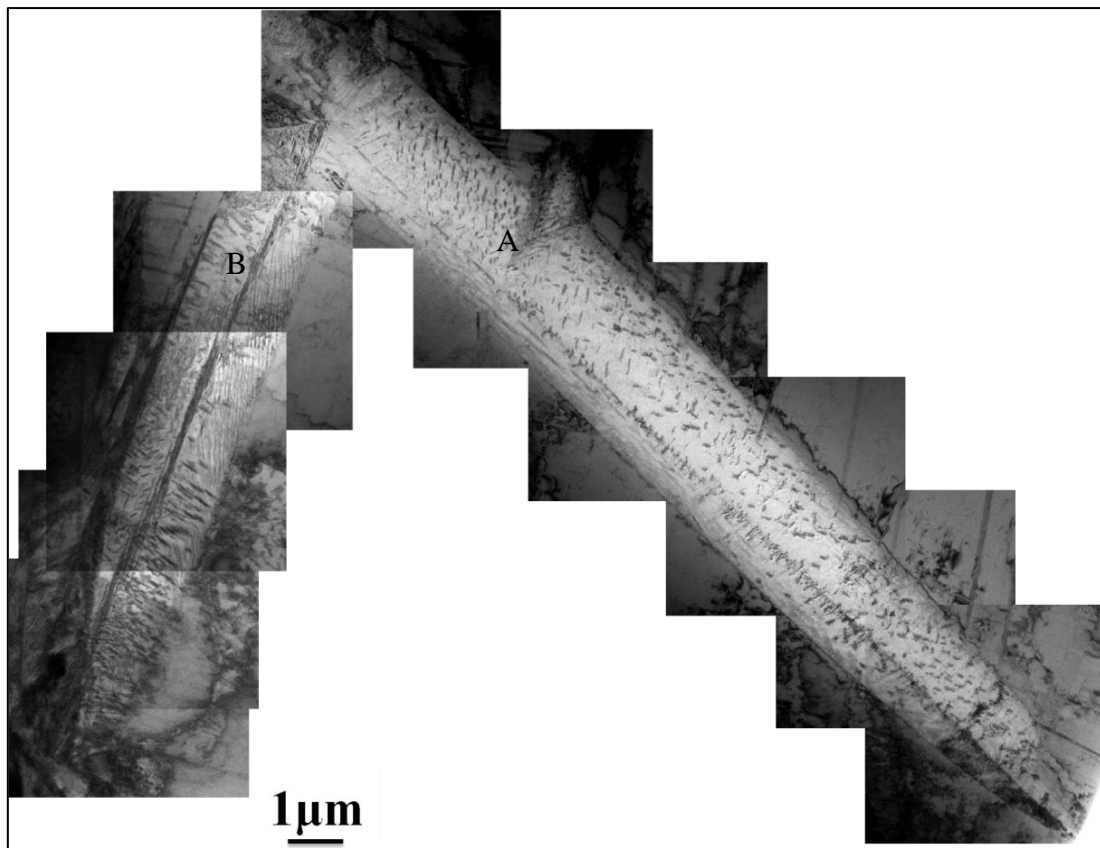


Figure 5-9 TEM images (bright-field) showing the microstructure of a tempered lenticular martensite from a specimen tempered at 400°C for 3 min.



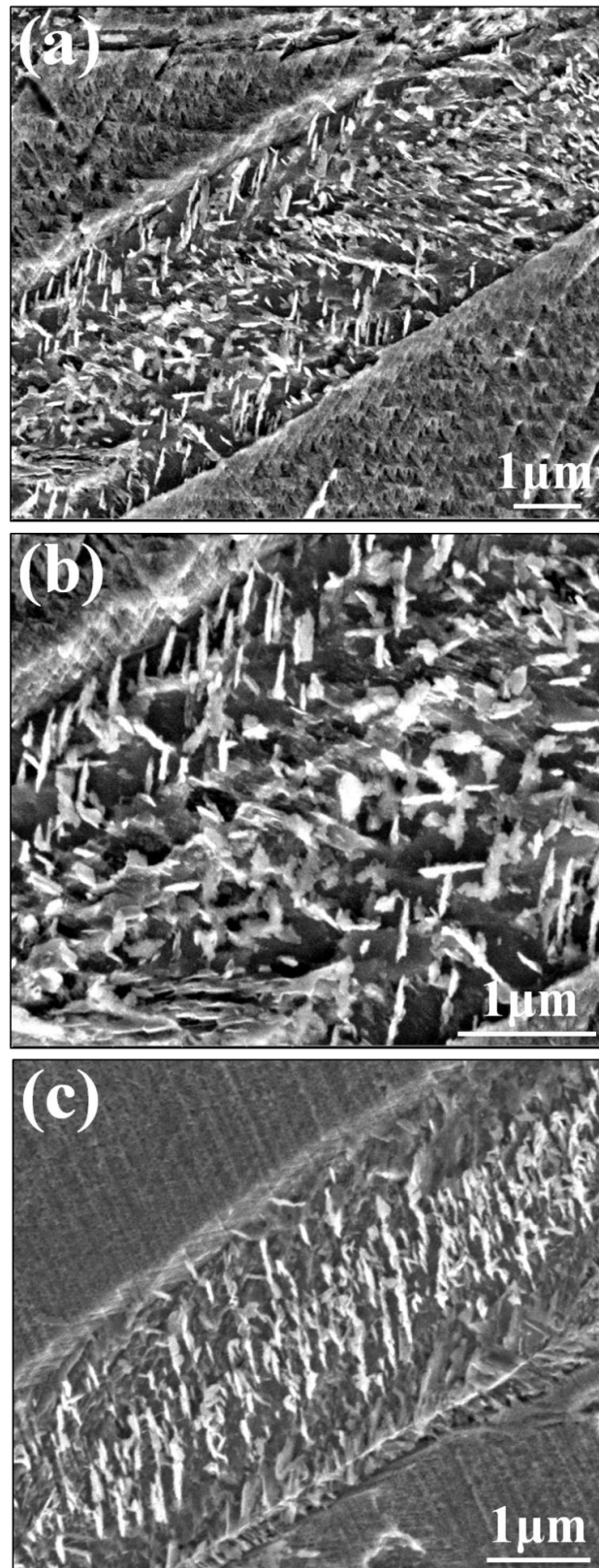


Figure 5-10 SEM images showing the microstructure of a tempered lenticular martensite from a specimen tempered at 400°C for (a) 10 min, (b) Partial enlarged drawing of (a), (c) 30 min

### 5.3.3 $M_7C_3$ carbides

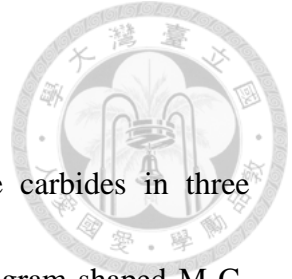
After tempering at 400°C for 60~120 min, the cementites in the untwinned region and twinned region gather and turn sphere-like, which reduces the surface energy, as indicated in Figure 5-11.

It was found that the twins in the lenticular martensite gradually disappeared with longer tempering time, which may have provided strain energy as the driving force for carbide growth. Figure 5-11 shows this procedure, in which parts of the cementite start to transform into  $M_7C_3$  carbides and the characteristic stripes of  $M_7C_3$  carbides can be observed. During this procedure, these sphere-like cementites first grow into long shapes, after which they accumulate and transform into lath-shaped  $M_7C_3$  carbides by the *in-situ* mechanism, which has no correlation with the solid solution and precipitation. In contrast to sphere-like cementites, these cementites that precipitate at the M/A interface and shear plane do not transform into  $M_7C_3$  carbides after longer tempering treatment. As the tempering time increases, the number of these cementite particles per unit volume decreases, and their size increases.

The transformation from cementite to  $M_7C_3$  carbide occurs mainly by the *in-situ* mechanism. The interface of cementite/ferrite is a preferred site for  $M_7C_3$  carbide nucleation, and the subsequent growth of  $M_7C_3$  carbides in cementite is more rapid than that in the ferrite matrix. TEM studies clarified that  $M_7C_3$  carbides usually contain

stacking fault characteristics, as shown in Figure 5-12.

After tempering at 400°C for 240~1040 min, the cementite carbides in three regions of lenticular martensite gather and transform into parallelogram-shaped  $M_7C_3$  carbides (Figure 5-13). The OR-I related to the matrix is close to the Dyson and Andrews OR. Another TEM observation result of tempered lenticular martensite morphology is shown in Figure 5-14.



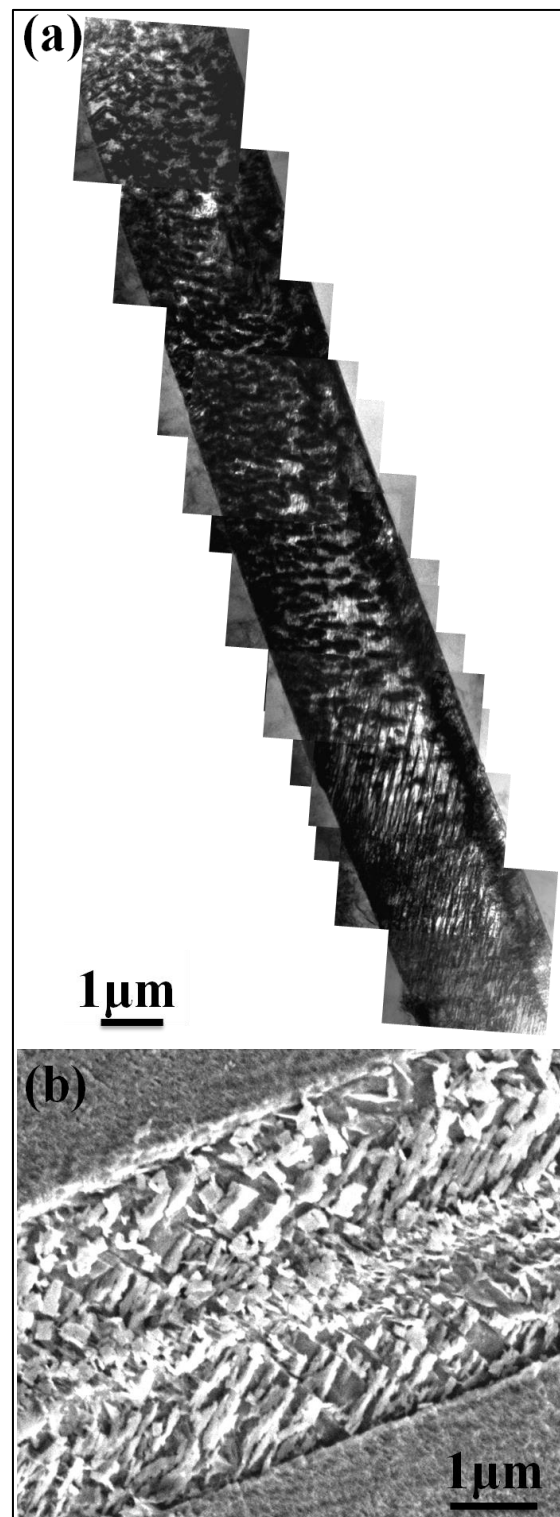


Figure 5-11 TEM images showing the microstructure of a tempered lenticular martensite from a specimen tempered at 400°C for 60 min (a) A bright-field image of a tempered lenticular martensite. (b) SEM images.

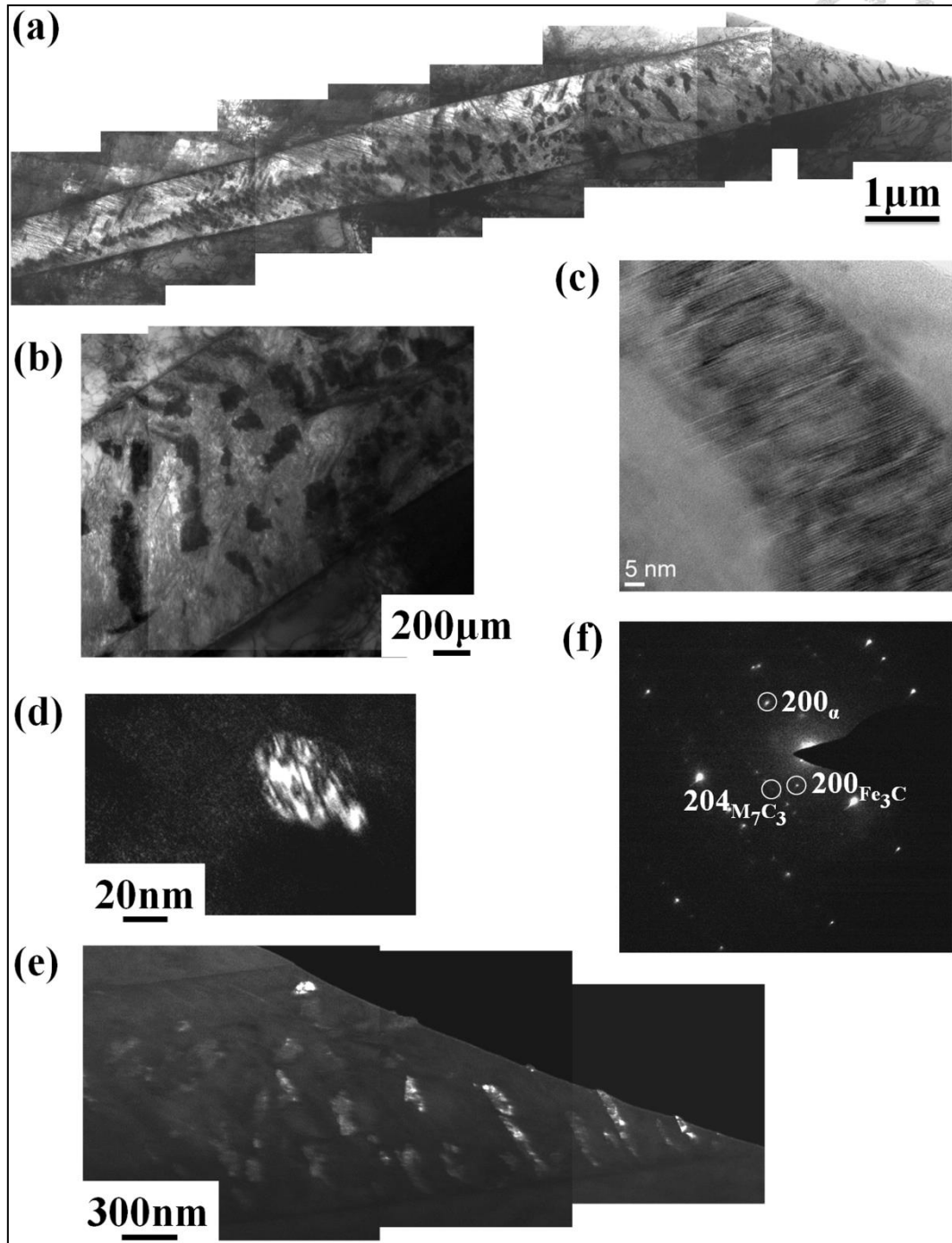
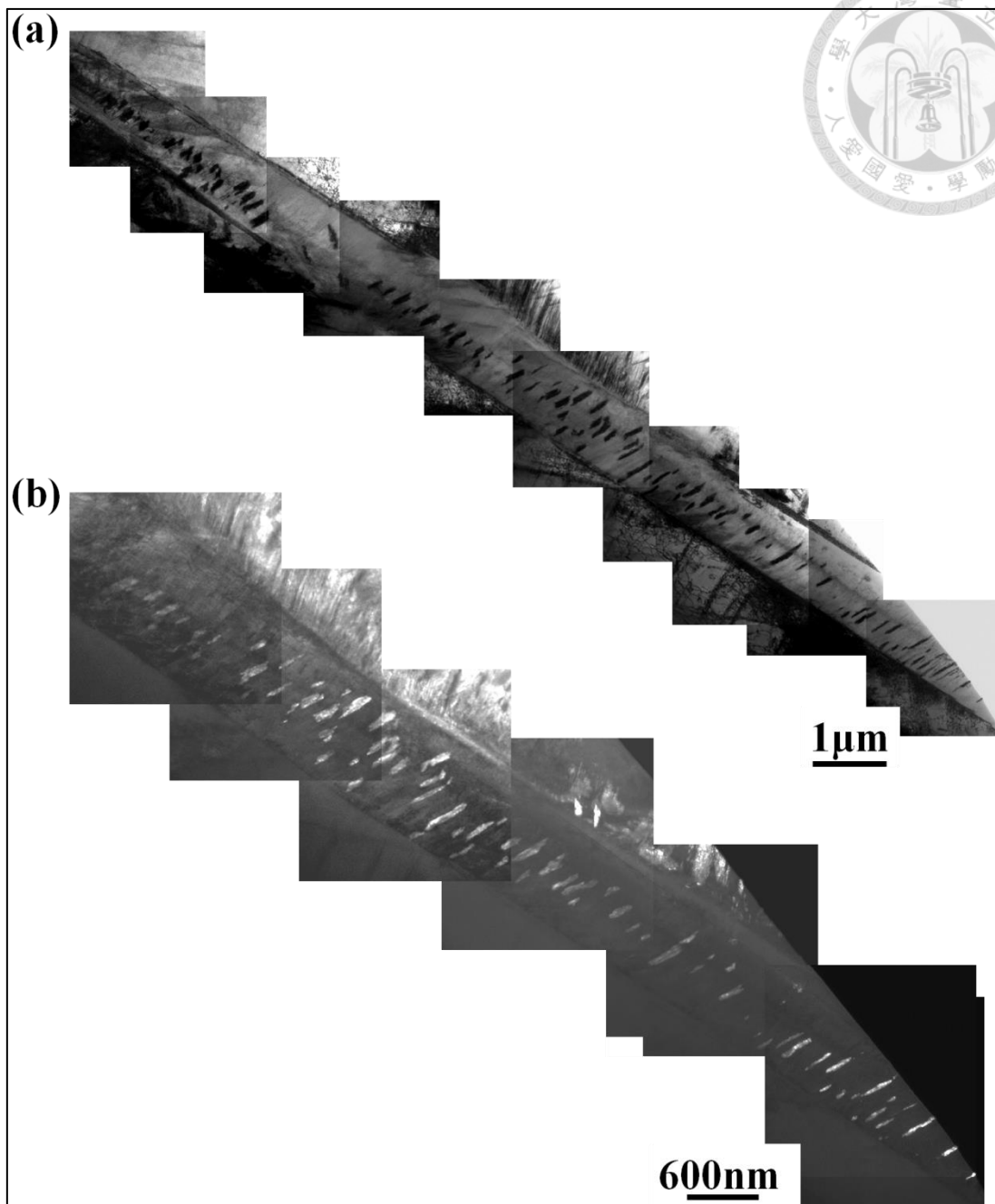


Figure 5-12 TEM images showing the microstructure of a tempered lenticular martensite from a specimen tempered at 400°C for 60 min (a) A bright-field image of a tempered lenticular martensite. (b) Partial enlarged drawing of the M<sub>7</sub>C<sub>3</sub> carbide. (c) HRTEM image of the M<sub>7</sub>C<sub>3</sub> carbide. (d) - (e) The corresponding dark-field images for cementite and M<sub>7</sub>C<sub>3</sub> carbide, respectively. (f) The selected area diffraction pattern and the corresponding analysis.











## 5.4 Discussion

### 5.4.1 Carbide precipitation

The discussed precipitation process is also related to a common kind of diffusion mechanism.

#### a. Needle-like cementite

The results show that the needle-like cementite and the martensite matrix most frequently have an Isaichiv orientation relationship. During low-temperature short-time tempering, the needle-like cementite nucleates quickly by the paraequilibrium condition. It is therefore can be assumed that the carbon atoms tend to diffuse from twins to nearby regions. Thus, the carbon concentration gradients must be high near the twinned region, where the twin boundaries induce a precipitation behavior similar to pearlite reaction and exhibit only one single variant of carbides. The primary rate-controlling factor for the precipitation of needle-like cementite is the carbon content. Since large atoms such as iron do not diffuse, the iron to substitutional solute atom ratio remains constant everywhere during this process. Therefore, one likely solution is a paraequilibrium (PE) condition, in which the substitutional atoms are rearranged without diffusion.

During tempering at low temperature for a few minutes, those high-carbon-concentration sites remain prior to nucleation and then stably grow along the same direction. Under this condition, the cementite has a relatively stable cementite

structure and does not transform into  $M_7C_3$  carbide after longer heat treatment.

#### **b. Rice-like cementites**

The cementite formation sequence in lenticular martensite can be described as follows: 1. the midrib (the high-density and high-energy twinning dislocations); 2. the untwinned region (the high-density dislocations); 3. the twinned region (few twinning dislocations). In the initial stage, rice-like cementites precipitate found that the apparent activation energy for carbide precipitation and growth during tempering is similar to the activation energy for pipe diffusion of iron and substitutional atoms along a high density of dislocations and twin that exist in the martensite matrix. Accordingly, G. B. Olson et al. suggested that such diffusion may be an essential part of the carbide growth process[43]. This mode is known as the partitioning local equilibrium (PLE) condition. The transformation and kinetics are controlled by the substitutional elements (Cr and Fe), and local equilibrium is maintained at the interface, so the diffusion velocity is low. These cementites have a Bagarytsky OR with the martensite matrix and develop different morphologies according to each variant. With longer tempering times, rice-like cementites start to accumulate and become sphere-like particles, which have lower surface energy. The final shape of the cementite is lath-like. The cementites transform into lath-shaped  $M_7C_3$  carbides, which depend on the diffusion of Cr along the boundary of the cementite and martensite matrix. It should be noted that this



transformation is unrelated to the solution of cementite and is a kind of *in-situ* mechanism.

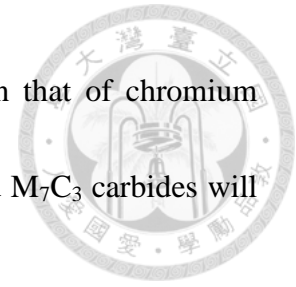


It is particularly interesting that the precipitation of rice-like cementite from martensite can occur under such conditions, where the diffusion rates of these large atoms are very slow as compared to the rate of needle-like cementite precipitation.

#### **5.4.2 Diffusion mechanism for alloy carbide precipitation**

In line with the above proposition, in the present research, the iron and substitutional atoms can be considered to diffuse along the twinning dislocations in the midrib and twinned regions, and along the dislocations in the untwinned region. The cementite therefore starts to nucleate and grow. For the initial steps in carbide precipitation, carbon is the primary controlling factor. As the tempering time increases, the alloy carbide precipitation starts to be controlled by the diffusion of other alloying elements, such as the chromium in this kind of stainless martensite steel, and then the cementite gradually transforms into  $M_7C_3$  carbides. Compared with the diffusion of carbon, there is also a strong driving force for chromium diffusion toward the surface of cementite particles. In this case, the chromium atoms can be transported through interface diffusion rather than through volume diffusion because the solubility of chromium in cementite is limited. However, the  $M_7C_3$  carbide growth needs to compete for carbon with the rice-like cementite growth. If the rice-like cementite keeps growing,

the flux of carbon toward cementite should be much greater than that of chromium because the growth of supersaturated cementite will slow down and  $M_7C_3$  carbides will precipitate instead of cementites.



There are strong driving forces for carbon diffusion away from the ferrite/cementite interface to the ferrite/ $M_7C_3$  interfaces. Thus it is expected that cementite particles will be rapidly dissolved in the vicinity of alloy carbides. If only alloy carbides exist, the driving force for chromium diffusion is rather small, and it will take much longer to complete the  $M_7C_3$  carbide dissolution. This reaction is diffusion controlled, and the kinetics of martensite decomposition changes from carbon diffusion to chromium diffusion controlled.

The possible diffusion directions of carbon and chromium atoms according to the driving forces are shown schematically in Figure 5-15. When cementite precipitates in this reaction, the difference in carbon activity between the  $\alpha/M_3C$  interface and the bulk martensite acts as a driving force for carbon diffusion (Figure 5-15(a)). With the diffusion of carbon, there is also a strong driving force for chromium diffusion towards the surface of cementite particles. In this case, chromium atoms can be supplied by interface diffusion rather than by volume diffusion. In order to allow for the growth of rice-like cementites, the flux of carbon toward cementite should be much greater than that of chromium because the growth of supersaturated cementites will slow down and

eventually stop, or alloy carbides will precipitate instead of cementites. Figure 5-15(c) shows schematically the possible directions for carbon and chromium diffusion due to the driving forces when all three types of carbides coexist. There are strong driving forces for carbon diffusion away from the  $\alpha/M_3C$  interface and toward the  $\alpha/M_7C_3$  and  $\alpha/M_{23}C_6$  interfaces. Thus it is expected that cementite particles will be rapidly dissolved in the vicinity of alloy carbides[168].

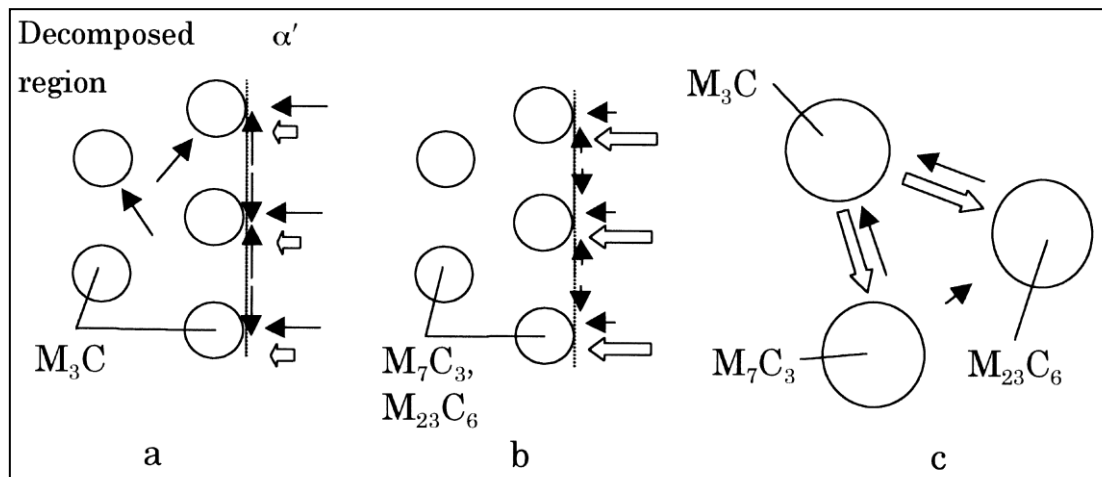
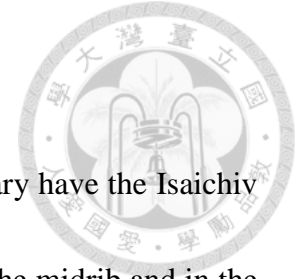


Figure 5-15 Possible diffusion directions of carbon (white arrows) and chromium (black arrows) atoms (schematic) as a result of the driving forces which exist when (a), (b) various carbides precipitate at the reaction front and (c) carbides coexist together as the reaction passes[168].

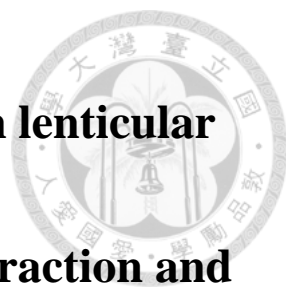
## 5.5 Conclusion



1. The observed cementites in the M/A interface and twin boundary have the Isaichi orientation relationship with the matrix, and the cementites in the midrib and in the twinned and untwinned regions follow the Bagaryatsky orientation relationship with the matrix.
2. During the tempering process, cementite precipitation first occurs at the M/A boundary and the twin boundary, then in the midrib and untwinned regions, and finally in the twinned region.
3. The cementite precipitation in tempered lenticular martensite is mainly influenced by the diffusivity of solute carbon atoms, which have the fastest diffusion rate. While those precipitate at the twin boundary in the twinned region, the high carbon concentration gradients cause a needle-like morphology and tend to stay in the  $\text{Fe}_3\text{C}$  structure. It is the paraequilibrium (PE) mode. The needle-like cementite will not transform into  $\text{M}_7\text{C}_3$  carbides, and they remain the same size after longer tempering treatment.
4. In contrast, the cementites precipitate at the midrib, in the untwinned region, and in the twinned region by the partitioning local equilibrium (PLE) mode, which is governed by the slowest diffusing species (substitutional element). The cementite, which is usually rice-shaped, then transforms into  $\text{M}_7\text{C}_3$  carbides with longer

tempering treatment. The  $M_7C_3$  carbides and the matrix have the OR-I orientation relationship.





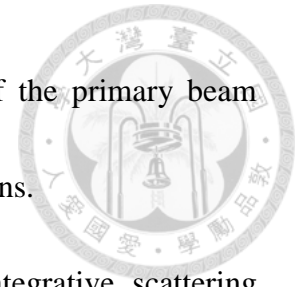
# **Chapter 6    The misorientation change in lenticular martensite by Electron Backscattered Diffraction and Convergent Beam Kikuchi Line Diffraction Pattern**

## **6.1 Introduction**

In this study, the two techniques, Convergent Beam Kikuchi Line Diffraction Patterns (CBKLDP) in TEM and Electron Backscatter Diffraction (EBSD), are used to investigate the crystal orientation relationships in lenticular martensite. These two techniques can provide information on different aspects of the crystal orientation and provide more details of the crystallography. The Kikuchi pattern of crystal is the core knowledge of the two techniques. Backscatter or reflection Kikuchi patterns were observed shortly after the discovery of Transmission Kikuchi Patterns (TKP) by Kikuchi and Nishikawa, who also gave the correct geometrical interpretation of these patterns[169]. In 1983, H. O. Martikainen proposed that with the application of TKP in TEM, crystal structures could be analyzed in greater detail[170]. The EBSD technique in SEM was also applied to investigate the crystal structure with Backscatter Kikuchi Pattern (BKP) images. Phenomenologically, the formation of BKPs is described, like



TKP, as a two-step process consisting of incoherent scattering of the primary beam electrons followed by elastic and coherent scattering of these electrons.



Kikuchi lines are mainly formed by electron beam non-integrative scattering (incoherent scattering), which belongs to elastic collision, and other electronic integrated scattering (coherent scattering). The incoherent scattering process produces electrons travelling in a wide range of directions. These electrons may be considered to stem from a very small volume inside of the crystal. According to Bragg's law, the locus of electrons being diffracted from such a small electron source is pairs of cones with a large opening angle of  $180^\circ - 2\theta$  and the cone axis perpendicular to the diffracting lattice planes, where  $\theta$  is the Bragg angle, as shown in Figure 5-1. These cones cut an observation plane that is positioned tangential to the propagation sphere of the electrons in almost straight and parallel pairs of lines, the Kikuchi lines [171-174].

However, the application of Kikuchi patterns in TEM is limited by the sample preparation, which must be conducted carefully to produce samples of appropriate thickness and size. Therefore, having less of a limitation, the application in SEM, EBSD, is widely used in material research such as metallurgy[31, 175, 176], ceramics[177-179], and geology[180, 181]. EBSD is well-established as a powerful tool for analyzing microstructure and crystallography.

Characterizing small grains or sub-grains and determining the orientation

distribution of microstructures require a combination of good spatial and angular resolution with appropriate operating conditions, and images also need to be acquired at a reasonable rate to avoid sample damage. Thus, the limits of EBSD should be considered further.

Field emission gun SEM (FEGSEM) has been developed to improve the spatial resolution. Due to the high probe currents and the small diameter of the electron beam in FEGSEM, the resolution is quite high. This improvement in the spatial resolution can be obtained by lowering the accelerating voltage and using materials with a high atomic number[182]. Delphic[183, 184] reported that the excitation volume extends further in the longitudinal direction at a high accelerating voltage than at a low accelerating voltage. The area from which an EBSD pattern is acquired with an electron beam focused on a sample tilted  $70^\circ$  is approximately elliptical[185, 186]. The shape of the excitation volume is in the form of an ellipse at a high voltage and in that of a circle at a low voltage. A small excitation volume is achieved by lowering the acceleration voltage. However, it is necessary to consider that contamination can degrade the quality of the Kikuchi pattern, especially at low voltage.

There is a range of beam currents over which the spatial resolution of EBSD is optimized. If the current is too small, the pattern quality is degraded, thereby worsening the spatial resolution. In contrast, a beam current that is too large will increase the beam

spread and thereby degrade the resolution[187, 188].

The best spatial resolution does not occur with the smallest probe currents, which correspond to the smallest probe sizes. A small probe has a small interaction volume with the sample and will give the best absolute resolution. However, measurement of the effective resolution is in part determined by the ability of the software to successfully discriminate between overlapping diffraction patterns, which will increase as the quality of the patterns improves with larger probe currents. The best spatial resolution is thus obtained for a probe size that is a compromise between pattern quality and absolute resolution[189].

The relative angular resolution may be measured by obtaining data points from a single crystal. The points can be collected whilst the beam or stage is scanned in a line or raster, or even when the beam is stationary, although the latter procedure may lead to surface contamination. From the data, the orientations of successive points are compared, and the apparent misorientation from within a single grain gives a measure of the relative precision of orientation determination. It is typically found that the “orientation noise” is about 1°. The orientation noise is very sensitive to the probe current and accelerating voltages. The main effect of the probe current is on the pattern quality, and the increase in the relative orientation resolution as the probe current increases corresponds to an increase in the quality of the diffraction patterns. The

angular resolution improves at higher accelerating voltage, and the reason is thought to be that the positions of the narrower Kikuchi bands can be determined more accurately[189-192].



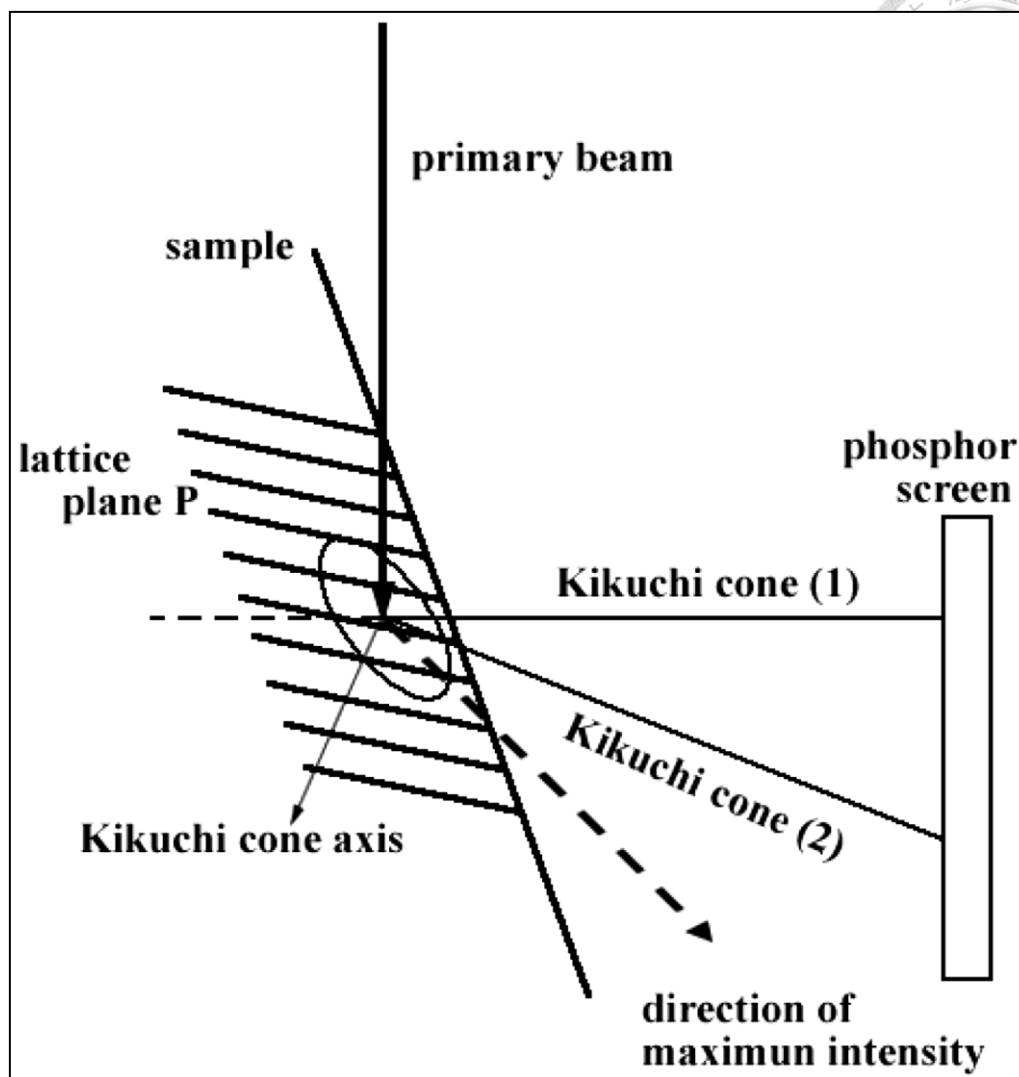


Figure 6-1 Scheme of backscatter Kikuchi pattern formation: The primary beam enters the sample at the angle  $\alpha$ . It travels a distance  $r/\cos \alpha$  inside of the material until it has reached a maximum depth  $d$  below the surface;  $r$  indicates the approximate spatial resolution of the technique. On its way, more and more primary electrons are incoherently scattered with an intensity distribution indicated by the ellipsis. The incoherently scattered electrons are subsequently coherently scattered by the lattice planes  $p$  into pairs of Kikuchi cones (1) and (2) with an opening angle  $2(90^\circ - 2\theta)$  around the cone axis. The cones leave the surface at approximately the angle  $\beta$ . The path length on which electrons undergo coherent scattering is therefore  $t = d/\sin\beta$ . For  $\beta = \alpha$ , maximum electron intensity is obtained[171].

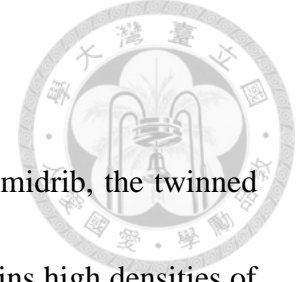
## 6.2 Experimental Procedure

The as-received material was a commercially wrought AISI 440C stainless steel bar (with a diameter of 122 mm). The chemical composition of this steel is Fe–1.0C–17.4Cr–0.45Mo–0.40Mn–0.38Si–0.40Ni (wt.%). The pieces of steel rod were machined from the half radius position of the original bar and then homogenized at 1200°C for 3 days in quartz capsules containing pure argon. After that, the specimens were quenched in liquid nitrogen (-196°C) for 15 min to obtain lenticular martensite.

TEM and EBSD samples were sliced from the rod specimens, thinned to 0.08mm by abrasion with SiC papers, and twin-jet electro-polished using a mixture of 5% perchloric acid, 25% glycerol, and 70% ethanol at 5~10°C with 45~55V polishing potential. The EBSD measurement was carried out with a FEI NOVA 450 operated at 20 kV. The orientation measurement and analysis were done with TSL-OIM software.

Misorientation angles were studied using convergent beam Kikuchi line diffraction patterns (CBKLDPs). The patterns were acquired using a Tecnai G<sup>2</sup> F30 FEG-STEM equipped with a Gatan 2001 energy filter, operated in STEM mode. In current experimental setting, the electron probe was measured to be < 1 nm, and the convergence angle  $2\alpha$  was 33.7 mrad.

## 6.3 Results and Discussion



The lenticular martensite structure includes three regions: the midrib, the twinned region, and the untwinned region (Figure 6-2 (a)). The midrib contains high densities of transformation twins holding a near G-T OR with austenite. The untwinned region contains a high density of dislocations and displays a close K-S OR with the austenite across the M/A interface. This difference indicates that the orientation relationship of lenticular martensite changes from the G-T OR to the K-S OR during growth. In other words, the orientation within a given lenticular martensite changes gradually by about  $3^\circ$  between the midrib and untwinned region near the M/A interface[15, 21, 23, 64, 65].

### 6.3.1 Convergent beam Kikuchi line diffraction patterns (CBKLDP)

In this study, convergent beam Kikuchi line diffraction patterns (CBKLDP) were used to measure the misorientation in lenticular martensite. The advantages of this technique are high angular precision, typically  $< 0.5^\circ$  [113, 193, 194], and high spatial resolution, determined by electron probe size ( $< 1$  nm). Therefore, CBKLDP is suitable for the current study. Figure 6-2 (a) shows a typical lenticular martensite, and the 10 marked points denote the positions where CBKLDPs were acquired, as shown in Figure 6-2 (b) to (g). The Kikuchi line pairs, identified as  $\bar{1}21$  and  $310$ , are marked using dashed lines; the region of interest is therefore close to a high index  $[\bar{1}3\bar{7}]$  zone. In

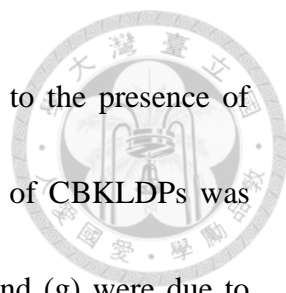


Figure 6-2 (b), the quality of CBKLDP was heavily degraded due to the presence of high residual strain, and away from the midrib region, the quality of CBKLDPs was slightly better. The rather blurred Kikuchi lines in Figure 6-2 (f) and (g) were due to thinner specimen thickness. From Figure 6-2 (b) to (g), misorientation from the midrib to untwinned region was clearly manifested by simply monitoring the shift in Kikuchi lines. Gradual change in the crystal orientation was observed. The misorientation angle between point (b) and point (g) was calculated to be 3.13°, moving from the left side to the right side as the collection area moved from the midrib region to the untwinned region, as shown in Figure 6-2. This finding was in accord with previous EBSD results.

To calculate the misorientation angles using convergent beam Kikuchi line diffraction patterns (CBKLDPs), in the current research, we adopted the method proposed by Martikainen [170]. In this method, the true zone  $\mathbf{p}$  can be calculated using the following equation:

$$\mathbf{p} = \mathbf{z} \cos \theta + \mathbf{g}_1 \times \mathbf{z} \sin \theta_2 \cos \theta_1 + \mathbf{g}_1 \sin \theta_1$$

where  $\mathbf{z}$  is the nearby zone axis,  $\mathbf{g}_1$  is the g-vector of the chosen Kikuchi lines,  $\theta$  is the measured angle between  $\mathbf{z}$  and  $\mathbf{p}$ , and  $\theta_2$  and  $\theta_1$  are the components of  $\theta$  and are respectively perpendicular and parallel to  $\mathbf{g}_1$ .



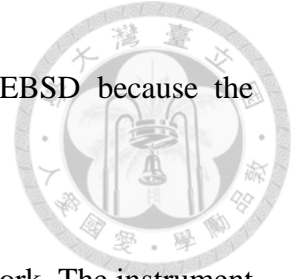
### 6.3.2 Electron Backscatter Diffraction (EBSD)



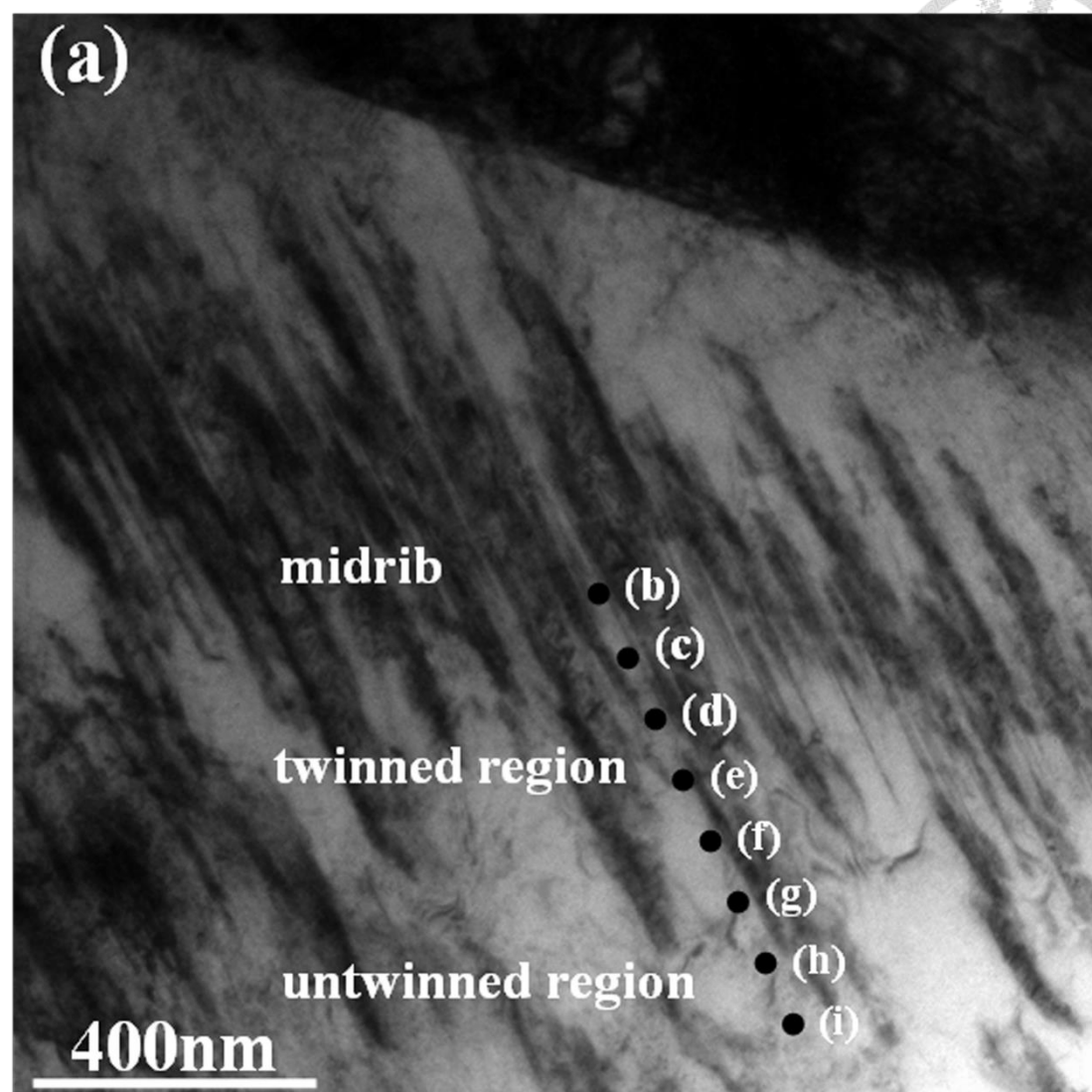
During an Electron Backscatter Diffraction (EBSD) experiment, the sample needs to be tilted approximately  $70^\circ$  towards the detector to provide the best resolution. However, this operation will cause a distorted interaction volume, whose cross-section in the sample surface is elliptical (1:3 in x-y axes). Thus, an effective way to obtain a better resolution of the twinning structure is to choose a lenticular martensite grain parallel to the horizontal axis. Figure 6-4(a) shows the IPF map of lenticular martensite in AISI 440C steel. Figure 6-4(b) shows the misorientation profile across the martensite from one side to the other side (as indicated by the arrow). The orientations inside the lenticular martensite in Figure 6-4 continuously change along the arrow direction, which covers a total misorientation of up to about  $3^\circ$  across a distance of  $2.5\ \mu\text{m}$ . The misorientation from the midrib region exceeds  $3^\circ$  at the M/A interface. The local orientations of the midrib and the twinned region are almost the same; the orientation changes gradually in the vicinity of the M/A interface.

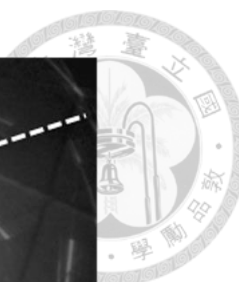
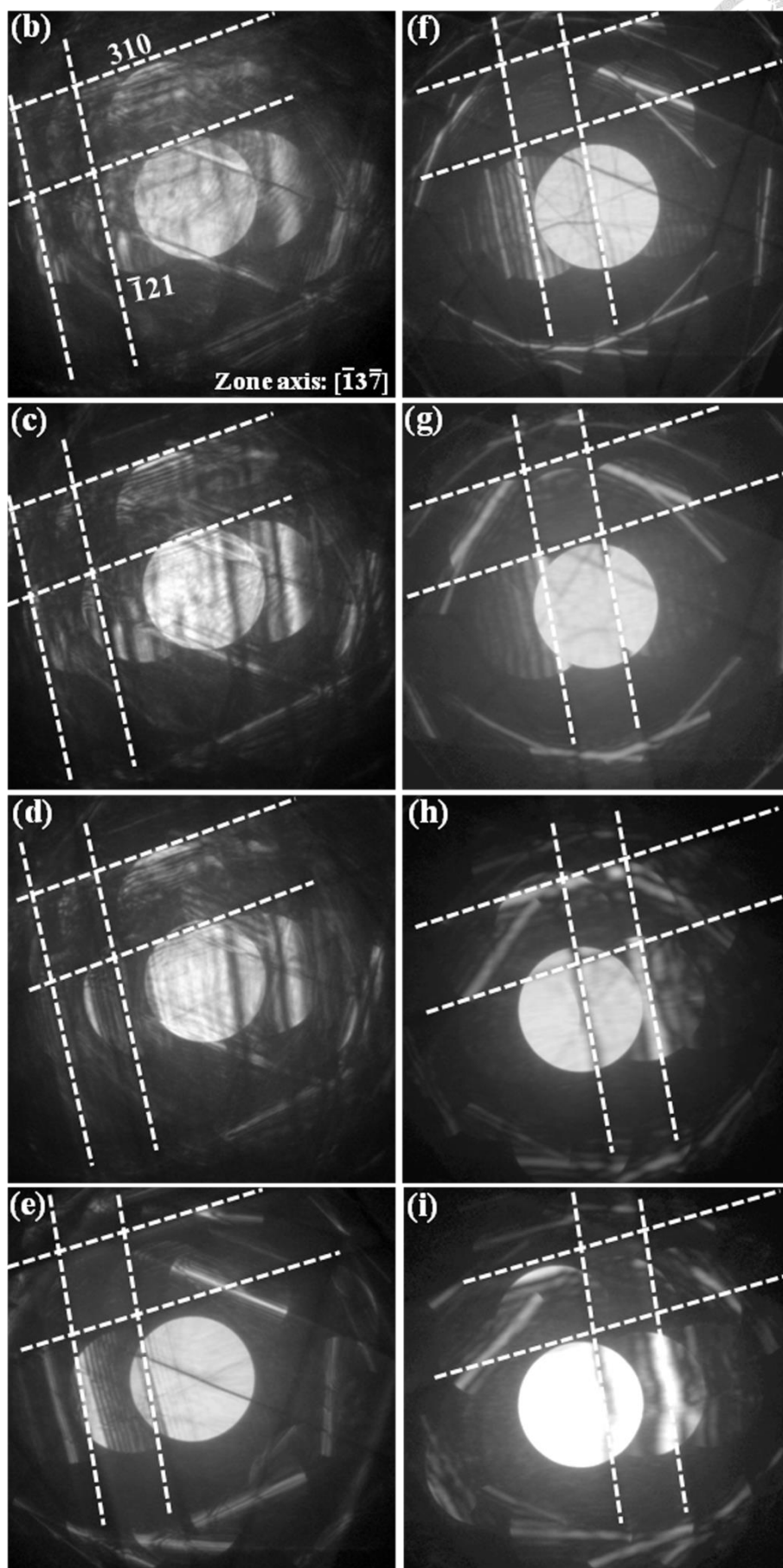
For EBSD, the sample needs to be tilted to a high angle, typically  $70^\circ$  from horizontal, and the spatial resolution is approximately three times worse low on the tilted surface. The projection of the electron beam on the sample changes from a circle to an ellipse, which deteriorates the spatial resolution. This is the reason why the twinning in the midrib cannot be clearly shown in the collected data (Figure 6-4). In

addition, the nano-sized twinning structure is hard to detect in EBSD because the misorientation changes in the nanometer range.



The precision of our EBSD was also examined in the present work. The instrument manual suggests that the angular precision of the EBSD procedure used here is about  $1^\circ$ . A set-up entirely the same as that in the above experimental condition was used to examine a Si plate (single grain). The result produced a measure of the relative precision of orientation determination. It is typically found that the “orientation noise” is  $\sim 0.5^\circ$ . Therefore, the above data, which show the misorientation in lenticular martensite changing within a range of  $3^\circ$ , is a reliable result.





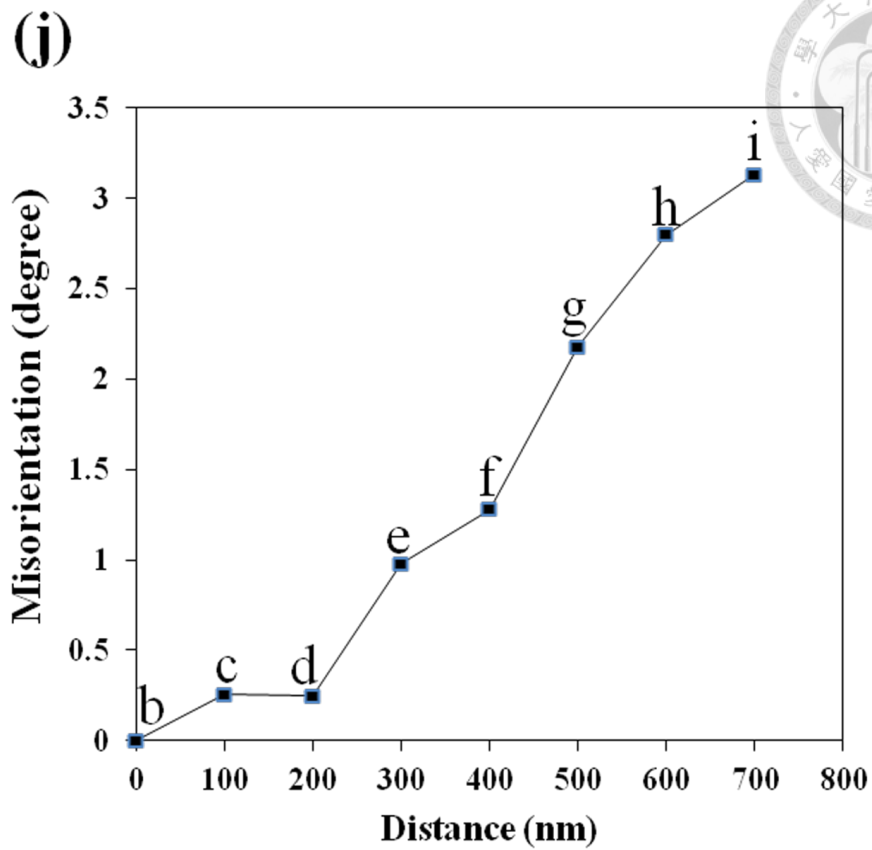


Figure 6-2 (a) TEM image showing the substructures of a lenticular martensite plate; convergent beam Kikuchi line diffraction patterns (CBKLDLP) taken from (b-c) midrib region, (d-f) extended twinned region, and (g-i) untwinned region; (j) misorientation profile indicating that a given lenticular martensite plate changes gradually from the midrib region, reaching about  $3^\circ$  at the martensite/austenite interface.

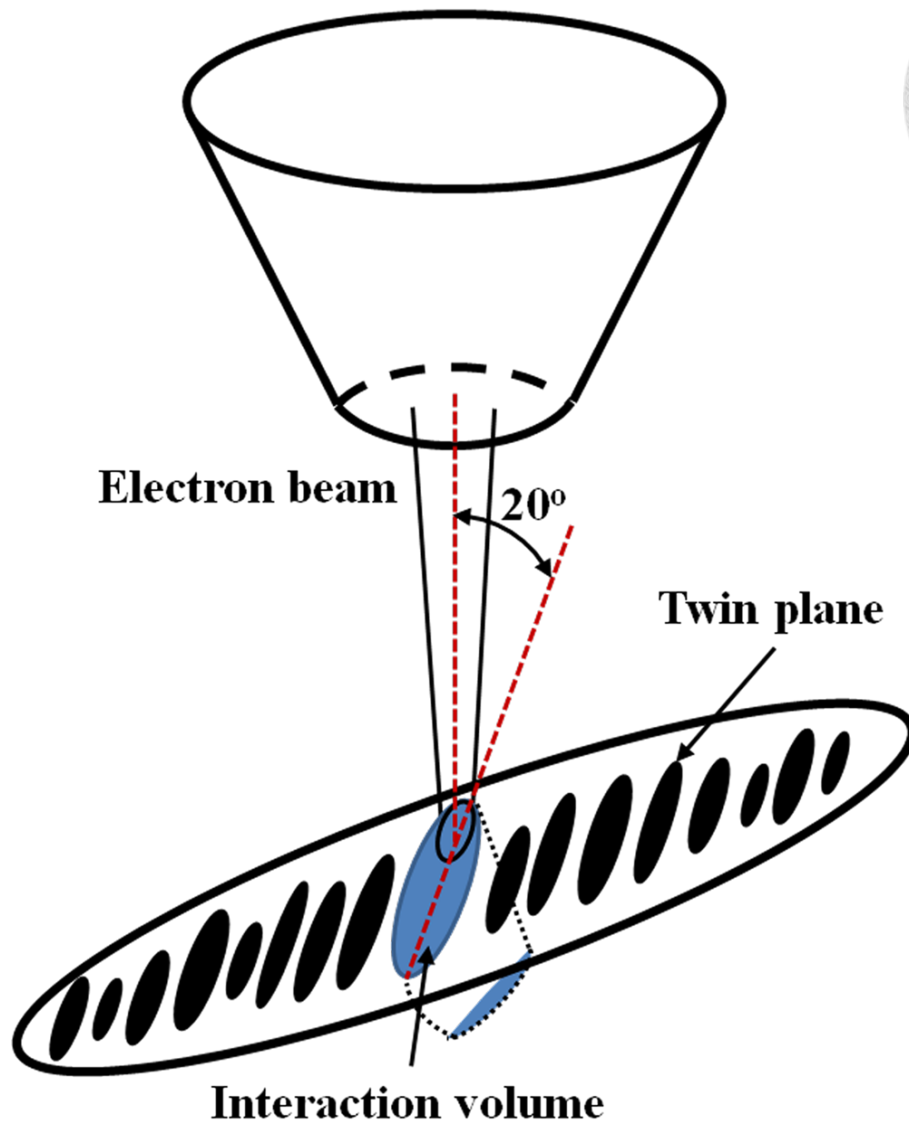


Figure 6-3 Interaction volume of the electron beam with the lenticular martensite

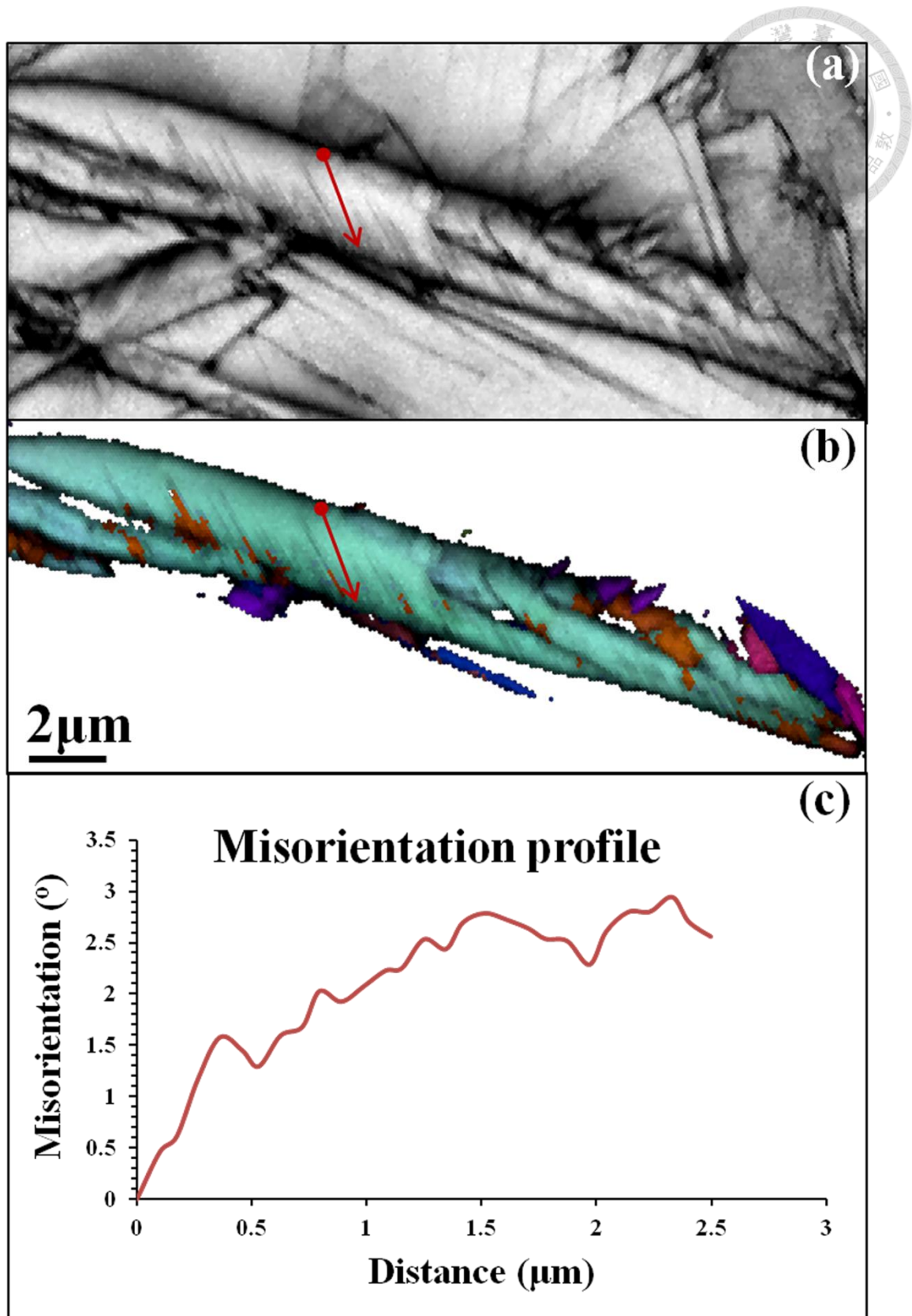


Figure 6-4 (a) and (b) show the PQ and IPF map of lenticular martensite in AISI 440C steel; (c) shows the misorientation profile across the martensite from one side to the other side (as the arrow indicates).



## 6.4 Conclusions

1. Comparison of two different crystal orientation analysis techniques (EBSD vs. CBKLDP)

Table 6-1 Comparison of crystal orientation analysis techniques

EBSD		CBKLDP
Sample preparation	Sample surface polishing	TEM sample (sufficiently thick)
Scanning area	Only limited by the flatness of sample surface	The vicinity of a hole edge in a twin-jet sample (with proper thickness)
Analysis process	Rapid and automated acquisition and analysis of the diffraction patterns	Manual computation, slow
Spatial resolution	20-200 nm	> 5 nm
Angular resolution	1° or better	0.5° or better

2. Analysis with EBSD and CBKLDP shows that in a lenticular martensite grain, the misorientation changes in different regions, and the range of this variation is about 3°.



## Chapter 7 General conclusion



In this work, an AISI 440C stainless steel was used to study the structure and transformation of martensite. The applied austenitization temperature is the critical factor for controlling the transformation process, which is deeply influenced by the solution degree of prior  $M_7C_3$  carbides in the matrix. In a highly austenitized sample, the  $M_s$  temperature is low, and after deep cryogenic treatment, thin plate martensite and lenticular martensite are transformed. In contrast, in a low austenitized sample, a higher  $M_s$  temperature induces the lath martensite structure. The aim of this present study was to investigate lenticular martensite, including its transformation, morphology, crystal orientation, and tempering behavior. The following conclusions can be drawn from the aforementioned experiments and divided into two parts:

### **The morphology and transformation of lenticular martensite**

1. At an appropriate austenitization temperature, a large lenticular martensite grain suitable for observation can be obtained. According to the TEM observation results, a lenticular martensite grain has 3 regions: the midrib, the twinned region, and the untwinned region. The midrib and twinned region are composed



of twins, and dislocations are distributed in the untwinned region. The Burgers vector of these dislocations was determined to be  $a/2[1\bar{1}1]$ .

2. From the macrostructure observation results, it is found that the twins in lenticular martensite have different lengths, and some of them are bent. This discrepancy is caused by the interference of each twin boundary during extension. Common techniques such as SEM and OM, which are based on 2-D observation, indicate that lenticular martensite has a long and thin leaf-like morphology. According to a model proposing that the growth and shape of lenticular martensite can be seen as wave propagation, it is assumed that the shape of lenticular martensite is a flat ellipsoid. In the present work, the focused ion beam technique was applied to examine this model in a mode of 3-D observation, and it was found that lenticular martensite is elliptical.
3. For a given coarse austenite grain with considerable variants of lenticular martensite, the pole figures indicate that the lenticular martensite in this steel approximately adopts a Kurdjumov-Sachs orientation relationship with respect to the austenite matrix. It has been clarified that the spread in diffracted intensity within pole figures is related to the misorientation gradient within the lenticular martensite plate. On the other hand, a given coarse austenite grain with a few variants of lenticular martensite was employed to analyze the orientation




relationships of the variant pairs of lenticular martensite plate. The results suggest that the coupling may be associated with variant selection.

4. The coupling results in three different morphologies of lenticular martensite: spear, kink, and zigzag array. In the research, it is noted that the zigzag array morphology may be composed of the spear type, which can be seen as a product of variant selection.
5. Analysis with EBSD and CBKLDP shows that in a lenticular martensite grain, the misorientation changes in different regions, and the range of this variation is about  $3^\circ$ .

### **The tempering behavior of lenticular martensite**

After  $400^\circ\text{C}$  tempering treatment, two kinds of cementite precipitated in the lenticular martensite matrix.


1. The needle-like cementite formed immediately after holding for 10 sec at  $400^\circ\text{C}$  and had the Isaichiv orientation relationship with the ferrite matrix. When the tempering time was extended to 25 hr, this cementite neither changed its shape nor transformed into alloy carbides. The formation mechanism of this needle-like cementite is the paraequilibrium (PE) mode. This process is involved only in the diffusion of carbon. Only a single variant of cementite.

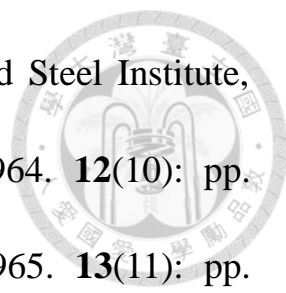
- 
2. After 1 min of holding at 400°C, rice-like cementite precipitated first at the midrib and then precipitated in the twinned and untwinned regions with longer tempering time. The rice-like cementite had a Bagaryatski orientation relationship with the ferrite matrix. When the sample was tempered for a longer time (>60 min), the rice-like cementites gradually accumulated and turned into sphere-like cementite particles. This is the partitioning local equilibrium (PLE) mode.
  3. Tempering treatment of longer than 60 min led to the transformation of cementites into  $M_7C_3$  carbides, which are parallelogram shaped.  $M_7C_3$  carbides retained the OR-I with the ferrite matrix. The OR-I relation to the matrix is close to the Dyson and Andrews OR. In conclusion, the growth and formation mechanism of rice-like carbides can be taken as a kind of diffusive transformation.


## References



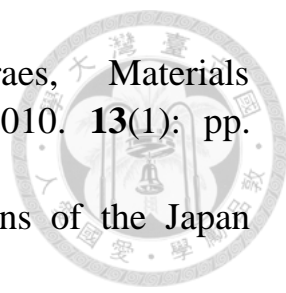
1. *ASM Handbook Volume 9: Metallography and Microstructures*, ed. G. F. V. Voort, 2004, ASM International. pp. 165-178.
2. G. Krauss, *Principles of Heat Treatment of Steel*, 1980, American Society for Metals. pp. 43-77.
3. K. Shimizu and T. Kakeshita, *Isij International*, 1989. **29**(2): pp. 97-116.
4. A. R. Marder and G. Krauss, *Asm Transactions Quarterly*, 1967. **60**(4): pp. 651-660.
5. K. W. Andrews, *Journal of the Iron and Steel Institute*, 1965. **203**: pp. 721-727.
6. T. N. Durlu, *Journal of Materials Science Letters*, 1992. **11**(10): pp. 702-705.
7. T. N. Durlu, *Journal of Materials Science*, 1999. **34**(12): pp. 2887-2890.
8. V. Shrinivas, S. K. Varma, and L. E. Murr, *Metallurgical and Materials Transactions A*, 1995. **26**(3): pp. 661-671.
9. T. Kakeshita, J. Katsuyama, T. Fukuda and T. Saburi, *Materials Science and Engineering A*, 2001. **312**(1-2): pp. 219-226.
10. S. Kajiwara, *Materials Transactions Jim*, 1992. **33**(11): p. 1027-1034.
11. Z. Nishiyama, *Transformation Temperature and Rate of Martensite Formation*, in *Martensitic Transformation*, ed. M. E. Fine, M. Meshii, et al., 1978, Academic Press. pp. 211-262.
12. M. Guener, E. Gueler, and H. Aktas, *Materials Characterization*, 2008. **59**(4): pp. 498-502.
13. Z. Nishiyama, *Crystallography of Martensite (General)*, in *Martensitic Transformation*, ed. M. E. Fine, M. Meshii, et al., 1978, Academic Press. pp. 14-134.
14. H. Kitahara, R. Ueji, M. Ueda, et al., *Materials Characterization*, 2005. **54**(4-5): pp. 378-386.
15. H. Sato and S. Zaefferer, *Acta Materialia*, 2009. **57**(6): pp. 1931-1937.
16. M. Umemoto, E. Yoshitake, and I. Tamura, *Journal of Materials Science*, 1983. **18**(10): pp. 2893-2904.
17. T. Maki. *Microstructure and mechanical behaviour of ferrous*

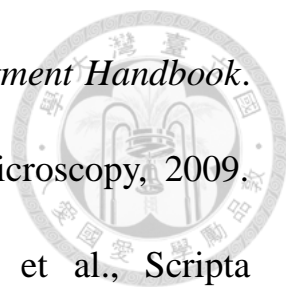
- 
- martensite*. in *Materials Science Forum*. 1991. Trans Tech Publ.
18. M. Umemoto, T. Hyodo, T. Maeda and I. Tamura, *Acta Metallurgica*, 1984. **32**(8): pp. 1191-1203.
  19. X. M. Zhang, E. Gautier, and A. Simon, *Acta Metallurgica*, 1989. **37**(2): pp. 477-485.
  20. X. M. Zhang, E. Gautier, and A. Simon, *Acta Metallurgica*, 1989. **37**(2): pp. 487-497.
  21. A. Shibata, S. Morito, T. Furuhashi, et al., *Scripta Materialia*, 2005. **53**(5): pp. 597-602.
  22. Z. Nishiyama and K. Shimizu, *Acta Metallurgica*, 1961. **9**(10): pp. 980-981.
  23. H. Sato, S. Zaefferer, and Y. Watanabe, *Isij International*, 2009. **49**(11): pp. 1784-1791.
  24. B. C. Muddle and J. F. Nie, *Martensite*, in *Encyclopedia of Materials: Science and Technology (Second Edition)*, ed. K. H. J. Buschow, R. W. Cahn, et al., 2001, Elsevier. pp. 5189-5193.
  25. H. K. D. H. Bhadeshia, *Martensitic Transformation*, in *Encyclopedia of Materials: Science and Technology (Second Edition)*, ed. K. H. J. Buschow, R. W. Cahn, et al., 2001, Elsevier. pp. 5203-5206.
  26. H. K. D. H. Bhadeshia, *Worked examples in the Geometry of Crystals*. second ed, 2006, Institute of Materials.
  27. C. M. Wayman, *Metallurgical and Materials Transactions A-Physical Metallurgy and Materials Science*, 1994. **25**(9): pp. 1787-1795.
  28. H. K. D. H. Bhadeshia and R. W. K. Honeycombe, *Formation of martensite*, in *Steels : microstructure and properties*, 2006, Elsevier, Butterworth-Heinemann.
  29. A. Stormvinter, P. Hedström, and A. Borgenstam, *Solid State Phenomena*, 2011. **172-174**: pp. 61-66.
  30. K. Shimizu, C. M. Wayman, O. Johari, et al., *Acta Metallurgica*, 1966. **14**(10): pp. 1390-1391.
  31. S. Morito, H. Tanaka, R. Konishi, et al., *Acta Materialia*, 2003. **51**(6): pp. 1789-1799.
  32. H. Kitahara, R. Ueki, N. Tsuji, et al., *Acta Materialia*, 2006. **54**(5): pp. 1279-1288.
  33. B. P. J. Sandvik and C. M. Wayman, *Metallurgical Transactions A*, 1983. **14**(5): pp. 809-822.
  34. S. Morito, X. Huang, T. Furuhashi, et al., *Acta Materialia*, 2006. **54**(19): pp. 5323-5331.

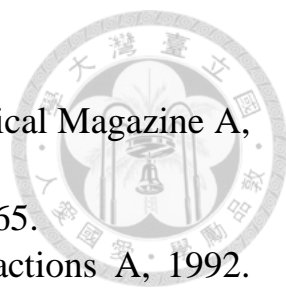
- 
35. P. M. Kelly and J. Nutting, *Journal of the Iron and Steel Institute*, 1961. **197**: pp. 199.
  36. O. Johari and G. Thomas, *Acta Metallurgica*, 1964. **12**(10): pp. 1153-1159.
  37. O. Johari and G. Thomas, *Acta Metallurgica*, 1965. **13**(11): pp. 1211-1212.
  38. T. Maki, S. Shimooka, S. Fujiwara and I. Tamura, *Transactions of the Japan Institute of Metals*, 1975. **16**(1): pp. 35-41.
  39. D. P. Dunne and C. M. Wayman, *Metallurgical Transactions*, 1973. **4**(1): pp. 147-152.
  40. T. Maki, S. Shimooka, T. Arimoto, et al., *Transactions of the Japan Institute of Metals*, 1973. **14**(1): pp. 62-67.
  41. K. Shimizu, M. Oka, and C. M. Wayman, *Acta Metallurgica*, 1970. **18**(9): pp. 1005-1011.
  42. E. O. Fearon and M. Bevis, *Acta Metallurgica*, 1974. **22**(8): pp. 991-1002.
  43. K. A. Taylor, G. B. Olson, M. Cohen, et al., *Metallurgical Transactions A*, 1989. **20**(12): pp. 2739-2747.
  44. A. Stormvinter, P. Hedstrom, and A. Borgenstam, *Journal of Materials Science & Technology*, 2013. **29**(4): pp. 373-379.
  45. P. C. Rowlands, E. O. Fearon, and M. Bevis, *Journal of Materials Science*, 1970. **5**(9): pp. 769-776.
  46. H. J. Neuhauser and W. Pitsch, *Acta Metallurgica*, 1971. **19**(4): pp. 337-344.
  47. T. Kakeshita, K. Shimizu, T. Maki, et al., *Scripta Metallurgica*, 1980. **14**(10): pp. 1067-1070.
  48. A. Shibata, T. Murakami, S. Morito, et al., *Materials Transactions*, 2008. **49**(6): pp. 1242-1248.
  49. R. L. Patterson and C. M. Wayman, *Acta Metallurgica*, 1964. **12**(11): pp. 1306-1311.
  50. T. Maki and C. M. Wayman, *Acta Metallurgica*, 1977. **25**(6): pp. 695-710.
  51. K. Shimizu, M. Oka, and C. M. Wayman, *Acta Metallurgica*, 1971. **19**(1): pp. 1-6.
  52. M. Dechamps and L. M. Brown, *Acta Metallurgica*, 1979. **27**(7): pp. 1281-1291.
  53. T. Maki and C. M. Wayman, *Acta Metallurgica*, 1977. **25**(6): pp. 681-693.

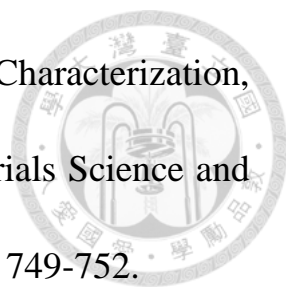
- 
54. M. A. Meyers, *Acta Metallurgica*, 1980. **28**(6): pp. 757-770.
  55. H.-Y. Lee, H.-W. Yen, H.-T. Chang, et al., *Scripta Materialia*, 2010. **62**(9): pp. 670-673.
  56. R. L. Patterso and C. M. Wayman, *Acta Metallurgica*, 1966. **14**(3): pp. 347-369.
  57. M. Umemoto, K. Minoda, and I. Tamura, *Metallography*, 1982. **15**(2): pp. 177-191.
  58. T. Maki, S. Shimooka, M. Umemoto, et al., *Transactions of the Japan Institute of Metals*, 1972. **13**(6): pp. 400-407.
  59. R. P. Reed, *Acta Metallurgica*, 1967. **15**(8): pp. 1287-1296.
  60. E. Guler, T. Kirindi, and H. Aktas, *Journal of Alloys and Compounds*, 2007. **440**(1-2): pp. 168-172.
  61. A. Shibata, H. Yonezawa, K. Yabuuchi, et al., *Materials Science and Engineering A*, 2006. **438**: pp. 241-245.
  62. A. Shibata, S. Morito, T. Furuhashi, et al., *Acta Materialia*, 2009. **57**(2): pp. 483-492.
  63. A. Shibata, T. Furuhashi, and T. Maki, *Acta Materialia*, 2010. **58**(9): pp. 3477-3492.
  64. G. Miyamoto, A. Shibata, T. Maki, et al., *Acta Materialia*, 2009. **57**(4): pp. 1120-1131.
  65. A. Shibata, H. Jafarian, and N. Tsuji, *Materials Transactions*, 2012. **53**(1): pp. 81-86.
  66. L. Zhang, T. Ohmura, A. Shibata, et al., *Materials Science and Engineering A*, 2010. **527**(7-8): pp. 1869-1874.
  67. X. M. Zhang, X. Zhao, J. X. Zhong, et al., *Scripta Metallurgica Et Materialia*, 1990. **24**(10): pp. 1953-1958.
  68. H. K. D. H. Bhadeshia, *Bainite in steels : transformations, microstructure and properties*, 2001, IOM Communications. pp. 42-44.
  69. H. K. D. H. Bhadeshia, *Journal of Materials Science*, 1982. **17**(2): pp. 383-386.
  70. C. L. Magee, *Phase Transformations*, ASM Seminar. p. 115.
  71. J. C. Bokros and E. R. Parker, *Acta Metallurgica*, 1963. **11**(12): pp. 1291-1301.
  72. R. M. Brito, R. B. C. Dasilva, and Guimarae.Jr, *Scripta Metallurgica*, 1974. **8**(5): pp. 527-532.
  73. D. R. Wollmann and Guimarae.Jr, *Scripta Metallurgica*, 1973. **7**(4): pp. 355-359.

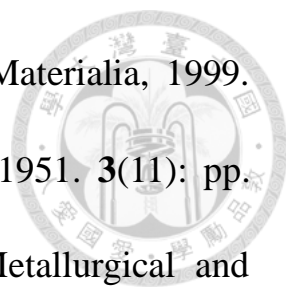


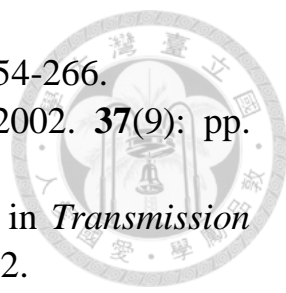
- 
74. P. R. Rios and J. R. Costa Guimaraes, Materials Research-Ibero-American Journal of Materials, 2010. **13**(1): pp. 119-124.
  75. H. Okamoto, M. Oka, and I. Tamura, Transactions of the Japan Institute of Metals, 1978. **19**(12): pp. 674-684.
  76. M. Umemoto and C. M. Wayman, Acta Metallurgica, 1978. **26**(10): pp. 1529-1549.
  77. Y. Liu and J. Pietikainen, Scripta Metallurgica Et Materialia, 1992. **27**(7): pp. 887-892.
  78. M. G. H. Wells, Acta Metallurgica, 1964. **12**(4): pp. 389-399.
  79. G. R. Speich and W. C. Leslie, Metallurgical Transactions, 1972. **3**(5): pp. 1043-1054.
  80. F. H. Samuel and A. A. Hussein, Materials Science and Engineering, 1983. **58**(1): pp. 113-120.
  81. F. H. Samuel and A. A. Hussein, Metallography, 1982. **15**(4): pp. 391-408.
  82. R. N. Caron and G. Krauss, Metallurgical Transactions, 1972. **3**(9): pp. 2381-2389.
  83. A. J. Clarke, M. K. Miller, R. D. Field, et al., Acta Materialia, 2014. **77**: p. 17-27.
  84. Y. Ohmori and S. Sugisawa, Transactions of the Japan Institute of Metals, 1971. **12**(3): pp. 170-178.
  85. R. W. K. Honeycombe, *Structure and strength of alloy steels*, 1975, Climax Molybdenum Co. Ltd. pp. 7-10.
  86. A. K. Seal and R. W. K. Honeycombe, J. of the Iron and Steel Institute, 1958. **188**: pp. 343-350.
  87. M. Tanino and K. Aoki, Transactions of the Iron and Steel Institute of Japan, 1968. **8**(5): pp. 337.
  88. D. H. Jack and K. H. Jack, Materials Science and Engineering, 1973. **11**(1): pp. 1-27.
  89. C. B. Ma, T. Ando, D. L. Williamson, et al., Metallurgical Transactions A, 1983. **14**(6): pp. 1033-1045.
  90. S. Nagakura, T. Suzuki, and M. Kusunoki, Transactions of the Japan Institute of Metals, 1981. **22**(10): pp. 699-709.
  91. P. V. Morra, A. J. Bottger, and E. J. Mittemeijer, Journal of Thermal Analysis and Calorimetry, 2001. **64**(3): pp. 905-914.
  92. C. Zhu, X. Y. Xiong, A. Cerezo, et al., Ultramicroscopy, 2007. **107**(9): pp. 808-812.

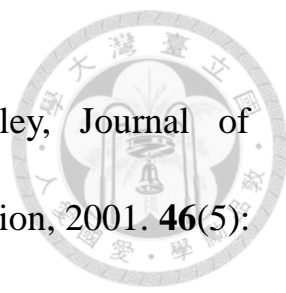
- 
93. G. E. Totten and M. A. H. Howes, *Steel Heat Treatment Handbook*. Second Edition ed, 2006, CRC Press. pp. 1-45.
  94. C. Zhu, A. Cerezo, and G. D. W. Smith, *Ultramicroscopy*, 2009. **109**(5): pp. 545-552.
  95. S. J. Barnard, G. D. W. Smith, M. Sarikaya, et al., *Scripta Metallurgica*, 1981. **15**(4): pp. 387-392.
  96. Y. Ohmori and I. Tamura, *Metallurgical Transactions a-Physical Metallurgy and Materials Science*, 1992. **23**(8): pp. 2147-2158.
  97. G. V. Kurdjumo and A. G. Khachatu, *Metallurgical Transactions*, 1972. **3**(5): pp. 1069.
  98. S. Nagakura, Y. Hirotsu, M. Kusunoki, et al., *Metallurgical Transactions a*, 1983. **14**(6): pp. 1025-1031.
  99. M. J. VanGenderen, M. Isac, A. Bottger, et al., *Metallurgical and Materials Transactions A*, 1997. **28**(3): pp. 545-561.
  100. C. A. Wert, *Physical Review*, 1950. **79**(4): pp. 601-605.
  101. P. Schaaf, A. Kramer, S. Wiesen, et al., *Acta Metallurgica Et Materialia*, 1994. **42**(9): pp. 3077-3081.
  102. H. L. Yakel, *International Metals Reviews*, 1985. **30**(1): pp. 17-44.
  103. D. H. Jack, *Materials Science and Engineering*, 1974. **13**(1): pp. 19-27.
  104. C. J. Barton, *Acta Metallurgica*, 1969. **17**(8): pp. 1085-1093.
  105. Y. Hirotsu and S. Nagakura, *Acta Metallurgica*, 1972. **20**(4): pp. 645-655.
  106. Y. Ohmori, *Transactions of the Japan Institute of Metals*, 1972. **13**(2): pp. 119-127.
  107. E. J. Fasiska and G. A. Jeffrey, *Acta Crystallographica*, 1965. **19**: pp. 463.
  108. K. W. Andrews, *Acta Metallurgica*, 1963. **11**(8): p.p 939-946.
  109. I. V. Isaichev, *Zhurnal Tekhnicheskoi Fiziki*, 1947. **17**(7): pp. 835-838.
  110. Y. A. Bagaryatskii, *Doklady Akademii Nauk SSSR*, 1950. **73**: pp. 1161-1164.
  111. N. J. Petch, *Acta Crystallographica*, 1953. **6**(1): pp. 96-96.
  112. M. X. Zhang and P. M. Kelly, *Acta Materialia*, 1998. **46**(11): pp. 4081-4091.
  113. M. X. Zhang and P. M. Kelly, *Scripta Materialia*, 1997. **37**(12): pp. 2009-2015.
  114. A. Czarski, T. Skowronek, and W. Osuch, *Metallurgy and Foundry*

- 
- Engineering, 2007. **33**(1): pp. 41-49.
115. D. V. Shtansky, K. Nakai, and Y. Ohmori, Philosophical Magazine A, 1999. **79**(7): pp. 1655-1669.
  116. Y. Ohmori, Isij International, 2001. **41**(6): pp. 554-565.
  117. D. S. Zhou and G. J. Shiflet, Metallurgical Transactions A, 1992. **23**(4): pp. 1259-1269.
  118. Y. Ohmori, R. W. K. Honeycombe, and A. T. Davenport, Transactions of the Iron and Steel Institute of Japan, 1972. **12**(2): pp. 112-117.
  119. V. Krasevec, M. Macek, and J. Rodic, Acta Metallurgica, 1980. **28**(2): pp. 223-229.
  120. I. Tkalcec, C. Azcoitia, S. Crevoiserat, et al., Materials Science and Engineering A, 2004. **387**: pp. 352-356.
  121. D. J. Dyson and K. W. Andrews, Journal of the Iron and Steel Institute, 1969. **207**: pp. 208-217.
  122. J. P. Morniroli, E. Bauergrosse, and M. Gantois, Philosophical Magazine A, 1983. **48**(3): pp. 311-327.
  123. E. Bauergrosse, J. P. Morniroli, C. Frantz, et al., Journal De Physique, 1982. **43**(NC-9): pp. 285-288.
  124. M. Palcut, M. Vach, R. Cicka, et al., Archives of Metallurgy and Materials, 2008. **53**(4): pp. 1157-1164.
  125. K. H. Kuo and C. L. Jia, Acta Metallurgica, 1985. **33**(6): p. 991-996.
  126. P. R. Howell, J. V. Bee, and R. W. K. Honeycombe, Metallurgical Transactions A, 1979. **10**(9): pp. 1213-1222.
  127. R. C. Thomson, Materials Characterization, 2000. **44**(1-2): pp. 219-233.
  128. D. Raynor, J. A. Whiteman, and R. W. K. Honeycom, Journal of the Iron and Steel Institute, 1966. **204**: pp. 1114-1116.
  129. A. Inoue, S. Arakawa, and T. Masumoto, Transactions of the Japan Institute of Metals, 1978. **19**(1): pp. 11-17.
  130. A. Inoue and T. Masumoto, Metallurgical Transactions A, 1980. **11**(5): pp. 739-747.
  131. A. Inoue and T. Masumoto, Journal of the Japan Institute of Metals, 1978. **42**(8): pp. 787-795.
  132. D. Raynor, J. A. Whiteman, and R. W. K. Honeycom, Journal of the Iron and Steel Institute, 1966. **204**: p. 349-354.
  133. H. K. D. H. Bhadeshia and R. W. K. Honeycombe, *Steels : microstructure and properties*, 2006, Elsevier, Butterworth-Heinemann. pp. 183-208.

- 
134. D. W. Hetzner and W. Van Geertruyden, *Materials Characterization*, 2008. **59**(7): pp. 825-841.
  135. B. Miao, D. O. Northwood, L. C. Lim, et al., *Materials Science and Engineering A*, 1993. **171**(1-2): pp. 21-33.
  136. H. O. Andren, *Scripta Metallurgica*, 1981. **15**(7): pp. 749-752.
  137. T. Masumoto, S. Takeda, and Y. Imai, *Science Reports of the Research Institutes Tohoku University Series a-Physics Chemistry and Metallurgy*, 1970. **22**(1): pp. 34.
  138. M. S. Bhat, W. M. Garrison, and V. F. Zackay, *Materials Science and Engineering*, 1979. **41**(1): pp. 1-15.
  139. C. R. Simcoe and Nehrenbe.Ae, *Asm Transactions Quarterly*, 1965. **58**(3): pp. 378.
  140. B. R. Banerjee, *Journal of the Iron and Steel Institute*, 1965. **203**: pp. 166-174.
  141. G. Krauss, *Steels: Heat Treatment and Processing Principles*, 1990, ASM International. pp. 205-261.
  142. J. A. Peters, J. V. Bee, B. Kolk, et al., *Acta Metallurgica*, 1989. **37**(2): pp. 675-686.
  143. R. M. Horn and R. O. Ritchie, *Metallurgical Transactions A*, 1978. **9**(8): pp. 1039-1053.
  144. G. Krauss, *Martensite before and after Tempering, Deformation and Fracture of*, in *Encyclopedia of Materials: Science and Technology (Second Edition)*, ed. K. H. J. Buschow, R. W. Cahn, et al., 2001, Elsevier. pp. 5193-5197.
  145. M. Yaso, S. Hayashi, S. Morito, et al., *Materials Transactions*, 2009. **50**(2): pp. 275-279.
  146. M. Yaso, S. Morito, T. Ohba, et al., *Materials Science and Engineering A*, 2008. **481**: pp. 770-773.
  147. A. Stormvinter, A. Borgenstam, and J. Agren, *Metallurgical and Materials Transactions A*, 2012. **43A**(10): pp. 3870-3879.
  148. E. Bauergrosse, J. P. Morniroli, M. Khachfi, et al., *Journal of the Less-Common Metals*, 1986. **117**(1-2): pp. 231-236.
  149. W. Dudzinski, J. P. Morniroli, and M. Gantois, *Journal of Materials Science*, 1980. **15**(6): pp. 1387-1401.
  150. J. T. H. Pearce, *Journal of Materials Science Letters*, 1983. **2**(8): pp. 428-432.
  151. S. D. Carpenter, D. E. O. S. Carpenter, and J. T. H. Pearce, *Journal of Alloys and Compounds*, 2010. **494**(1-2): pp. 245-251.

- 
152. D. V. Shtansky, K. Nakai, and Y. Ohmori, *Acta Materialia*, 1999. **47**(4): pp. 1105-1115.
  153. E. S. Machlin and M. Cohen, *Journal of Metals*, 1951. **3**(11): pp. 1019-1029.
  154. G. Ghosh, C. E. Campbell, and G. B. Olson, *Metallurgical and Materials Transactions A*, 1999. **30**(3): pp. 501-512.
  155. G. Ghosh and G. B. Olson, *Acta Materialia*, 2002. **50**(8): pp. 2099-2119.
  156. S. S. Babu, K. Hono, and T. Sakurai, *Metallurgical and Materials Transactions A*, 1994. **25**(3): pp. 499-508.
  157. J. R. Yang, T. H. Yu, and C. H. Wang, *Materials Science and Engineering A*, 2006. **438**: pp. 276-280.
  158. C. Servant and G. Cizeron, *Materials Science and Engineering A*, 1989. **117**: pp. 175-189.
  159. I. Tamura, H. Yoshimura, M. Ibaraki, et al., *Transactions of the Japan Institute of Metals*, 1964. **5**(2): pp. 97-99.
  160. J. W. Stewart, R. C. Thomson, and H. Bhadeshia, *Journal of Materials Science*, 1994. **29**(23): pp. 6079-6084.
  161. R. C. Thomson and M. K. Miller, *Applied Surface Science*, 1995. **87-8**(1-4): pp. 185-193.
  162. S. S. Babu, K. Hono, and T. Sakurai, *Applied Surface Science*, 1993. **67**(1-4): pp. 321-327.
  163. R. C. Thomson and M. K. Miller, *Applied Surface Science*, 1996. **94-5**: pp. 313-319.
  164. R. C. Thomson and H. Bhadeshia, *Applied Surface Science*, 1993. **67**(1-4): pp. 334-341.
  165. R. C. Thomson and M. K. Miller, *Acta Materialia*, 1998. **46**(6): pp. 2203-2213.
  166. A. Matsuzaki, H. K. D. H. Bhadeshia, and H. Harada, *Tempering of Martensite Under the Influence of an Externally Applied Stress*, in *G. R. Speich symposium*, 1992, Iron and Steel Society AIME. pp. 47-52.
  167. L. C. Chang and H. Bhadeshia, *Journal of Materials Science*, 1996. **31**(8): pp. 2145-2148.
  168. D. V. Shtansky, K. Nakai, and Y. Ohmori, *Acta Materialia*, 2000. **48**(4): pp. 969-983.
  169. D. P. Field, *Ultramicroscopy*, 1997. **67**(1-4): pp. 1-9.
  170. H. O. Martikainen, M. A. Korhonen, and V. K. Lindroos, *Physica Status Solidi a-Applied Research*, 1983. **75**(2): pp. 559-566.

- 
171. S. Zaefferer, *Ultramicroscopy*, 2007. **107**(2-3): pp. 254-266.
  172. K. Z. Baba-Kishi, *Journal of Materials Science*, 2002. **37**(9): pp. 1715-1746.
  173. D. Williams and C. B. Carter, *Kikuchi Diffraction*, in *Transmission Electron Microscopy*, 2009, Springer US. pp. 311-322.
  174. D. G. Coates, *Philosophical Magazine*, 1967. **16**(144): pp. 1179-1185.
  175. A. F. Gourgues, H. M. Flower, and T. C. Lindley, *Materials Science and Technology*, 2000. **16**(1): pp. 26-40.
  176. M. R. Barnett, A. Ghaderi, J. Quinta da Fonseca, et al., *Acta Materialia*, 2014. **80**(0): pp. 380-391.
  177. F. Ernst, M. L. Mulvihill, O. Kienzle, et al., *Journal of the American Ceramic Society*, 2001. **84**(8): pp. 1885-1890.
  178. A. Koblischka-Veneva and F. Mucklich, *Crystal Engineering*, 2002. **5**(3-4): pp. 235-242.
  179. J. Hou, Z. Zhang, W. Preis, et al., *Journal of the European Ceramic Society*, 2011. **31**(5): pp. 763-771.
  180. M. Bestmann and D. J. Prior, *Journal of Structural Geology*, 2003. **25**(10): pp. 1597-1613.
  181. D. J. Prior, E. Mariani, and J. Wheeler, *EBSD in the Earth Sciences: Applications, Common Practice, and Challenges*, in *Electron Backscatter Diffraction in Materials Science*, ed. A. J. Schwartz, M. Kumar, et al., 2009, Springer US. pp. 345-360.
  182. S. X. Ren, E. A. Kenik, K. B. Alexander, et al., *Microscopy and Microanalysis*, 1998. **4**(1): pp. 15-22.
  183. D. Chen, J.-C. Kuo, and W.-T. Wu, *Ultramicroscopy*, 2011. **111**(9-10): pp. 1488-1494.
  184. D. R. Steinmetz and S. Zaefferer, *Materials Science and Technology*, 2010. **26**(6): pp. 640-645.
  185. F. J. Humphreys, *Journal of Microscopy-Oxford*, 1999. **195**: pp. 170-185.
  186. F. J. Humphreys, *Journal of Materials Science*, 2001. **36**(16): pp. 3833-3854.
  187. F. J. Humphreys, *Scripta Materialia*, 2004. **51**(8): pp. 771-776.
  188. D. Dingley, *Journal of Microscopy-Oxford*, 2004. **213**: pp. 214-224.
  189. F. J. Humphreys, Y. Huang, I. Brough, et al., *Journal of Microscopy-Oxford*, 1999. **195**: pp. 212-216.
  190. Y. Chen, J. Hjelen, S. S. Gireesh, et al., *Journal of Microscopy*, 2012.

- 
- 245**(2): pp. 111-118.
191. F. J. Humphreys, P. S. Bate, and P. J. Hurley, *Journal of Microscopy-Oxford*, 2001. **201**: pp. 50-58.
192. A. W. Wilson and G. Spanos, *Materials Characterization*, 2001. **46**(5): pp. 407-418.
193. M. X. Zhang and P. M. Kelly, *Materials Characterization*, 1998. **40**(3): pp. 159-168.
194. S. Zaefferer, *Crystal Research and Technology*, 2011. **46**(6): pp. 607-628.